Theoretical microfluidics

Henrik Bruus
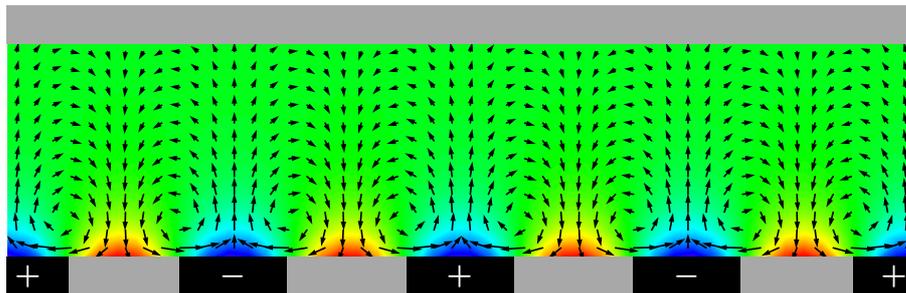
Preface

In the fall 2003 MIC launched a new fifth semester course at the Technical University of Denmark (course no. 33241, 5 ECTS) to provide a general and broad introduction to theoretical aspects of the new field of lab-on-a-chip systems.

In the first run of the course I tried to use existing books as basic material. However, it soon became clear that these books did not cover the material I wanted to teach. I let more and more of the teaching rely on substantial exercises, many of which were based on experimental problems from the laboratories at MIC. These exercises form the basis of the lecture notes at hand. The notes are being written during the course from September to December 2004. The first chapter is ready for the first lecture, while the rest will follow at a rate of one chapter per week.

I hope that the students will bear over with the many printing mistakes and less than optimal formulations that undoubtedly will appear, and that they will participate actively in the efforts to create new and up-to-date teaching material at the right level of difficulty. Hopefully, these lecture notes will be both inspiring and challenging.

<div align="center">

Henrik Bruus
MIC – Department of Micro and Nanotechnology
Technical University of Denmark
30 August 2004

</div>

This second edition of the lecture notes has benefited from numerous corrections and comments from my students and colleagues. Moreover, three new chapters and two appendices have been added. I hope that the notes appear even more useful in their present form.

<div align="center">

Henrik Bruus
MIC – Department of Micro and Nanotechnology
Technical University of Denmark
28 August 2005

</div>

As with the previous editions, this third edition of the lecture notes has benefited from numerous corrections and comments from my students and colleagues. Moreover, solutions to most of the exercises as well as a new chapter on acoustics in microfluidcs have been added. I hope that these last modifications have improved the lecture notes further.

<div align="center">

Henrik Bruus

MIC – Department of Micro and Nanotechnology

Technical University of Denmark

29 August 2006

</div>

Contents

Chapter 1

Basic concepts in microfluidics

The field of lab-on-a-chip systems has evolved dramatically since it was initiated in the early 1990ies. It is a field that is mainly driven by technological applications, the main vision being to develop entire bio/chemical laboratories on the surface of silicon or polymer chips. Many of the techniques developed the past fifty years in connection with the revolutionary microelectronics industry can be used to fabricate lab-on-chip systems. It is, e.g., relatively easy to etch 100 μm wide channels for fluid handling at the surface of silicon wafers using well-established protocols. But as we shall see, polymer-based lab-on-a-chip systems have emerged the recent years, and these systems promise cheaper and faster production cycles. The study of fluid motion in microsystems is denoted microfluidics.

There are several advantages of scaling down standard laboratories setups by a factor of 1000 or more from the decimeter scale to the 100 μm scale. One obvious advantage is the dramatic reduction in the amount of required sample. A linear reduction by a factor of 10^3 amounts to a volume reduction by a factor of 10^9, so instead of handling 1 L or 1 mL a lab-on-a-chip system could easily deal with as little as 1 nL or 1 pL. Such small volumes allow for very fast analysis, efficient detection schemes, and analysis even when large amounts of sample are unavailable. Moreover, the small volumes makes it possible to develop compact and portable systems that might ease the use of bio/chemical handling and analysis systems tremendously. Finally, as has been the case with microelectronics, it is the hope by mass production to manufacture very cheap lab-on-a-chip systems.

Lab-on-a-chip (LOC) systems can be thought of as the natural generalization of the existing integrated electronic circuits (IC) and microelectromechanical systems (MEMS). Why confine the systems to contain only electric and mechanical parts? Indeed, a lab-on-chip system can really be thought of a the shrinking of an entire laboratory to a chip. One example of a system going in that direction is shown in Fig. 1.1: an integrated lab-on-a-chip system fabricated at MIC , DTU. This particular system contains optical (lasers and wave guides), chemical (channels and mixers), and electronic (photodiodes) components. Perhaps, only our imagination sets the limits of what could be in a lab-on-a-chip system. It is expected that lab-on-a-chip systems will have great impact in biotech industries, pharmacology, medical diagnostics, forensics, environmental monitoring and basic research.
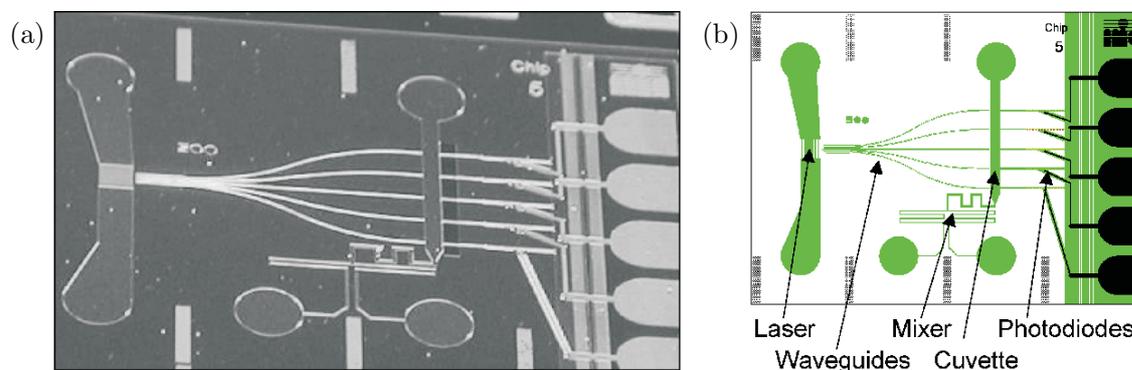
Figure 1.1: (a) A picture of a 2 cm by 3 cm lab-on-a-chip system fabricated at MIC in 2003 for optical analysis of chemical reactions. The system is a hybrid polymer/silicon device. (b) Overview of the components of the system. The device is made on a silicon substrate containing the integrated photodiodes, while the laser, waveguides, mixer and cuvette are made in a polymer film on top of the substrate. Courtesy the groups of Geschke, Kristensen, and Kutter   (MIC, DTU).

The fundamental laws of Nature underlying our understanding of the operation of lab-on-a-chip systems are all well-known. We shall draw on our knowledge from mechanics, fluid dynamics, electromagnetism, thermodynamics and physical chemistry during this course. What is new, however, is the interplay between many different forces and the change of the relative importance of these forces in the micro-regime as compared to the macro-regime. Surface effects that often can be neglected at the macro-scale become increasingly dominant in microfluidics as size is diminished. For example, it turns out that volume forces like gravity and inertia that are very prominent in our daily life become largely unimportant in lab-on-a-chip systems. Instead, we must get used to the fact that surface related forces, like surface tension and viscosity, become dominant. As a consequence, we must rebuild our intuition and be prepared for some surprises on the way.

1.1   Fluids and fields

The main purpose of a lab-on-a-chip system is to handle fluids. A fluid, i.e., either a liquid or a gas, is characterized by the property that it will deform continuously and with ease under the action of external forces. A fluid does not have a preferred shape, and different parts of it may be rearranged freely without affecting the macroscopic properties of the fluid. In a fluid the presence of shear forces, however small in magnitude, will result in large changes in the relative positions of the fluid elements. In contrast, the changes in the relative positions of the atoms in a solid remain small under the action of any small external force. When applied external forces cease to act on a fluid, it will not necessarily retract to its initial shape. This property is also in contrast to a solid, which relaxes to its initial shape when no longer influenced by external forces.
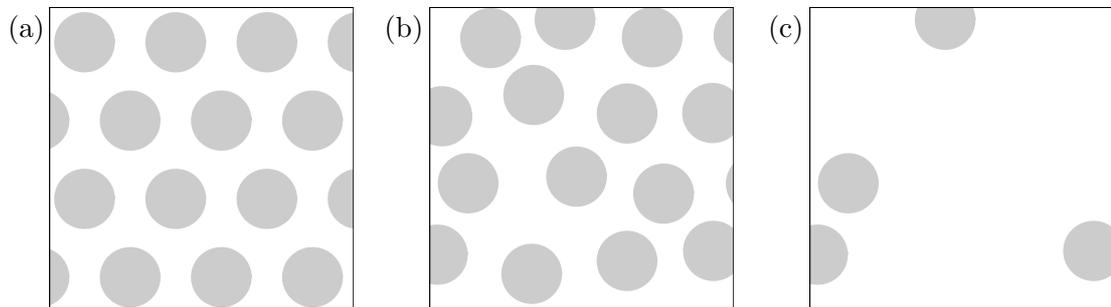
Figure 1.2: (a) A sketch of a typical solid with 0.1 nm wide molecules (atoms) and a lattice constant of 0.3 nm. The atoms oscillate around the indicated equilibrium points forming a regular lattice. (b) A sketch of a liquid with the same molecules and same average inter-molecular distance 0.3 nm as in panel (a). The atoms move around in an thermally induced irregular pattern. (c) A sketch of a gas with the same atoms as in panel (a). The average inter-atomic distance is 3 nm, and the motion is free between the frequent inter-atomic collisions.

1.1.1 Fluids: liquids and gases

The two main classes of fluids, the liquids and the gases, differ primarily by the densities and by the degree of interaction between the constituent molecules as sketched in Fig. 1.2. The density $\rho_{gas} \approx 1$ kg m^{-3} of an ideal gas is so low, at least a factor of 10^3 smaller than that of a solid, that the molecules move largely as free particles that only interact by direct collisions at atomic distances, ≈ 0.1 nm. The relatively large distance between the gas molecules, ≈ 3 nm, makes the gas compressible. The density $\rho_{liq} \approx 10^3$ kg m^{-3} of a liquid is comparable to that of a solid, i.e., the molecules are packed as densely as possible with a typical average inter-molecular distance of 0.3 nm, and a liquid can for many practical purposes be considered incompressible.

The inter-molecular forces in a liquid are of quite intricate quantum and electric nature since each molecule is always surrounded by a number of molecules within atomic distances. In model calculations of simple liquids many features can be reproduced by assuming the simple Lennard–Jones pair-interaction potential, $V_{LJ}(r) = 4\varepsilon\big[(\sigma/r)^{12} - (\sigma/r)^6\big]$, between any pair of molecules. Here r is the distance betweens the molecules, while the maximal energy of attraction ε and the collision diameter σ are material parameters typical of the order 100 K$\times k_B$ and 0.3 nm, respectively. The corresponding inter-molecular force is given by the derivative $F_{LJ}(r) = -dV_{LJ}/dr$. The Lennard–Jones potential is shown in Fig. 1.3a and discussed further in Exercise 1.2.

At short time intervals and up to a few molecular diameters the molecules in a liquid are ordered almost as in a solid. However, whereas the ordering in solids remains fixed in time and space,[1] the ordering in liquids fluctuates. In some sense the thermal fluctuations are strong enough to overcome the tendency to order, and this is the origin of the ability

---

[1] the molecules in a solid execute only small, thermal oscillations around equilibrium points well-described by a regular lattice
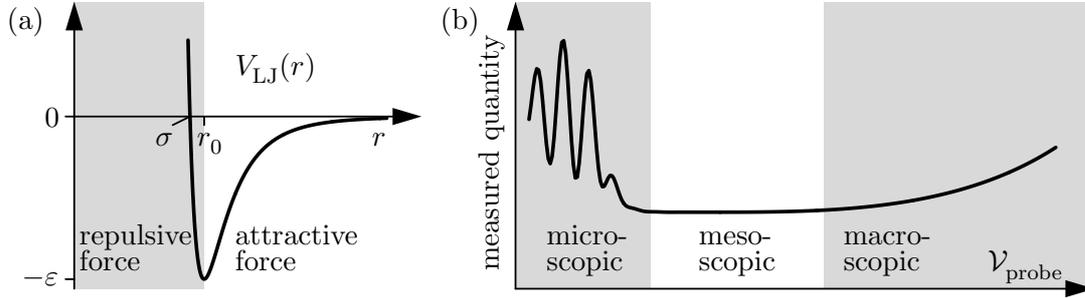
Figure 1.3: (a) The Lennard–Jones pair-potential $V_{\mathrm{LJ}}(r)$ often used to describe the interaction potential between two molecules at distance r, see also Exercise 1.2. For small distances, $r < r_0 \approx 0.3$ nm the interaction forces are strongly repulsive (gray region), while for large distances, $r > r_0$, they are weakly attractive. (b) A sketch of some measured physical quantity of a liquid as a function of the volume $\mathcal{V}_{\mathrm{probe}}$ probed by some instrument. For microscopic probe volumes (left gray region) large molecular fluctuations will be observed. For mesoscopic probe volumes (white region) a well-defined local value of the property can be measured. For macroscopic probe volumes (right gray region) gentle variations in the fluid due to external forces can be observed.

of liquids to flow.

1.1.2   The continuum hypothesis and fluid particles

Although fluids are quantized on the length scale of inter-molecular distances (of the order 0.3 nm for liquids and 3 nm for gases), they appear continuous in most lab-on-a-chip applications, since these typically are defined on macroscopic length scales of the order 10 μm or more. In this course we shall therefore assume the validity of the continuum hypothesis, which states that the macroscopic properties of a fluid is the same if the fluid were perfectly continuous in structure instead of, as in reality, consisting of molecules. Physical quantities such as the mass, momentum and energy associated with a small volume of fluid containing a sufficiently large number of molecules are to be taken as the sum of the corresponding quantities for the molecules in the volume.

The continuum hypothesis leads to the concept of fluid particles, the basic constituents in the theory of fluids. In contrast to an ideal point-particle in ordinary mechanics, a fluid particle in fluid mechanics has a finite size. But how big is it? Well, the answer to this question is not straightforward. Imagine, as illustrated in Fig. 1.3b, that we probe a given physical quantity of a fluid with some probe sampling a volume $\mathcal{V}_{\mathrm{probe}}$ of the fluid at each measurement. Let $\mathcal{V}_{\mathrm{probe}}$ change from (sub-)atomic to macroscopic dimensions. At the atomic scale (using, say, a modern AFM or STM) we would encounter large fluctuations due to the molecular structure of the fluid, but as the probe volume increases we soon enter a size where steady and reproducible measurements are obtained. This happens once the probe volume is big enough to contain a sufficiently large number of molecules, such that well-defined average values with small statistical fluctuations are obtained. As

studied in Exercise 1.3 a typical possible side length λ^* in a cubic fluid particle is

$$\lambda^* \approx 10 \text{ nm}. \tag{1.1}$$

Such a fluid particle contains approximately 4×10^4 molecules and exhibits number fluctuations of the order 0.5%. If the size of the fluid particle is taken too big the probe volume could begin to sample regions of the fluid with variations in the physical properties due to external forces. In that case we are beyond the concept of a constituent particle and enters the regime we actually would like to study, namely, how do the fluid particles behave in the presence of external forces.

A fluid particle must thus be ascribed a size λ^* in the mesoscopic range. It must be larger than microscopic lengths ($\simeq 0.3$ nm) to contain a sufficiently large amount of molecules, and it must be smaller than macroscopic lengths ($\simeq 10~\mu$m) over which external forces change the property of the fluid. Of course, this does not define an exact size, and in fluid mechanics it is therefore natural to work with physical properties per volume, such as mass density, energy density, force density and momentum density. In such considerations the volume is taken to the limit of a small, but finite, fluid particle volume, and not to the limit of an infinitesimal volume.

The continuum hypothesis breaks down when the system under consideration approaches molecular scale. This happens in nanofluidics, e.g., in liquid transport through nano-pores in cell membranes or in artificially made nano-channels.

1.1.3 The velocity, pressure and density field

Once the concept of fluid particles in a continuous fluid has been established we can move on and describe the physical properties of the fluid in terms of fields. This can basically be done in two ways as illustrated in Fig. 1.4 for the case of the velocity field. In these notes we shall use the Eulerian description, Fig. 1.4a, where one focuses on fixed points $\mathbf{r}$ in space and observe how the fields evolve in time at these points, i.e., the position $\mathbf{r}$ and the time t are independent variables. The alternative is the Lagrangian description, Fig. 1.4b, where one follows the history of individual fluid particles as the move through the system, i.e., the coordinate $\mathbf{r}_a(t)$ of particle a depends on time.

In the Eulerian description the value of any field variable $F(\mathbf{r}, t)$ is defined as the average value of the corresponding molecular quantity $F_{\text{mol}}(\mathbf{r}', t)$ for all the molecules contained in some liquid particle of volume $\Delta\mathcal{V}(\mathbf{r})$ positioned at $\mathbf{r}$ at time t,

$$F(\mathbf{r}, t) = \left\langle F_{\text{mol}}(\mathbf{r}', t) \right\rangle_{\mathbf{r}' \in \Delta\mathcal{V}(\mathbf{r})}. \tag{1.2}$$

The field variables can be scalars (such as density ρ, viscosity η, pressure p, temperature T, and free energy $\mathcal{F}$), vectors (such as velocity $\mathbf{v}$, current density $\mathbf{J}$, pressure gradient $\boldsymbol{\nabla}p$, force densities $\mathbf{f}$, and electric fields $\mathbf{E}$) and tensors (such as stress tensor σ and velocity gradient $\boldsymbol{\nabla}\mathbf{v}$).

To obtain a complete description of the state of a moving fluid it is necessary to know the three components of the velocity field $\mathbf{v}(\mathbf{r}, t)$ and any two of the thermodynamical variables of the fluid, e.g., the pressure field $p(\mathbf{r}, t)$ and the density field $\rho(\mathbf{r}, t)$. All other
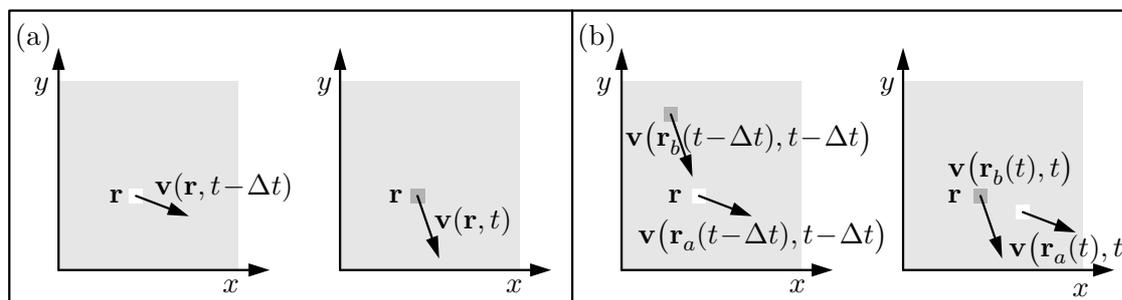
Figure 1.4: (a) The velocity field $\mathbf{v}(\mathbf{r}, t)$ in the Eulerian description at the point $\mathbf{r}$ at the two times $t - \Delta t$ and t. The spatial coordinates $\mathbf{r}$ are independent of the temporal coordinate t. (b) The Lagrangian velocity fields $\mathbf{v}(\mathbf{r}_a(t), t)$ and $\mathbf{v}(\mathbf{r}_b(t), t)$ of fluid particles a (white) and b (dark gray). The particles pass the point $\mathbf{r}$ at time $t - \Delta t$ and t, respectively. The particle coordinates $\mathbf{r}_{a,b}(t)$ depend on t. Note that $\mathbf{r}_a(t - \Delta t) = \mathbf{r}$ and $\mathbf{r}_b(t) = \mathbf{r}$.

thermodynamical quantities can be derived from these fields together with the equation of state of the fluid.

1.2   SI units and mathematical notation

Notation is an important part in communicating scientific and technical material. Especially in fluid mechanics the mathematical notation is important due to the involved many-variable differential calculus on the scalar, vector and tensor fields mentioned in the previous section. Instead of regarding units and notation as an annoying burden the student should instead regard it as part of the trade that need to be mastered by the true professional. Learn the basic rules, and stick to them thereafter.

1.2.1   SI units

Throughout these notes we shall use the SI units. If not truly familiar with this system, the name and spelling of the units, and the current best values of the fundamental physical constants of Nature the reader is urged to consult the web-site of National Institute of Standards and Technology (NIST) for constants, units, and uncertainty at

$$\text{http://physics.nist.gov/cuu/} \ . \tag{1.3}$$

A scalar physical variable is given by a number of significant digits, a power of ten and a proper SI unit. The power of ten can be moved to the unit using the prefixes (giga, kilo, micro, atto etc.). The SI unit can be written in terms of the seven fundamental units or using the derived units. As an example the viscosity η of water at 20°C is written as

$$\eta = 1.002 \times 10^{-3} \ \text{kg m}^{-1}\text{s}^{-1} = 1.002 \ \text{mPa s}. \tag{1.4}$$

Note the multiplication sign before the power of ten and the space after it, and note that the SI units are written in roman and *not in italics*. Most type setting systems will

automatically use italics for letters written in equations. Note also the use of space and no multiplication signs between the units. Be aware that even though many units are capitalized as are the names of the physicists given rise to them, e.g., Pa and Pascal, the unit itself is never capitalized when written in full, e.g., pascal. Also, the unit is written pascal without plural form whether there is one, five or 3.14 of them.

There will be two exceptions from the strict use of SI units. Sometimes, just as above, temperatures will be given in °C, so be careful when inserting values for temperature in formulae. Normally, a temperature T in an expression calls for values in kelvin. The other exception from SI units is the atomic unit of energy, electronvolt (eV),

$$1 \text{ eV} = 1.602 \times 10^{-19} \text{ J} = 0.1602 \text{ aJ}. \tag{1.5}$$

Note, that it would be possible to use attojoule instead of electronvolt, but this is rarely done.

1.2.2 Vectors, derivatives and the index notation

The mathematical treatment of microfluidic problems is complicated due to the presence of several scalar, vector and tensor fields and the non-linear partial differential equations that govern them. To facilitate the treatment some simplifying notation is called for.

First, a suitable coordinate system must be chosen. We shall encounter three: Cartesian coordinates (x, y, z) with corresponding unit vectors $\mathbf{e}_x$, $\mathbf{e}_y$, and $\mathbf{e}_z$; cylindrical coordinates (r, ϕ, z) with corresponding unit vectors $\mathbf{e}_r$, $\mathbf{e}_\phi$, and $\mathbf{e}_z$; and spherical coordinates (r, θ, ϕ) with corresponding unit vectors $\mathbf{e}_r$, $\mathbf{e}_\theta$, and $\mathbf{e}_\phi$. The Cartesian unit vectors are special since they are constant in space, whereas all other sets of unit vectors depend on position in space. For simplicity, we postpone the usage of the curvilinear coordinates to later chapters and use only Cartesian coordinates in the following.

The position vector $\mathbf{r} = (r_x, r_y, r_z) = (x, y, z)$ can be written as

$$\mathbf{r} = r_x \, \mathbf{e}_x + r_y \, \mathbf{e}_y + r_z \, \mathbf{e}_z = x \, \mathbf{e}_x + y \, \mathbf{e}_y + z \, \mathbf{e}_z. \tag{1.6}$$

In fact, any vector $\mathbf{v}$ can be written in terms of its components v_i (where for Cartesian coordinates $i = x, y, z$) as

$$\mathbf{v} = \sum_{i=x,y,z} v_i \, \mathbf{e}_i \equiv v_i \, \mathbf{e}_i \tag{1.7}$$

In the last equality we have introduced the Einstein summation convention: per definition a repeated index always implies a summation over that index. Other examples of this handy notation, the so-called index notation, is the scalar product,

$$\mathbf{v} \cdot \mathbf{u} = v_i u_i, \tag{1.8}$$

the length v of a vector $\mathbf{v}$,

$$v = |\mathbf{v}| = \sqrt{\mathbf{v}^2} = \sqrt{\mathbf{v} \cdot \mathbf{v}} = \sqrt{v_i v_i}, \tag{1.9}$$

and the ith component of the vector-matrix equation $\mathbf{u} = M\mathbf{v}$,

$$u_i = M_{ij}\, v_j. \tag{1.10}$$

Further studies of the index notation can be found in Exercise 1.4.

For the partial derivatives of some function $F(\mathbf{r}, t)$ we use the symbols ∂_i, with $i = x, y, z$, and ∂_t,

$$\partial_x F \equiv \frac{\partial F}{\partial x}, \quad \text{and} \quad \partial_t F \equiv \frac{\partial F}{\partial t}, \tag{1.11}$$

while for the total time-derivative, as, e.g., in the case of the Lagrangian description of some variable $F\big(\mathbf{r}(t), t\big)$ following the fluid particles (see Fig. 1.4b), we use the symbol d_t,

$$d_t F \equiv \frac{\mathrm{d}F}{\mathrm{d}t} = \partial_t F + \big(\partial_t r_i\big)\partial_i F = \partial_t F + v_i \partial_i F. \tag{1.12}$$

The nabla operator $\boldsymbol{\nabla}$ containing the spatial derivatives plays an important role in differential calculus. In Cartesian coordinates it is given by

$$\boldsymbol{\nabla} \equiv \mathbf{e}_x \partial_x + \mathbf{e}_y \partial_y + \mathbf{e}_z \partial_z = \mathbf{e}_i \partial_i. \tag{1.13}$$

Note that we have written the differential operators to the right of the unit vectors. While not important in Cartesian coordinates it is crucial when working with curvilinear coordinates. The Laplace operator, which appears in numerous partial differential equations in theoretical physics, is just the square of the nabla operator,

$$\boldsymbol{\nabla}^2 = \nabla^2 \equiv \partial_i \partial_i. \tag{1.14}$$

In terms of the nabla-operator the total time derivative in Eq. (1.12) can be written as

$$d_t F\big(\mathbf{r}(t), t\big) = \partial_t F + (\mathbf{v} \cdot \boldsymbol{\nabla})F. \tag{1.15}$$

Concerning integrals, we denote the 3D integral measure by $\mathrm{d}\mathbf{r}$, so that in Cartesian coordinates we have $\mathrm{d}\mathbf{r} = \mathrm{d}x\,\mathrm{d}y\,\mathrm{d}z$, in cylindrical coordinates $\mathrm{d}\mathbf{r} = r\mathrm{d}r\,\mathrm{d}\phi\,\mathrm{d}z$, and in spherical coordinates $\mathrm{d}\mathbf{r} = r^2\mathrm{d}r\,\sin\theta\mathrm{d}\theta\,\mathrm{d}z$. We also consider definite integrals as operators acting on the integrand, thus we keep the integral sign and the associated integral measure together to the left of the integrand. As an example, the integral over a spherical body with radius a of the scalar function $S(\mathbf{r})$ is written as

$$\int_{\text{sphere}} S(x, y, z)\, \mathrm{d}x\mathrm{d}y\mathrm{d}z = \int_{\text{sphere}} \mathrm{d}\mathbf{r}\, S(\mathbf{r}) = \int_0^a r^2\mathrm{d}r \int_0^\pi \sin\theta\mathrm{d}\theta \int_0^{2\pi} \mathrm{d}\phi\, S(r, \theta, \phi). \tag{1.16}$$

When working with vectors and tensors it is advantageous to use the following two special symbols: the Kronecker delta δ_{ij},

$$\delta_{ij} = \begin{cases} 1, & \text{for } i = j, \\ 0, & \text{for } i \neq j, \end{cases} \tag{1.17}$$

and the Levi–Civita symbol ϵ_{ijk},

$$\epsilon_{ijk} = \begin{cases} +1, & \text{if } (ijk) \text{ is an even permutation of (123) or } (xyz), \\ -1, & \text{if } (ijk) \text{ is an odd permutation of (123) or } (xyz), \\ 0, & \text{otherwise.} \end{cases} \qquad (1.18)$$

In the index notation the Levi–Cevita symbol appears directly in the definition of the cross product of two vectors $\mathbf{u}$ and $\mathbf{v}$,

$$(\mathbf{u} \times \mathbf{v})_i \equiv \epsilon_{ijk} u_j v_k. \qquad (1.19)$$

and in the definition of the rotation $\boldsymbol{\nabla} \times \mathbf{v}$ of a vector $\mathbf{v}$. The expression for the ith component of the rotation is:

$$(\boldsymbol{\nabla} \times \mathbf{v})_i \equiv \epsilon_{ijk} \partial_j v_k. \qquad (1.20)$$

To calculate in the index notation the rotation of a rotation, such as $\boldsymbol{\nabla} \times \boldsymbol{\nabla} \times \mathbf{v}$, or the rotation of a cross product it is very helpful to know the following expression for the product of two Levi–Civita symbols with one pair of repeated indices (here k):

$$\epsilon_{ijk}\epsilon_{lmk} = \delta_{il}\delta_{jm} - \delta_{im}\delta_{jl}. \qquad (1.21)$$

Note the plus sign when pairing index 1 with 1 and 2 with 2 (direct pairing), while a minus sign appears when pairing index 1 with 2 and 2 with 1 (exchange pairing).

Let us end this short introduction to the index notation by an explicit example, namely proof of the double cross product identity

$$\mathbf{a} \times \mathbf{b} \times \mathbf{c} = (\mathbf{a} \cdot \mathbf{c})\mathbf{b} - (\mathbf{a} \cdot \mathbf{b})\mathbf{c}. \qquad (1.22)$$

First we write out the ith component of the left-hand side using the Levi–Civita symbol for each cross product, one at a time,

$$\begin{aligned} (\mathbf{a} \times \mathbf{b} \times \mathbf{c})_i = \left[\mathbf{a} \times (\mathbf{b} \times \mathbf{c})\right]_i &= \epsilon_{ijk} a_j (\mathbf{b} \times \mathbf{c})_k \\ &= \epsilon_{ijk} a_j \left(\epsilon_{klm} b_l c_m\right) = \epsilon_{ijk}\epsilon_{lmk}\, a_j b_l c_m, \end{aligned} \qquad (1.23)$$

where in the last equation we have made an even permutation of the indices in the second Levi-Civita symbol, $\epsilon_{klm} = \epsilon_{lmk}$. Finally, we use Eq. (1.21) to express the product of the two Levi-Civita symbols as a linear combination of Kronecker deltas,

$$\begin{aligned} \epsilon_{ijk}\epsilon_{lmk}\, a_j b_l c_m &= \left(\delta_{il}\delta_{jm} - \delta_{im}\delta_{jl}\right) a_j b_l c_m = a_j c_j b_i - a_j b_j c_i \\ &= (\mathbf{a} \cdot \mathbf{c})b_i - (\mathbf{a} \cdot \mathbf{b})c_i = \left[(\mathbf{a} \cdot \mathbf{c})\mathbf{b} - (\mathbf{a} \cdot \mathbf{b})\mathbf{c}\right]_i, \end{aligned} \qquad (1.24)$$

which is the ith component of the right-hand side of Eq. (1.22).

1.3 The continuity equation

We have now cleared the ground for the derivation of our first fundamental equation of fluid mechanics, the continuity equation. This equation expresses the conservation of mass in classical mechanics.
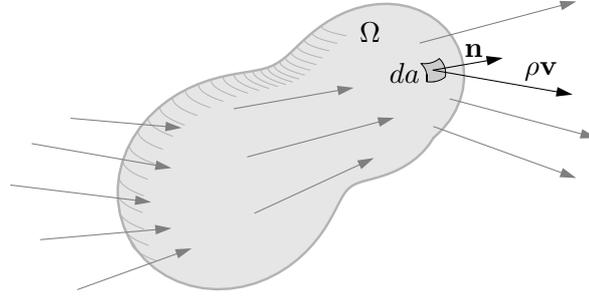
Figure 1.5: A sketch of the current density field $\rho\mathbf{v}$ flowing through an arbitrarily shaped region Ω. Any infinitesimal area da is associated with an outward pointing unit vector $\mathbf{n}$ perpendicular to the local surface. The current through the area da is given by da times the projection $\rho\mathbf{v} \cdot \mathbf{n}$ of the current density on the surface unit vector.

1.3.1   Compressible fluids

We begin by considering the general case of a compressible fluid, i.e., a fluid where the density ρ may vary as function of space and time. Consider an arbitrarily shaped, but fixed, region Ω in the fluid as sketched in Fig. 1.5. The total mass $M(\Omega, t)$ inside Ω can be expressed as a volume integral over the density ρ,

$$M(\Omega, t) = \int_\Omega d\mathbf{r}\, \rho(\mathbf{r}, t), \tag{1.25}$$

where we have written the infinitesimal integration volume as $d\mathbf{r}$. Since mass can neither appear nor disappear spontaneously in non-relativistic mechanics, $M(\Omega, t)$ can only vary if mass is flowing into or out from the region Ω through its surface $\partial\Omega$. The mass current density $\mathbf{J}$ is defined as the mass density ρ times the convection velocity $\mathbf{v}$, or the mass flow per oriented unit area per unit time (hence the unit $\mathrm{kg\,m^{-2}\,s^{-1}}$):

$$\mathbf{J}(\mathbf{r}, t) = \rho(\mathbf{r}, t)\, \mathbf{v}(\mathbf{r}, t), \tag{1.26}$$

where $\mathbf{v}$ is the Eulerian velocity field.

Since the region Ω is fixed the time-derivative of the mass $M(\Omega, t)$ can be calculated either as a volume integral by using Eq. (1.25),

$$\partial_t M(\Omega, t) = \partial_t \int_\Omega d\mathbf{r}\, \rho(\mathbf{r}, t) = \int_\Omega d\mathbf{r}\, \partial_t \rho(\mathbf{r}, t), \tag{1.27}$$

or as a surface integral over $\partial\Omega$ of the mass current density using Eq. (1.26) and Fig. 1.5,

$$\partial_t M(\Omega, t) = -\int_{\partial\Omega} da\, \mathbf{n}\cdot\Big(\rho(\mathbf{r}, t)\mathbf{v}(\mathbf{r}, t)\Big) = -\int_\Omega d\mathbf{r}\, \boldsymbol{\nabla}\cdot\Big(\rho(\mathbf{r}, t)\mathbf{v}(\mathbf{r}, t)\Big). \tag{1.28}$$

The last expression is obtained by applying Gauss's theorem. The minus sign is there since the mass inside Ω diminishes if $\rho\mathbf{v}$ is parallel to the outward pointing surface vector

n. From Eqs. (1.27) and (1.28) it follows immediately that

$$\int_\Omega d\mathbf{r} \left[\partial_t \rho(\mathbf{r}, t) + \boldsymbol{\nabla} \cdot \Big(\rho(\mathbf{r}, t) \mathbf{v}(\mathbf{r}, t) \Big) \right] = 0. \tag{1.29}$$

This results is true for any choice of region Ω. But this is only possible if the integrand is zero. Thus we have derived the continuity equation,

$$\partial_t \rho + \boldsymbol{\nabla} \cdot \big(\rho \mathbf{v} \big) = 0 \quad \text{or} \quad \partial_t \rho + \boldsymbol{\nabla} \cdot \mathbf{J} = 0 \tag{1.30}$$

Note that since also electric charge is a conserved quantity, the argument holds if ρ is substituted by the charge density ρ_{el}, and Eq. (1.30) can be read as the continuity equation for charge instead as for mass.

1.3.2 Incompressible fluids

In many cases, especially in microfluidics, where the flow velocities are much smaller than the sound velocity in the liquid, the fluid can be treated as being incompressible. This means that ρ is constant in space and time, and the continuity equation (1.30) is simplified to the following form,

$$\boldsymbol{\nabla} \cdot \mathbf{v} = 0 \quad \text{or} \quad \partial_i v_i = 0, \tag{1.31}$$

a result we shall use extensively in this course.

1.4 The Navier–Stokes equation

Newton's second law for fluid particles is called the Navier–Stokes equation. It constitutes the equation of motion for the Eulerian velocity field $\mathbf{v}(\mathbf{r}, t)$. For an ordinary particle of mass m influenced by external forces $\sum_j \mathbf{F}_j$ Newton's second law reads

$$m\, d_t \mathbf{v} = \sum_j \mathbf{F}_j. \tag{1.32}$$

In fluid mechanics, as discussed in Section 1.1.3, we divide by the volume of the fluid particle and thus work with the density ρ and the force densities $\mathbf{f}_j$. Moreover, in fluid mechanics we must be careful with the time-derivative of the velocity field $\mathbf{v}$. As illustrated in Fig. 1.4 the Eulerian velocity field $\mathbf{v}(\mathbf{r}, t)$ is not the velocity of any particular fluid particle, as it should be in Newton's second law Eq. (1.32). To obtain a physically correct equation of motion a special time-derivative, the so-called material time-derivative D_t defined in the following subsection, is introduced for Eulerian velocity fields. Our first version of the Navier–Stokes equation thus takes the form

$$\rho\, D_t \mathbf{v} = \sum_j \mathbf{f}_j. \tag{1.33}$$

In the following we derive explicit expressions for the material time-derivative D_t and various force densities $\mathbf{f}_j$.

1.4.1   The material time-derivative

The material (or substantial) time-derivative is the one obtained when following the flow of a particle, i.e., when adopting a Lagrangian description. We have already in Eq. (1.15) found the appropriate expression, so using that on the velocity field $\mathbf{v}$ we arrive at

$$\rho\, D_t\mathbf{v}(\mathbf{r},t) \equiv \rho\, d_t\mathbf{v}\big(\mathbf{r}(t),t\big) = \rho\left[\partial_t\mathbf{v}(\mathbf{r},t) + (\mathbf{v}\cdot\boldsymbol{\nabla})\mathbf{v}(\mathbf{r},t)\right]. \tag{1.34}$$

Note the use of the Lagrangian velocity field in the definition.

We can derive the same result by first noting that the total differential of the Eulerian velocity field in general is given by $d\mathbf{v} = dt\partial_t\mathbf{v} + (d\mathbf{r}\cdot\boldsymbol{\nabla})\mathbf{v}$. Second, if we insist on calculating the change due to the flow of a particular fluid particle we must have $d\mathbf{r} = \mathbf{v}dt$. Combining these two expression leads to Eq. (1.34). The same analysis applies for any flow variable, and we can conclude that the material time-derivative D_t is given by

$$D_t = \partial_t + (\mathbf{v}\cdot\boldsymbol{\nabla}). \tag{1.35}$$

The Navier–Stokes equation now takes the form

$$\rho\Big(\partial_t\mathbf{v} + (\mathbf{v}\cdot\boldsymbol{\nabla})\mathbf{v}\Big) = \sum_j \mathbf{f}_j, \tag{1.36}$$

and we proceed by finding the expressions for the force densities $\mathbf{f}_j$.

1.4.2   Body forces

The body forces are external forces that act throughout the entire body of the fluid. In this course we shall in particular work with the gravitational force (in terms of the density ρ and the acceleration of gravity $\mathbf{g}$) and the electrical force (in terms of the charge density ρ_{el} of the fluid and the external electric field $\mathbf{E}$). The resulting force density from these two body forces is

$$\mathbf{f}_{\mathrm{grav}} + \mathbf{f}_{\mathrm{el}} = \rho\mathbf{g} + \rho_{\mathrm{el}}\mathbf{E}. \tag{1.37}$$

1.4.3   The pressure-gradient force

Consider a region Ω in a fluid with a surface $\partial\Omega$ with a surface normal vector $\mathbf{n}$. The total external force $\mathbf{F}_{\mathrm{pres}}$ acting on this region due to the pressure p is given by the surface integral of $-\mathbf{n}p$,

$$\mathbf{F}_{\mathrm{pres}} = \int_{\partial\Omega} da\,(-\mathbf{n}p) = \int_{\partial\Omega} da\,\mathbf{n}(-p) = \int_{\Omega} d\mathbf{r}\,(-\boldsymbol{\nabla}p). \tag{1.38}$$

The minus sign is necessary since $\mathbf{n}p$ is the outward force per area from the region acting on the surroundings, and not the other way around. In the last step of Eq. (1.38) the surface integral is converted to a volume integral using Gauss's theorem.[2] The integrand of the volume integral can thus be identified as the force density due to the pressure:

$$\mathbf{f}_{\mathrm{pres}} = -\boldsymbol{\nabla}p. \tag{1.39}$$

---

[2]The ith component of Eq. (1.38) is found by Gauss's theorem using the vector field $-p\mathbf{e}_i$:
$$\mathbf{e}_i\cdot\int_{\partial\Omega} da\,\mathbf{n}(-p) = \int_{\partial\Omega} da\,\mathbf{n}\cdot(-p\mathbf{e}_i) = \int_{\Omega} d\mathbf{r}\,\boldsymbol{\nabla}\cdot(-p\mathbf{e}_i) = \mathbf{e}_i\cdot\int_{\Omega} d\mathbf{r}\,(-\boldsymbol{\nabla}p).$$

1.4.4   The viscous force and the viscous stress tensor

Consider the same region Ω of the fluid as in the previous subsection. Due to the viscous nature of the fluid, Ω will be subject to frictional forces on its surface $\partial\Omega$ from the flow of the surrounding liquid. The frictional force $\mathrm{d}\mathbf{F}$ on a surface element da with the normal vector $\mathbf{n}$ must be characterized by a tensor rank two since two vectors are needed to determine it: the force and the surface normal need not point in the same direction. This tensor is denoted the viscous stress tensor σ'_{ik}, and it expresses the ith component of the friction force per area acting on a surface element oriented with the surface normal parallel to the kth unit vector $\mathbf{e}_k$. Thus

$$\mathrm{d}F_i = \sigma'_{ik} n_k \, \mathrm{d}a. \tag{1.40}$$

The internal friction is only non-zero when fluid particles move relative to each other, hence σ' depends only on the spatial derivatives of the velocity. For the small velocity gradients encountered in microfluidics we can safely assume that only first order derivatives enter the expression for σ', thus σ'_{ik} must depend linearly on the velocity gradients $\partial_i v_k$.

We can pinpoint the expression for σ'_{ik} further by noticing that it must vanish when the liquid is rotating as a whole, i.e., when the velocity field has the form $\mathbf{v} = \boldsymbol{\omega} \times \mathbf{r}$, where $\boldsymbol{\omega}$ is an angular velocity vector. For this velocity field we have the anti-symmetric relation $\partial_k v_i = -\partial_i v_k$, so σ' vanishes if it only contains the symmetric combinations $\partial_k v_i + \partial_i v_k$ and $\partial_j v_j$ of the first order derivatives. The most general tensor of rank two satisfying these conditions is

$$\sigma'_{ik} = \eta\left(\partial_k v_i + \partial_i v_k - \frac{2}{3}\delta_{ik}\partial_j v_j\right) + \zeta\,\delta_{ik}\partial_j v_j. \tag{1.41}$$

The coefficients η and ζ are denoted the viscosity and second viscosity, respectively. Note, that the viscous stress tensor in Eq. (1.41) has been normalized such that the term with the prefactor η has zero trace. To determine the values of the viscosity coefficients one must go beyond the symmetry consideration presented here, and either measure them experimentally or calculate them by some microscopic model of the liquid. We shall take the phenomenological approach and simply employ the experimental values, however, in Exercise 4.8 we study one example of a simple theoretical model leading to an estimate of the viscosity η.

In analogy with the pressure force, the viscous force $\mathbf{F}_{\mathrm{visc}}$ can be written as a surface integral, which by use of Gauss's theorem is converted into a volume integral,

$$\left(\mathbf{F}_{\mathrm{visc}}\right)_i = \int_{\partial\Omega} \mathrm{d}a\, n_k \sigma'_{ik} = \int_\Omega \mathrm{d}\mathbf{r}\, \partial_k \sigma'_{ik}. \tag{1.42}$$

The integrand is simply the ith component of the viscous force density $\mathbf{f}_{\mathrm{visc}}$,

$$\left(\mathbf{f}_{\mathrm{visc}}\right)_i = \partial_k \sigma'_{ik} = \eta\partial_k\partial_k v_i + \left(\tfrac{1}{3}\eta + \zeta\right)\partial_i(\partial_k v_k). \tag{1.43}$$

1.4.5   The Navier–Stokes equation for compressible fluids

It is customary to combine the force densities due to pressure and viscosity since they both are expressed as gradients. The stress tensor σ_{ik} is defined as

$$\sigma_{ik} \equiv -p\,\delta_{ik} + \sigma'_{ik}, \tag{1.44}$$

which then allow us to write

$$\left(\mathbf{f}_{\mathrm{pres}} + \mathbf{f}_{\mathrm{visc}}\right)_i = \partial_k \sigma_{ik}. \tag{1.45}$$

Inserting the force density expressions Eqs. (1.37) and (1.45) into Eq. (1.36) we obtain the full Navier–Stokes equation for compressible fluids, here written for constant viscosities η and ζ,

$$\rho\left(\partial_t \mathbf{v} + (\mathbf{v}\cdot\boldsymbol{\nabla})\mathbf{v}\right) = -\boldsymbol{\nabla}p + \eta\nabla^2\mathbf{v} + \left(\tfrac{1}{3}\eta + \zeta\right)\boldsymbol{\nabla}(\boldsymbol{\nabla}\cdot\mathbf{v}) + \rho\,\mathbf{g} + \rho_{\mathrm{el}}\mathbf{E}. \tag{1.46}$$

1.4.6 The Navier–Stokes equation for incompressible fluids

In case of incompressible fluids the continuity equation is valid in its simple form $\partial_k v_k = 0$. This reduces the stress tensor Eq. (1.41) to

$$\sigma'_{ik} = \eta\left(\partial_k v_i + \partial_i v_k\right). \tag{1.47}$$

If furthermore the viscosity η is constant, the divergence of the stress tensor is simply

$$\partial_k \sigma_{ik} = -\partial_i p + \eta\partial_k\partial_k v_i. \tag{1.48}$$

The resulting form of the Navier–Stokes equation is the one we shall use in this course,

$$\rho\left(\partial_t \mathbf{v} + (\mathbf{v}\cdot\boldsymbol{\nabla})\mathbf{v}\right) = -\boldsymbol{\nabla}p + \eta\nabla^2\mathbf{v} + \rho\,\mathbf{g} + \rho_{\mathrm{el}}\mathbf{E}, \tag{1.49}$$

and we have succeeded in deriving the second fundamental equation of fluid mechanics.

1.5   Exercises

Exercise 1.1
The inter-molecular distance in air
Assume that air at room temperature and a pressure of 1000 hPa is an ideal gas. Estimate the average inter-molecular distance. Compare the result with that of liquids.

Exercise 1.2
The Lennard-Jones potential for inter-molecular pair-interaction
An approximative but quite useful expression for inter-molecular pair-interactions is the so-called Lennard-Jones potential,

$$V_{\mathrm{LJ}}(r) = 4\varepsilon\left[\left(\frac{\sigma}{r}\right)^{12} - \left(\frac{\sigma}{r}\right)^{6}\right]. \tag{1.50}$$

Let r_0 be the distance at which the pair of molecules experience the smallest possible interaction energy.

(a) Determine r_0 in units of the collision diameter σ and calculate the corresponding interaction energy $V(r_0)$ in units of the maximum attraction energy ε.

(b) Calculate $V_{\mathrm{LJ}}(3\sigma)$ and use the result to discuss the applicability of the ideal gas model to air, given that for nitrogen $\sigma_{\mathrm{N_2}} = 0.3667$ nm and $\varepsilon_{\mathrm{N_2}}/k_{\mathrm{B}} = 99.8$ K.

Exercise 1.3
The size of the fundamental fluid particle
Consider a small cube of side length λ^* in the middle of some liquid. The typical average inter-molecular distance in the liquid is the one discussed in Section 1.1.1. Due to random thermal fluctuations the molecules inside the cube are continuously exchanged with the surrounding liquid, but on average there are N molecules inside the cube. For sufficiently small fluctuations the cube can play the role as a fundamental fluid particle.

(a) Use the standard result from basic statistics that the standard deviation of the counting number of random events (here the number N of molecules inside the cube) is given by $\sqrt{N}$ to estimate the side length λ, such that the relative uncertainty $\sqrt{N}/N$ of the number of molecules is 1%.

(b) Determine λ^* such that the relative uncertainty of the number of molecules is 0.1%.

Exercise 1.4
The index notation
To become familiar with the index notation try to work out the following problems.

(a) Use the index notation to prove that $\partial_k\left(p\,\delta_{ik}\right) = (\boldsymbol{\nabla}p)_i$.

(b) Use the index notation to prove that $\boldsymbol{\nabla}\cdot(\rho\mathbf{v}) = (\boldsymbol{\nabla}\rho)\cdot\mathbf{v} + \rho\boldsymbol{\nabla}\cdot\mathbf{v}$.

(c) Prove that Eq. (1.20) for the rotation of a vector is correct.

(d) Use Eqs. (1.20) and (1.21) to prove that $\boldsymbol{\nabla}\times\boldsymbol{\nabla}\times\mathbf{v} = \boldsymbol{\nabla}(\boldsymbol{\nabla}\cdot\mathbf{v}) - \nabla^2\mathbf{v}$.

Exercise 1.5
The mass current density J
Argue why it is correct as stated in Eq. (1.26) that $\mathbf{J} = \rho\mathbf{v}$ indeed is the mass current density. What is the SI unit of $\mathbf{J}$?

Exercise 1.6
A heuristic derivation of the continuity equation
The continuity equation (1.30) can be derived heuristically by considering the rate of change, $\partial_t(\rho\Delta x\Delta y\Delta z)$, of the mass inside the small cube (shown to the right) due to the flow of mass through the walls. Show that $\partial_t\rho = \partial_x J_x$ if only the x component J_x of the current density is non-zero, and obtain the full continuity equation by generalization.
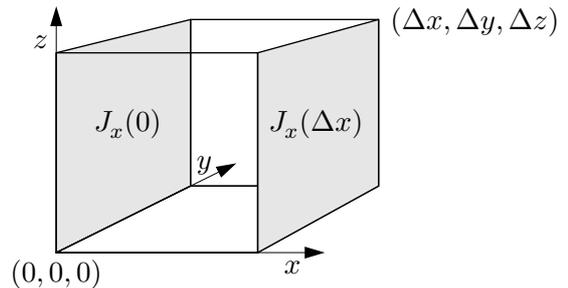
Exercise 1.7
A heuristic derivation of the force densities from pressure and viscosity
Use the figure below to give an heuristic derivation of the pressure-gradient and viscous force density on the right-hand-side of the incompressible Navier–Stokes equation (1.49).

Hints: Consider the three pairs of opposite sides in the cubic fluid element defined by the corners $(0,0,0)$ and $(\Delta x, \Delta y, \Delta z)$. For the pressure, Fig. (a), use that the force

$\Delta\mathbf{F}$ on an area $\Delta\mathcal{A}$ with surface normal $\mathbf{n}$ is given by $p\,\Delta\mathcal{A}\,(-\mathbf{n})$. For the viscosity, Fig. (b), use that the ith force component $(\Delta\mathbf{F})_i$ on an area $\Delta\mathcal{A}$ with a surface normal $\mathbf{n}$ is given by $\sigma'_{ik}n_k\,\Delta\mathcal{A} = \eta(\partial_i v_k + \partial_k v_i)n_k\,\Delta\mathcal{A}$. Let Δx, Δy, and Δz go to zero at the end.
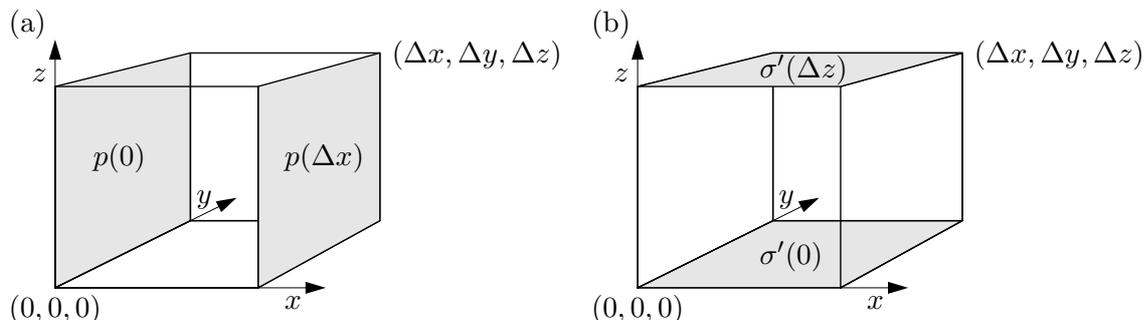
Exercise 1.8
Viscosity of water: measured temperature dependence
Plot two graphs of the viscosity η of water based on Table B.2. One graph of η versus t and another, a so-called Arrhenius plot, of $\ln(\eta)$ versus $1/T$, where T is the temperature in kelvin. Discuss the temperature dependence of the viscosity of water.

1.6 Solutions

Solution 1.1
The inter-molecular distance in air
A single air molecule occupies the volume $\lambda^3 = \mathcal{V}/N$, where $\mathcal{V}$ is the volume of air containing N molecules. The length scale λ thus represents the average inter-molecular distance. Using $p\mathcal{V} = Nk_{\mathrm{B}}T$, with $p = 10^5$ Pa and $T = 300$ K, we find

$$\lambda = \left(\frac{\mathcal{V}}{N}\right)^{\frac{1}{3}} = \left(\frac{k_{\mathrm{B}}T}{p}\right)^{\frac{1}{3}} = 3.5 \text{ nm}. \tag{1.51}$$

Solution 1.2
The Lennard-Jones potential for inter-molecular pair-interaction
   (a) The minimum is found by solving $\partial_r V_{\mathrm{LJ}}(r) = 0$, which yields $r_0 = 2^{\frac{1}{6}}\sigma \approx 1.12\sigma$, and a corresponding interaction energy of $V_{\mathrm{LJ}}(r_0) = -\varepsilon$.
   (b) $V_{\mathrm{LJ}}(3\sigma) = -0.0055\varepsilon$. For nitrogen this means that in the distance $3\sigma_{\mathrm{N}_2} = 1.1$ nm the interaction energy in kelvin is $V_{\mathrm{LJ}}(3\sigma_{\mathrm{N}_2})/k_{\mathrm{B}} = -0.5$ K. The average inter-molecular distance is 3.5 nm, while the average kinetic translation energy in kelvin is $\frac{3}{2}T = 450$ K. Thus, the interaction effects are minute and can be neglected.

Solution 1.3
The size of the fundamental fluid particle
Consider a cube of liquid with side length λ^* in which $\alpha = \sqrt{N}/N$ is a given relative

uncertainty in the number of molecules inside the cube. Each molecule occupies the volume λ^3, where $\lambda = 0.3$ nm is a typical value of the inter-molecular distance in a liquid. Clearly $(\lambda^*)^3 = N\lambda^3$ and $N = \alpha^{-2}$ and thus $\lambda^*(\alpha) = \alpha^{-\frac{2}{3}}\lambda$.

(a) With $\alpha = 10^{-2}$ we find $\lambda^* = 6.5$ nm.

(b) With $\alpha = 10^{-3}$ we find $\lambda^* = 30$ nm.

Solution 1.4

The index notation

(a) Since δ_{ij} is a constant we have $\partial_k \delta_{ij} \equiv 0$ for any value of i, j and k.
We thus find $\partial_k(p\delta_{ij}) = (\partial_k p)\delta_{ij} + p(\partial_k \delta_{ij}) = \partial_i p + 0 = (\boldsymbol{\nabla}p)_i$.

(b) For the divergence of the current density we get
$\boldsymbol{\nabla}\cdot(\rho\mathbf{v}) = \partial_j(\rho v_j) = (\partial_j \rho)v_j + \rho(\partial_j v_j) = (\boldsymbol{\nabla}\rho)\cdot\mathbf{v} + \rho\boldsymbol{\nabla}\cdot\mathbf{v}$

(c) Let us consider the z component of the rotation. Per definition we have $(\boldsymbol{\nabla}\times\mathbf{v})_z = \partial_x v_y - \partial_y v_x$. Using index notation we obtain $(\boldsymbol{\nabla}\times\mathbf{v})_z = \epsilon_{zjk}\partial_j v_k$. the only non-zero terms are carrying the indices $(j,k) = (x,y)$ or $(j,k) = (y,x)$, and since $\epsilon_{zxy} = +1$ and $\epsilon_{zyx} = -1$ we get the desired result: $(\boldsymbol{\nabla}\times\mathbf{v})_z = \epsilon_{zjk}\partial_j v_k = \partial_x v_y - \partial_y v_x$. Likewise for the x and y component of the rotation.

(d) For the rotation of the rotation of the velocity we get
$(\boldsymbol{\nabla}\times\boldsymbol{\nabla}\times\mathbf{v})_i = \epsilon_{ijk}\partial_j(\boldsymbol{\nabla}\times\mathbf{v})_k = \epsilon_{ijk}\partial_j(\epsilon_{klm}\partial_l v_m) = \epsilon_{ijk}\epsilon_{klm}\,\partial_j\partial_l v_m = \epsilon_{ijk}\epsilon_{lmk}\,\partial_j\partial_l v_m$
$= (\delta_{il}\delta_{jm} - \delta_{im}\delta_{jl})\,\partial_j\partial_l v_m = \delta_{il}\delta_{jm}\,\partial_j\partial_l v_m - \delta_{im}\delta_{jl}\,\partial_j\partial_l v_m$
$= \partial_j\partial_i v_j - \partial_j\partial_j v_i = \partial_i(\partial_j v_j) - (\partial_j\partial_j)v_i = \partial_i(\boldsymbol{\nabla}\cdot\mathbf{v}) - \nabla^2 v_i = [\boldsymbol{\nabla}(\boldsymbol{\nabla}\cdot\mathbf{v}) - \nabla^2\mathbf{v}]_i$.

Solution 1.5

The mass current density J

Consider a fluid of mass density ρ occupying the volume $\Delta\mathcal{V} = \Delta x\,\Delta y\,\Delta z$. Let the volume move along the x axis with speed v_x so that the entire volume has passed through the cross section area $\Delta\mathcal{A} = \Delta y\,\Delta z$ in the time $\Delta t = \Delta x/v_x$. The mass current density is thus $J_x = \text{mass/area/time} = (\rho\Delta\mathcal{V})/(\Delta\mathcal{A})/\Delta t = \rho\Delta x/\Delta t = \rho v_x$, as was to be shown. The SI unit of $\mathbf{J}$ is $[\mathbf{J}] = [\rho\mathbf{v}] = (\text{kg m}^{-3})(\text{m s}^{-1}) = \text{kg m}^{-2}\,\text{s}^{-1}$.

Solution 1.6

A heuristic derivation of the continuity equation

The mass ΔM inside the small, fixed volume $\Delta\mathcal{V} = \Delta x\,\Delta y\,\Delta z$ can change in time if and only if the density ρ changes in time:

$$\partial_t(\Delta M) = (\partial_t \rho)\,\Delta x\,\Delta y\,\Delta z. \tag{1.52}$$

However, due to mass conservation, this change in mass can only occur if the mass current density $\mathbf{J} = J_x\mathbf{e}_x$ causes different amounts of mass to enter the volume at the left side and to leave it at the right side. Therefore, the rate of change in mass can also be written as

$$\partial_t(\Delta M) = +J_x(0)\Delta y\Delta z - J_x(\Delta x)\Delta y\Delta z = -[J_x(\Delta x) - J_x(0)]\Delta y\Delta z. \tag{1.53}$$

Equating the two right-hand sides of Eqs. (1.52) and (1.53) and dividing by $\Delta\mathcal{V}$ leads to

$$\partial_t \rho = -\frac{J_x(\Delta x) - J_x(0)}{\Delta x} \quad \xrightarrow[\Delta x\to 0]{} \quad -\partial_x J_x. \tag{1.54}$$

If the current density also has non-zero components along the y and the z direction, the corresponding two terms appear on the right-hand side of Eq. (1.54) leading to

$$\partial_t \rho = -\frac{J_x(\Delta x) - J_x(0)}{\Delta x} - \frac{J_y(\Delta y) - J_y(0)}{\Delta y} - \frac{J_z(\Delta z) - J_z(0)}{\Delta z} \quad \xrightarrow[\Delta \mathcal{V} \to 0]{} \quad -\boldsymbol{\nabla} \cdot \mathbf{J}. \quad (1.55)$$

Solution 1.7
A heuristic derivation of the force densities from pressure and viscosity
Use the figure below to give an heuristic derivation of the pressure-gradient and viscous force density on the right-hand-side of the incompressible Navier–Stokes equation (1.49).

Solution 1.8
Viscosity of water: measured temperature dependence
Plot two graphs of the viscosity η of water based on Table B.2. One graph of η versus t and another, a so-called Arrhenius plot, of $\ln(\eta)$ versus $1/T$, where T is the temperature in kelvin. Discuss the temperature dependence of the viscosity of water.

Chapter 2

Analytical Navier–Stokes solutions

The Navier–Stokes equation is notoriously difficult to solve analytically because it is a non-linear differential equation. Analytical solutions can however be found in a few, but very important cases. Some of these solutions are the topic for this chapter. In particular, we shall solve a number of steady-state problems, among them Poiseuille flow problems, i.e., pressure induced steady-state fluid flow in infinitely long, translation-invariant channels. It is important to study such idealized flows, since they provide us with basic understanding of the behavior of liquids flowing in the microchannels of lab-on-a-chip systems.

Before analyzing the Poiseuille problem we treat three even simpler flow problems: fluids in mechanical equilibrium, the gravity-driven motion of a thin liquid film on an inclined plane, and the motion of a fluid between two parallel plates driven by the relative motion of theses plates (Couette flow).

In all cases we shall employ the so-called no-slip boundary condition for the velocity field at the part $\partial\Omega$ of the boundary that is a solid wall,

$$\mathbf{v}(\mathbf{r}) = \mathbf{0}, \quad \text{for } \mathbf{r} \in \partial\Omega \text{ (no-slip).} \tag{2.1}$$

The microscopic origin of this condition is the assumption of complete momentum relaxation between the molecules of the wall, which are at rest, and the outermost molecules of the fluid that collide with the wall. The momentum is relaxed on a length scale of the order the molecular mean free path in the fluid, which for liquids and high density fluids means one inter-molecular distance ($\simeq 0.3$ nm). Only for rarified gases or narrow channels, where the mean free path of the gas molecules is comparable with the channel dimensions, is it necessary to abandon the no-slip boundary condition.

2.1   Fluids in mechanical equilibrium

A fluid in mechanical equilibrium must be at rest relative to the walls of the vessel containing it, because otherwise it would continuously loose kinetic energy by heat conversion due to internal friction originating from viscous forces inside the fluid. The velocity field is therefore trivially zero everywhere, a special case of steady-state defined by $\partial_t \mathbf{v} \equiv \mathbf{0}$.
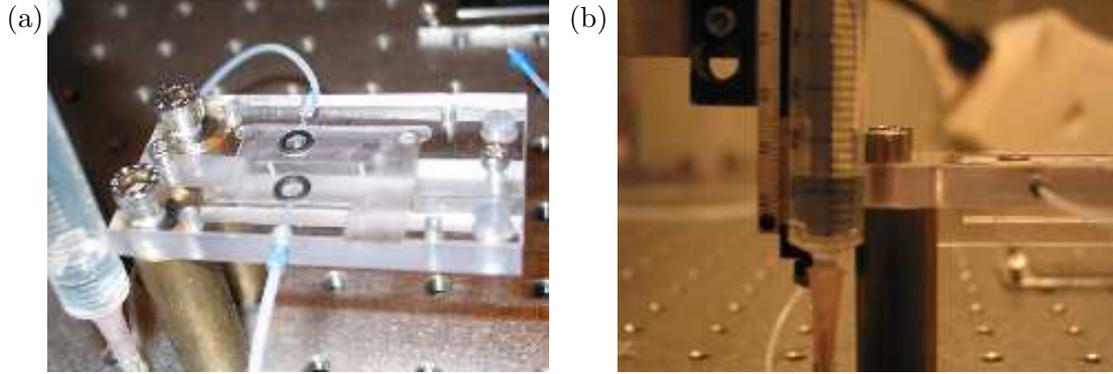
Figure 2.1: (a) A water column (the syringe to the left) used in a lab-on-a-chip system (the polymer chip in the center) to establish the pressure needed for sending water through the silicone tube into the microchannels of the chip. (b) Adjusting the water level in the syringe to level with the chip. Courtesy the groups of Kristensen and Bruus at MIC.

If we let gravity, described by the gravitational acceleration $\mathbf{g} = -g\mathbf{e}_z$ in the negative z direction, be the only external force, the Navier–Stokes equation reduces to

$$\mathbf{v}(\mathbf{r}) = \mathbf{0}, \tag{2.2a}$$

$$\mathbf{0} = -\boldsymbol{\nabla}p - \rho g\mathbf{e}_z. \tag{2.2b}$$

For an incompressible fluid, say water, Eq. (2.2b) is easily integrated to give

$$p = p_0 - \rho gz, \tag{2.3}$$

where p_0 is the pressure at the arbitrarily defined zero-level $z = 0$. This relation points to an easy way of generating pressure differences in liquids: the pressure at the bottom of a liquid column of height H is ρgH higher than the pressure at height H. Liquids with different densities, such as mercury with $\rho_{\mathrm{Hg}} = 1.36 \times 10^4$ kg m^{-3} and water with $\rho_{\mathrm{H_2O}} = 1.00 \times 10^3$ kgm^{-3} can be used to generate different pressures for given heights. The use of this technique in lab-on-a-chip systems is illustrated in Fig. 2.1 and in Exercise 2.1.

Consider a compressible fluid, say, an ideal gas under isothermal conditions for which

$$\rho = \frac{\rho_0}{p_0}\, p, \tag{2.4}$$

where ρ_0 and p_0 is the density and pressure, respectively, for one particular state of the gas. With this equation of state Eqs. (2.2a) and (2.2b) are changed into

$$\mathbf{v}(\mathbf{r}) = \mathbf{0}, \tag{2.5a}$$

$$\mathbf{0} = -\boldsymbol{\nabla}p - \frac{\rho_0}{p_0}\, pg\mathbf{e}_z. \tag{2.5b}$$

Integration of Eq. (2.5b) yields

$$p(z) = p_0\, \exp\left(-\frac{1}{p_0}\, \rho_0 gz\right). \tag{2.6}$$
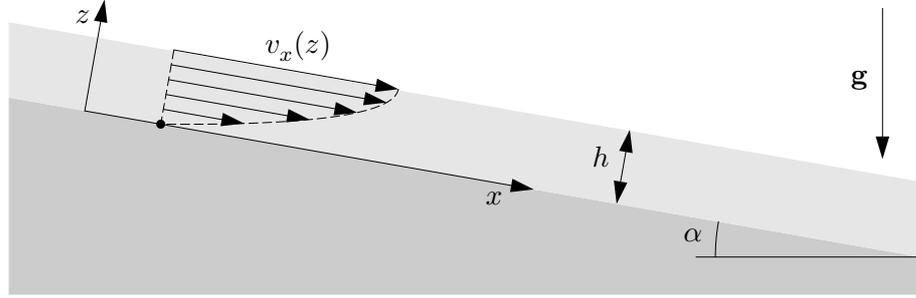
Figure 2.2: A liquid film (light gray) of uniform thickness h flowing down along an inclined plane (dark gray). The plane has the inclination angle α and is assumed to be infinitely long and infinitely wide. The x and z axis is chosen parallel and normal to the plane, respectively. The gravitational acceleration is thus given by $\mathbf{g} = g\sin\alpha\,\mathbf{e}_x - g\cos\alpha\,\mathbf{e}_z$. In steady-state the resulting velocity profile of the liquid film is parabolic as shown.

Inserting the parameter values for air at the surface of the Earth (hardly a microfluidic system), the thickness of the atmosphere is readily estimated to be of the order 10 km; see Exercise 2.2.

2.2 Liquid film flow on an inclined plane

The first example of a non-trivial velocity field is that of a liquid film flowing down along an infinitely long and infinitely wide inclined plane. Consider the geometry defined in Fig. 2.2. The component g_z of the gravitational acceleration normal to the inclined plane is balanced by the normal forces. The component g_x parallel to the plane accelerates the film down along the inclined plane until the velocity of the film is so large that the associated viscous friction forces in the film compensates g_x. When this happens the motion of the film has reached steady-state, a situation we analyze in the following.

The translation invariance of the setup along the x and y direction dictates that the velocity field can only depend on z. Moreover, since the driving force points along the x direction only the x component of the velocity field is non-zero. Finally, no pressure gradients play any role in this free-flow problem, so the steady-state Navier–Stokes equation (i.e., $\partial_t \mathbf{v} = 0$) becomes

$$\mathbf{v}(\mathbf{r}) = v_x(z)\,\mathbf{e}_x, \tag{2.7a}$$

$$\rho(\mathbf{v}\cdot\boldsymbol{\nabla})\mathbf{v} = \eta\,\partial_z^2\mathbf{v} + \rho g\sin\alpha\,\mathbf{e}_x. \tag{2.7b}$$

The special symmetry Eq. (2.7a) of the velocity field implies an enormous simplification of the flow problem. Straightforward differentiation shows namely that the non-linear term in the Navier–Stokes equation (2.7b) vanishes,

$$(\mathbf{v}\cdot\boldsymbol{\nabla})\mathbf{v} = v_x(z)\partial_x\big[v_x(z)\big] = 0. \tag{2.8}$$

We thus only need to solve a linear second-order ordinary differential equation. This demands two boundary conditions, which are given by demanding no-slip of $\mathbf{v}$ at the
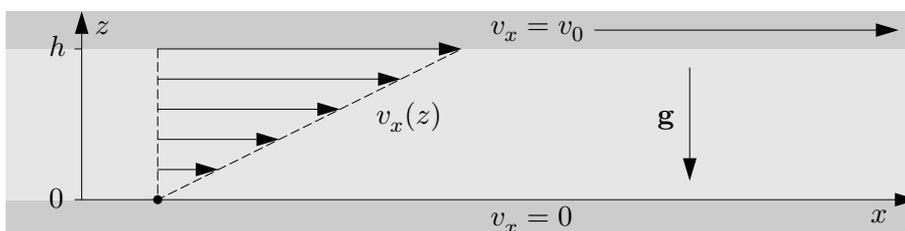
Figure 2.3: An example of Couette flow. A fluid is occupying the space of height h between two horizontally placed, parallel, infinite planar plates. The top plate is moved with the constant speed v_0 relative to the bottom plate. The no-slip boundary condition at both plates forces the liquid into motion, resulting in the linear velocity profile shown.

plane $z = 0$ and no viscous stress on the free surface, i.e., σ'_{xz} from Eq. (1.47) is zero at $z = h$. We arrive at

$$\eta\, \partial_z^2 v_x(z) = -\rho g \sin\alpha, \tag{2.9a}$$

$$v_x(0) = 0, \quad \text{(no-slip)} \tag{2.9b}$$

$$\eta\, \partial_z v_x(h) = 0, \quad \text{(no stress).} \tag{2.9c}$$

The solution is seen to be the well-known half-parabola

$$v_x(z) = \sin\alpha\, \frac{\rho g}{2\eta}\, (2h - z)z = \sin\alpha\, \frac{\rho g h^2}{2\eta}\left(1 - \frac{z}{h}\right)\frac{z}{h}. \tag{2.10}$$

As studied in Exercise 2.3 a typical speed for a 100 μm thick film of water is 1 cm/s.

2.3 Couette flow

Couette flow is a flow generated in a liquid by moving one or more of the walls of the vessel containing the fluid relative to the other walls. An important and very useful example is the Couette flow set up in a fluid held in the space between two concentric cylinders rotating axisymmetrically relative to each other. This setup is used extensively in rheology[1] because it is possible to determine the viscosity η of the fluid very accurately by measuring the torque necessary to sustain a given constant speed of relative rotation.

Here we study the simpler case of planar Couette flow as illustrated in Fig. 2.3. A liquid is placed between two infinite planar plates. The plates are oriented horizontally in the xy plane perpendicular to the gravitational acceleration $\mathbf{g}$. The bottom plate at $z = 0$ is kept fixed in the laboratory, while the top plate at $z = h$ is moved in the x direction with the constant speed v_0.

As in the previous example there is translation invariance of the setup along the x and y direction implies that the velocity field can only depend on z. Moreover, since the driving force points along the x direction, only the x component of the velocity field is

---

[1]Rheology is the study of deformation and flow of matter

non-zero. Finally, neither body forces nor pressure forces play a role since both gravity and the only non-zero pressure gradient (the z component due to hydrostatic pressure) are compensated by the reaction forces of the bottom plate. As in the previous example the symmetry again implies $(\mathbf{v} \cdot \boldsymbol{\nabla})\mathbf{v} = 0$, and the steady-state Navier–Stokes equation then reads

$$\mathbf{v}(\mathbf{r}) = v_x(z)\,\mathbf{e}_x, \tag{2.11a}$$

$$\eta\,\partial_z^2 \mathbf{v} = \mathbf{0}. \tag{2.11b}$$

The boundary conditions on $\mathbf{v}$ is no-slip at the top and bottom plane plane $z = 0$ and $z = h$, respectively, so we arrive at the following second-order ordinary differential equation with two boundary conditions:

$$\eta\,\partial_z^2 v_x(z) = 0, \tag{2.12a}$$

$$v_x(0) = 0, \quad \text{(no-slip)} \tag{2.12b}$$

$$v_x(h) = v_0, \quad \text{(no-slip)}. \tag{2.12c}$$

The solution is seen to be the well-known linear profile

$$v_x(z) = v_0\,\frac{z}{h}. \tag{2.13}$$

Assuming this expression to be valid for large, but finite, plates with area $\mathcal{A}$ we can, by use of the viscous stress tensor σ', determine the horizontal external force $\mathbf{F} = F_x\mathbf{e}_x$ necessary to apply to the top plate to pull it along with fixed speed v_0,

$$F_x = \sigma'_{xz}\,\mathcal{A} = \eta\,\frac{v_0\mathcal{A}}{h}. \tag{2.14}$$

This expression allows for a simple experimental determination of the viscosity η.

2.4 Poiseuille flow

We now turn to the final class of analytical solutions to the Navier–Stokes equation: the pressure-driven, steady-state flows in channels, also known as Poiseuille flows or Hagen–Poiseuille flows. This class is of major importance for the basic understanding of liquid handling in lab-on-a-chip systems

In a Poiseuille flow the fluid is driven through a long, straight, and rigid channel by imposing a pressure difference between the two ends of the channel. Originally, Hagen and Poiseuille studied channels with circular cross-sections, as such channels are straightforward to produce. However, especially in microfluidics, one frequently encounters other shapes. One example, shown in Fig. 2.4, is the Gaussian-like profile that results from producing microchannels by laser ablation in the surface of a piece of the polymer PMMA. The heat from the laser beam cracks the PMMA into MMA, which by evaporation leaves the substrate. A whole network of microchannels can then be created by sweeping the laser beam across the substrate in a well-defined pattern. The channels are sealed by placing and bonding a polymer lid on top of the structure.
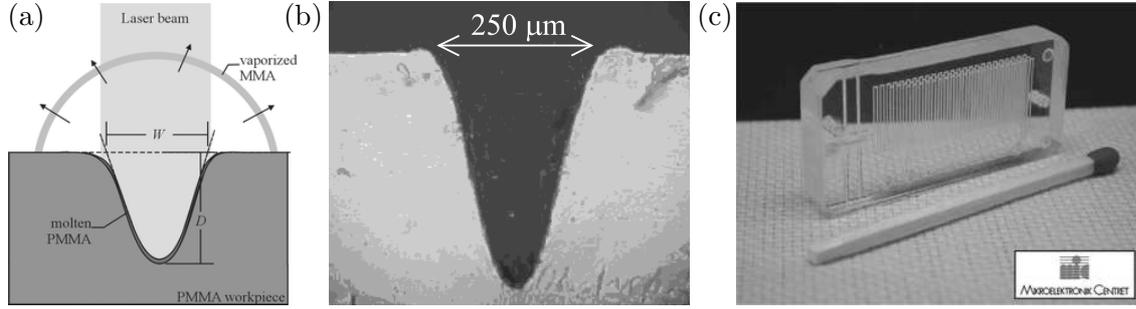
Figure 2.4: Fabrication of microchannels by laser ablation in the surface a substrate made of the polymer PMMA. (a) Schematic diagram of the laser beam, the laser ablated groove, including the molten PMMA and the vaporized hemispherical cloud of MMA leaving the cut-zone. (b) Scanning electron microscope (SEM) micrograph of the cross-section of an actual microchannel showing the resulting Gaussian-like profile. (c) A three-layered PMMA-microfluidic system for the detection of ammonia in aqueous samples sent through the meandering microchannel fabricated by laser ablation. Courtesy the group of Geschke at MIC.

2.4.1   Arbitrary cross-sectional shape

We first study the steady-state Poiseuille flow problem with an arbitrary cross-sectional shape as illustrated in Fig. 2.5. Although not analytically solvable, this example nevertheless provide us with the structural form of the solution for the velocity field.

The channel is parallel to the x axis, and it is assumed to be translation invariant in that direction. The constant cross-section in the yz plane is denoted $\mathcal{C}$ with boundary $\partial\mathcal{C}$, respectively. A constant pressure difference Δp is maintained over a segment of length L of the channel, i.e., $p(0) = p_0 + \Delta p$ and $p(L) = p_0$. The gravitational force is balanced by a hydrostatic pressure gradient in the vertical direction. These two forces are therefore left out of the treatment. The translation invariance of the channel in the x direction combined with the vanishing of forces in the yz plane implies the existence of a velocity field independent of x, while only its x component can be non-zero, $\mathbf{v}(\mathbf{r}) = v_x(y, z)\,\mathbf{e}_x$.[2] Consequently $(\mathbf{v}\cdot\boldsymbol{\nabla})\mathbf{v} = 0$ and the steady-state Navier–Stokes equation becomes

$$\mathbf{v}(\mathbf{r}) = v_x(y, z)\,\mathbf{e}_x, \tag{2.15a}$$

$$\mathbf{0} = \eta\nabla^2\big[v_x(y, z)\,\mathbf{e}_x\big] - \boldsymbol{\nabla}p. \tag{2.15b}$$

Since the y and z components of the velocity field are zero, it follows that $\partial_y p = 0$ and $\partial_z p = 0$, and consequently that the pressure field only depends on x, $p(\mathbf{r}) = p(x)$. Using this result the x component of the Navier–Stokes equation (2.15b) becomes

$$\eta\big[\partial_y^2 + \partial_z^2\big]v_x(y, z) = \partial_x p(x). \tag{2.16}$$

---

[2]Although a valid mathematical solution at any flow speed, the translation invariant velocity field is only stable at low velocities. The translation invariance symmetry is spontaneously broken as the flow speed is increased, and eventually an unsteady turbulent flow appears as the physical solution having the smallest possible entropy production rate.
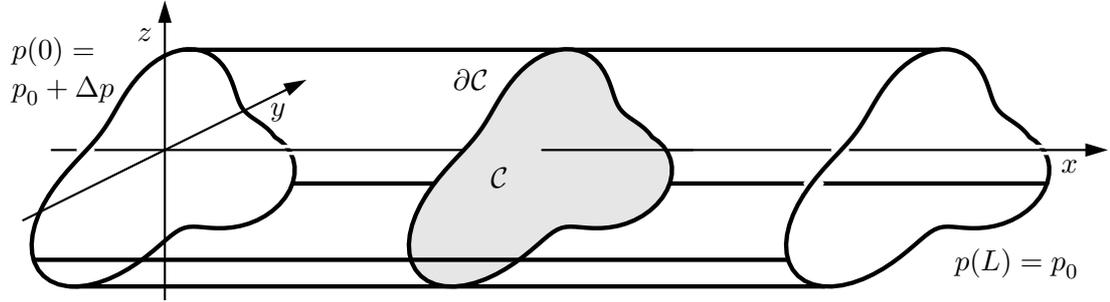
Figure 2.5: The Poiseuille flow problem in a channel, which is translation invariant in the x direction, and which has an arbitrarily shaped cross-section $\mathcal{C}$ in the yz plane. The boundary of $\mathcal{C}$ is denoted $\partial\mathcal{C}$. The pressure at the left end, $x = 0$, is an amount Δp higher than at the right end, $x = L$.

Here it is seen that the left-hand side is a function of y and z while the right-hand side is a function of x. The only possible solution is thus that the two sides of the Navier–Stokes equation equal the same constant. However, a constant pressure gradient $\partial_x p(x)$ implies that the pressure must be a linear function of x, and using the boundary conditions for the pressure we obtain

$$p(\mathbf{r}) = \frac{\Delta p}{L}\,(L - x) + p_0. \tag{2.17}$$

With this we finally arrive at the second-order partial differential equation that $v_x(y, z)$ must fulfil in the domain $\mathcal{C}$ given the usual no-slip boundary conditions at the solid walls of the channel described by $\partial\mathcal{C}$,

$$\left[\partial_y^2 + \partial_z^2\right] v_x(y, z) = -\frac{\Delta p}{\eta L}, \quad \text{for } (y, z) \in \mathcal{C} \tag{2.18a}$$

$$v_x(y, z) = 0, \qquad \text{for } (y, z) \in \partial\mathcal{C}. \tag{2.18b}$$

Once the velocity field is determined it is possible to calculate the so-called flow rate Q, which is defined as the fluid volume discharged by the channel per unit time. For compressible fluids it becomes important to distinguish between the flow rate Q and the mass flow rate Q_{mass} defined as the discharged mass per unit time. In the case of the geometry of Fig. 2.5 we have

$$Q \equiv \int_{\mathcal{C}} \mathrm{d}y\,\mathrm{d}z\, v_x(y, z), \tag{2.19a}$$

$$Q_{\text{mass}} \equiv \int_{\mathcal{C}} \mathrm{d}y\,\mathrm{d}z\, \rho\, v_x(y, z). \tag{2.19b}$$

This is how far we can get theoretically without specifying the actual shape of the channel.

2.4.2 Elliptic cross-section

Our first explicit example is the elliptic cross-section. We let the center of the ellipse be at $(y, z) = (0, 0)$. The major axis of length a and the minor axis of length b are parallel

to the y axis and z axis, respectively, as shown in Fig. 2.6(a). The boundary $\partial\mathcal{C}$ of the ellipse is given by the expression

$$\partial\mathcal{C}: \quad 1 - \frac{y^2}{a^2} - \frac{z^2}{b^2} = 0. \tag{2.20}$$

If we therefore as a trial solution choose

$$v_x(y, z) = v_0\left(1 - \frac{y^2}{a^2} - \frac{z^2}{b^2}\right), \tag{2.21}$$

we are guarantied that $v_x(y, z)$ satisfies the no-slip boundary condition Eq. (2.18b). Insertion of the trial solution into the left-hand side of the Navier–Stokes equation (2.18a) yields

$$\left[\partial_y^2 + \partial_z^2\right]v_x(y, z) = -2v_0\left(\frac{1}{a^2} + \frac{1}{b^2}\right). \tag{2.22}$$

Thus the Navier–Stokes equation (2.18a) will be satisfied by choosing the constant v_0 as

$$v_0 = \frac{\Delta p}{2\eta L}\frac{a^2 b^2}{a^2 + b^2}. \tag{2.23}$$

To calculate the flow rate Q for the elliptic channel we need to evaluate a 2d integral in an elliptically shaped integration region. This we handle by the following coordinate transformation. Let (ρ, ϕ) be the polar coordinates of the unit disk, i.e., the radial and azimuthal coordinates obey $0 \leq \rho \leq 1$ and $0 \leq \phi \leq 2\pi$, respectively. Our physical coordinates (y, z) and the velocity field v_x can then be expressed as functions of (ρ, ϕ):

$$y(\rho, \phi) = a\rho\,\cos\phi, \tag{2.24}$$
$$z(\rho, \phi) = b\rho\,\sin\phi, \tag{2.25}$$
$$v_x(\rho, \phi) = v_0\big(1 - \rho^2\big). \tag{2.26}$$

The advantage is that now the boundary $\partial\mathcal{C}$ can be expressed in terms of just one coordinate instead of two,

$$\partial\mathcal{C}: \quad \rho = 1. \tag{2.27}$$

The (y, z) surface integral in Eq. (2.19a) is transformed into (ρ, ϕ) coordinates by use of the Jacobian determinant $|\partial_{(\rho,\phi)}(y, z)|$,

$$\int_\mathcal{C}\mathrm{d}y\,\mathrm{d}z = \int_\mathcal{C}\mathrm{d}\rho\,\mathrm{d}\phi\left|\frac{\partial(y, z)}{\partial(\rho, \phi)}\right| = \int_\mathcal{C}\mathrm{d}\rho\,\mathrm{d}\phi\left|\begin{array}{cc}\partial_\rho y & \partial_\rho z\\ \partial_\phi y & \partial_\phi z\end{array}\right|$$

$$= \int_0^1\mathrm{d}\rho\int_0^{2\pi}\mathrm{d}\phi\left|\begin{array}{cc}+a\cos\phi & +b\sin\phi\\ -a\rho\sin\phi & +b\rho\cos\phi\end{array}\right| = ab\int_0^{2\pi}\mathrm{d}\phi\int_0^1\mathrm{d}\rho\,\rho. \tag{2.28}$$

The flow rate Q for the elliptic channel is now easily calculated as

$$Q = \int_\mathcal{C}\mathrm{d}y\,\mathrm{d}z\,v_x(y, z) = ab\int_0^{2\pi}\mathrm{d}\phi\int_0^1\mathrm{d}\rho\,\rho\,v_x(\rho, \phi) = \frac{\pi}{4}\frac{1}{\eta L}\frac{a^3 b^3}{a^2 + b^2}\,\Delta p. \tag{2.29}$$
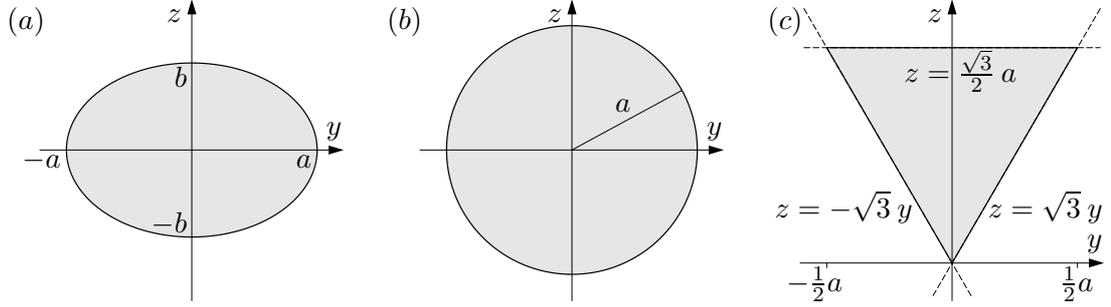
Figure 2.6: The definition of three specific cross-sectional shapes for the Poiseuille flow problem. (a) The ellipse with major axis a and minor axis b, (b) the circle with radius a, and (c) the equilateral triangle with side length a.

2.4.3 Circular cross-section

Since the circle Fig. 2.6(b) is just the special case $a = b$ of the ellipse, we can immediately write down the result for the velocity field and flow rate for the Poiseuille flow problem in a circular channel. From Eqs. (2.21), (2.23), and (2.29) using $a = b$ it follows that

$$v_x(y, z) = \frac{\Delta p}{4\eta L}\left(a^2 - y^2 - z^2\right),\tag{2.30a}$$

$$Q = \frac{\pi a^4}{8\eta L}\,\Delta p.\tag{2.30b}$$

However, the same result can also be obtained by direct calculation using cylindrical coordinates (x, r, ϕ) thereby avoiding the trial solution Eq. (2.21). For cylindrical coordinates, see Appendix A.2, with the x axis chosen as the cylinder axis we have

$$(x,\ y,\ z) = (x,\ r\cos\phi,\ r\sin\phi),\tag{2.31a}$$

$$\mathbf{e}_x = \mathbf{e}_x,\tag{2.31b}$$

$$\mathbf{e}_r = +\cos\phi\,\mathbf{e}_y + \sin\phi\,\mathbf{e}_z,\tag{2.31c}$$

$$\mathbf{e}_\phi = -\sin\phi\,\mathbf{e}_y + \cos\phi\,\mathbf{e}_z,\tag{2.31d}$$

$$\nabla^2 = \partial_x^2 + \partial_r^2 + \frac{1}{r}\partial_r + \frac{1}{r^2}\partial_\phi^2.\tag{2.31e}$$

The symmetry considerations reduces the velocity field to $\mathbf{v} = v_x(r)\mathbf{e}_x$, so that the Navier–Stokes equation (2.18a) becomes an ordinary differential equation of second order,

$$\left[\partial_r^2 + \frac{1}{r}\,\partial_r\right]v_x(r) = -\frac{\Delta p}{\eta L}.\tag{2.32}$$

The solutions to this inhomogeneous equation is the sum of a general solution to the homogeneous equation, $v_x'' + v_x'/r = 0$, and one particular solution to the inhomogeneous equation. It is easy to see that the general homogeneous solution has the linear form

$v_x(r) = A + B \ln r$, while a particular inhomogeneous solution is $v_x(r) = -(\Delta p/4\eta L)\, r^2$. Given the boundary conditions $v_x(a) = 0$ and $v_x'(0) = 0$ we arrive at

$$v_x(r, \phi) = \frac{\Delta p}{4\eta L} \left(a^2 - r^2\right) \tag{2.33a}$$

$$Q = \int_0^{2\pi} d\phi \int_0^a dr\, r\, \frac{\Delta p}{4\eta L} \left(a^2 - r^2\right) = \frac{\pi}{8} \frac{a^4}{\eta L} \Delta p. \tag{2.33b}$$

2.4.4 Equilateral triangular cross-section

There exists no analytical solution to the Poiseuille flow problem with a general triangular cross-section. In fact, it is only for the equilateral triangle defined in Fig. 2.6(c) that an analytical result is known.

The domain $\mathcal{C}$ in the yz plane of the equilateral triangular channel cross-section can be thought of as the union of the three half-planes $(\sqrt{3}/2)a \geq z$, $z \geq \sqrt{3}y$, and $z \geq -\sqrt{3}y$. Inspired by our success with the trial solution of the elliptic channel, we now form a trial solution by multiplying together the expression for the three straight lines defining the boundaries of the equilateral triangle,

$$v_x(y, z) = \frac{v_0}{a^3} \left(\frac{\sqrt{3}}{2}a - z\right)\left(z - \sqrt{3}y\right)\left(z + \sqrt{3}y\right) = \frac{v_0}{a^3} \left(\frac{\sqrt{3}}{2}a - z\right)\left(z^2 - 3y^2\right). \tag{2.34}$$

By construction this trial solution satisfies the no-slip boundary condition on $\partial\mathcal{C}$. Luckily, it turns out that the Laplacian acting on the trial solution yields a constant,

$$\left[\partial_y^2 + \partial_z^2\right] v_x(y, z) = -2\sqrt{3}\, \frac{v_0}{a^2}. \tag{2.35}$$

Thus the Navier–Stokes equation will be satisfied by choosing the constant v_0 as

$$v_0 = \frac{1}{2\sqrt{3}} \frac{\Delta p}{\eta L} a^2. \tag{2.36}$$

The flow rate Q is most easily found by first integrating over y and then over z,

$$Q = 2 \int_0^{\frac{\sqrt{3}}{2}a} dz \int_0^{\frac{1}{\sqrt{3}}z} dy\, v_x(y, z) = \frac{4v_0}{3\sqrt{3}\, a^3} \int_0^{\frac{\sqrt{3}}{2}a} dz \left(\frac{\sqrt{3}}{2}\, a - z\right) z^3$$

$$= \frac{3}{160} v_0\, a^2 = \frac{\sqrt{3}}{320} \frac{a^4}{\eta L} \Delta p. \tag{2.37}$$

2.4.5 Rectangular cross-section

For lab-on-a-chip systems many fabrication methods leads to microchannels having a rectangular cross-section. One example is the microreactor shown in panel (a) and (b) of Fig. 2.7. This device is made in the polymer SU-8 by hot embossing, i.e., the SU-8 is heated up slightly above its glass transition temperature, where it gets soft, and then a hard stamp containing the negative of the desired pattern is pressed into the polymer. The
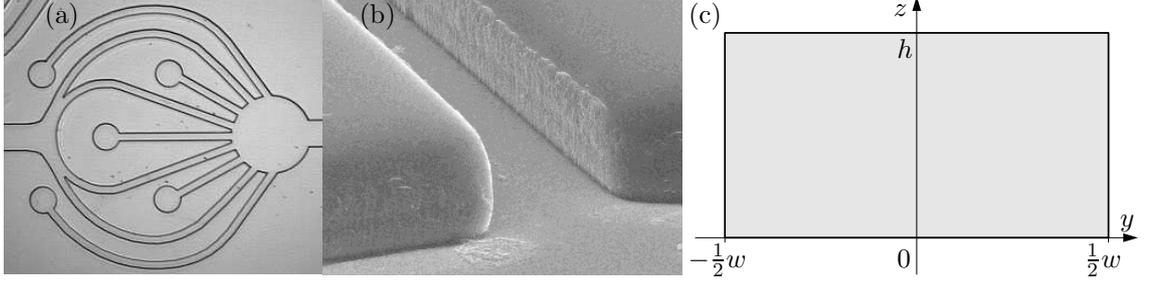
Figure 2.7: (a) A top-view picture of a micro-reactor with nine inlet microchannels made by hot embossing in the polymer SU-8 before bonding on a polymer lid. (b) A zoom-in on one of the inlet channels having a near perfect rectangular shape of height $h = 50$ μm and width $w = 100$ μm . Courtesy the group of Geschke at MIC. (c) The definition of the rectangular channel cross-section of height h and width w, which is analyzed in the text.

stamp is removed and later a polymer lid is placed on top of the structure and bonded to make a leakage-free channel.

It is perhaps a surprising fact that no analytical solution is known to the Poiseuille flow problem with a rectangular cross-section. In spite of the high symmetry of the boundary the best we can do analytically is to find a Fourier sum representing the solution.

In the following we always take the width to be larger than the height, $w > h$. By rotation this situation can always be realized. The Navier–Stokes equation and associated boundary conditions are

$$\left[\partial_y^2 + \partial_z^2\right] v_x(y, z) = -\frac{\Delta p}{\eta L}, \quad \text{for} \quad -\frac{1}{2}w < y < \frac{1}{2}w, \ \ 0 < z < h, \tag{2.38a}$$

$$v_x(y, z) = 0, \qquad \text{for} \ \ y = \pm\frac{1}{2}w, \ z = 0, \ z = h. \tag{2.38b}$$

We begin by expanding all functions in the problem as Fourier series along the short vertical z direction. To ensure the fulfilment of the boundary condition $v_x(y, 0) = v_x(y, h) = 0$ we use only terms proportional to $\sin(n\pi z/h)$, where n is a positive integer. A Fourier expansion of the constant on the right-hand side in Eq. (2.38a) yields,

$$-\frac{\Delta p}{\eta L} = -\frac{\Delta p}{\eta L} \frac{4}{\pi} \sum_{n,\text{odd}}^{\infty} \frac{1}{n} \sin\left(n\pi\frac{z}{h}\right), \tag{2.39}$$

a series containing only odd integers n. The coefficients $f_n(y)$ of the Fourier expansion in the z coordinate of the velocity are constants in z, but functions in y:

$$v_x(y, z) \equiv \sum_{n=1}^{\infty} f_n(y) \sin\left(n\pi\frac{z}{h}\right). \tag{2.40}$$

Inserting this series in the left-hand side of Eq. (2.38a) leads to

$$\left[\partial_y^2 + \partial_z^2\right] v_x(y, z) = \sum_{n=1}^{\infty} \left[f_n''(y) - \frac{n^2\pi^2}{h^2} f_n(y)\right] \sin\left(n\pi\frac{z}{h}\right). \tag{2.41}$$
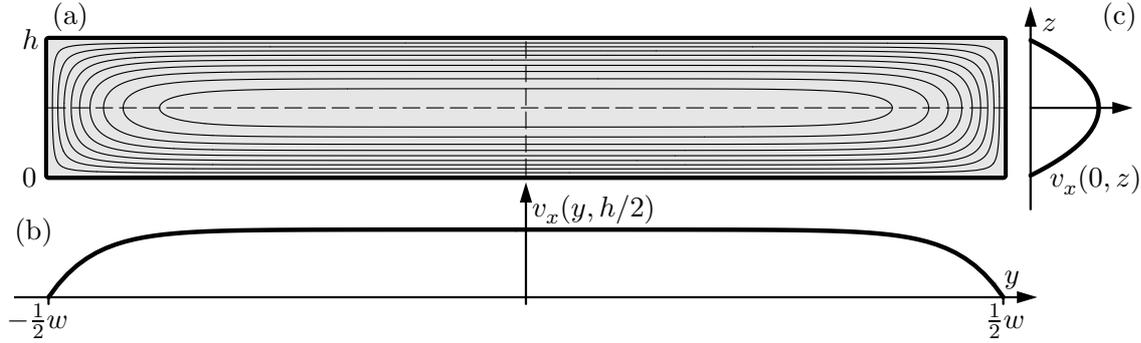
Figure 2.8: (a) Contour lines for the velocity field $v_x(y, z)$ for the Poiseuille flow problem in a rectangular channel. The contour lines are shown in steps of 10% of the maximal value $v_x(0, h/2)$. (b) A plot of $v_x(y, h/2)$ along the long center-line parallel to $\mathbf{e}_y$. (c) A plot of $v_x(0, z)$ along the short center-line parallel to $\mathbf{e}_z$.

A solution to the problem must satisfy that for all values of n the nth coefficient in the pressure term Eq. (2.39) must equal the nth coefficient in the velocity term Eq. (2.41). The functions $f_n(y)$ are therefore given by

$$f_n(y) = 0, \qquad \text{for } n \text{ even}, \tag{2.42a}$$

$$f_n''(y) - \frac{n^2\pi^2}{h^2} \, f_n(y) = -\frac{\Delta p}{\eta L} \frac{4}{\pi} \frac{1}{n}, \quad \text{for } n \text{ odd}. \tag{2.42b}$$

To determine $f_n(y)$, for n being odd, we need to solve the inhomogeneous second order differential equation (2.42b). A general solution can be written as

$$f_n(y) = f_n^{\text{inhom}}(y) + f_n^{\text{homog}}(y), \tag{2.43}$$

where $f_n^{\text{inhom}}(y)$ is a particular solution to the inhomogeneous equation and $f_n^{\text{homog}}(y)$ a general solution to the homogeneous equation (where the right-hand side is put equal to zero). It is easy to find one particular solution to Eq. (2.42b). One can simply insert the trial function $f_n^{\text{inhom}}(y) = \text{const}$ and solve the resulting algebraic equation,

$$f_n^{\text{inhom}}(y) = \frac{4h^2\Delta p}{\pi^3\eta L} \frac{1}{n^3}, \quad \text{for } n \text{ odd}. \tag{2.44}$$

The general solution to the homogeneous equation, $f_n''(y) - (n^2\pi^2/h^2)\, f_n(y) = 0$ is the linear combination

$$f_n^{\text{homog}}(y) = A \cosh\left(\frac{n\pi}{h}\, y\right) + B \sinh\left(\frac{n\pi}{h}\, y\right). \tag{2.45}$$

The solution $f_n(y)$ that satisfies the no-slip boundary conditions $f_n\left(\pm \frac{1}{2}w\right) = 0$ is

$$f_n(y) = \frac{4h^2\Delta p}{\pi^3\eta L} \frac{1}{n^3} \left[1 - \frac{\cosh\left(n\pi \frac{y}{h}\right)}{\cosh\left(n\pi \frac{w}{2h}\right)}\right], \quad \text{for } n \text{ odd}, \tag{2.46}$$

which leads to the velocity field for the Poiseuille flow in a rectangular channel,

$$v_x(y, z) = \frac{4h^2 \Delta p}{\pi^3 \eta L} \sum_{n,\text{odd}}^{\infty} \frac{1}{n^3} \left[1 - \frac{\cosh\left(n\pi \frac{y}{h}\right)}{\cosh\left(n\pi \frac{w}{2h}\right)} \right] \sin\left(n\pi \frac{z}{h}\right). \tag{2.47}$$

In Fig. 2.8 are shown some plots of the contours of the velocity field and of the velocity field along the symmetry axes.

The flow rate Q is found by integration as follows,

$$Q = 2 \int_0^{\frac{1}{2}w} dy \int_0^h dz \, v_x(y, z) \tag{2.48a}$$

$$= \frac{4h^2 \Delta p}{\pi^3 \eta L} \sum_{n,\text{odd}}^{\infty} \frac{1}{n^3} \frac{2h}{n\pi} \left[w - \frac{2h}{n\pi} \tanh\left(n\pi \frac{w}{2h}\right) \right] \tag{2.48b}$$

$$= \frac{8h^3 w \Delta p}{\pi^4 \eta L} \sum_{n,\text{odd}}^{\infty} \left[\frac{1}{n^4} - \frac{2h}{\pi w} \frac{1}{n^5} \tanh\left(n\pi \frac{w}{2h}\right) \right] \tag{2.48c}$$

$$= \frac{h^3 w \Delta p}{12 \eta L} \left[1 - \sum_{n,\text{odd}}^{\infty} \frac{1}{n^5} \frac{192}{\pi^5} \frac{h}{w} \tanh\left(n\pi \frac{w}{2h}\right) \right], \tag{2.48d}$$

where we have used $\displaystyle \sum_{n,\text{odd}}^{\infty} \frac{1}{n^4} = \frac{\pi^4}{96}$.

Very useful approximate results can be obtained in the limit $\frac{h}{w} \to 0$ of a flat and very wide channel, for which $\frac{h}{w} \tanh\left(n\pi \frac{w}{2h}\right) \to \frac{h}{w} \tanh(\infty) = \frac{h}{w}$, and Q becomes

$$Q \approx \frac{h^3 w \Delta p}{12 \eta L} \left[1 - \frac{192}{\pi^5} \frac{h}{w} \sum_{n,\text{odd}}^{\infty} \frac{1}{n^5} \right]$$

$$= \frac{h^3 w \Delta p}{12 \eta L} \left[1 - \frac{192}{\pi^5} \frac{31}{32} \zeta(5) \frac{h}{w} \right]$$

$$\approx \frac{h^3 w \Delta p}{12 \eta L} \left[1 - 0.630 \frac{h}{w} \right]. \tag{2.49}$$

Here we have on the way used the Riemann zeta function, $\zeta(x) \equiv \sum_{n=1}^{\infty} 1/n^x$,

$$\sum_{n,\text{odd}}^{\infty} \frac{1}{n^5} = \sum_{n=1}^{\infty} \frac{1}{n^5} - \sum_{n,\text{even}}^{\infty} \frac{1}{n^5} = \zeta(5) - \sum_{k=1}^{\infty} \frac{1}{(2k)^5} = \zeta(5) - \frac{1}{32} \zeta(5) = \frac{31}{32} \zeta(5). \tag{2.50}$$

The approximative result Eq. (2.49) for Q is surprisingly good. For the worst case, the square with $h = w$, the error is just 13%, while already at aspect ratio a half, $h = w/2$, the error is down to 0.2%.

If we neglect the side walls completely we arrive at the case of an infinitely wide channel, which is studied in the following subsection.
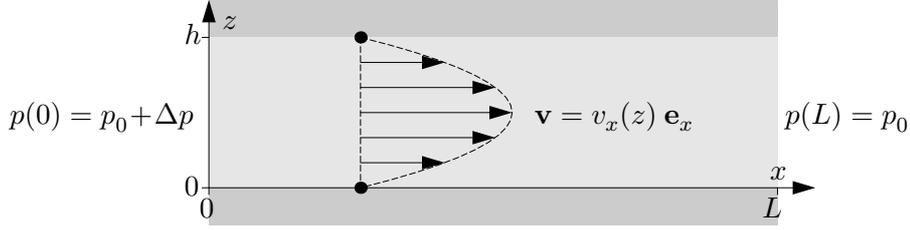
Figure 2.9: A sketch in the xz plane of an infinite, parallel-plate channel of height h. The system is translation invariant in the y direction and fluid is flowing in the x direction due to a pressure drop Δp over the section of length L.

2.4.6 Infinite parallel-plate channel

In microfluidics the aspect ratio of a rectangular channel can often be so large that the channel is well approximated by an infinite parallel-plate configuration. The geometry shown in Fig. 2.9 is much like the one shown for the Couette flow in Fig. 2.3, but now the both plates are kept fixed and a pressure difference Δp is applied. Due to the symmetry the y coordinate drops out and we end with the following ordinary differential equation,

$$\partial_z^2 v_x(z) = -\frac{\Delta p}{\eta L}, \tag{2.51a}$$

$$v_x(0) = 0, \qquad \text{(no-slip)} \tag{2.51b}$$

$$v_x(h) = 0, \qquad \text{(no-slip)}. \tag{2.51c}$$

The solution is a simple parabola

$$v_x(z) = \frac{\Delta p}{2\eta L}(h-z)z, \tag{2.52}$$

and the flow rate Q through a section of width w is found as

$$Q = \int_0^w dy \int_0^h dz \, \frac{\Delta p}{2\eta L}(h-z)z = \frac{h^3 w}{12\eta L} \Delta p. \tag{2.53}$$

This approximate expression for the flow rate in flat rectangular channels can be used instead of the more accurate expression Eq. (2.49) to obtain good order-of-magnitude estimates. However, note that the error is 23% for aspect ratio one third, $h = w/3$, and by 7% for aspect ratio one tenth, $h = w/10$.

2.5 Shape perturbation in Poiseuille flow problems

By use of shape perturbation theory it is possible to extend the analytical results for Poiseuille flow beyond the few cases of regular geometries that we have treated above. In shape perturbation theory the starting point is an analytically solvable case, which then is deformed slightly characterized by some small perturbation parameter ϵ. As illustrated in

(a)

(b)

$\phi = \theta$

$r = a\rho\big[1 + \epsilon \sin(k\theta)\big]$

$\eta = \rho\cos\theta$

$\zeta = \rho\sin\theta$

$y = a\rho\big[1 + \epsilon \sin(k\theta)\big]\cos\theta$

$z = a\rho\big[1 + \epsilon \sin(k\theta)\big]\sin\theta$
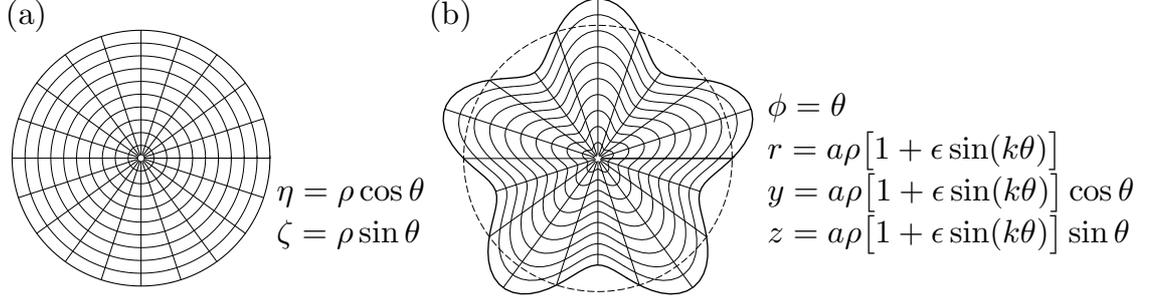
Figure 2.10: (a) The geometry of the unperturbed and analytically solvable cross-section, the unit circle, described by coordinates (η, ζ) or (ρ, θ). (b) The geometry of the perturbed cross-section described by coordinates (y, z) or (r, ϕ) and the perturbation parameter ϵ. Here $a = 1$, $k = 5$ and $\epsilon = 0.2$.

Fig. 2.10 the unperturbed shape is described by parametric coordinates (η, ζ) in Cartesian form or (ρ, θ) in polar form. The coordinates of the physical problem we would like to solve are (y, z) in Cartesian form and (r, ϕ) in polar form.

As a concrete example we take the multipolar deformation of the circle defined by the transformation

$$\phi = \theta, \qquad\qquad 0 \le \theta \le 2\pi, \qquad\qquad (2.54\text{a})$$

$$r = a\,\rho\big[1 + \epsilon \sin(k\theta)\big], \qquad 0 \le \rho \le 1, \qquad\qquad (2.54\text{b})$$

$$y(\rho,\theta) = a\,\rho\big[1 + \epsilon \sin(k\theta)\big]\cos\theta, \qquad\qquad (2.54\text{c})$$

$$z(\rho,\theta) = a\,\rho\big[1 + \epsilon \sin(k\theta)\big]\sin\theta, \qquad\qquad (2.54\text{d})$$

where a is length scale and k is an integer defining the order of the multipolar deformation. Note that for $\epsilon = 0$ the shape is unperturbed. The boundary of the perturbed shape is simply described by fixing the unperturbed coordinate $\rho = 1$ and sweeping in θ

$$\partial C : \quad \big(y, z\big) = \big(y(1,\theta),\, z(1,\theta)\big). \qquad\qquad (2.55)$$

It is therefore desirable to formulate the perturbed Poiseuille problem using the unperturbed coordinates. To obtain analytical results it is important to make the appearance of the perturbation parameter explicit. When performing a perturbation calculation to order m all terms containing ϵ^l with $l > m$ are discarded, while the remaining terms containing the same power of ϵ are grouped together, and the equations are solved power by power.

To carry out the perturbation calculation the velocity field $v_x(y, z)$ is written as

$$v_x(y, z) = v_x\big(y(\rho,\theta), z(\rho,\theta)\big) = v_x^{(0)}(\rho, \theta) + \epsilon\, v_x^{(1)}(\rho, \theta) + \epsilon^2\, v_x^{(2)}(\rho, \theta) + \cdots \qquad (2.56)$$

Likewise, the Laplacian operator in the Navier–Stokes equation must be expressed in terms of ρ, θ, and ϵ. The starting point of this transformation is the transformation of

the gradients

$$\partial_r = (\partial_r \rho)\, \partial_\rho + (\partial_r \theta)\, \partial_\theta, \tag{2.57a}$$

$$\partial_\phi = (\partial_\phi \rho)\, \partial_\rho + (\partial_\phi \theta)\, \partial_\theta. \tag{2.57b}$$

The derivatives $(\partial_r \rho)$, $(\partial_r \theta)$, $(\partial_\phi \rho)$, and $(\partial_\phi \theta)$ is obtained from the inverse transformation of Eqs. (2.54b) and (2.54a),

$$\rho(r, \phi) = \frac{1}{1 + \epsilon \sin(k\phi)}\, \frac{r}{a}, \tag{2.58a}$$

$$\theta(r, \phi) = \phi. \tag{2.58b}$$

The expansion Eq. (2.56) can now be inserted into the Navier–Stokes equation and by use of the derivatives Eqs. (2.57a) and (2.57b) we can carry out the perturbation scheme. The calculation is straightforward but tedious. We shall here just quote the first order perturbation result for the velocity field:

$$v_x(\rho, \theta) = \left[\left(1 - \rho^2\right) - 2\left(\rho^2 - \rho^k\right)\sin(k\theta)\,\epsilon \right] \frac{a^2 \Delta p}{4\eta L} + \mathcal{O}\!\left(\epsilon^2\right). \tag{2.59}$$

This example may appear rather artificial. However, almost any shape deformation of the circle can by analyzed based on this example. An arbitrarily shaped boundary can be written as a Fourier series involving a sum over infinitely many multipole deformations like the kth one studied in this section.

2.6   Stokes drag on a sphere moving in steady-state

As the last example we study the steady-state motion of a rigid sphere in a fluid. This is relevant for many applications of lab-on-a-chip systems where small objects, such as magnetic beads, fluorescent markers, or biological cells, are moved around inside the microfluidic channels. We shall restrict our treatment to rigid spherical bodies.

We choose a coordinate system where the sphere with radius a is at rest and the surrounding fluid moves past it. The goal is to calculate the velocity and pressure fields, and from that find the stress tensor at the sphere, which finally will give us the force acting on the sphere. At infinity the fluid is assumed to move with a constant velocity $\mathbf{v} = V_0 \mathbf{e}_z$ along the z axis, while at the surface of the sphere we have the no-slip boundary condition, $\mathbf{v}(r = a) = \mathbf{0}$.

Due to the symmetry we choose to work with spherical coordinates (r, θ, ϕ), and we notice that only the radial coordinate r as well as the polar angle θ (the angle to the z axis) enters. The azimuthal angle ϕ is therefore suppressed in the following.

To simplify the problem we consider the low Reynolds number limit, $Re = \eta a V_0 / \rho \ll 1$,
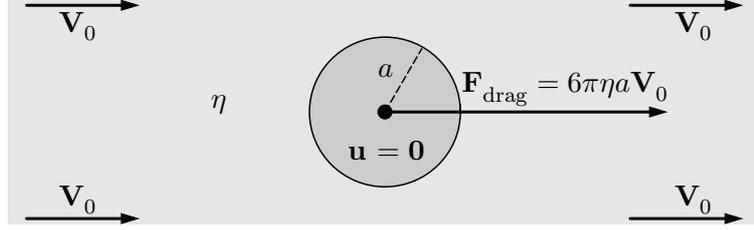
Figure 2.11: The Stokes drag force $\mathbf{F}_{\text{drag}}$ on a rigid sphere of radius a, when the sphere is at rest, $\mathbf{u} = \mathbf{0}$, and the fluid of viscosity η has the constant velocity $\mathbf{V}_0$ at infinity as indicated by the four vectors $\mathbf{V}_0$.

and the linear steady-state Navier–Stokes equation and the continuity equation become

$$\partial_r^2 v_r + \frac{2}{r}\,\partial_r v_r - \frac{2}{r^2}v_r + \frac{1}{r^2}\partial_\theta^2 v_r + \frac{\cot\theta}{r^2}\partial_\theta v_r - \frac{2}{r^2\sin\theta}\partial_\theta v_\theta - \frac{2\cot\theta}{r^2\sin\theta}v_\theta = \frac{1}{\eta}\,\partial_r p, \quad (2.60a)$$

$$\partial_r^2 v_\theta + \frac{2}{r}\,\partial_r v_\theta - \frac{1}{r^2\sin^2\theta}v_\theta + \frac{1}{r^2}\partial_\theta^2 v_\theta + \frac{\cot\theta}{r^2}\partial_\theta v_\theta + \frac{2}{r^2}v_r = \frac{1}{\eta}\frac{1}{r}\partial_\theta p, \quad (2.60b)$$

$$\partial_r v_r + \frac{2}{r}\,v_r + \frac{1}{r}\,\partial_\theta v_\theta + \frac{\cot\theta}{r}\,v_\theta = 0. \quad (2.60c)$$

Fortunately, the solutions for the three fields v_r, v_θ, and p are not very complicated. By inspection one can verify that the solutions are

$$v_r = +V_0\cos\theta\left[1 - \frac{3a}{2r} + \frac{a^3}{2r^3}\right], \quad (2.61a)$$

$$v_\theta = -V_0\sin\theta\left[1 - \frac{3a}{4r} - \frac{a^3}{4r^3}\right], \quad (2.61b)$$

$$p = p_0 - \frac{3}{2}\frac{\eta V_0}{a}\cos\theta\,\frac{a^2}{r^2}. \quad (2.61c)$$

The total frictional force acting on the sphere is the integral of the surface forces,

$$F_{\text{drag}} = \int_{\partial\Omega} da\left(-p\cos\theta + \sigma'_{rr}\cos\theta - \sigma'_{r\theta}\sin\theta\right). \quad (2.62)$$

The stress tensor components in spherical coordinates are

$$\sigma'_{rr} = 2\eta\,\partial_r v_r, \qquad \sigma'_{r\theta} = \eta\left(\frac{1}{r}\partial_\theta v_r + \partial_r v_\theta - \frac{1}{r}\,v_\theta\right). \quad (2.63)$$

Using our explicit results for the velocity and pressure fields we find at the surface $r = a$ of the sphere that

$$\sigma'_{rr} = 0, \qquad \sigma'_{r\theta} = -\frac{3\eta V_0}{2a}\sin\theta, \qquad p = p_0 - \frac{3\eta V_0}{2a}\cos\theta. \quad (2.64)$$

Inserting this into Eq. (2.62) yields the famous formula for the Stokes drag

$$F_{\text{drag}} = 6\pi\eta\,aV_0. \quad (2.65)$$

Consider a particle moving with the velocity $\mathbf{u}$ at a position where the velocity of the fluid would have been $\mathbf{v}$ had the particle not been present. In this case, given that no walls or other obstacles are near by, the expression Eq. (2.65) can be generalized to

$$\mathbf{F}_{\text{drag}} = 6\pi\eta\, a\, (\mathbf{v} - \mathbf{u}). \tag{2.66}$$

2.7   Exercises

Exercise 2.1
Generation of hydrostatic pressure in microchannels
We study some aspect of the difference in hydrostatic pressure between points at different depths in some incompressible liquid.

(a) Check that Eq. (2.3) is a solution to the static Navier–Stokes equation (2.2b).

(b) Consider the figure shown below illustrating a microchannel filled with water. Calculate the pressure generated by the water column of height $H = 10$ cm at the points A, B, and C inside the circular microchannel of radius $a = 100$ μm.

(c) Calculate the heights of mercury- and water-columns generating a pressure difference of 1 atm $= 1.013 \times 10^5$ Pa.
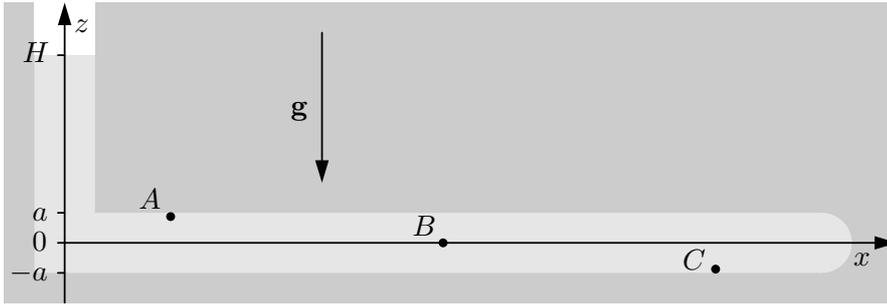
Exercise 2.2
The thickness of the atmosphere of the Earth
Prove the validity of Eqs. (2.4) and (2.6) for an ideal gas under isothermal conditions, and estimate the thickness of the atmosphere. Discuss the result.

Exercise 2.3
The flow of a liquid film on an inclined plane
We study the flow defined in Fig. 2.2 of a liquid film of thickness h on an inclined plane with inclination angle α.

(a) Check the correctness of the form of the Navier–Stokes equation (2.9a) and of the solution for $v_x(z)$ given in Eq. (2.10).

(b) Let the liquid be water and calculate the speed $v_x(h)$ of the free surface of the film in the case of $h = 100$ μm and $\alpha = 30°$.

Exercise 2.4
Symmetry and the structure of the Poiseuille flow solution
Prepare a black-board presentation of the symmetry arguments leading from the Navier–Stokes equation in the general case to the special form of the solution Eq. (2.18a) of the velocity field for the steady-state Poiseuille flow.

Exercise 2.5
Poiseuille flow profile in a circular channel
Sketch the flow profile $v_x(r, \phi)$ of Eq. (2.33a) valid for a circular channel.

Exercise 2.6
The physical origin of the correction term in the rectangular channel
Find a qualitative argument that explains the correction term in Eq. (2.49) for the Poiseuille flow rate Q in a flat, rectangular channel.

Exercise 2.7
Couette flow in an inclined channel
Consider the inclined-plane flow of Fig. 2.2 but substitute the no-stress boundary condition $\partial_z v_x(h) = 0$ of Eq. (2.9c) with the Coeutte flow boundary $v_x(h) = v_0$ of Eq. (2.12c) similar to the one shown in Fig. 2.3. Determine the resulting velocity field $v_x(z)$.

Exercise 2.8
Poiseuille flow in an inclined channel
Extend the analysis presented in Section 2.4.1 for the Poiseuille flow through a channel with an arbitrary cross section by inclining the channel an angle α with respect to the yz plane and taking the effect of gravity into account.

Exercise 2.9
Combined Poiseuille and Couette flow
Extend the analysis presented in Section 2.3 for the planar Couette flow by applying a pressure difference Δp over a section of length L in the x direction. Determine the velocity field $v_x(y, z)$ and the flow rate Q for this combined Poiseuille and Couette flow.

Exercise 2.10
Contour plots of the velocity fields
Use your favorite computer program to generate contour or surface plots illustrating the different Poiseuille velocity fields calculated in Section 2.4.

Exercise 2.11
Stokes drag on a spherical particle in a microchannel
Consider the Stokes drag discussed in Section 2.6.
    (a) Beginning from Eq. (2.65) prove the general expression Eq. (2.66) for the Stokes drag force on a spherical, rigid particle.
    (b) Discuss under which circumstances this expression can be applied to the motion of spherical particles inside microchannels.

2.8 Solutions

Solution 2.1
Generation of hydrostatic pressure in microchannels
We use $g = 9.82$ m/s^2, $\rho_{H_2O} = 10^3$ kg/m^3, and $\rho_{Hg} = 13.6 \times 10^3$ kg/m^3.

(a) $\boldsymbol{\nabla}p = \boldsymbol{\nabla}p_0 - \boldsymbol{\nabla}(\rho g z) = 0 - \rho g\,(0,0,1) = -\rho g\mathbf{e}_z$.

(b) For height H we have $p(x,y,z) = p_H(z) = \rho g(H{-}z) = 9.82\times 10^3\,\mathrm{Pa\,m}^{-1}(0.1\ \mathrm{m}{-}z)$, so $p_A = p_H(100\ \mu\mathrm{m}) = 981$ Pa, $p_B = p_H(0\ \mu\mathrm{m}) = 982$ Pa, $p_C = p_H(-100\ \mu\mathrm{m}) = 983$ Pa.

(c) $H(\rho) = p_0/(\rho g) = \frac{1}{\rho}\,9.82\times 10^3$ kg/m^2 so $H_{H_2O} = 10.3$ m and $H_{Hg} = 0.76$ m.

Solution 2.2
The thickness of the atmosphere of the Earth
Let $p_0 = 10^5$ Pa and $\rho_0 = 1$ kg m^{-3} be the pressure and density of air at ground level. For an ideal isothermal gas $p\mathcal{V}$ or p/ρ is constant, so $\rho = (\rho_0/p_0)\,p$. Thus Eq. (2.2b) becomes $0 = -\partial_z p - (\rho_0 g/p_0)\,p$ or $\partial_z p = -(1/\lambda_{\mathrm{air}})\,p$, where $\lambda_{\mathrm{air}} = p_0/(\rho_0 g) = 10^4$ m. This leads to $p(z) = p_0 \exp(-z/\lambda_{\mathrm{air}})$.

In the isothermal model the density of the atmosphere decreases exponentially with a characteristic length of 10 km. This is in accordance with the fact that a 10 m high water column having $\rho = 1000$ kg m^{-3} can be balanced by a 10 km high air column having $\rho = 1$ kg m^{-3}. Also commercial jet airliners fly at an altitude of 10 km, where there is enough air for the jet engines to work, but less density providing less air resistance.

Solution 2.3
The flow of a liquid film on an inclined plane
Check carefully the assumptions and calculations leading to Eqs. (2.7), (2.8), and (2.9).

(a) Upon insertion of Eq. (2.10) into the left-hand side of Eq. (2.9) we get $\eta\partial_z^2 v_x(z) = \eta\left[\sin\alpha\rho g/(2\eta)\right]\partial_z^2\left[2hz{-}z^2\right] = \sin\alpha(\rho g/2)[0{-}2] = -\rho g\sin\alpha$. Moreover, for the boundary conditions we find $v_x(0) = 0$ and $\partial_z v_x = \left[\sin\alpha\rho g/(2\eta)\right](2h - 2z) \Rightarrow \partial_z v_x(h) = 0$.

(b) $v_x(h{=}100\mu\mathrm{m}) = \left[\sin(30°)(10^3\,\tfrac{\mathrm{kg}}{\mathrm{m}^3} \times 10\,\tfrac{\mathrm{m}}{\mathrm{s}^2})/(2\times10^{-3}\ \mathrm{Pa\,s})\right](10^{-4}\ \mathrm{m})^2 = 0.025\,\tfrac{\mathrm{m}}{\mathrm{s}}$.

Solution 2.4
Symmetry and the structure of the Poiseuille flow solution
Distinguish clearly between physical and mathematical arguments. Begin by a clear formulation of the physical assumptions and arguments that leads to the special form of the velocity field. Insert this velocity field in the full Navier–Stokes equation and reduce it using mathematical arguments.

Solution 2.5
Poiseuille flow profile in a circular channel
Utilizing the connection between Cartesian and
cylindrical coordinates we get

$$v_x(y, z) = v_x(r \cos \phi, r \sin \phi) = v_0 \left[1 - \left(\frac{r}{a} \right)^2 \right],$$

which is plotted in the figure to the right.
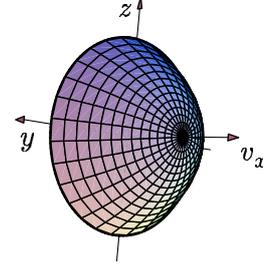
Solution 2.6
The physical origin of the correction term in the rectangular channel
The flow rate is $Q_\parallel = h^3 w \Delta p / (12\eta L)$ in a section of width w in the infinite parallel-plate channel. The flow rate $Q_\square = (1 - \alpha) Q_\parallel$ in a rectangular channel of the same width must be smaller by a relative amount α, since the velocity at the side walls must be zero. The difference between the two channels is solely due to the two side-regions closer than $h/2$ from the sides, since for any point outside these regions the two channels appear identical as the top and bottom walls are closer than the sides. In the parallel-plate channel the flow rate in one side-region of width $h/2$ is $Q_\parallel(h/2)/w$. Assuming a linear drop in local flow rate in the two side regions of the rectangular channel we can estimate the flow rate as $Q_\square = Q_\parallel - 2 \times \frac{1}{2} \times Q_\parallel(h/2)/w = (1 - 0.5h/w)Q_\parallel$ not far from the more exact expression $Q_\square = (1 - 0.63h/w)Q_\parallel$.

Solution 2.7
Couette flow in an inclined channel
The given problem turns Eq. (2.9) into $\eta \, \partial_z^2 v_x(z) = -\rho g \sin \alpha$, $v_x(0) = 0$, and $v_x(h) = 0$. Only the last boundary condition has changed, so the solution $v_x(z)$ is still a parabola, but with changed zeros compared to Eq. (2.10). Introducing the constant $u_0 \equiv \sin \alpha \frac{\rho g}{2\eta} h^2$ of dimension velocity, it is readily verified that the solution is

$$v_x(z) = u_0 \left[\left(1 + \frac{v_0}{u_0} \right) - \frac{z}{h} \right] \frac{z}{h}.$$

Solution 2.8
Poiseuille flow in an inclined channel
Eq. (2.18) for the horizontal Poiseuille flow is only changed by adding a gravity-related term like Eq. (2.9a) to the Navier–Stokes equation Eq. (2.18a) resulting in the equations $v_x(y, z) = 0$ and $\left[\partial_y^2 + \partial_z^2 \right] v_x(y, z) = -\frac{\Delta p}{\eta L} - \frac{\rho g}{\eta} \sin \alpha = -\frac{1}{\eta L} \left(\Delta p + \rho g L \sin \alpha \right)$. The result is a Poiseuille flow an effective pressure drop given by $\Delta p_{\text{eff}} = \Delta p + \rho g L \sin \alpha$.

Solution 2.9
Combined Poiseuille and Couette flow
To the planar Couette flow presented in Section 2.3 is applied a pressure difference Δp over a section of length L in the x direction. The differential equation and boundary condtions

for $v_x(z)$ becomes

$$\partial_z^2 v_x(z) = -\frac{\Delta p}{\eta L}, \tag{2.67a}$$

$$v_x(0) = 0, \quad \text{(no-slip)} \tag{2.67b}$$

$$v_x(h) = v_0, \quad \text{(no-slip on moving wall).} \tag{2.67c}$$

Utilizing the linear structure of the differential equation it is easily verified that the following sum is a solution:

$$v_x(z) = v_x^P(z) + v_x^C(z). \tag{2.68}$$

Here $v_x^P(z)$ solves the Poiseuille problem Eq. (2.51),

$$\partial_z^2 v_x^P(z) = -\frac{\Delta p}{\eta L}, \tag{2.69a}$$

$$v_x^P(0) = 0, \quad \text{(no-slip)} \tag{2.69b}$$

$$v_x^P(h) = 0, \quad \text{(no-slip),} \tag{2.69c}$$

and $v_x^C(z)$ solves the Couette problem Eq. (2.12),

$$\eta \, \partial_z^2 v_x^C(z) = 0, \tag{2.70a}$$

$$v_x^C(0) = 0, \quad \text{(no-slip)} \tag{2.70b}$$

$$v_x^C(h) = v_0, \quad \text{(no-slip on moving wall).} \tag{2.70c}$$

By direct insertion it is easily verified that

$$v_x(0) = v_x^P(0) + v_x^C(0) = 0 + 0 \ = 0, \tag{2.71}$$

$$v_x(h) = v_x^P(h) + v_x^C(h) = 0 + v_0 = v_0, \tag{2.72}$$

and furthermore that

$$\partial_z^2 v_x = \partial_z^2 \left(v_x^P + v_x^C \right) = \partial_z^2 v_x^P + \partial_z^2 v_x^C = -\frac{\Delta p}{\eta L} + 0 = -\frac{\Delta p}{\eta L}. \tag{2.73}$$

Combining this with Eqs. (2.13) and (2.52) leads to the velocity field for the combined Poiseuille and Couette flow,

$$v_x(z) = \frac{\Delta p}{2\eta L} (h - z)z + v_0 \, \frac{z}{h}. \tag{2.74}$$

The flow rate Q is found by integration,

$$Q = Q^P + Q^C = \frac{h^3 w}{12\eta L} \Delta p + \frac{v_0}{h} \int_0^w \mathrm{d}y \int_0^h \mathrm{d}z \, z = \frac{h^3 w}{12\eta L} \Delta p + \frac{1}{2} v_0 h w. \tag{2.75}$$

Solution 2.10
Contour plots of the velocity fields
Using Mathematica the contours plot of the velocity fields in an elliptical, a circular and
an equilateral triangular shaped channel become
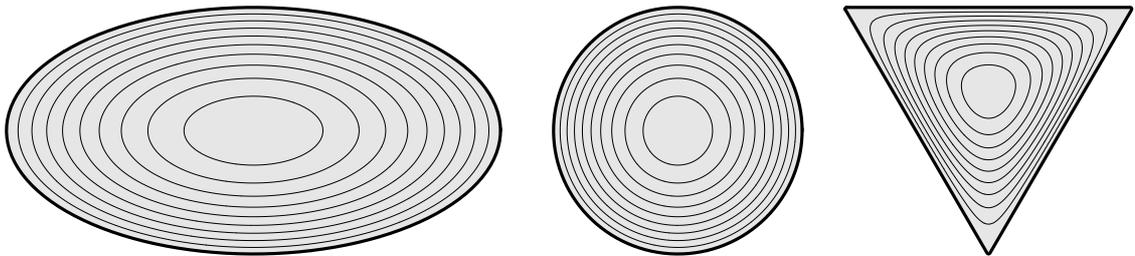
Solution 2.11
Stokes drag on a spherical particle in a microshannel
Fig. 2.11 and the corresponding analysis concern the situation where the velocity of the
unperturbed fluid and of the sphere is $\mathbf{V}_0$ and $\mathbf{0}$, respectively.

(a) Translating the whole system by a constant velocity $\mathbf{u}$ the velocity of the unper-
turbed fluid and of the sphere is $\mathbf{v} = \mathbf{V}_0 + \mathbf{u}$ and $\mathbf{u}$, respectively. This constant-velocity
translation does not change the forces involved, so from Eq. (2.65) we get the desired
result: $\mathbf{F}_{\mathrm{drag}} = 6\pi\eta\, a\, \mathbf{V}_0 = 6\pi\eta\, a\, (\mathbf{v} - \mathbf{u})$.

(b) The Stokes drag formula is only valid in infinite containers in which the liquid
moves very slowly. Hence for microsystems the formula is only valid a very low Reynolds
numbers and when the spherical particles are moving at distances several times their radius
away from the channel walls.

Chapter 3

Hydraulic resistance

In Chapter 2 we studied the pressure driven, steady-state flow of an incompressible fluid through a straight channel, the Poiseuille flow. We found that a constant pressure drop Δp resulted in a constant flow rate Q. This result can be summarized in the Hagen–Poiseuille law

$$\Delta p = R_{\mathrm{hyd}}\, Q = \frac{1}{G_{\mathrm{hyd}}}\, Q, \tag{3.1}$$

where we have introduced the proportionality factors R_{hyd} and G_{hyd} known as the hydraulic resistance and conductance, respectively. The Hagen–Poiseuille law Eq. (3.1) is completely analogous to Ohm's law, $\Delta V = R\, I$, relating the electrical current I through a wire with the electrical resistance R of the wire and the electrical potential drop ΔV along the wire. The SI units used in the Hagen–Poiseuille law are

$$[Q] = \frac{\mathrm{m}^3}{\mathrm{s}}, \qquad [\Delta p] = \mathrm{Pa} = \frac{\mathrm{N}}{\mathrm{m}^2} = \frac{\mathrm{kg}}{\mathrm{m\, s}^2}, \qquad [R_{\mathrm{hyd}}] = \frac{\mathrm{Pa\, s}}{\mathrm{m}^3} = \frac{\mathrm{kg}}{\mathrm{m}^4\, \mathrm{s}}. \tag{3.2}$$

The concept of hydraulic resistance is central in characterizing and designing microfluidic channels in lab-on-a-chip systems. In this chapter we study both fundamental and applied aspects of hydraulic resistance.

3.1 Viscous dissipation of energy for incompressible fluids

Just as electrical resistance is intimately connected to dissipation of energy in the form of Joule heating, hydraulic resistance is due to viscous dissipation of mechanical energy into heat by internal friction in the fluid.

3.1.1 Viscous dissipation in time-dependent systems

To obtain an expression for the energy dissipation in terms of the viscosity and the velocity field, we study the thought experiment sketched in Fig. 3.1. Consider an incompressible fluid inside a channel performing an ideal steady-state Poiseuille flow at times $t < 0$. The constant velocity field $\mathbf{v}$ is maintained by a constant over-pressure Δp applied to the left
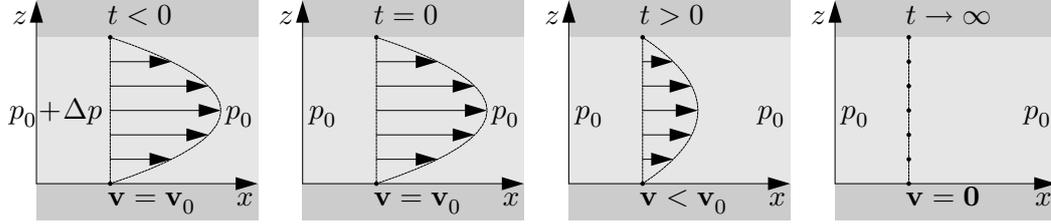
Figure 3.1: A sketch of a liquid (light gray) performing a Poiseuille flow inside a channel (dark gray). For times $t < 0$ the flow is in steady-state, and due to the over-pressure Δp applied to the left, the flow profile is a characteristic parabola. Δp is suddenly turned off at $t = 0$, but inertia keeps up flow. For $t > 0$ the fluid velocity diminishes due to viscous friction, and in the limit $t \to \infty$ the fluid comes to rest relative to the channel walls.

end of the channel. The over-pressure Δp is suddenly removed at $t = 0$, but of course the fluid flow continues due to the inertia of the fluid. However, it is clear that the internal viscous friction of the fluid gradually will slow down the motion of the fluid, and eventually in the limit $t \to \infty$ the fluid will come to rest relative to the channel walls. As time passes the kinetic energy of the fluid at $t = 0$ is gradually transformed into heat by the viscous friction.

In the following we calculate the rate of change of the kinetic energy at any instant $t > 0$, where the over-pressure has been removed. We neglect any influence of gravitational and electrical forces, and we use that for an incompressible fluid the continuity equation reads $\partial_j v_j = 0$. The kinetic energy of the fluid can be expressed as an integral over the space Ω occupied by the channel,

$$E_{\text{kin}} = \int_\Omega d\mathbf{r} \, \frac{1}{2} \, \rho \, \mathbf{v}^2 = \int_\Omega d\mathbf{r} \, \frac{1}{2} \, \rho \, v_i v_i, \tag{3.3}$$

where we use the index notation. The rate of change of E_{kin} is

$$\partial_t E_{\text{kin}} = \int_\Omega d\mathbf{r} \, \rho \, v_i \partial_t v_i. \tag{3.4}$$

We can express the time-derivative $\partial_t v_i$ using the Navier–Stokes equation (1.49),

$$\rho \, \partial_t v_i = -\rho \, v_j \partial_j v_i + \eta \, \partial_j \partial_j v_i. \tag{3.5}$$

The rate of change of the kinetic energy can thus be written as

$$\begin{aligned}
\partial_t E_{\text{kin}} &= \int_\Omega d\mathbf{r} \left\{ -\rho \, v_i v_j \partial_j v_i + \eta \, v_i \partial_j \partial_j v_i \right\} \\
&= \int_\Omega d\mathbf{r} \left\{ -\partial_j \left[v_j \left(\tfrac{1}{2} \rho \, v_i^2 \right) - \eta \, v_i \partial_j v_i \right] - \eta \left(\partial_j v_i \right)\left(\partial_j v_i \right) \right\} \\
&= -\int_{\partial\Omega} da \, n_j \left[v_j \left(\tfrac{1}{2} \rho \, v_i^2 \right) - \eta \, v_i \partial_j v_i \right] - \eta \int_\Omega d\mathbf{r} \left(\partial_j v_i \right)\left(\partial_j v_i \right).
\end{aligned} \tag{3.6}$$
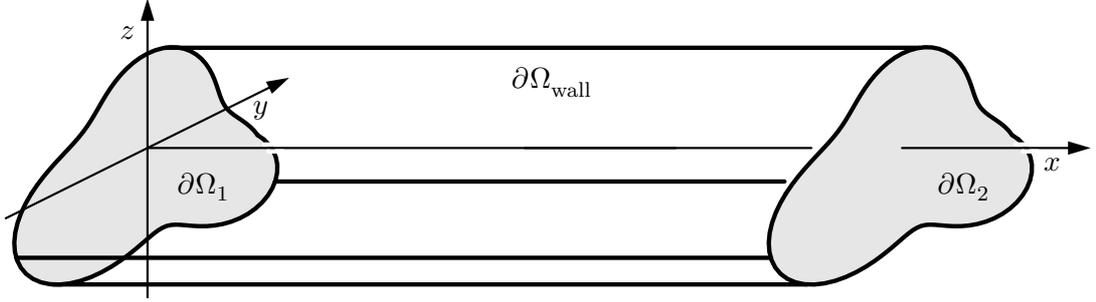
Figure 3.2: A sketch of the geometry for calculating the viscous energy dissipation in a Poiseuille flow. The surface $\partial\Omega$ consists of three parts: the solid side wall $\partial\Omega_{\text{wall}}$ (transparent), the open inlet $\partial\Omega_1$ to the left (light gray), and the open outlet $\partial\Omega_2$ to the right (light gray). The velocity field is parallel to the x direction, $\mathbf{v} = v_x \, \mathbf{e}_x$.

As indicated in Fig. 3.2 the surface $\partial\Omega$ consists of three parts: the solid side wall $\partial\Omega_{\text{wall}}$, the open inlet $\partial\Omega_1$, and the open outlet $\partial\Omega_2$. The contribution to the surface integral in Eq. (3.6) from $\partial\Omega_{\text{wall}}$ is zero due to the no-slip boundary condition that ensures $v_i \equiv 0$ on solid walls. The two contribution from $\partial\Omega_1$ and $\partial\Omega_2$ exactly cancels each other. The reason is that the translation invariance of the Poiseuille flow problem makes the expression in the square bracket independent of x and hence it is the same on the two end surfaces, while the two normal vectors are opposite to each other $\mathbf{n}(\partial\Omega_1) = -\mathbf{e}_x = -\mathbf{n}(\partial\Omega_2)$.

The viscous energy dissipation in a Poiseuille flow relaxing towards thermodynamical equilibrium is therefore given by the volume integral

$$\partial_t E_{\text{kin}} = -\eta \int_\Omega d\mathbf{r} \, (\partial_j v_i)(\partial_j v_i) = -\eta \int_\Omega d\mathbf{r} \left[(\partial_y v_x)^2 + (\partial_z v_x)^2 \right]. \tag{3.7}$$

In the last equality we have used the special form of the Poiseuille flow, $\mathbf{v} = v_x(y,z) \, \mathbf{e}_x$. We note that since the kinetic energy is diminishing in time, so that $\partial_t E_{\text{kin}} < 0$, and since the integrand is always positive, the viscosity coefficient η must be positive.

We let W_{visc} denote the heat generated by the viscous friction. Thus $\partial_t E_{\text{kin}} = -\partial_t W_{\text{visc}}$ and we can write

$$\partial_t W_{\text{visc}} = -\partial_t E_{\text{kin}} = \eta \int_\Omega d\mathbf{r} \, (\partial_j v_i)(\partial_j v_i) = \eta \int_\Omega d\mathbf{r} \left[(\partial_y v_x)^2 + (\partial_z v_x)^2 \right]. \tag{3.8}$$

3.1.2   Viscous dissipation of energy in steady-state

After having used the relaxing Poiseuille flow to obtain an expression for the rate of viscous dissipation of energy, $\partial_t W_{\text{visc}}$, we now turn to the steady-state Poiseuille flow. Consider the usual case where the pressure $p(\partial\Omega_1)$ to the left on $\partial\Omega_1$ is higher than the pressure $p(\partial\Omega_2)$ to the right on $\partial\Omega_2$,

$$p(\partial\Omega_1) = p(\partial\Omega_2) + \Delta p. \tag{3.9}$$

For such a flow the velocity field is constant and consequently the kinetic energy of the fluid is constant. The rate $\partial_t W_{\text{visc}}$ of heat generation by viscous friction is balanced by
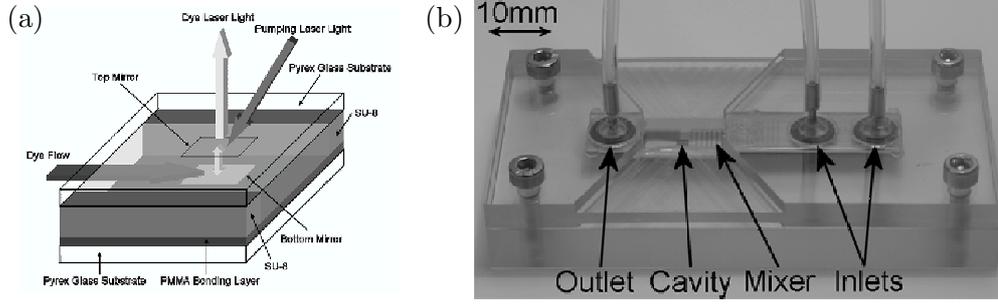
Figure 3.3: (a) A sketch of the active part of a microfluidic dye laser: a rectangular microchannel (the cavity) where the active dye is flowing in a liquid solution. (b) A picture of the actual polymer-based laser chip. For proper functioning a certain flow rate must be used, and hence it is crucial to know the hydraulic resistance of the channel (see Exercise 3.7). Courtesy the group of Kristensen at MIC.

the mechanical power $\partial_t W_{\mathrm{mech}}$ put into the fluid by the pressure force,

$$\partial_t E_{\mathrm{kin}} = \partial_t W_{\mathrm{mech}} - \partial_t W_{\mathrm{visc}} = 0. \qquad (3.10)$$

To calculate W_{mech} we note that in comparison with Eq. (3.5) the Navier–Stokes equation now contains a non-zero pressure gradient and reads

$$\rho\, \partial_t v_i = -\rho\, v_j \partial_j v_i + \eta\, \partial_j \partial_j v_i - \partial_i p. \qquad (3.11)$$

In analogy with Eq. (3.6) we can determine W_{mech} by multiplying the pressure term in Eq. (3.11) by v_i and integrating over volume,

$$\partial_t W_{\mathrm{mech}} = \int_\Omega d\mathbf{r}\, v_i\big(-\partial_i p\big) = -\int_\Omega d\mathbf{r}\, \partial_i\big(v_i p\big) = -\int_{\partial\Omega} da\, n_i\big(v_i p\big). \qquad (3.12)$$

As before the contribution from the solid walls at $\partial\Omega_{\mathrm{wall}}$ is zero due to the no-slip boundary condition and only the inlet $\partial\Omega_1$ and outlet $\partial\Omega_2$ surface yield non-zero contributions. The surface normals are opposite, $\mathbf{n}(\partial\Omega_1) = -\mathbf{e}_x = -\mathbf{n}(\partial\Omega_2)$, and the pressure is constant at each end-face, so we get

$$\partial_t W_{\mathrm{mech}} = p(\partial\Omega_1) \int_{\partial\Omega_1} da\, v_x - p(\partial\Omega_2) \int_{\partial\Omega_2} da\, v_x = \Delta p \int_{\partial\Omega_1} da\, v_x(y, z) = Q\, \Delta p. \qquad (3.13)$$

The second equality is obtained by using the translation invariance $v_x(\partial\Omega_2) = v_x(\partial\Omega_1)$. The result for the viscous dissipation of energy in steady-state Poiseuille flow is thus, as expected, analogous to the expression for the electric power consumed by Joule heating in a resistor, $\partial_t W_{\mathrm{elec}} = I\, \Delta V$,

$$\partial_t W_{\mathrm{visc}} = \eta \int_\Omega d\mathbf{r}\, \Big[\big(\partial_y v_x\big)^2 + \big(\partial_z v_x\big)^2\Big] = Q\, \Delta p. \qquad (3.14)$$

See Exercise 3.2 for further examples of viscous power consumption in hydraulic resistors.

3.2 Hydraulic resistance of some straight channels

In this section we will list a selection of the hydraulic resistance of specific channels, such as the one shown in Fig. 3.3 and studied in Exercise 3.7.

Using the results derived in Section 2.4 for the Poiseuille flow in straight channels, it is easy to list the hydraulic resistance R_{hyd} for the six different cross sections as done in Table 3.1. Next to the analytical expressions for R_{hyd} is given numerical values for R_{hyd}. These values are calculated using the viscosity of water and fixing the length L along the channel axis to be 1 mm. The length-scales perpendicular to the axis are also of the order 100 μm.

The quoted results are all valid for the special case of a translation invariant (straight) channel. This symmetry led to the vanishing of the non-linear term $(\mathbf{v}\cdot\boldsymbol{\nabla})\mathbf{v}$ in the Navier–Stokes equation. However, to handle more general cases it would be very useful to find out when the results for R_{hyd} can be used. This analysis is carried out in the next section, where we shall learn that the dimensionless Reynolds number plays central role.

shape		R_{hyd} expression	R_{hyd} $[10^{11} \frac{\text{Pa s}}{\text{m}^3}]$	reference
circle		$\frac{8}{\pi}\,\eta L\,\frac{1}{a^4}$	0.25	Eq. (2.30b)
ellipse		$\frac{4}{\pi}\,\eta L\,\frac{1+(b/a)^2}{(b/a)^3}\,\frac{1}{a^4}$	3.93	Eq. (2.29)
triangle		$\frac{320}{\sqrt{3}}\,\eta L\,\frac{1}{a^4}$	18.48	Eq. (2.37)
two plates		$12\,\eta L\,\frac{1}{h^3 w}$	0.40	Eq. (2.53)
rectangle		$\frac{12\,\eta L}{1-0.63(h/w)}\,\frac{1}{h^3 w}$	0.51	Eq. (2.49)
square		$\frac{12\,\eta L}{1-0.917\times 0.63}\,\frac{1}{h^4}$	2.84	Exercise 3.4
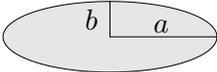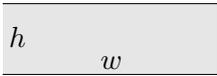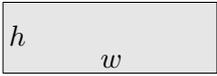
Table 3.1: A list over the hydraulic resistance for straight channels with different cross sectional shapes. The numerical values are calculated using the following parameters: $\eta = 1$ mPa s (water), $L = 1$ mm, $a = 100$ μm, $b = 33$ μm, $h = 100$ μm, and $w = 300$ μm.

3.3   Shape dependence of hydraulic resistance

Given the results in Table 3.1 of the hydraulic resistance R_{hyd} in some straight channels parallel to the x axis, it is natural to ask how R_{hyd} depends on the area $\mathcal{A}$ and perimeter $\mathcal{P}$ of the cross section Ω in the yz plane with boundary $\partial\Omega$,

$$\mathcal{A} \equiv \int_{\Omega} \mathrm{d}x\mathrm{d}y, \tag{3.15a}$$

$$\mathcal{P} \equiv \int_{\partial\Omega} \mathrm{d}\ell. \tag{3.15b}$$

A natural unit for the hydraulic resistance is R_{hyd}^{*}, which is given by dimensional analysis as

$$R_{\mathrm{hyd}}^{*} \equiv \frac{\eta L}{\mathcal{A}^2}, \tag{3.16}$$

where L is the channel length and η the dynamic viscosity of the liquid. Typically, the fluid flow is subject to a no-slip boundary condition at the walls $\partial\Omega$ and thus the actual hydraulic resistance will depend on the perimeter as well as the cross-section area. This dependence can therefore be characterized by the dimensionless geometrical correction factor α given by

$$\alpha \equiv \frac{R_{\mathrm{hyd}}}{R_{\mathrm{hyd}}^{*}} = \frac{\mathcal{A}^2}{\eta L}\, R_{\mathrm{hyd}}. \tag{3.17}$$

For Poiseuille flow the relation between the pressure drop Δp, the velocity $v_x(y,z)$, and the geometrical correction factor α becomes

$$\Delta p = R_{\mathrm{hyd}} Q = \alpha R_{\mathrm{hyd}}^{*} Q = \alpha R_{\mathrm{hyd}}^{*} \int_{\Omega} \mathrm{d}x\mathrm{d}y\, v_x(y,z), \tag{3.18}$$

where Q is the volume flow rate.

   In lab-on-a-chip applications, where large surface-to-volume ratios are encountered, the problem of the bulk Poiseuille flow is typically accompanied by other surface-related physical or bio-chemical phenomena in the fluid. The list of examples includes surface chemistry, DNA hybridization on fixed targets, catalysis, interfacial electrokinetic phenomena such as electro-osmosis, electrophoresis and electro-viscous effects as well as continuous edge-source diffusion. Though the phenomena are of very different nature, they have at least one thing in common; they are all to some degree surface phenomena and their strength and effectiveness depends strongly on the surface-to-volume ratio. It is common to quantify this by the dimensionless compactness $\mathcal{C}$ given by

$$\mathcal{C} \equiv \frac{\mathcal{P}^2}{\mathcal{A}}. \tag{3.19}$$

Below we demonstrate a simple dependence of the geometrical correction factor α on the compactness $\mathcal{C}$ and our results thus point out a unified dimensionless measure of flow properties as well as the strength and effectiveness of surface-related phenomena central to lab-on-a-chip applications. Furthermore, our results allow for an easy evaluation

of the hydraulic resistance for elliptical, rectangular, and triangular cross-sections with the geometrical measure $\mathcal{C}$ being the only input parameter. Above we have emphasized microfluidic flows because here a variety of shapes are frequently encountered. However, our results are generally valid for all laminar flows.

Our main objective is to find the relation between the geometrical correction factor α and the compactness $\mathcal{C}$ for various families of geometries.

The family of elliptical cross-sections is special in the sense that R_{hyd} is know analytically for given semi-axis lengths a and b, see Table 3.1. An explicit expression for the geometrical correction factor α is obtained as follows

$$\alpha(a,b) = \frac{R_{\mathrm{hyd}}}{R_{\mathrm{hyd}}^*} = \frac{\frac{4}{\pi}\,\eta L\,\frac{1+(b/a)^2}{(b/a)^3}\,\frac{1}{a^4}}{\eta L\,\frac{1}{(\pi ab)^2}} = 4\pi\left(\frac{a}{b}+\frac{b}{a}\right), \tag{3.20}$$

which for a circle yields $\alpha(a,a) = 8\pi$.

By straightforward algebra we can express the line integral for the perimeter $\mathcal{P}$ as an integral over an angle θ, and the compactness $\mathcal{C}$ follows as

$$\mathcal{C}(\alpha) = \frac{1}{2\pi^2}\left(\int_0^\pi \mathrm{d}\theta\sqrt{\alpha+\sqrt{\alpha^2-(8\pi)^2}\cos\theta}\,\right)^2. \tag{3.21}$$

Expanding $\mathcal{C}(\alpha)$ in α around $\alpha = 8\pi$ and inverting we get

$$\alpha(\mathcal{C}) = \frac{8}{3}\,\mathcal{C} - \frac{8\pi}{3} + \mathcal{O}([\mathcal{C}-4\pi]^2), \tag{3.22}$$

and in Fig. 3.4 we compare this approximate result (dashed line) with the exact solution (solid line), obtained from a numerical evaluation of Eq. (3.21). Results of a numerical finite-element solution of Poiseuille flow are also included ($\circ$ points). As seen, there is a close-to-linear dependence of α on $\mathcal{C}$ as described by Eq. (3.22).

For the rectangular channel with a width-to-height ratio $\gamma = w/h$, we can by combining Eqs. (2.48c) and (3.17) obtain

$$\alpha(\gamma) = \frac{\pi^3\gamma^2}{8}\left(\sum_{n,\mathrm{odd}}^{\infty}\frac{n\gamma}{\pi n^5} - \frac{2}{\pi^2 n^5}\tanh(n\pi\gamma/2)\right)^{-1}. \tag{3.23}$$

The compactness is easily found as

$$\mathcal{C}(\gamma) = \frac{\mathcal{P}^2}{\mathcal{A}} = \frac{(2w+2h)^2}{wh} = 8 + 4\gamma + 4/\gamma. \tag{3.24}$$

Using that $\tanh(x) \simeq 1$ for $x \gg 1$ we get

$$\alpha(\gamma) \simeq \frac{12\pi^5\gamma^2}{\pi^5\gamma - 186\zeta(5)}, \quad \gamma \gg 1, \tag{3.25}$$
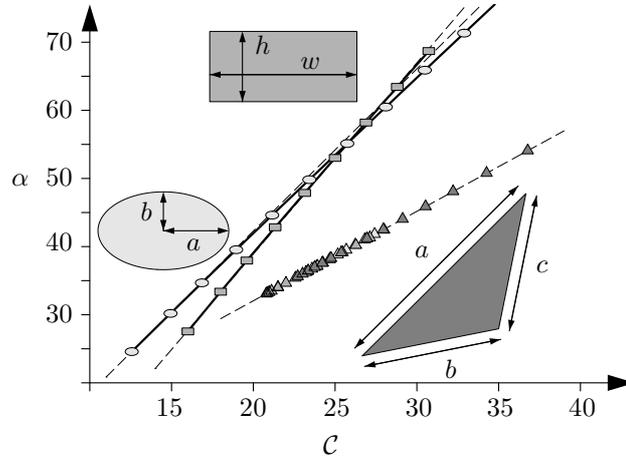
Figure 3.4: Correction factor versus compactness for the elliptical, rectangular, and triangular classes. The solid lines are the exact results, and the dashed lines indicate Eqs. (3.22), (3.26), and (3.27). Numerical results from a finite-element simulation are also included ($\circ$, $\square$, and $\triangle$). Note that in the case of triangles all classes (right, isosceles, and acute/obtuse scalene triangles — marked by different grayscale triangles) fall on the same straight line.

and by substituting $\gamma(\mathcal{C})$ into this expression and expanding $\mathcal{C}(\gamma)$ around $\gamma = 2$ with $\mathcal{C}(2) = 18$, we obtain again a linear relation between α and $\mathcal{C}$:

$$\alpha(\mathcal{C}) \approx \frac{22}{7}\,\mathcal{C} - \frac{65}{3} + \mathcal{O}\big([\mathcal{C} - 18]^2\big). \tag{3.26}$$

In Fig. 3.4 we compare the exact solution, obtained by a parametric plot of Eqs. (3.23) and (3.24), to the approximate result, Eq. (3.26). Results of a numerical finite-element solution of Eq. (12.3a) are also included ($\square$ points). As in the elliptical case, there is a close-to-linear dependence of α on $\mathcal{C}$ as described by Eq. (3.26).

For the equilateral triangle it follows from Table 3.1 that $\alpha = 20\sqrt{3}$ and $\mathcal{C} = 12\sqrt{3}$. However, in the general case of a triangle with side lengths a, b, and c we are referred to numerical solutions of the Poiseuille flow. In Fig. 3.4 we show numerical results ($\triangle$ points), from finite-element simulations, for scaling of right triangles, isosceles triangles, and acute/obtuse scalene triangles. The dashed line shows

$$\alpha(\mathcal{C}) = \frac{25}{17}\,\mathcal{C} + \frac{40\sqrt{3}}{17}, \tag{3.27}$$

where the slope is obtained from a numerical fit. As seen, the results for different classes of triangles fall onto the same straight line. Since we have

$$\mathcal{C}(a,b,c) = \frac{8(a+b+c)^2}{\sqrt{\frac{1}{2}\big(a^2+b^2+c^2\big)^2 - \big(a^4+b^4+c^4\big)}} \tag{3.28}$$

the result in Eq. (3.27) allows for an easy evaluation of R_{hyd} for triangular channels.

Finally, by using the results given in Section 2.5 we can calculate the kth multipolar deformation of the circular cross section and thereby extend the analytical results for Poiseuille flow beyond the few cases of regular geometries that we have treated above. By continuing the perturbation calculation to fourth order in the perturbation parameter ϵ, we can obtain analytical expressions for both the velocity field and the boundary shape. This leads to analytical expressions for $\mathcal{A}$ and $\mathcal{P}$, which in turns results in the following expressions for α and $\mathcal{C}$:

$$\alpha = 8\pi \left[1 + 2(k-1)\,\epsilon^2 + \frac{47 - 78k + 36k^2 - 4k^3}{8}\,\epsilon^4 \right] + \mathcal{O}\!\left(\epsilon^6\right), \qquad (3.29)$$

$$\mathcal{C} = 4\pi + 2\pi(k^2 - 1)\,\epsilon^2. \qquad (3.30)$$

The result only involves even powers of ϵ since $\epsilon \to -\epsilon$ is equivalent to a shape-rotation, which should leave α and $\mathcal{C}$ invariant, and as a consequence α depends linearly on $\mathcal{C}$ to fourth order in ϵ,

$$\alpha(\mathcal{C}) = \frac{8}{1+k}\,\mathcal{C} - 8\frac{3-k}{1+k}\,\pi + \mathcal{O}\!\left(\epsilon^4\right). \qquad (3.31)$$

Note that although derived for $k > 2$ this expression coincides with that of the ellipse, Eq. (3.22), for $k = 2$. Comparing Eq. (3.29) [to second order in ϵ] with exact numerics we find that for ϵ up to 0.4 the relative error is less than 0.2% and 0.5% for $k = 2$ and $k = 3$, respectively.

In summary, we have considered pressure-driven, steady state Poiseuille flow in straight channels with various shapes, and found a close-to-linear relation between α and $\mathcal{C}$. Since the hydraulic resistance is $R_{\mathrm{hyd}} \equiv \alpha R_{\mathrm{hyd}}^*$, we conclude that R_{hyd} depends linearly on $\mathcal{C} R_{\mathrm{hyd}}^*$. Different classes of shape all display this linear relation, but the coefficients are non-universal. However, for each class only two points need to be calculated to fully specify the relation for the entire class. The difference is due to the smoothness of the boundaries. The elliptical and harmonic-perturbed classes have boundaries without any cusps whereas the rectangular and triangular classes have sharp corners. The over-all velocity profile tends to be convex and maximal near the center-of-mass of the channel. If the boundary is smooth the velocity in general goes to zero in a convex parabolic manner whereas a concave parabolic dependence is generally found if the boundary has a sharp corner, as can be proved explicitly for the equilateral triangle Eq. (2.34). Since the concave drop is associated with a region of low velocity compared to the convex drop, geometries with sharp changes in the boundary tend to have a higher hydraulic resistance compared to smooth geometries with equivalent cross-sectional area.

3.4 The dimensionless Reynolds number

The proper way to see if the non-linear term $(\mathbf{v}\cdot\boldsymbol{\nabla})\mathbf{v}$ in the Navier–Stokes equation can be neglected is to make the equation dimensionless. This means that we express all physical quantities, such as length and velocity, in units of the characteristic scales, e.g., L_0 for length and V_0 for velocity.

3.4.1   Reynolds number for systems with only one length scale

If the system under consideration is characterized by only one length scale L_0 and one velocity scale V_0, the expression of coordinates and velocity in terms of dimensionless coordinates and velocity is

$$\mathbf{r} = L_0\,\tilde{\mathbf{r}}, \qquad \mathbf{v} = V_0\,\tilde{\mathbf{v}}, \tag{3.32}$$

where the tilde on top of a symbol indicates that the symbol is a quantity without physical dimension, i.e., pure numbers. Once the length and velocity scale L_0 and V_0 has been fixed the scales T_0 and P_0 for time and pressure follows,

$$t = \frac{L_0}{V_0}\,\tilde{t} = T_0\,\tilde{t}, \qquad p = \frac{\eta V_0}{L_0}\,\tilde{p} = P_0\,\tilde{p}. \tag{3.33}$$

Note that a quantity often can be made dimensionless in more than one way. Regarding the pressure it is for example possible to choose P_0 either as $\eta V_0/L_0$ or as $\rho\,V_0{}^2$. The former gives the scale of pressure in the case of small velocities, such as in microfluidics, whereas the latter is used at high velocities.

By insertion of Eqs. (3.32) and (3.33) into the Navier–Stokes equation and using the straightforward scaling of the derivatives, $\partial_t = (1/T_0)\,\tilde{\partial}_t$ and $\boldsymbol{\nabla} = (1/L_0)\,\tilde{\boldsymbol{\nabla}}$, we get

$$\rho\left[\frac{V_0}{T_0}\,\tilde{\partial}_t\tilde{\mathbf{v}} + \frac{V_0{}^2}{L_0}\left(\tilde{\mathbf{v}}\cdot\tilde{\boldsymbol{\nabla}}\right)\tilde{\mathbf{v}}\right] = -\frac{P_0}{L_0}\,\tilde{\boldsymbol{\nabla}}\tilde{p} + \frac{\eta V_0}{L_0{}^2}\,\tilde{\boldsymbol{\nabla}}^2\tilde{\mathbf{v}}, \tag{3.34}$$

which after reduction becomes

$$Re\left[\tilde{\partial}_t\tilde{\mathbf{v}} + \left(\tilde{\mathbf{v}}\cdot\tilde{\boldsymbol{\nabla}}\right)\tilde{\mathbf{v}}\right] = -\tilde{\boldsymbol{\nabla}}\tilde{p} + \tilde{\boldsymbol{\nabla}}^2\tilde{\mathbf{v}}. \tag{3.35}$$

Here we have introduced the dimensionless number Re, which is called the Reynolds number, and which is defined as

$$Re \equiv \frac{\rho V_0 L_0}{\eta}. \tag{3.36}$$

We clearly see from Eq. (3.35) that for $Re \ll 1$ the viscous term $\tilde{\boldsymbol{\nabla}}^2\tilde{\mathbf{v}}$ dominates, whereas in steady-state for $Re \gg 1$ the inertia term $\left(\tilde{\mathbf{v}}\cdot\tilde{\boldsymbol{\nabla}}\right)\tilde{\mathbf{v}}$ is the most important term.

The corresponding dimensionless form of the incompressibility condition $\partial_i v_i = 0$ is quite simple since $\partial_i = (1/L_0)\tilde{\partial}_i$ and $v_i = V_0\,\tilde{v}_i$,

$$\tilde{\partial}_i\tilde{v}_i = 0. \tag{3.37}$$

From this little analysis we can conclude that the solutions obtained for the ideal Poiseuille flows, where the non-linear term $(\mathbf{v}\cdot\boldsymbol{\nabla})\mathbf{v}$ is identically zero, remains approximately valid if the Reynolds number is small, $Re \ll 1$.
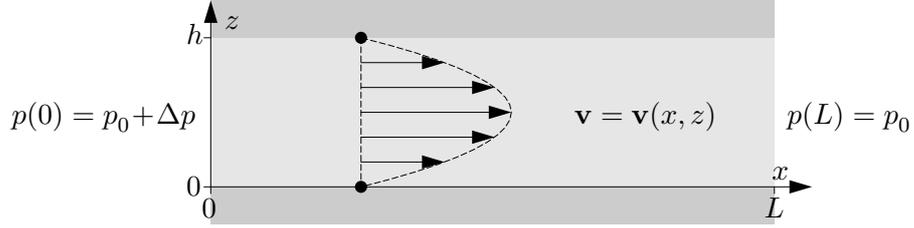
Figure 3.5: A sketch in the xz plane of an infinite, parallel-plate channel of height h. The system is translation invariant in the y direction and fluid is flowing in the x direction due to a pressure drop Δp over the section of length L.

3.4.2 Reynolds number for systems with two length scales

Most systems are characterized by more than one length, which leads to a more involved Reynolds number analysis. As an example, consider a section of length L and width w of the infinite, parallel-plate channel with height h shown in Fig. 3.5. The system is translation invariant in the y direction so that only the x and z coordinates enter in the following analysis. Although the system as shown is also translation invariant in the x direction, we perform the analysis as if this invariance is weakly broken rendering a non-zero vertical velocity v_z.

The two length scales entering the problem are the length L and the height h,

$$x = L\,\tilde{x}, \qquad z = h\,\tilde{z}, \tag{3.38}$$

yielding the spatial derivatives

$$\partial_x = \frac{1}{L}\,\tilde{\partial}_x \equiv \varepsilon\,\frac{1}{h}\,\tilde{\partial}_x, \qquad \partial_z = \frac{1}{h}\,\tilde{\partial}_z, \tag{3.39}$$

where we have introduced the aspect ratio ε defined by

$$\varepsilon \equiv \frac{h}{L} \ll 1. \tag{3.40}$$

The characteristic velocity in the x direction is given by the mean velocity $V_0 = Q/(wh)$, where Q is the flow rate through a section of width w and height h. The characteristic time T_0 is therefore given by

$$t = \frac{L}{V_0}\,\tilde{t} = T_0\,\tilde{t}. \tag{3.41}$$

From this follows the expressions for the two velocity components,

$$v_x = V_0\,\tilde{v}_x, \qquad v_z = \frac{h}{T_0}\,\tilde{v}_z = \varepsilon\,V_0\,\tilde{v}_z. \tag{3.42}$$

Finally, the characteristic pressure is given by the pressure drop P_0, see Table 3.1,

$$P_0 = R_{\text{hyd}}Q \simeq \frac{\eta L}{h^3 w}\,Q = \frac{\eta V_0 L}{h^2}, \tag{3.43}$$
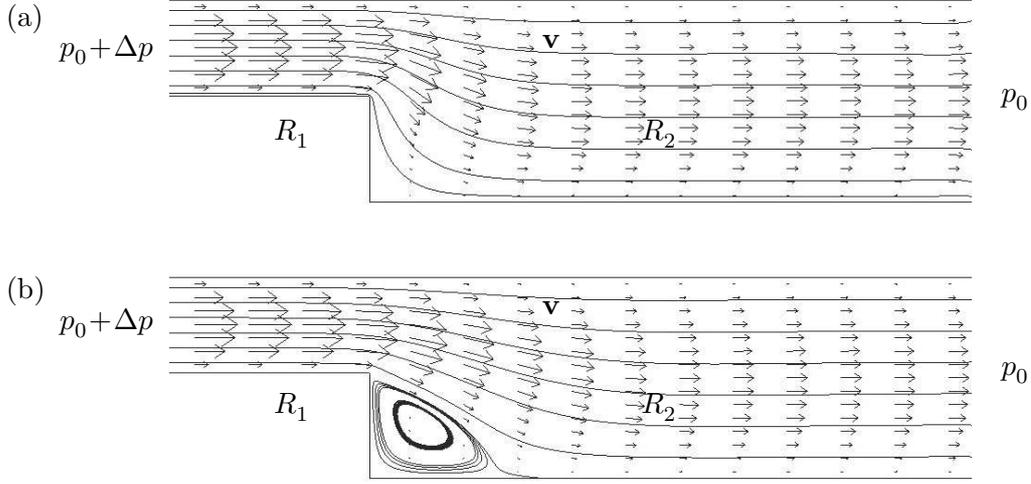
Figure 3.6: (a) Two hydraulic resistors, R_1 and R_2, connected in series forming a back-step of height $h_2 - h_1$. The shown velocity field and streamlines are calculated in FemLab. Here $Re = 0.01$ so for this series coupling the Hagen–Poiseuille law states $\Delta p = (R_1 + R_2)Q$. (b) Here $Re = 100$ and a convection roll appears after the back-step. The large inertia forces makes the simple Hagen–Poiseuille law invalid, $\Delta p \neq (R_1 + R_2)Q$.

where for convenience we have dropped the numerical factor of 12.

If we follow the convention that the Reynolds number Re should contain the smallest length scale of the problem, here h, we define

$$Re \equiv \frac{\rho V_0 h}{\eta}. \tag{3.44}$$

Using the above mentioned expressions we can rewrite the two-component Navier–Stokes equation and the continuity equation in terms of dimensionless variables. The result is

$$\varepsilon Re\left(\tilde{\partial}_t + \tilde{v}_x\tilde{\partial}_x + \tilde{v}_z\tilde{\partial}_z\right)\tilde{v}_x = -\tilde{\partial}_x\tilde{p} + \left(\tilde{\partial}_z^2 + \varepsilon^2\tilde{\partial}_x^2\right)\tilde{v}_x, \tag{3.45a}$$

$$\varepsilon^3 Re\left(\tilde{\partial}_t + \tilde{v}_x\tilde{\partial}_x + \tilde{v}_z\tilde{\partial}_z\right)\tilde{v}_z = -\tilde{\partial}_z\tilde{p} + \left(\varepsilon^2\tilde{\partial}_z^2 + \varepsilon^4\tilde{\partial}_x^2\right)\tilde{v}_z, \tag{3.45b}$$

$$\tilde{\partial}_x\tilde{v}_x + \tilde{\partial}_z\tilde{v}_z = 0. \tag{3.45c}$$

To first order in ε in the limit of high aspect ratios, $\varepsilon \to 0$, these equations become

$$\varepsilon Re\left(\tilde{\partial}_t + \tilde{v}_x\tilde{\partial}_x + \tilde{v}_z\tilde{\partial}_z\right)\tilde{v}_x = -\tilde{\partial}_x\tilde{p} + \tilde{\partial}_z^2\tilde{v}_x, \tag{3.46a}$$

$$0 = -\tilde{\partial}_z\tilde{p}, \tag{3.46b}$$

$$\tilde{\partial}_x\tilde{v}_x + \tilde{\partial}_z\tilde{v}_z = 0, \tag{3.46c}$$

and we can conclude that the effective Reynolds number Re_{eff} for this two-length-scale problem is

$$Re_{\text{eff}} = \varepsilon\, Re = \frac{\rho V_0 h}{\eta}\frac{h}{L}. \tag{3.47}$$

This effective Reynolds number can therefore be arbitrarily small compared to the conventional Reynolds number given a sufficiently long channel.

3.5 Hydraulic resistance, two connected straight channels

When two straight channels of different dimensions are connected to form one long channel the translation invariance will in general be broken, and the expressions for the ideal Poiseuille flow no longer apply. However, we expect the ideal description to be approximatively correct if the Reynolds number Re of the flow is sufficiently small. This is because a very small value of Re corresponds to a vanishing small contribution from the non-linear term in the Navier–Stokes equation, a term that is strictly zero in ideal Poiseuille flows due to translation invariance.

The influence of the Reynolds number on the velocity field is illustrated in Fig. 3.6, where results of numerical simulations using FemLab have been shown. Two infinite parallel-plate channels with heights h_1 and h_2 and hydraulic resistances R_1 and R_2 are joined in a series coupling forming a back-step of height $h_2 - h_1$. At low Reynolds number $Re = \rho V_0 h_1 / \eta = 0.01$, panel (a), the transition from a perfect Poiseuille flow in R_1 is smooth and happens on a length scale shorter than h_1. At high Reynolds number $Re = \rho V_0 h_1 / \eta = 100$, panel (b), the transition happens on a length scale larger than h_1, and a convection roll forms in the entrance region of R_2. This is a simple example of how it is a fair approximation to assume ideal Poiseuille flows in individual parts of a microfluidic network at low Reynolds numbers, whereas the approximation is dubious at high Reynolds numbers.

Note that in microfluidics the Reynolds number $Re = \rho V_0 L_0 / \eta$ tends to be low due to the small length scales L_0 involved.

3.5.1 Two straight channels in series

Consider the series coupling of two hydraulic resistors as shown in Fig. 3.7. If we assume the validity of the Hagen–Poiseuille law for each of the resistors after they are connected,
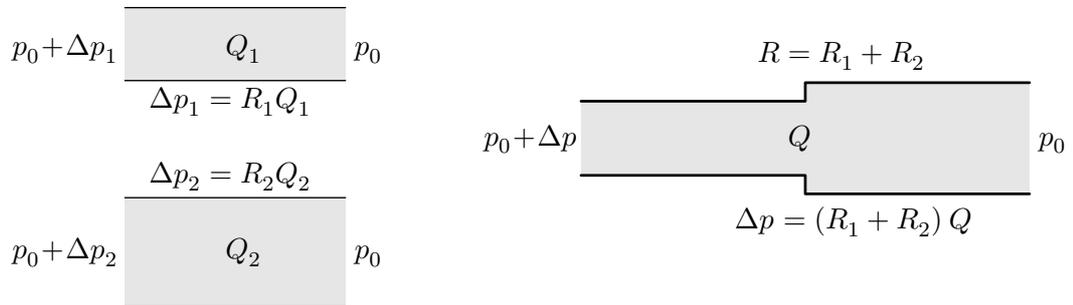
Figure 3.7: The series coupling of two channels with hydraulic resistance R_1 and R_2. The simple additive law $R = R_1 + R_2$ is only valid in the limit of low Reynolds number, $Re \to 0$, and for long narrow channels.
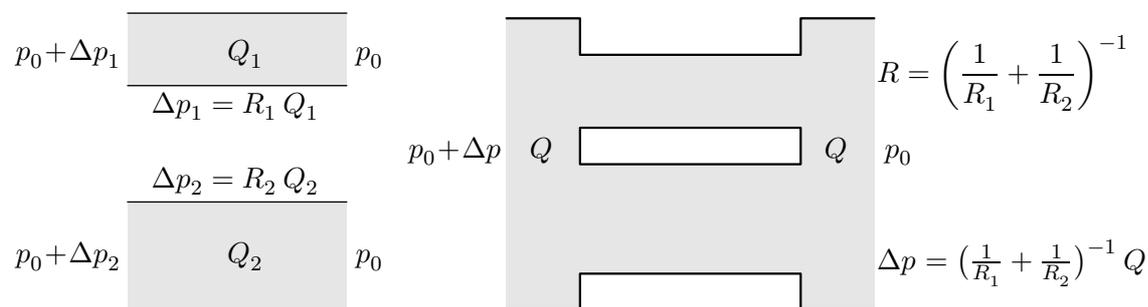
Figure 3.8: The parallel coupling of two channels with hydraulic resistance R_1 and R_2. The additive law for the inverse resistances $R^{-1} = R_1{}^{-1} + R_2{}^{-1}$ is only valid in the limit of low Reynolds number, $Re \to 0$, and for long narrow channels far apart.

then using the additivity of the pressure drop along the series coupling it is straightforward to show the law of additivity of hydraulic resistors in a series coupling,

$$R = R_1 + R_2. \tag{3.48}$$

Bearing in mind the discussion in the previous subsection, the additive law is only valid for low Reynolds numbers and for long and narrow channels.

3.5.2   Two straight channels in parallel

Consider the parallel coupling of two hydraulic resistors as shown in Fig. 3.8. If we assume the validity of the Hagen–Poiseuille law for each of the resistors after they are connected, then using the conservation of flow rate, i.e., $Q = Q_1 + Q_2$ in the parallel coupling it is straightforward to show the law of additivity of inverse hydraulic resistances in a parallel coupling,

$$R = \left(\frac{1}{R_1} + \frac{1}{R_2}\right)^{-1} = \frac{R_1 \, R_2}{R_1 + R_2}. \tag{3.49}$$

Bearing in mind the discussion in the previous subsection, the inverse-additive law is only valid for low Reynolds numbers and for long and narrow channels far apart.

3.6   Compliance

The same form of Hagen-Poiseuille's law and Ohm's law means that pressure drop Δp and flow rate Q (volume $\mathcal{V}$ per time) are analogous to voltage drop ΔU and current I (charge q per time), respectively. Now, since electric capacitance is given by $C = \mathrm{d}q/\mathrm{d}U$ we are led to introduce hydraulic capacitance, also known as compliance, given by

$$C_{\mathrm{hyd}} \equiv -\frac{\mathrm{d}\mathcal{V}}{\mathrm{d}p}, \tag{3.50}$$

where the minus is chosen since the volume diminishes as the pressure increases. Compliance exists because neither real fluids nor the chambers or channels containing them
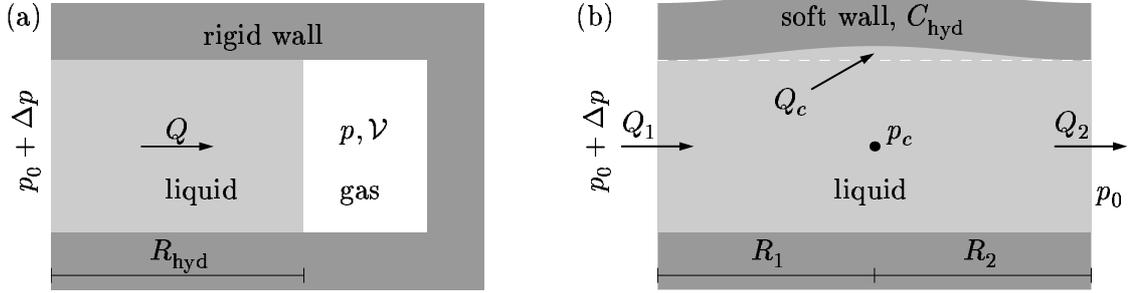
Figure 3.9: (a) Compliance due to a volume $\mathcal{V}$ of gas (white) trapped inside a closed rigid-walled channel (dark gray) partly filled with a liquid piston (light gray). The hydraulic resistance of the liquid-filled part of the channel is denoted R_{hyd}. Mass conservation yields $Q = -\partial_t \mathcal{V}$. (b) Compliance due to a soft-walled channel (dark gray) filled with liquid (light gray). The pressure in the center of the channel is denoted p_c, while the hydraulic resistances of the first and second part of the channel are denoted R_1 and R_2, respectively. Mass conservation yields $Q_1 = Q_2 + Q_c$.

are completely rigid. Their volume change, often only by minute amounts, as the ambient pressure changes.

As a simple example of compliance consider an amount of gas being trapped by an advancing liquid acting as a liquid piston in a closed channel, as shown in Fig. 3.9(a). The compliance of the gas is very large compared to that of the liquid and the channel wall, so the latter two can be neglected. At atmospheric pressure p_0 the gas fills the volume $\mathcal{V}_0$, but as the liquid advances the volume $\mathcal{V}$ and pressure p of the gas changes. Assuming an isothermal process, the ideal gas law leads to $p\mathcal{V} = p_0\mathcal{V}_0$ and consequently $C_{\mathrm{hyd}} = p_0\mathcal{V}_0/p^2$. If the pressure does not deviate much from p_0 we get $C_{\mathrm{hyd}} \approx \mathcal{V}_0/p_0$. For time $t < 0$ the pressure is everywhere p_0. Then assume that at time $t = 0$ the pressure at the liquid inlet suddenly is increased from p_0 to $p_0 + \Delta p$. The liquid begins to advance with a flow rate $Q(t)$ leading to a decrease in the volume of the gas given by $-\partial_t \mathcal{V} = Q(t)$. The chain-rule gives us $Q(t) = -\partial_t \mathcal{V} = -(\partial_p \mathcal{V})\partial_t p = C_{\mathrm{hyd}}\partial_t p$, and hence by Hagen-Poiseuille's law

$$(p_0 + \Delta p) - p = R_{\mathrm{hyd}}Q = -R_{\mathrm{hyd}}\partial_t \mathcal{V} = R_{\mathrm{hyd}}C_{\mathrm{hyd}}\partial_t p. \tag{3.51}$$

The solution for the gas pressure $p(t)$ is easily seen to be analogous to the voltage across a charging capacitor with a characteristic RC-time τ,

$$p(t) = p_0 + \left(1 - e^{-t/\tau}\right)\Delta p, \quad \tau \equiv R_{\mathrm{hyd}}C_{\mathrm{hyd}}. \tag{3.52}$$

As a second example of compliance we consider a simple model of a soft-walled channel filled with an incompressible liquid as sketched in Fig. 3.9(b). If the pressure increases inside the channel, the latter will expand. The compliance C_{hyd} of the channel is a given constant related to the geometry and the material properties of the channel walls. As a simplification we model the channel as consisting of two sub-channels with hydraulic resistances R_1 and R_2, respectively, connected in series. The pressure p_c at the point,

(a)

(b)
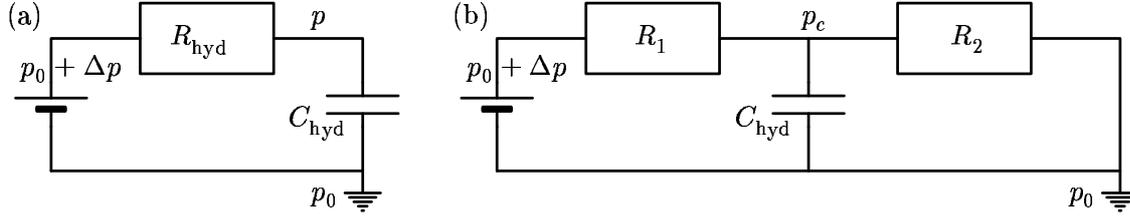
Figure 3.10: (a) The equivalent circuit diagram corresponding to the liquid piston setup of Fig. 3.9(a) where R_{hyd} is the hydraulic resistance of the liquid-filled part of the channel, while C_{hyd} is the compliance of the trapped air. (b) The equivalent circuit diagram corresponding to the soft-walled channel of Fig. 3.9(b), where R_1 and R_2 are the hydraulic resistances of each part of the channel, while C_{hyd} is the compliance of the soft wall.

where the two sub-channels connect, determines the expansion of the whole channel. As before we let the pressure at the inlet be p_0 for time $t < 0$ and $p_0 + \Delta p$ for time $t > 0$. The flow rate at the inlet and the outlet are given by $Q_1 = (p_0 + \Delta p - p_c)/R_1$ and $Q_2 = (p_c - p_0)/R_2$, respectively, while the rate of volume expansion inside the chamber is given by $Q_c = -\partial_t \mathcal{V} = C_{\mathrm{hyd}} \partial_t p_c$. Since the liquid is assumed to be incompressible, conservation of mass leads to $Q_1 = Q_2 + Q_c$, and we arrive at the following differential equation for the pressure p_c inside the channel:

$$\partial_t p_c = -\left(\frac{1}{\tau_1} + \frac{1}{\tau_2}\right)p_c + \left(\frac{1}{\tau_1} + \frac{1}{\tau_2}\right)p_0 + \frac{1}{\tau_1}\Delta p, \tag{3.53}$$

where $\tau_1 = R_1 C_{\mathrm{hyd}}$ and $\tau_2 = R_2 C_{\mathrm{hyd}}$ are the hydraulic RC-times. The solution,

$$p_c(t) = p_0 + \left(1 - e^{-\left[\tau_1^{-1} + \tau_2^{-1}\right]t}\right)\frac{\tau_2}{\tau_1 + \tau_2}\Delta p, \tag{3.54}$$

is analogous to the voltage across a capacitor being charged through a voltage divider.

3.7   Equivalent circuit theory and Kirchhoff's laws

Given the complete analog between the Hagen–Poiseuille law and Ohm's law even to the point of the rules for series/parallel couplings of resistors and capacitors, it is an obvious advantage to apply the well-known methods from electric circuit theory to microfluidic networks on lab-on-a-chip systems. For a given microfluidic network one draws the equivalent electric network. Channels with hydraulic resistances R_{hyd} become resistors, channels with hydraulic compliance C_{hyd} become capacitors, flow rates Q become currents, and pumps delivering pressure differences Δp become batteries. The equivalent network for the two hydraulic systems of Fig. 3.9 are shown in Fig. 3.10, where the common ground for pressure quite naturally has been chosen to be the atmospheric pressure p_0. For any given fluidic network or circuit one can then apply Kirchhoff's laws:

a) The sum of flow rates entering/leaving any node in the circuit is zero.
b) The sum of all pressure differences in any closed loop of the circuit is zero. $\qquad$ (3.55)
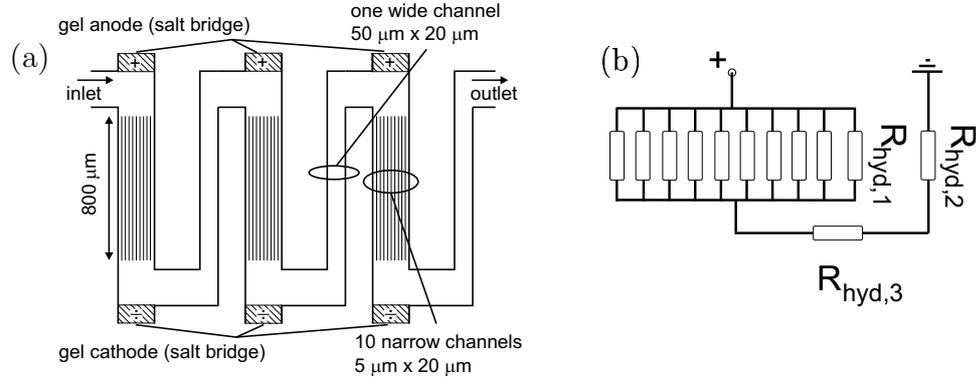
Figure 3.11: An equivalent circuit analysis on a so-called cascade electro-osmotic micro-pump from Brask, Goranović and Bruus, Sensor. Actuat. Chem-B **92**, 127-132 (2003). (a) A sketch of three identical stages in the micropump, each consisting of ten narrow channels in parallel followed by a single wide channel in series. (b) The equivalent circuit diagram for calculation of the hydraulic resistance of a single stage. Courtesy the group of Bruus at MIC.

The analogy is even more complete. The concept of impedance also applies for fluidic circuits. As studied in Exercise 3.10 the flow rate response $Q(t)$ to a harmonic pressure stimulus $p(t) = p_0 + \Delta p \, e^{i\omega t}$ can be analyzed in terms of the resistive and capacitive impedances Z_R and Z_C, respectively. Furthermore, although rarely important in microfluidics, the inertia $L_{\text{hyd}} = \rho L / \mathcal{A}$ of fluids is analogous electrical inductance with the inductive impedance Z_L. The three impedances are given by

$$Z_R \equiv R_{\text{hyd}}, \qquad Z_C \equiv \frac{-i}{\omega C_{\text{hyd}}}, \text{ and } \qquad Z_L \equiv i\omega L_{\text{hyd}}. \qquad (3.56)$$

We end this chapter by an example provided by the group of Bruus at MIC. In Fig. 3.11 is shown a sketch of a so-called cascade electro-osmotic pump. In Section 8.6 we shall study how this pump work, but here we shall only consider the hydraulic resistance of the device. The microfluidic network of the pump is not simple. It is crucial for the functionality of the device that it consists of a series of identical stages. In Fig. 3.11(a) is shown three such stages. Each stage contains two main parts, the collection of ten parallel narrow channels, and the following wide single-channel. Each channel i is rectangular in shape, so using Table 3.1 we can calculate the basic hydraulic resistances $R_{\text{hyd}}^{(i)}$. Then we need to figure out the equivalent circuit diagram of the pump. This is a series coupling of the hydraulic resistance R_{stage} of each single stages in the pump. In Fig. 3.11(b) R_{stage} has been broken further down into a series coupling of three hydraulic resistors, one of which is a parallel coupling of ten identical narrow channels. Thus, by using equivalent circuit theory it is possible to obtain a good estimate of the total hydraulic resistance of the microfluidic network without performing complicated numerical simulations. This is extremely helpful when designing lab-on-a-chip systems, and if all the involved channels are long and narrow, then the result is very accurate.

3.8   Exercises

Exercise 3.1
The rate of dissipation of kinetic energy
Verify the calculation in Eqs. (3.6) and (3.7) for the dissipation of kinetic energy of an incompressible fluid flowing inside a channel with rigid walls.

Exercise 3.2
Viscous power consumption in hydraulic resistors
The power consumption P due to Joule heating in an electrical wire is given by $P = IU$. Likewise, the power consumption P due to viscous friction in a Poiseuille flow is given by $P = Q\Delta p$.
    (a) Use the Hagen–Poiseuille law for a circular channel and for a section of width w of an infinite parallel-plate channel to express P in terms of viscosity, length scales and pressure drop.
    (b) Discuss how the power consumption depends on the various parameters.

Exercise 3.3
Series and parallel coupling of two hydraulic resistors
Prove the expressions Eqs. (3.48) and (3.49) for the total hydraulic resistance of two hydraulic resistors coupled in series and in parallel, respectively.

Exercise 3.4
The hydraulic resistance of a square channel
An often used approximation for the flow rate Q in a rectangular channel induced by a pressure drop Δp is given in Eq. (2.49), while the exact result is the infinite series given in Eq. (2.48d). Dividing by Δp yields the inverse hydraulic resistance $1/R_{\text{hyd}}$.
    (a) Calculate the difference between the approximate and the exact $1/R_{\text{hyd}}$ for a square where $w = h$.
    (b) Show by paying special attention to the $n = 1$ term in the series Eq. (2.48d) that an improved approximation for $1/R_{\text{hyd}}$ is

$$\frac{1}{R_{\text{hyd}}} \approx \frac{h^3 w}{12\,\eta L}\left[1 - \left\{0.630 - \frac{192}{\pi^5}\left[1 - \tanh\left(\frac{\pi}{2}\,\frac{w}{h}\right)\right]\right\}\frac{h}{w}\right], \qquad (3.57)$$

and calculate for a square the deviation from the exact result.

Exercise 3.5
Reynolds number of a man and of a bacterium
A living species of linear size L moving in water can typically move its own distance per second, implying a characteristic velocity $U = L/(1\text{ s})$. Estimate the Reynolds number of a man and of a bacterium swimming in water. Comment the result.

Exercise 3.6
Reynolds number in a two-length-scale system
Consider the two-length-scale system of Section 3.4.2. Prove that Eqs. (3.45a)–(3.45c) are correct forms of the dimensionless Navier–Stokes equation.

Exercise 3.7
The pressure needed to run a lab-on-chip laser
Consider the fluidic lab-on-a-chip dye laser shown in Fig. 3.3. The liquid used in the laser is ethanol with a viscosity at room temperature of 1.197 mPa s. The dimensions of the rectangular channel are length $L = 122$ mm, width $w = 300$ μm, and height $h = 10$ μm. For proper functioning the flow rate in the channel must be $Q = 10$ μL/hour. Calculate the pressure needed to run this device properly.

Exercise 3.8
The hydraulic resistance of an actual micromixer
The micro-mixer below is designed to obtain a well-controlled mix of six different chemicals dissolved in water. Assume that all six inlet pressures are the same, $p_0 + \Delta p$, and that the outlet pressure is p_0.

(a) Construct the equivalent circuit diagram of the mixer.

(b) Calculate the total hydraulic resistance of the micro-mixer.
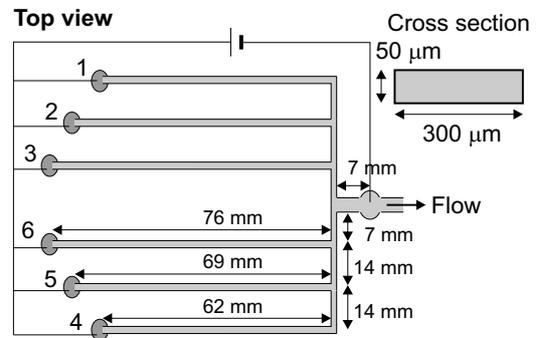
Exercise 3.9
The hydraulic resistance of a slightly deformed cylindrical channel
Consider a Poiseuille flow in a slightly deformed cylindrical channel, where the radius $a(x)$ depends weakly on x. The result Eq. (2.59) to lowest order in the deformation ϵ of another shape-deformed Poiseuille flow problem indicates that the velocity field can be approximated by the unperturbed field fitted into the deformed channel. Therefore, for the deformed cylindrical channel we assume the x-dependent velocity field

$$v_x(x, y, z) \approx \frac{\partial_x p}{4\eta} \left(a(x)^2 - y^2 - z^2 \right). \tag{3.58}$$

Use this to derive an approximate expression for the hydraulic resistance R_{hyd} for an deformed cylinder of length L with a weakly varying radius $a(x)$.

Exercise 3.10
A model of a microchannel with compliance
Consider the model Fig. 3.9(b) of a microchannel with compliance due to soft walls. Assume an oscillating inlet pressure $\Delta p(t) = \Delta p\ e^{i\omega t}$, and use the equivalent circuit diagram of Fig. 3.10(b) to analyze the flow rate $Q_1(t) = Q_1\ e^{i\omega t}$ in steady-state.

(a) Find the hydraulic impedance Z_{hyd} of the microchannel by use of Fig. 3.10(b).

(b) Assume $R_1 = R_2 = R$ and find Q_1 in terms of a frequency-dependent prefactor and the ratio $\Delta p / R$.

(c) Calculate Q_1 in the limits $\omega \to 0$ and $\omega \to \infty$ and discuss the result.

3.9   Solutions

Solution 3.1
The rate of dissipation of kinetic energy
Distinguish clearly between physical and mathematical arguments. Begin by a clear formulation of the physical assumptions and arguments that leads to the starting point of the analysis. Remember that a repeated index in the index notation implies a summation over that index: $\partial_j v_j \equiv \sum_{j=1}^{3} \partial_j v_j = \partial_x v_x + \partial_y v_y + \partial_z v_z$.

Solution 3.2
Viscous power consumption in hydraulic resistors
The power consumption in a circular and an infinite parallel-plate channel are denoted $P_\bigcirc$ and $P_\parallel$, respectively.

(a) $P = Q\Delta p = R_{\mathrm{hyd}}(\Delta p)^2$, so $P_\bigcirc = 8\eta L(\Delta p)^2/(\pi a^4)$ and $P_\parallel = 12\eta L(\Delta p)^2/(wh^3)$.

(b) In both cases $P \propto \eta L(\Delta p)^2$. The geometries influence P slightly differently: $P_\bigcirc \propto a^{-4}$ while $P_\parallel \propto w^{-1}h^{-3}$, but in both cases the power increases significantly upon down-scaling of the smallest transverse length, channel radius a or channel height h.

Solution 3.3
Series and parallel coupling of two hydraulic resistors
For a series coupling the flow rates in each resistor are identical, $Q_1 = Q_2 = Q$, while the partial pressure drops add up to the total pressure drop, $\Delta p = \Delta p_1 + \Delta p_2$. Using Hagen–Poiseuille's law on the latter relation yields

$$R_{\mathrm{hyd}}Q = R_1 Q_1 + R_2 Q_2 = (R_1 + R_2)Q, \tag{3.59}$$

from which the desired result follows after division by Q.

For a parallel coupling the pressure drop over each resistor are identical, $\Delta p_1 = \Delta p_2 = \Delta p$, while the flow rates add up to the total flow rate, $Q = Q_1 + Q_2$. Using Hagen–Poiseuille's law on the latter relation yields

$$\frac{\Delta p}{R} = \frac{\Delta p_1}{R_1} + \frac{\Delta p_2}{R_2} = \left(\frac{1}{R_1} + \frac{1}{R_2}\right)\Delta p, \tag{3.60}$$

from which the desired result follows after division by Δp.

Solution 3.4
The hydraulic resistance of a square channel
The exact result for the flow rate in a square channel, where $h = w$, is obtained numerically from Eq. (2.48d) by summing a large but finite number of terms in the rapidly converging sum,

$$Q_{\mathrm{exact}} = Q_0 \left[1 - \sum_{n,\mathrm{odd}}^{\infty} \frac{1}{n^5}\frac{192}{\pi^5}\tanh\left(\tfrac{1}{2}n\pi\right)\right] = 0.4217\, Q_0. \tag{3.61}$$

(a) For a square channel, where $h = w$, the approximation Eq. (2.49) for the flow rate can be written as

$$Q_{\mathrm{approx},1} \approx Q_0\left[1 - 0.630\right] = 0.370\, Q_0. \tag{3.62}$$

The relative error is

$$\frac{Q_{\text{approx},1} - Q_{\text{exact}}}{Q_{\text{exact}}} = -0.1227. \tag{3.63}$$

(b) An improved approximation for Q in the square channel is obtained as follows. We note that $\tanh(\pi/2) = 0.9172$, while $\tanh(3\pi/2) = 0.9998$. It is thus a fair approximation to state that $\tanh(n\pi/2) = 1$ for $n \geq 3$, and we arrive at

$$\frac{Q_{\text{approx},2}}{Q_0} = 1 - \sum_{n,\text{odd}}^{\infty} \frac{1}{n^5} \frac{192}{\pi^5} \tanh\left(\frac{1}{2}n\pi\right) \tag{3.64}$$

$$\approx 1 - \frac{192}{\pi^5} \tanh\left(\frac{1}{2}\pi\right) - \frac{192}{\pi^5} \sum_{n=3,5,7}^{\infty} \frac{1}{n^5} \tag{3.65}$$

$$= 1 - \frac{192}{\pi^5} \sum_{n=1,3,5}^{\infty} \frac{1}{n^5} + \frac{192}{\pi^5} - \frac{192}{\pi^5} \tanh\left(\frac{1}{2}\pi\right) \tag{3.66}$$

$$= 1 - \left\{ 0.630 - \frac{192}{\pi^5}\left[1 - \tanh\left(\frac{1}{2}\pi\right)\right] \right\}. \tag{3.67}$$

Calculating the numerical value leads to

$$Q_{\text{approx},2} = 0.4220\, Q_0. \tag{3.68}$$

The relative error of this approximation is

$$\frac{Q_{\text{approx},2} - Q_{\text{exact}}}{Q_{\text{exact}}} = 0.0006. \tag{3.69}$$

Solution 3.5
Reynolds number of a man and of a bacterium
Since $U = L/(1\,\text{s})$ we find $Re = \rho U L/\eta = L^2 \times 10^6 \text{m}^{-2}$. Now $L_{\text{man}} \approx 1\,\text{m}$ and $L_{\text{bact}} \approx 1\,\mu\text{m}$ imply $Re_{\text{man}} = 10^6$ and $Re_{\text{man}} = 10^{-4}$. The motion in water of a man and of a bacterium is clearly dominated by inertia and viscous damping, respectively.

Solution 3.6
Reynolds number in a two-length-scale system
Once the dimensionless derivatives in Eq. (3.39) have been introduced, the result Eqs. (3.45a)–(3.45c) follow by direct substitution into the Navier–Stokes and continuity equations.

Solution 3.7
The pressure needed to run a lab-on-chip laser
The required flow rate is $Q = 10\ \mu\text{L/hour} = 10 \times 10^{-9}\ \text{m}^3/(3600\,\text{s}) = 2.77 \times 10^{-12}\ \text{m}^3/\text{s}$ while the hydraulic resistance is $R_{\text{hyd}} = 12\eta L/[wh^3(1-h/w)] = 5.97 \times 10^{15}\ \text{Pa s/m}^3$. This results in an operating pressure of $\Delta p = R_{\text{hyd}}Q = 16.6\ \text{kPa}$.

Solution 3.8
The hydraulic resistance of an actual micromixer
The equivalent diagram of the micro-mixer is shown to the right, where each piece of channel is represented by a resistor. The top six resistors 1-3 and a-c in the first part of the diagram forms an effective resistor R^* identical to the bottom six resistors. The circuit is thus equivalent to a parallel coupling of two R^*-resistors in series with the outlet resistor R_0, thus $R_{\mathrm{hyd}} = \frac{1}{2}R^* + R_0$. Resistor R^* consists of R_1 and R_a in series, the resultant of which is coupled in parallel with R_2, the resultant of which is coupled in series with R_b, the resultant of which is coupled in parallel with R_3, the resultant of which is coupled in series with R_c.
We thus get

$$R_{\mathrm{hyd}} = \frac{1}{2}\left[\left(\left\{\left[(R_1 + R_a)^{-1} + R_2^{-1}\right]^{-1} + R_b\right\}^{-1} + R_3^{-1}\right)^{-1} + R_c\right] + R_0. \qquad (3.70)$$

The resistance of each channel segment i is $R_i = \alpha L_i = 12\eta L_i/[wh^3(1 - h/w)] = L_i \times 3.84 \times 10^{14}$ Pa s/m^4. The constant α can be taken outside all the parentheses in Eq. (3.70) leaving just the lengths, where $L_0 = 14$ mm, $L_1 = 62$ mm, $L_2 = 69$ mm, $L_3 = 76$ mm, $L_a = 14$ mm, $L_b = 14$ mm, and $L_c = 76$ mm. The final result is $R_{\mathrm{hyd}} = 1.25 \times 10^{13}$ Pa s/m^3.
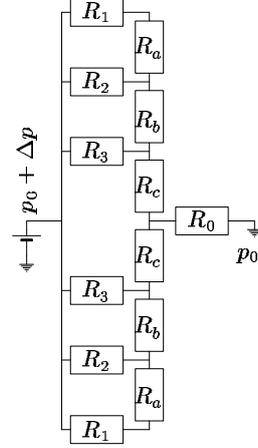
Solution 3.9
The hydraulic resistance of a slightly deformed cylindrical channel
As a and $\partial_x p$ now depend of x we write Eq. (2.30b) as $Q = (\pi/8\eta)a^4(x)\,\partial_x p(x)$. Hence

$$\Delta p = \int_0^L \mathrm{d}x\,\partial_x p = \left[\frac{8\eta}{\pi}\int_0^L \mathrm{d}x\,\frac{1}{a^4(x)}\right]Q, \quad \text{or} \quad R_{\mathrm{hyd}} = \frac{8\eta}{\pi}\int_0^L \mathrm{d}x\,\frac{1}{a^4(x)}. \qquad (3.71)$$

Solution 3.10
A model of a microchannel with compliance
R_1 is in series with the parallel coupling of R_2 and C_{hyd} having the RC-time $\tau = R_2 C_{\mathrm{hyd}}$.

(a) $Z_{\mathrm{hyd}} = R_1 + \left(R_2^{-1} + i\omega C_{\mathrm{hyd}}\right)^{-1} = R_1 + R_2\left(1 + i\omega\tau\right)^{-1}$.

(b) $Q_1 = \dfrac{\Delta p}{Z_{\mathrm{hyd}}} = \dfrac{1}{1 + (1 + i\omega\tau)^{-1}}\dfrac{\Delta p}{R} = \dfrac{[2 + (\omega\tau)^2] + i\omega\tau}{4 + (\omega\tau)^2}\dfrac{\Delta p}{R}$

(c) For $\omega \to 0$ we obtain $Q_1 = \frac{\Delta p}{2R}$, i.e., the channel wall is always fully expanded thus leading all flow through both resistors. For $\omega \to \infty$ we obtain $Q_1 = \frac{\Delta p}{R}$, i.e., no liquid flows through R_2 as it after passing R_1 stays inside the ever expanding/relaxing channel.

Chapter 4

Time-dependent phenomena

So far we have only made in-depth analysis of systems in steady-state. The theme in this chapter is time-dependent phenomena. Three selected topics will be treated: diffusion and convection of uncharged particles dissolved in liquid solutions, the transient decay of a Poiseuille flow in a cylindrical microfluidic channel when a constant driving pressure is applied abruptly, and the accelerated motion of a spherical body in a fluid. Not surprisingly, the mathematical treatment becomes more complex than in the previous chapters.

4.1 A random walk model of diffusion

Consider a solution consisting of some particles, the solute, dissolved in a liquid, the solvent. Diffusion is the motion of the solute in the solvent from regions of high to low concentrations of the solute, and it is the result of thermally induced random motion of the particles, such as Brownian motion. Pure diffusion of the solute occurs when the velocity field of the solvent is zero, while in case of non-zero velocity fields the motion of the solute is partly convective, since the dissolved particles are carried along by the solvent.

Our discussion of diffusion begins by studying the simple constant-step random walker model of diffusion. Later we formulate and solve the diffusion equation for continuous concentration fields of the solute.

As a 1D toy-model of diffusion we consider a particle that executes a constant-step random walk along the x axis. Such a random walk consists of a number of consecutive, uncorrelated steps. It takes the same time τ for each step to be performed, and during each step the particle moves the distance $\Delta x_i = \pm \ell$, where ℓ is a constant step length, and where there is equal probability for choosing either sign. That the steps are statistically uncorrelated is expressed mathematically through the mean value $\langle \Delta x_i \Delta x_j \rangle$ as

$$\langle \Delta x_i \Delta x_j \rangle = \ell^2 \, \delta_{ij}. \tag{4.1}$$

At time $t = 0$ the particle is at $x = x_0 = 0$. At time $t = N\tau$ the particle has performed N

steps, and it is at the position x_N given by

$$x_N = \sum_{i=1}^{N} \Delta x_i, \qquad \Delta x_i = \pm \ell. \tag{4.2}$$

Consider M such constant-step random walks ending at $x_N^{(j)}$, $j = 1, 2, \ldots, M$. Each of these random walks consists of N random steps $\Delta x_i^{(j)} = \pm \ell$. The mean value $\langle x_N \rangle$ of the final positions is

$$\langle x_N \rangle \equiv \frac{1}{M} \sum_{j=1}^{M} x_N^{(j)} = \frac{1}{M} \sum_{j=1}^{M} \left(\sum_{i=1}^{N} \Delta x_i^{(j)} \right) = \sum_{i=1}^{N} \left(\frac{1}{M} \sum_{j=1}^{M} \Delta x_i^{(j)} \right) = \sum_{i=1}^{N} \langle \Delta x_i \rangle = 0. \tag{4.3}$$

The last equality follows from the assumption of equal probability for stepping either $+\ell$ or $-\ell$. As expected the mean value is zero, and clearly this quantity does not reveal the kinematics of diffusion. We therefore continue by calculating $\langle x_N^2 \rangle$ related to the statistical spread in the final position of the particles,

$$\langle x_N^2 \rangle \equiv \frac{1}{M} \sum_{j=1}^{M} \left[x_N^{(j)} \right]^2 = \frac{1}{M} \sum_{j=1}^{M} \left(\sum_{i=1}^{N} \Delta x_i^{(j)} \right) \left(\sum_{k=1}^{N} \Delta x_k^{(j)} \right) = \frac{1}{M} \sum_{j=1}^{M} \sum_{i=1}^{N} \sum_{k=1}^{N} \Delta x_i^{(j)} \Delta x_k^{(j)}. \tag{4.4}$$

Now follows a standard trick often used in statistics. In the ik double sum we collect the terms where $k = i$, the so-called diagonal terms, and those where $k \neq i$, the so-called off-diagonal terms. This enables a straightforward evaluation of the average over the ensemble of random walks j,

$$\langle x_N^2 \rangle = \frac{1}{M} \sum_{j=1}^{M} \left(\sum_{i=1}^{N} \left[\Delta x_i^{(j)} \right]^2 + \sum_{i=1}^{N} \sum_{k \neq i}^{N} \Delta x_i^{(j)} \Delta x_k^{(j)} \right) = N\ell^2 + \sum_{i=1}^{N} \sum_{k \neq i}^{N} \langle \Delta x_i \Delta x_k \rangle. \tag{4.5}$$

In the last equality we have used that $\left[\Delta x_i^{(j)} \right]^2 = (\pm \ell)^2 = \ell^2$ regardless of the sign of the random step. We now use that $k \neq i$ in the last term implies that Δx_i and Δx_k are statistically independent so the probability of having the summand equal to $(+\ell)(-\ell) = (-\ell)(+\ell) = -\ell^2$ is the same of that of having $(+\ell)(+\ell) = (-\ell)(-\ell) = +\ell^2$. Thus the last term vanish upon averaging over random walkers, and we get

$$\langle x_N^2 \rangle = N\ell^2. \tag{4.6}$$

From Eqs. (4.3) and (4.6) we find the root-mean-square displacement by diffusion, the so-called diffusion length $\ell_{\text{diff},N}^{1D}$, of the random walker taking N steps in 1D to be

$$\ell_{\text{diff},N}^{1D} \equiv \sqrt{\langle x_N^2 \rangle - \langle x_N \rangle^2} = \sqrt{N}\, \ell. \tag{4.7}$$

Reintroducing time as $t = N\tau$, where τ is the time it takes to perform one step, leads to

$$\ell_{\text{diff}}^{1D}(t) = \sqrt{\frac{t}{\tau}}\, \ell = \sqrt{\frac{\ell^2}{\tau}}\, t = \sqrt{Dt}, \tag{4.8}$$
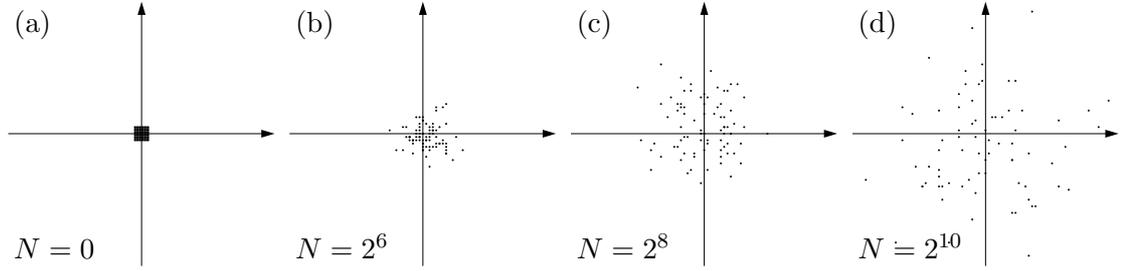
Figure 4.1: Constant-step random walk with step-length ℓ in 2D illustrating molecular diffusion. The diffusion length after N steps is expected to be $\ell_{\text{diff}}^{2D} = \sqrt{2N}\,\ell$. (a) Initial configuration of 81 particles near the origin of the coordinate system. (b) The position of the particles after 2^6 random-walk steps. The observed and expected diffusion lengths are $0.57\,\ell$ and $0.57\,\ell$, respectively. (c) After 2^8 random-walk steps; the observed and expected diffusion lengths are $1.18\,\ell$ and $1.13\,\ell$, respectively. (d) After 2^{10} random-walk steps; the observed and expected diffusion lengths are $2.30\,\ell$ and $2.26\,\ell$, respectively.

where the so-called diffusion constant D has been introduced,

$$D \equiv \frac{\ell^2}{\tau}. \tag{4.9}$$

It is a typical and remarkable feature of diffusion kinematics that the diffusion length depends on the square-root of time as seen in Eq. (4.8). Ultimately, this dependence makes diffusion an extremely slow process of mixing over macroscopical distances. Even in microfluidic systems diffusion may still be a very slow process, see Eq. (4.26).

The random walk model of diffusion is easily extended to the 2D xy plane. Starting at the origin, the particle position $\mathbf{R}_N$ after N steps $\Delta \mathbf{r}_i$ is given by

$$\mathbf{R}_N = \sum_{i=1}^{N} \Delta \mathbf{r}_i, \qquad \Delta \mathbf{r}_i = (\pm \ell)\,\mathbf{e}_x + (\pm \ell)\,\mathbf{e}_y, \tag{4.10}$$

where there is an equal probability for any combination of the signs. If we decompose the motion in x and y components, which are statistically independent, we find

$$\langle R_N^2 \rangle = \langle x_N^2 + y_N^2 \rangle = \langle x_N^2 \rangle + \langle y_N^2 \rangle = 2N\ell^2. \tag{4.11}$$

Thus in 2D the diffusion length becomes

$$\ell_{\text{diff}}^{2D}(t) = \sqrt{2N}\,\ell = \sqrt{2Dt}. \tag{4.12}$$

A numerical example of such a random walk in 2D is shown in Fig. 4.1

4.2 The convection-diffusion equation for solutions

In Chapter 1 we studied the continuity equation and the Navier–Stokes equation for a homogeneous liquid with density $\rho(\mathbf{r})$ and momentum density $\rho(\mathbf{r})\,\mathbf{v}(\mathbf{r})$. This concept is

now extended to the case of a solution where several fluids α are mixed each with density ρ_α; the actual mass per volume in the solution. The total density of the fluid is called ρ,

$$\rho(\mathbf{r}) \equiv \sum_\alpha \rho_\alpha(\mathbf{r}), \tag{4.13}$$

and likewise the fluid velocity $\mathbf{v}$ is defined in terms of the total momentum density of the solution — including that due to diffusion. The arguments leading to the continuity equation (1.30) for the homogeneous fluid thus still holds for the heterogeneous solution,

$$\partial_t \rho + \boldsymbol{\nabla} \cdot (\rho \mathbf{v}) = 0. \tag{4.14}$$

The concentration $c_\alpha(\mathbf{r}, t)$ of the solute is defined as the density fraction

$$c_\alpha(\mathbf{r}, t) \equiv \frac{\rho_\alpha(\mathbf{r}, t)}{\rho(\mathbf{r}, t)}, \tag{4.15}$$

while the mass current density $\mathbf{J}_\alpha$ for solute α must be written in terms of a convection current density $\mathbf{J}_\alpha^{\mathrm{conv}}$, due to the global velocity field $\mathbf{v}$ of the solution, and a diffusion current density $\mathbf{J}_\alpha^{\mathrm{diff}}$, due to the random motion of the solute relative to the solution as discussed in the previous section,

$$\mathbf{J}_\alpha \equiv \mathbf{J}_\alpha^{\mathrm{conv}} + \mathbf{J}_\alpha^{\mathrm{diff}} = \rho_\alpha \mathbf{v} + \mathbf{J}_\alpha^{\mathrm{diff}} = c_\alpha \rho \mathbf{v} + \mathbf{J}_\alpha^{\mathrm{diff}}. \tag{4.16}$$

The continuity equation for the solute density $c_\alpha \rho$ can now be formulated in analogy with Eqs. (1.27) and (1.28), but now with the extra current density $\mathbf{J}_\alpha^{\mathrm{diff}}$ added to the flux through the surface,

$$\int_\Omega d\mathbf{r}\, \partial_t(c_\alpha \rho) = -\int_{\partial\Omega} da\, \mathbf{n} \cdot \Big(c_\alpha \rho \mathbf{v}(\mathbf{r}, t) + \mathbf{J}_\alpha^{\mathrm{diff}} \Big) = -\int_\Omega d\mathbf{r}\, \boldsymbol{\nabla} \cdot \Big(c_\alpha \rho \mathbf{v}(\mathbf{r}, t) + \mathbf{J}_\alpha^{\mathrm{diff}} \Big). \tag{4.17}$$

This equation can only be true for arbitrary Ω if the integrands are identical,

$$\partial_t(c_\alpha \rho) = -\boldsymbol{\nabla} \cdot \Big(c_\alpha \rho \mathbf{v}(\mathbf{r}, t) + \mathbf{J}_\alpha^{\mathrm{diff}} \Big), \tag{4.18}$$

which by use of Eq. (4.14) can be reduced to

$$\rho \Big[\partial_t c_\alpha + \mathbf{v} \cdot \boldsymbol{\nabla} c_\alpha \Big] = -\boldsymbol{\nabla} \cdot \mathbf{J}_\alpha^{\mathrm{diff}}. \tag{4.19}$$

The diffusion current density is non-zero only when gradients in the density of the solute are present. For weak solutions we expect only the lowest order gradients to play a role, which is expressed by Fick's law,

$$\mathbf{J}_\alpha^{\mathrm{diff}} = -D_\alpha\, \rho\, \boldsymbol{\nabla} c_\alpha. \tag{4.20}$$

Inserting Fick's law into Eq. (4.19) leads to the convection-diffusion equation for the concentration c_α of solutes in weak solutions having a velocity field $\mathbf{v}$,

$$\partial_t c_\alpha + \mathbf{v} \cdot \boldsymbol{\nabla} c_\alpha = D_\alpha\, \nabla^2 c_\alpha. \tag{4.21}$$

The constant D_α is in analogy with Eq. (4.9) known as the diffusion constant for solute α in the solvent,

$$D_\alpha, \text{the diffusion constant of solute } \alpha \text{ in the solvent; SI unit is m}^2/\text{s.} \tag{4.22}$$

4.3 The diffusion equation

In the following we consider the diffusion of a single solute and therefore suppress the index α. If the velocity field $\mathbf{v}$ of the solvent is zero, convection is absent and Eq. (4.21) becomes the diffusion equation,

$$\partial_t c = D \, \nabla^2 c. \tag{4.23}$$

Simple dimensional analysis of this equation can already reveal some important physics. It is clear that if T_0 and L_0 denotes the characteristic time- and length-scale over which the concentration $c(\mathbf{r}, t)$ varies, then

$$L_0 = \sqrt{DT_0} \qquad \text{or} \qquad T_0 = \frac{L_0^2}{D}, \tag{4.24}$$

which resembles Eq. (4.8). The diffusion constant D thus determines how fast a concentration diffuses a certain distance. Typical values of D are

$$D \approx 2 \times 10^{-9} \ \text{m}^2/\text{s}, \quad \text{small ions in water}, \tag{4.25a}$$

$$D \approx 4 \times 10^{-11} \ \text{m}^2/\text{s}, \quad \text{30-base-pair DNA molecules in water}, \tag{4.25b}$$

$$D \approx 1 \times 10^{-12} \ \text{m}^2/\text{s}, \quad \text{5000-base-pair DNA molecules in water}, \tag{4.25c}$$

which yield the following times T_0 for diffusion across the typical microfluidic distance $L_0 = 100 \ \mu\text{m}$,

$$T_0(100 \ \mu\text{m}) \approx 5 \ \text{s}, \qquad\qquad\quad \text{small ions in water}, \tag{4.26a}$$

$$T_0(100 \ \mu\text{m}) \approx 250 \ \text{s} \approx 4 \ \text{min}, \quad \text{30-base-pair DNA molecules in water}, \tag{4.26b}$$

$$T_0(100 \ \mu\text{m}) \approx 10^4 \ \text{s} \approx 3 \ \text{h}, \qquad \text{5000-base-pair DNA molecules in water}. \tag{4.26c}$$

Let us now turn to some analytical solutions of the diffusion equation.

4.3.1 Limited point-source diffusion

Consider a small drop containing N_0 ink molecules injected at position $\mathbf{r} = 0$ at time $t = 0$ in the middle of a huge tank of water. The initial point-like concentration acts as the source of the diffusion, and it can be written as a Dirac delta function[1]

$$c(\mathbf{r}, t = 0) = N_0 \, \delta(\mathbf{r}). \tag{4.27}$$

The ink immediately begins to diffuse out into the water, and it is easy to show by inspection that the solution to the diffusion equation (4.23) given the initial condition Eq. (4.27) is

$$c(\mathbf{r}, t > 0) = \frac{N_0}{(4\pi Dt)^{\frac{3}{2}}} \exp\left(-\frac{r^2}{4Dt}\right). \tag{4.28}$$

This is an example of a limited diffusion process because the amount of solute is fixed and hence limited. The result Eq. (4.28) is discussed in Fig. 4.2.

---

[1]The Dirac delta function $\delta(\mathbf{r})$ is defined by: $\delta(\mathbf{r}) = 0$ for $\mathbf{r} \neq 0$ and $\int_{-\infty}^{\infty} \int_{-\infty}^{\infty} \int_{-\infty}^{\infty} d\mathbf{r} \, \delta(\mathbf{r}) = 1$.
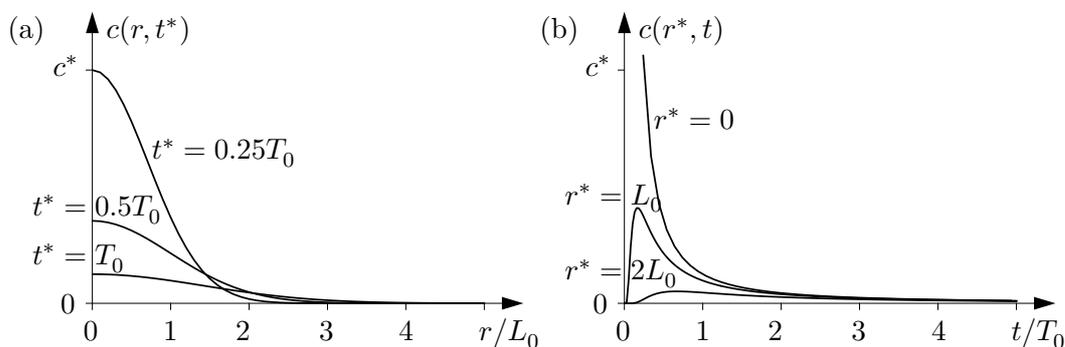
Figure 4.2: The concentration $c(\mathbf{r}, t > 0)$ from Eq. (4.28) in the case of limited point-source diffusion. The length scale in the radial direction r has been chosen to be L_0, which fixes the time scale to be $T_0 = L_0^2/D$. (a) The r dependence of $c(r, t^*)$ for three given times $t^* = 0.25T_0$, $0.5T_0$, and T_0. (b) The time dependence of $c(r^*, t)$ for three given radial positions $r^* = 0$, L_0, and $2L_0$.

4.3.2   Limited planar-source diffusion

Another limited diffusion process is limited planar-source diffusion. Let the semi-infinite half-space $x > 0$ be filled with some liquid. Consider then an infinitely thin slab covering the yz plane at $x = 0$ containing n_0 molecules per area that at time $t = 0$ begin to diffuse out into the liquid. With a factor 2 inserted to normalize the half-space integration, the initial condition is

$$c(\mathbf{r}, t = 0) = n_0 \, 2\delta(x), \tag{4.29}$$

which results in the solution

$$c(\mathbf{r}, t > 0) = \frac{n_0}{(\pi D t)^{\frac{1}{2}}} \, \exp\left(-\frac{x^2}{4Dt} \right). \tag{4.30}$$

4.3.3   Constant planar-source diffusion

We end by an example of diffusion with a constant source, i.e., a constant influx of solute is maintained at one of the boundary surfaces. Consider the same geometry as in the previous example, but change the boundary condition as follows. At time $t = 0$ a source filling the half-space $x < 0$ suddenly begins to provide an influx of molecules to the boundary plane $x = 0$ such that the density there remains constant at all later times,

$$c(x = 0, y, z, t > 0) = c_0. \tag{4.31}$$

By inspection it is straightforward to show that the solution can be written in terms of the complementary error function $\mathrm{erfc}(s)$,[2]

$$c(\mathbf{r}, t > 0) = c_0 \, \mathrm{erfc}\left(\frac{x}{\sqrt{4Dt}} \right). \tag{4.32}$$

---

[2]The complementary error function is defined as $\mathrm{erfc}(s) \equiv \dfrac{2}{\sqrt{\pi}} \displaystyle\int_s^\infty e^{-u^2} \, \mathrm{d}u.$
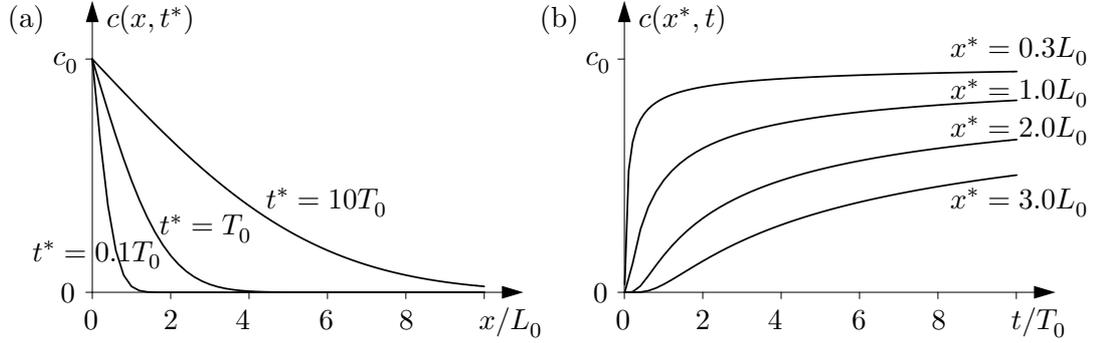
Figure 4.3: The concentration $c(\mathbf{r}, t > 0)$ from Eq. (4.32) in the case of constant planar-source diffusion. The length scale in the x direction has been chosen to be L_0, which fixes the time scale to be $T_0 = L_0^2/D$. (a) The x dependence of $c(x, t^*)$ for three given times $t^* = 0.1T_0$, T_0, and $10T_0$. (b) The time dependence of $c(x^*, t)$ for four given positions $x^* = 0.3L_0$, L_0, $2L_0$, and $10L_0$.

4.3.4 Diffusion of momentum and the Navier–Stokes equation

It is not only mass that can diffuse as described above. Another important example is heat, but also for momentum there exists a diffusion equation. In fact, we have already through the Navier–Stokes equation worked with diffusion of mechanical momentum without noticing it. That the Navier–Stokes equation contains momentum diffusion becomes most clear if we consider the case of the decelerating Poiseuille flow discussed in Fig. 3.1 in Section 3.1, where the Navier–Stokes equation becomes very simple,

$$\rho \partial_t v_x = \eta \, \nabla^2 v_x. \tag{4.33}$$

In terms of the momentum density ρv_x we indeed obtain a diffusion equation like Eq. (4.23),

$$\partial_t(\rho v_x) = \nu \, \nabla^2(\rho v_x), \tag{4.34}$$

where the kinematic viscosity ν appears as the diffusion constant for momentum,

$$\nu \equiv \frac{\eta}{\rho} \quad (\approx 10^{-6} \text{ m}^2/\text{s for water}). \tag{4.35}$$

In analogy with Eq. (4.24) there exists a momentum diffusion time T_0 for diffusion a characteristic length a, e.g., the radius of the microchannel,

$$T_0 = \frac{a^2}{\nu} \quad (\approx 10 \text{ ms for water in a microchannel of radius 100 } \mu\text{m}). \tag{4.36}$$

The dimensionless ratio of the diffusivity ν of momentum relative to the diffusivity D of mass is denoted the Schmidt number Sc,

$$Sc = \text{Schmidt number} \equiv \frac{\nu}{D} = \frac{\eta}{\rho D}. \tag{4.37}$$

Note that the Schmidt number is an intrinsic property of the solution. This is in contrast to the Reynolds number which due to its dependence on the velocity is a property of the flow.
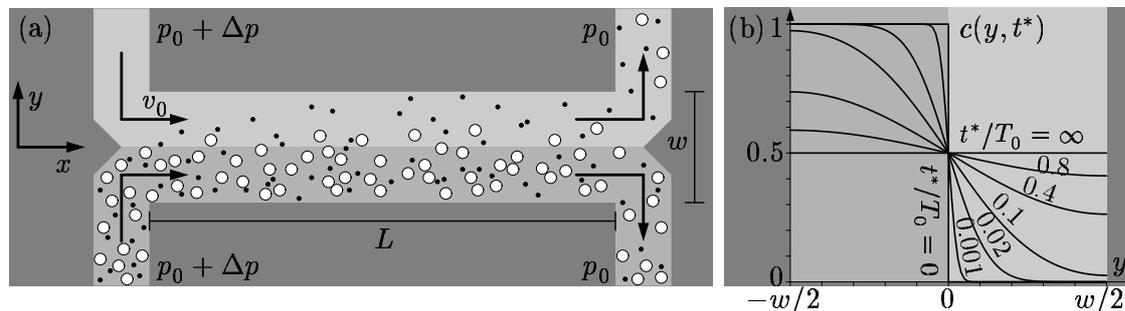
Figure 4.4: (a) A top-view in the xy plane of a flat (height h) H-filter consisting of a central channel (length L and width w) with two inlet channels to the left and two outlet channels to the right. A pure buffer liquid (light gray) and a buffer liquid (gray) containing big (white) and small (black) solutes are introduced one inlet each, and perform a pressure driven, steady-state, laminar flow with average velocity v_0. (b) Concentration profiles $c(y, t^*)$ in the central channel as a function of the transverse direction y at different positions $x^* = v_0 t^*$ along the channel.

4.4 The H-filter: separating solutes by diffusion

Diffusion is an old, well-known and much used method to separate solutes with different diffusion constants. The method has also be employed in microfluidics, where the advantages of laminar flow and fast diffusion over small distances can be combined and utilized. Here we shall briefly study one such example, the so-called H-filter, which was among some of the first commercial microfluidic products.

The name of the H-filter is derived from its geometrical appearance, see the the xy-plane top-view in Fig. 4.4(a). The legs of the H are the two inlet channels to the left, kept at pressure $p_0 + \Delta p$, and the two outlet channels to the right, kept at pressure p_0. The cross-bar of the H is the central channel where diffusion takes place. A pure buffer liquid (light gray) is introduced at one inlet, while another buffer liquid (gray) containing big (white) and small (black) solutes are introduced in another inlet. All channels are flat having the same width w and height $h \ll w$, the central channel has the length L, and the two buffer liquids are both taken to be water. Working with length scales in the micrometer range, say $h = 10$ μm, $w = 100$ μm and $L = 1$ mm, and a flow velocities below 1 mm/s, the flow is laminar, and the two buffer liquids do not mix, as indicated by the gray and light gray shading in Fig. 4.4(a). As seen in Fig. 2.8 the average velocity profile in a flat channel is constant across the width w except within a distance of $h/2$ from either side-wall. We denote this velocity v_0.

Regarding the behavior in the H-filter of a given solute with diffusion constant D in the buffer, two time scales become relevant, namely the time τ_{conv} it takes to be convected down-stream from the inlet to the outlet, and the time τ_{diff} it takes to diffuse across the half-width of the channel. They are given by

$$\tau_{\text{conv}} = \frac{L}{v_0}, \tag{4.38a}$$

$$\tau_{\text{diff}} = \frac{\left(\frac{1}{2}w\right)^2}{D} = \frac{w^2}{4D}. \tag{4.38b}$$

For a solute with $\tau_{\text{conv}} \ll \tau_{\text{diff}}$ diffusion does not have time enough to act, and it will (largely) remain in its original buffer stream leaving the other buffer stream (relatively) pure, see the white particles in Fig. 4.4(a). For the case $\tau_{\text{conv}} \gtrsim \tau_{\text{diff}}$ the solute has time enough to diffuse across the central channel and the concentration of the solute will be the same in the two buffer streams, see the black particles in Fig. 4.4(a). Consequently, operating the H-filter with two solutes in one buffer stream and making sure that they fulfil $\tau_{\text{conv},1} \ll \tau_{\text{diff},1}$ and $\tau_{\text{conv},2} \gtrsim \tau_{\text{diff},2}$, it is possible to separate out solute 2 from solute 1, although arriving only at half the initial concentration. For a given choice of L, w and v_0 the critical value D^* of the diffusion constant, where complete mixing by diffusion happens, can be found by requiring $\tau_{\text{diff}}(D^*) = \tau_{\text{conv}}$. This gives

$$D^* = \frac{v_0 w^2}{4L}. \tag{4.39}$$

For $L = 1$ mm, $w = 100$ μm and $v_0 = 1$ mm/s we find $D^* = 2.5 \times 10^{-9}$ m^2/s, which according to Eq. (4.25) is close to the diffusion constant of small ions in water. Thus it is possible to sperate these from larger molecules using the H-filter.

It is important to realize that the inherent randomness of diffusion processes makes the separation obtained by the H-filter statistical in nature. One cannot expect to achieve 100% separation, since in the separated outlet stream a fraction α, the impurity fraction, of the solute concentration will be the unwanted slowly diffusing solute. However, by making a multistage setup with several H-filters in series, one can in principle come arbitrarily close to 100% separation of the fast diffusing solute from the slow one, at the prize of halving the concentration at each stage.

Quantitative estimates of the impurity fraction α can be obtained by solving the diffusion equation 4.23. Here we utilize the laminarity of microfluidics, which ensures that time is converted into position: the position x down-stream in the central channel is given by the time t as $x = v_0 t$. In a slice across the channel of thickness Δx near $x = 0$ there are $N_0 = c_0 w h \Delta x$ solute molecules, where c_0 is the concentration in the inlet buffer. Since on average these molecules are convected down-stream by the speed v_0 there will be the same number of molecules in each slice of thickness Δx, and the consecutive slices x correspond to consecutive time instants t. Hence we study the evolution of the concentration profile $c(y,t)$, which is an example of limited source diffusion, where the initial condition is the half-box profile $c(y,0) = c_0$, for $-w/2 < y < 0$, and $c(y,0) = 0$, for $0 < y < w/2$, which emerges right at the point $x = 0$, where the two buffer streams meet. The boundary condition is zero current at the side-walls, which according to Fick's law Eq. (4.20) becomes $\partial_y c(\pm w/2, t) = 0$. The solution to this limited source diffusion problem is shown in Fig. 4.4(b). Note that due to symmetry around the center line $y = 0$ the concentration

remains $c(0,t) = \frac{1}{2}c_0$, and the solution for small times, where the side-walls has not yet been reached by the diffusing molecules, the solution is identical to the constant planar source diffusion shown in Fig. 4.3.

4.5   Taylor dispersion; a convection-diffusion example

In the following section we will study an example of combined convection and diffusion, which occurs if a concentration $c(\mathbf{r},t)$ of some solute is placed in a solution flowing with the non-zero velocity field $\mathbf{v}(\mathbf{r},t)$. The most simple case, which nevertheless turns out to be complicated, is obtained for the steady-state Poiseuille flow in a cylindrical microchannel, where $\mathbf{v} = v_x(r)\,\mathbf{e}_x$. The corresponding convection-diffusion equation (4.21) becomes

$$\partial_t c + v_x \partial_x c = D\left(\partial_r^2 c + \frac{1}{r}\,\partial_r c + \partial_x^2 c\right), \tag{4.40}$$

where

$$v_x(r) = 2\left(1 - \frac{r^2}{a^2}\right)V_0, \tag{4.41}$$

so that $V_0 \equiv \frac{1}{\pi a^2}\int_0^a \mathrm{d}r\, 2\pi r\, v_x(r)$ is the average velocity of the Poiseuille flow.

In the Taylor dispersion problem, sketched in Fig. 4.5 we consider a homogeneous band of solute placed in the microchannel at $t = 0$ and study how this concentration profile disperses due to convection from the Poiseuille flow and the diffusion due to the concentration gradients.

If diffusion did not play any role the band of solute would become stretched into an increasingly longer paraboloid shaped band due to the Poiseuille flow. However, diffusion is present and it counteracts the stretching: in the front end of the concentration profile diffusion brings solute particles from the high concentration near the center out towards the low concentration sides, whereas in the back end it brings solute particles from the high concentration sides towards the low concentration near the center. As we shall see the result is quite evenly shaped plug moving down stream with a speed equal to the average Poiseuille flow velocity V_0.

4.5.1   Dimensional analysis and the Péclet number

To get a first insight into the problem we make a dimensional analysis of the convection-diffusion equation (4.40). The characteristic lengths over which the concentration changes in the radial and axial direction are denoted a and L_0, respectively. In microfluidics the radial length scale a is the radius or width of the channel, and it is often much smaller than L_0. The characteristic flow velocity is denoted V_0, but combining this with either of the two length scales and the diffusivity D we have four possible choices for the time
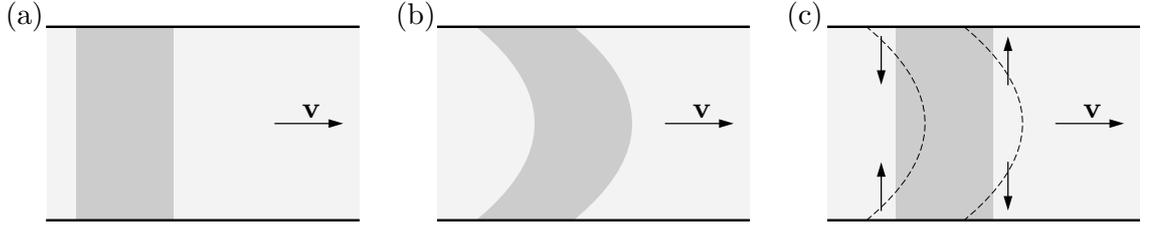
Figure 4.5: A sketch of the Taylor dispersion problem in a cylindrical microchannel of radius a with a stationary Poiseuille flow (horizontal arrow **v**). (a) The initial flat concentration (dark gray) of the solute. (b) Neglecting diffusion the solute gets stretched out in a paraboloid shaped plug. (c) With diffusion, indicated by the vertical arrows, the deformed concentration profile gets evened out.

scale T_0:

$$\tau_{\text{diff}}^{\text{rad}} = \frac{a^2}{D}, \quad \text{time to move the distance } a \text{ by radial diffusion} \tag{4.42a}$$

$$\tau_{\text{diff}}^{\text{ax}} = \frac{L_0^2}{D}, \quad \text{time to move the distance } L_0 \text{ by axial diffusion} \tag{4.42b}$$

$$\tau_{\text{conv}}^{L} = \frac{L_0}{V_0}, \quad \text{time to move the distance } L_0 \text{ by axial convection} \tag{4.42c}$$

$$\tau_{\text{conv}}^{a} = \frac{a}{V_0}, \quad \text{time to move the distance } a \text{ by axial convection.} \tag{4.42d}$$

It is customary to use $T_0 = \tau_{\text{conv}}^{a} = a/V_0$ as the characteristic time scale. With $x = L_0\tilde{x}$, $r = a\tilde{r}$, $t = T_0\tilde{t}$, and $v_x = V_0\tilde{v}_x$ the dimensionless convection-diffusion equation becomes

$$\frac{V_0}{a} \partial_{\tilde{t}}c + \frac{V_0}{L_0} \tilde{v}_x\partial_{\tilde{x}}c = \frac{D}{a^2}\left(\partial_{\tilde{r}}^2 c + \frac{1}{\tilde{r}}\partial_{\tilde{r}}c\right) + \frac{D}{L_0^2}\partial_{\tilde{x}}^2 c. \tag{4.43}$$

Introducing the diffusion Péclet number Pe, defined as

$$Pe \equiv \frac{\text{diffusion time}}{\text{convection time}} = \frac{\tau_{\text{diff}}^{\text{rad}}}{\tau_{\text{conv}}^{a}} = \frac{\frac{a^2}{D}}{\frac{a}{V_0}} = \frac{V_0\,a}{D}, \tag{4.44}$$

the diffusion-convection equation can be written as

$$Pe\,\partial_{\tilde{t}}c + Pe\,\frac{a}{L_0}\tilde{v}_x\partial_{\tilde{x}}c = \left(\partial_{\tilde{r}}^2 c + \frac{1}{\tilde{r}}\partial_{\tilde{r}}c\right) + \frac{a^2}{L_0^2}\partial_{\tilde{x}}^2 c. \tag{4.45}$$

For high Péclet numbers, where $\tau_{\text{conv}}^{a} \ll \tau_{\text{diff}}^{\text{rad}}$ and convection thus happens much faster than diffusion, the terms on the left-hand side of the convection-diffusion equation dominates, and we are in the convection dominated regime. Conversely, for low Péclet numbers, where $\tau_{\text{diff}}^{\text{rad}} \ll \tau_{\text{conv}}^{a}$ and diffusion happens much faster than convection, the terms on the right-hand side dominates, and we are in the diffusion dominated regime. Note that due to the factor a^2/L_0^2 on the right-hand side the radial diffusion sets in at different time scales than the axial diffusion. This fact will be exploited in the Taylor dispersion model.

4.5.2 Taylor's model for dispersion in microfluidic channels

In Taylor's model for the dispersion problem sketched in Fig. 4.5, the convection-diffusion equation is studied in the frame reference moving with average speed V_0 of the imposed Poiseuille flow. Furthermore, we consider the limit of large times $t \gg \tau_{\text{diff}}^{\text{rad}}$, where the diffusion process has had time to act over the short radial distance a yielding an radially averaged concentration profile. The concentration profile in the axial direction changes over the long length scale $L_0 \gg a$, and the axial diffusion of this profile can be studied separately. In terms of the characteristic time scales Eq. (4.42) we can formulate the domain of validity of the model as two inequalities. The central time scale is the radial diffusion time $\tau_{\text{diff}}^{\text{rad}}$, which must be smaller than the long axial convection time τ_{conv}^{L}, to ensure the radial smearing of the concentration profile, ie., $\tau_{\text{diff}}^{\text{rad}} \ll \tau_{\text{conv}}^{L}$. On the other hand, the short convection time τ_{conv}^{L} must be smaller than $\tau_{\text{diff}}^{\text{rad}}$ to ensure that convection does play a role, ie., $\tau_{\text{conv}}^{a} \ll \tau_{\text{diff}}^{\text{rad}}$. From this rough argument we have established the domain of validity of Taylor's model,

$$\tau_{\text{conv}}^{a} \ll \tau_{\text{diff}}^{\text{rad}} \ll \tau_{\text{conv}}^{L} \qquad \Rightarrow \qquad 1 \ll Pe \ll \frac{L_0}{a}. \tag{4.46}$$

As we proceed with the actual solution of the convection-diffusion equation for Taylor's model, we shall show that these two inequalities are fulfilled except for some numerical pre-factors that appear on the way.

As $L_0 \gg a$ in the large-time limit, we see that the axial diffusion term $(a^2/L_0^2)\partial_{\tilde{x}}^2 c$-term in Eq. (4.43) can be neglected compared to the radial diffusion term, $\partial_{\tilde{r}}^2 c + (1/r)\partial_r tic$. As a consequence, the only axial change in concentration follows from convection. It is therefore natural to make a coordinate transformation to a coordinate system (r, x') that moves along with the mean velocity V_0 of the paraboloid Poiseuille flow Eq. (4.41),

$$x' \equiv x - V_0\, t, \qquad \text{and} \qquad v'_x(r) = v_x(r) - V_0 = \left(1 - 2\frac{r^2}{a^2}\right)V_0. \tag{4.47}$$

In the moving coordinate system the convection-diffusion equation without the discarded axial diffusion becomes

$$\partial_t c + V_0\left(1 - 2\frac{r^2}{a^2}\right)\partial_{x'}c = D\left(\partial_r^2 c + \frac{1}{r}\,\partial_r c\right). \tag{4.48}$$

Moreover, in the time-limit we are working, where radial diffusion dominates, it follows consistently that in the moving coordinate system the concentration profile is stationary and the axial gradient of the concentration is independent of r, i.e., $\partial_t c = 0$ and $\partial_{\tilde{x}}c = \partial_{\tilde{x}}c(x')$. The validity of this assumption can always be checked once the solution is obtained. The problem is thus reduced to

$$\left(1 - 2\frac{r^2}{a^2}\right)V_0\,\partial_{x'}c = D\left(\partial_r^2 c + \frac{1}{r}\,\partial_r c\right), \tag{4.49}$$

which, as $\partial_{x'}c$ is independent of r, is an ordinary differential equation for $c(r)$ with the solution

$$c(r, x') = \bar{c}(x') + \frac{a^2 V_0}{4D}\,\partial_{x'}c(x')\left(-\frac{1}{3} + \frac{r^2}{a^2} - \frac{1}{2}\frac{r^4}{a^4}\right), \tag{4.50}$$

where $\bar{c}(x')$ is the concentration averaged over the cross section at x'. We can easily derive the condition for having an r-independent axial gradient of c by differentiating Eq. (4.50) with respect to x' and demand the second term to be negligible small,

$$\partial_{x'} c = \partial_{x'} \bar{c}(x'), \quad \text{if} \quad \frac{a^2 V_0}{4D} \frac{1}{L_0} \ll 1. \tag{4.51}$$

The last equality can be expressed in terms of Pe as

$$Pe \ll 4 \frac{L_0}{a}. \tag{4.52}$$

4.5.3   The solution to the Taylor dispersion problem

By calculating the average current density $\bar{J}(x')$ through the cross section at x' using Eqs. (4.47) and (4.50), we can derive Fick's law for the average concentration $\bar{c}(x')$ and read off the effective diffusion coefficient D_{eff} for the resulting 1D diffusion problem,

$$\bar{J}(x') = \frac{1}{\pi a^2} \int_0^a dr\, 2\pi r\, \rho c(r, x') v'_x(r) = -\frac{a^2 V_0^2}{48D} \rho \partial_{x'} \bar{c} \equiv -D_{\text{eff}} \rho \partial_{x'} \bar{c}, \tag{4.53}$$

where D_{eff}, also known as the Taylor dispersion coefficient, is defined as

$$D_{\text{eff}} \equiv \frac{a^2 V_0^2}{48D}. \tag{4.54}$$

Conservation of mass applied in the moving coordinate system yields

$$\rho \partial_t \bar{c} = -\partial_{x'} \bar{J} \quad \Rightarrow \quad \partial_t \bar{c} = D_{\text{eff}} \partial_{x'}^2 \bar{c}. \tag{4.55}$$

Using the result Eq. (4.30) for limited planar-source diffusion we can immediately write down the solution to the Taylor dispersion problem (transformed back to the un-moved coordinate system)

$$\bar{c}(x, t) = \frac{n_0}{(\pi D_{\text{eff}} t)^{\frac{1}{2}}} \exp\left[-\frac{(x - V_0 t)^2}{4 D_{\text{eff}} t} \right]. \tag{4.56}$$

The result is only valid if molecular diffusion is negligible compared to dispersion,

$$D \ll D_{\text{eff}} \quad \Rightarrow \quad D \ll \frac{a^2 V_0^2}{48D} \quad \Rightarrow \quad \sqrt{48} \ll Pe. \tag{4.57}$$

Combining this with the earlier condition Eq. (4.52) we arrive at the domain of validity of the solution Eq. (4.56)

$$\sqrt{48} \ll Pe \ll 4\frac{L_0}{a}. \tag{4.58}$$

This inequality replaces the more rough estimate given in Eq. (4.46).

4.6   Stopping a Poiseuille flow by viscous forces

In Section 2.4.3 we analyzed the steady-state Poiseuille flow in a channel with a circular cross section. In the following we study in detail what was already alluded to in Fig. 3.1, namely how such a flow decays and stops, when the pressure drop suddenly vanishes. We consider a finite section of length L of the infinite channel, and we assume that for time $t < 0$ a steady-state Poiseuille flow was present driven by the pressure drop $p(0) = p_0 + \Delta p$ and $p(L) = p_0$. Then suddenly at $t = 0$ the overpressure Δp is suddenly removed such that for $t > 0$ the pressure is given by $p(0) = p(L) = p_0$. In reality, the new pressure is not established instantly, but it is set up with the speed of sound in the liquid, typically of the order 10^3 m/s. However, this is much faster than the velocities obtained by the liquid, so it is a good approximation to assume that the new pressure is set up instantly in accordance with the usual assumption of incompressibility of the liquid. In the following we calculate how the velocity field of the liquid evolves in time for $t > 0$.

Due to the cylindrical symmetry the non-linear term $\rho(\mathbf{v}\cdot\boldsymbol{\nabla})\mathbf{v}$ in the Navier-Stokes equation remains zero, but in contrast to the steady-state version Eq. (2.32) we must now keep the explicit time-derivative. Since $\Delta p = 0$ we arrive at

$$\rho\,\partial_t v_x(r,t) - \eta\left[\partial_r^2 + \frac{1}{r}\,\partial_r\right]v_x(r,t) = 0. \tag{4.59}$$

The boundary and initial conditions for $v_x(r,t)$ are

$$v_x(a,t) = 0, \qquad \partial_r v_x(0,t) = 0, \qquad v_x(r,0) = \frac{\Delta p}{4\eta L}\left(a^2 - r^2\right), \qquad v_x(r,\infty) = 0, \tag{4.60}$$

where we have utilized that starting from the steady-state solution Eq. (2.33a) the liquid ends at rest. Note that the azimuthal angle ϕ does not enter the problem.

The disappearance of the non-linear term and the appearance of a zero right-hand side makes Eq. (4.59) a homogeneous linear differential equation. To proceed, we do not set out to find the solution $v_x(r,t)$ directly, but instead we seek some simpler solutions $u_n(r,t)$, which can be used in a Fourier-like expansion

$$v_x(r,t) = \sum_n \tilde{c}_n\, u_n(r,t), \tag{4.61}$$

where $\tilde{c}_n$ are some expansion coefficients. One particular class of solutions $u_n(r,t)$ to Eq. (4.59) can be found by separation of the variables using the following trial solution,

$$u_n(r,t) \equiv T_n(t)\,\tilde{u}_n(r). \tag{4.62}$$

Inserting this into Eq. (4.59) and dividing by $T_n(t)\,\tilde{u}_n(r)$ yields

$$\frac{1}{T_n(t)}\,\partial_t T_n(t) = \frac{\nu}{\tilde{u}_n(r)}\left[\partial_r^2 + \frac{1}{r}\,\partial_r\right]\tilde{u}_n(r). \tag{4.63}$$

The t-dependent left-hand side can only equal the r-dependent right-hand side if the two sides equal the same constant $-\lambda_n$. Thus we arrive at

$$\partial_t T_n(t) = -\lambda_n\,T_n(t), \tag{4.64a}$$

$$\left[\partial_r^2 + \frac{1}{r}\,\partial_r\right]\tilde{u}_n(r) = -\frac{\lambda_n}{\nu}\,\tilde{u}_n(r). \tag{4.64b}$$

The solutions to these standard differential equations are

$$T_n(t) = \exp\left(-\lambda_n t\right), \tag{4.65a}$$

$$\tilde{u}_n(r) = \tilde{c}_n^{(0)} J_0\left(\sqrt{\tfrac{\lambda_n}{\nu}}\, r\right) + \tilde{c}_n^{(1)} Y_0\left(\sqrt{\tfrac{\lambda_n}{\nu}}\, r\right), \tag{4.65b}$$

where $\tilde{c}_n^{(0)}$ and $\tilde{c}_n^{(1)}$ are constants, and where J_0 and Y_0 are Bessel functions of the first and second kind, respectively, both of order zero.[3]

To narrow down the possible solutions we use three of the four boundary conditions Eq. (4.60). From $v_x(r, \infty) = 0$ follows $T_n(\infty) = 0$ and thus $\lambda_n > 0$. From $\partial_r v_x(0, t) = 0$ follows $\partial_r \tilde{u}_n(0) = 0$, so the Bessel function $Y_0(r)$, which diverges for $r \to 0$, must be excluded and thus $\tilde{c}_n^{(1)} = 0$. From $v_x(a, t) = 0$ follows that $\tilde{u}_n(a) = 0$ and thus

$$\sqrt{\tfrac{\lambda_n}{\nu}}\, a = \gamma_n, \quad \text{where} \quad J_0(\gamma_n) \equiv 0, \quad n = 1, 2, 3, \ldots \tag{4.66}$$

Here we have introduced the countable number of roots γ_n of the Bessel function J_0.[4] This provides us with a complete set of basis functions which can be used to express any solution of Eq. (4.59) in the form of a Fourier-Bessel series

$$v_x(r, t) = \sum_{n=1}^{\infty} \tilde{c}_n^{(0)} J_0\left(\gamma_n \tfrac{r}{a}\right) \exp\left(-\gamma_n^2 \tfrac{\nu}{a^2} t\right). \tag{4.67}$$

The unknown coefficients $\tilde{c}_n^{(0)}$ are determined by the third boundary condition in Eq. (4.60) for $u(r, 0)$,

$$u(r, 0) = \sum_{n=1}^{\infty} \tilde{c}_n^{(0)} J_0\left(\gamma_n \tfrac{r}{a}\right) \equiv \frac{\Delta p}{4\eta L}\left(a^2 - r^2\right). \tag{4.68}$$

Introducing the dimensionless coordinate $\rho = r/a$, multiplying Eq. (4.68) by $\rho J_0(\gamma_m \rho)$, integrating over ρ, and using the orthogonality relation

$$\int_0^1 \mathrm{d}\rho\, \rho\, J_0(\gamma_m \rho) J_0(\gamma_n \rho) = \tfrac{1}{2}\left[J_1(\gamma_m)\right]^2 \delta_{mn} \tag{4.69}$$

for the Bessel functions $J_0(\gamma_n \rho)$, we can calculate coefficient $\tilde{c}_m^{(0)}$,

$$\tilde{c}_m^{(0)} = \frac{a^2 \Delta p}{2\eta L} \frac{1}{\left[J_1(\gamma_m)\right]^2} \int_0^1 \mathrm{d}\rho\, \left(\rho - \rho^3\right) J_0(\gamma_m \rho) = \frac{2a^2 \Delta p}{\eta L} \frac{1}{\gamma_m^3 J_1(\gamma_m)}. \tag{4.70}$$

Note that the Bessel function J_1 of order 1 now appears.[5]

---

[3] The solution Eq. (4.65b) is the cylindrical coordinate analog of the Cartesian case:

$$\partial_x^2 \tilde{u}_n(x) = -\frac{\lambda_n}{\nu}\, \tilde{u}_n(x) \quad \Rightarrow \quad \tilde{u}_n(x) = \tilde{c}_n^{(0)} \sin\left(\sqrt{\tfrac{\lambda_n}{\nu}}\, x\right) + \tilde{c}_n^{(1)} \cos\left(\sqrt{\tfrac{\lambda_n}{\nu}}\, x\right).$$

[4] The first four roots of $J_0(\gamma_i) = 0$ are $\gamma_1 = 2.405$, $\gamma_2 = 5.520$, $\gamma_3 = 8.654$, and $\gamma_4 = 11.792$.

[5] The integral in Eq. (4.70) is calculated by using $\int \mathrm{d}x\, x J_0(x) = x J_1(x)$ and the recursive formula $\int \mathrm{d}x\, x^k J_0(x) = x^k J_1(x) + (k-1) x^{k-1} J_0(x) - (k-1)^2 \int \mathrm{d}x\, x^{k-2} J_0(x).$
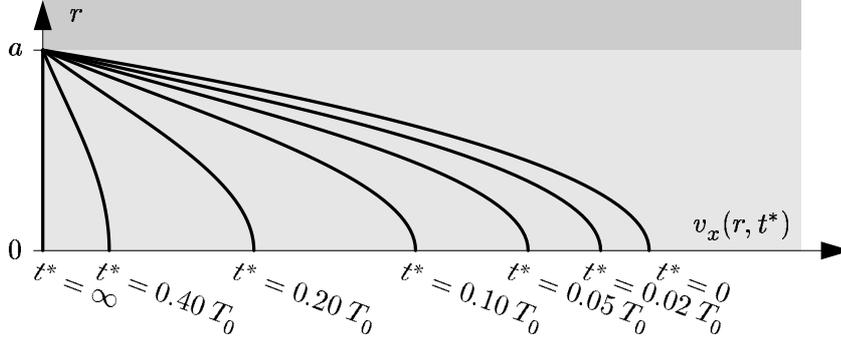
Figure 4.6: The evolution in time of the velocity profile $v_x(r,t)$ in a cylindrical channel with radius a for a decelerating Poiseuille flow due to the abrupt disappearance of the driving pressure Δp at $t = 0$. The time is expressed in units of the momentum diffusion time $T_0 = a^2/\nu$. The velocity profile is shown at seven different times t^* spanning from the paraboloid velocity profile at $t^* = 0$ to the zero-velocity field at $t^* = \infty$.

The final result for the velocity field $v_x(r,t)$ of a starting Poiseuille flow can now be obtained by combining Eqs. (4.67) and (4.70),

$$v_x(r,t) = \frac{a^2\Delta p}{4\eta L} \sum_{n=1}^{\infty} \frac{8}{\gamma_n^3 \, J_1(\gamma_n)} \, J_0\!\left(\gamma_n \, \frac{r}{a}\right) \, \exp\left(-\gamma_n^2 \frac{\nu}{a^2} \, t\right). \tag{4.71}$$

The velocity profile at different times during the evolution of the full Poiseuille flow paraboloid is shown in Fig. 4.6. Note that the time scale $t_{\rm acc}$ characteristic for the deceleration basically is the momentum diffusion time $T_0 = a^2/\nu$, but more accurately it is determined by the exponential factor containing the smallest Bessel function root $\gamma_1 = 2.405$. In the case of a water in a typical microfluidic channel with radius $a = 100~\mu$m we get

$$t_{\rm acc} = \frac{1}{\gamma_1^2} \frac{a^2}{\nu} = \frac{1}{\gamma_1^2} \, T_0 \approx 2 \times 10^{-3}~{\rm s}. \tag{4.72}$$

4.7   Accelerated motion of a spherical body in a liquid

As mentioned in Section 2.6 many applications of lab-on-a-chip systems involves the motion of small objects, such as magnetic beads, fluorescent markers, or biological cells, inside the microfluidic channels. In the following we study two aspects beyond steady-state motion of spherical bodies, namely simple acceleration and Brownian motion. As before we restrict our analysis to rigid bodies.

4.7.1   A spherical body approaching steady-state in a liquid

We begin by a studying the acceleration of a sphere with radius a and mass $(4\pi/3)a^3\rho_{\rm sph}$ as it approaches steady-state in a fluid. Initially, both the sphere and the fluid is at complete rest. Suddenly, at time $t = 0$ a constant external force $F_{\rm ext} \, \mathbf{e}_x$ begins to act on the sphere.

As the force is constant all motion in the following takes place along the direction given by $\mathbf{e}_x$, and the resulting velocity of the sphere is denoted $\mathbf{u}(t) = u(t)\,\mathbf{e}_x$. The equation of motion for the sphere becomes

$$\frac{4}{3}\pi a^3 \rho_{\mathrm{sph}} \partial_t u = -6\pi\eta a\, u + F_{\mathrm{ext}}. \tag{4.73}$$

The solution to this standard differential equation is

$$u(t) = \frac{F_{\mathrm{ext}}}{6\pi\eta a} - u_0\,\exp\left(-\frac{9\eta}{2\rho_{\mathrm{sph}}a^2}\,t\right), \tag{4.74}$$

where u_0 is an integration constant that needs to be specified by the boundary conditions. If the sphere is at rest for $t = 0$ then

$$u(t) = \frac{F_{\mathrm{ext}}}{6\pi\eta a}\left[1 - \exp\left(-\frac{9\eta}{2\rho_{\mathrm{sph}}a^2}\,t\right)\right]. \tag{4.75}$$

The characteristic time scale in the exponential is seen to be very small for a microsystem. For a cell we can take the density to be that of water while $a = 5\ \mu$m. This yields

$$\frac{2\rho_{\mathrm{sph}}a^2}{9\eta} \approx 5\ \mu\mathrm{s}. \tag{4.76}$$

Thus in a viscous environment inertial forces are indeed negligible, and for the case of the microsphere it is reasonable to assume that it is always moving in local steady-state.

4.7.2   A diffusing spherical body and the Einstein relation

Another accelerated motion of a sphere is the random diffusion or Brownian motion. Here, we shall derive the very useful Einstein relation, which gives the diffusion constant D of the Brownian motion in terms of the parameters of the liquid and the sphere.

A sphere of radius a moving with velocity $\mathbf{v}$ through a liquid of viscosity η experience the Stokes drag force $\mathbf{F}_{\mathrm{drag}}$. Consider a position-dependent solution of density $\rho(\mathbf{r})$ of spherical molecules in the same liquid. Due to gradients in the density these molecules will diffuse according to Fick's law, $\mathbf{J} = -D\,\boldsymbol{\nabla}\rho$. Since the chemical potential μ by definition is the free energy of the last added molecule, the force $\mathbf{F}_{\mathrm{diff}}$ driving the diffusion is given by minus the gradient μ,

$$\mathbf{F}_{\mathrm{diff}} = -\boldsymbol{\nabla}\mu. \tag{4.77}$$

In steady state the forces from diffusion and drag exactly balance each other. Combining this force balance with Fick's law and the thermodynamic relation $\mu(T,\rho) = \mu_0 + k_{\mathrm{B}}T\ln(\rho/\rho_0)$, where the subscript 0 refer to some constant standard concentration, we arrive at the Einstein relation,

$$D = \frac{k_{\mathrm{B}}T}{6\pi a\eta}. \tag{4.78}$$

It is useful to note that at room temperature

$$k_{\mathrm{B}}T = 1.3805 \times 10^{-23}\mathrm{J/K} \times 300\ \mathrm{K} = 4.14 \times 10^{21}\ \mathrm{J}. \tag{4.79}$$

4.8 Exercises

Exercise 4.1
Constant-step random walk in 1D
Consider the random walk in 1D defined in Section 4.1 with constant step-size $\Delta x_i = \pm \ell$.

(a) List all possible end-positions x_N for random walks with $N = 4$ steps, and note in how many ways each can be reached.

(b) Argue why the constant-step random walk with N steps can be described as a binomial distribution, and use this fact to as an alternative way to calculate $\langle x_N \rangle$ and $\langle x_N^2 \rangle$.

Exercise 4.2
Constant-step, continuous-direction random walk in 2D and 3D
Consider a random walk in 2D like $\mathbf{R}_N$ of Eq. (4.10), but now allow for a step $\Delta \mathbf{r}_i$ of length ℓ in any direction, $\Delta \mathbf{r}_i = \ell \cos \theta_i \, \mathbf{e}_x + \ell \sin \theta_i \, \mathbf{e}_y$, given by the angle θ_i.

(a) Calculate the diffusion length $\ell_{\mathrm{diff}}^{2D}$ in this model.

(b) Extend the model to 3D and calculate the corresponding diffusion length $\ell_{\mathrm{diff}}^{3D}$.

Exercise 4.3
The convection-diffusion equation
Verify that Eqs. (4.14) and (4.18) indeed lead to Eq. (4.19).

Exercise 4.4
Solutions to the diffusion equation
Study the various analytic solutions to the diffusion equation presented in Section 4.3 and prove that the solutions Eqs. (4.28), (4.30), and (4.32) indeed are solutions to the diffusion equation given the respective initial conditions Eqs. (4.27), (4.29), and (4.31).

Exercise 4.5
The Einstein relation linking diffusion to viscosity
Consider the Einstein relation Eq. (4.78) for the diffusion constant of a sphere.

(a) Estimate the diffusion constant D in water at room temperature for a rigid sphere with the same radius as a typical small ion. Comment the result.

(b) Fluorescent latex spheres used for bio-detection in lab-on-chip systems have typically a radius $a = 0.5$ μm. Estimate how long time τ_{diff} it takes such a sphere to diffuse across a 100 μm wide water-filled microchannel at room temperature.

Exercise 4.6
Thermally induced jump rates for molecules in water
Locally, within a few atomic distances around a given H_2O molecule in water there is spatial order. The molecule is thus lying in the potential minimum created by the surrounding molecules. The molecule of mass M executes small harmonic oscillations of angular frequency $\omega = 2\pi f$. To jump to a neighboring site, a water molecule needs to overcome the potential barrier of height ΔE. It attempts to jump with the harmonic

oscillator frequency f, but each attempt is only successful with the thermal probability factor $\exp(-\Delta E/k_{\mathrm{B}}T)$.

The frequency of the harmonic oscillations can be estimated as follows. Write the potential as $V(x) = \frac{1}{2}Kx^2$. The maximum of the barrier occurs at $x = \frac{1}{2}d$, so it is reasonable to put $V(\frac{1}{4}d) = \frac{1}{2}\Delta E$. Using this, show that the rate Γ for successful jumps is

$$\Gamma = \frac{2}{\pi d}\sqrt{\frac{\Delta E}{M}}\,e^{-\Delta E/k_{\mathrm{B}}T}. \tag{4.80}$$

Exercise 4.7
The current density from thermally induced molecular jumping
Let the thickness of one molecular layer be denoted d.

(a) Argue that the particle current density in the x direction from a given layer situated at the plane $x = 0$ is $J_x(0) = \rho(0)d\,\Gamma$.

(b) Write a similar expression for the particle current density coming from the layer at $x = d$ going back to the first layer. Argue that the total current density is given by $J_x^{\mathrm{tot}} = J_x(0) - J_x(d) \approx -\partial_x\rho\,d^2\Gamma$.

(c) Show that this result gives the diffusion constant $D = d^2\Gamma$.

Exercise 4.8
A theoretical expression for the viscosity
Combine the results of the previous exercises and obtain the following expression for η:

$$\eta = \frac{k_{\mathrm{B}}T}{12ad}\sqrt{\frac{M}{\Delta E}}\,e^{\Delta E/k_{\mathrm{B}}T}. \tag{4.81}$$

Compare this result with the experimental values for water given in Section B.1. Use the following parameter values: $a = 0.1$ nm, $d = 0.4$ nm, and M you figure out yourself. The value for ΔE we estimate from the specific vaporization energy of water, $E_{\mathrm{vap}}/M = 2.26 \times 10^6$ J/kg (i.e. the latent heat for producing steam from boiling water at 100 °C): $\Delta E \approx \frac{1}{2}\,\frac{1}{2}\,E_{\mathrm{vap}}$. One factor $\frac{1}{2}$ is because the barrier height is roughly half the binding energy, and the other because on average there are two hydrogen bonds per molecule.

Exercise 4.9
Starting a Poiseuille flow in a circular channel
Consider the setup given in Section 4.6 for the decelerating Poiseuille flow in a circular channel, but invert the problem, so that the starting point is a liquid at complete rest for $t < 0$ and no pressure drop, $p(0) = p(L) = p_0$. Then suddenly at $t = 0$ a constant pressure drop is applied such that $p(0) = p_0 + \Delta p$ and $p(L) = p_0$ for $t > 0$. Determine the velocity field $u_x(r,t)$ for the accelerating Poiseuille flow.

Exercise 4.10
Starting a Poiseuille flow in a parallel-plate channel
Redo the previous exercise but change the cross-section of the channel from circular to that of an infinite parallel-plate channel of height h.

4.9   Solutions

Solution 4.1
Constant-step random walk in 1D
For each step in the constant step-size random walk in 1D there are two possibilities, so N steps result in 2^N paths. Any path has P positive steps $+\ell$, where $0 \leq P \leq N$, and $N - P$ negative steps $-\ell$, so the paths can end at $x_N/\ell = P - (N - P) = 2P - N$.

(a) For $N = 4$ steps there are $2^4 = 16$ paths ending at $x_4/\ell = -4, -2, 0, 2, 4$. The extreme points can each be reach in only one way: either all steps are negative or all are positive. The point $x_4/\ell = 2$ is reached after 3 positive and 1 negative step. There are four ways to place the negative step in the sequence, so the end point can be reached by four different paths. Similarly, there are four paths leading to $x_4/\ell = -2$. Now we have accounted for 10 of the 16 paths, which leaves six paths to end at $x_4/\ell = 0$.

(b) A N-step random walk consists of N consecutive and uncorrelated binary choices, $+\ell$ or $-\ell$. Let us consider $+\ell$ as the successful outcome occurring with probability $p = \frac{1}{2}$. This is the very definition of a binomial process with the distribution $f(P) = C_{N,P}\left(\frac{1}{2}\right)^N\left(1 - \frac{1}{2}\right)^{(N-P)} = \frac{1}{2^N}C_{N,P}$ for successful outcome. here $C_{N,P} = N!/[P!(N-P)!]$ is the binomial coefficient. Well known results are $\langle P \rangle = Np = \frac{1}{2}N$ and $\langle (P - \langle P \rangle)^2 \rangle = Np(1-p) = \frac{1}{4}N$. As $x_N/\ell = 2P - N$ we obtain directly $\langle x_N \rangle = 0$ and $\langle x_N^2 \rangle = N\ell^2$.

Solution 4.2
Constant-step, continuous-direction random walk in 2D and 3D
The ith step as $\Delta\mathbf{r}_i = \ell\mathbf{e}_i$, where $\mathbf{e}_i$ is a unit vector pointing in an arbitrary direction.

(a) $\langle \mathbf{R}_N \rangle = \langle \sum_i^N \mathbf{e}_i \rangle = \ell \sum_i^N \langle \mathbf{e}_i \rangle = \mathbf{0}$, as the unit vectors have random directions. Hence the diffusion length in this model is given by $\left(\ell_{\text{diff}}^{2D}\right)^2 = \langle \mathbf{R}_N^2 \rangle = \ell^2 \langle \sum_i^N \mathbf{e}_i \cdot \sum_j^N \mathbf{e}_j \rangle = \ell^2 \sum_{i,j}^N \langle \mathbf{e}_i \cdot \mathbf{e}_j \rangle = \ell^2 \sum_i^N \langle \mathbf{e}_i \cdot \mathbf{e}_i \rangle = N\ell^2$. All the off-diagonal scalar-products average to zero due to the random direction of the unit vectors.

(b) We did not use the dimension in the previous argument, so the diffusion length in 3D is the same for the given model, $\ell_{\text{diff}}^{3D} = \sqrt{N}\ell$.

Solution 4.3
The convection-diffusion equation
We keep the total mass current density $\rho\mathbf{v}$ together as a unit, thus separating it from the solute concentration c_α. Carrying out the differentiation in Eq. (4.18) we get

$$\rho\partial_t c_\alpha + c_\alpha\partial_t\rho = -(\rho\mathbf{v})\cdot\boldsymbol{\nabla}c_\alpha - c_\alpha\boldsymbol{\nabla}\cdot(\rho\mathbf{v}) - \boldsymbol{\nabla}\cdot\mathbf{J}_\alpha^{\text{diff}}. \tag{4.82}$$

By using Eq. (4.14) $c_\alpha\partial_t\rho$ cancels $-c_\alpha\boldsymbol{\nabla}\cdot(\rho\mathbf{v})$, and we arrive at Eq. (4.19).

Solution 4.4
Solutions to the diffusion equation
To simplify the calculations below we note that for a function of the form $f(x) = Ax^\alpha$ we can write its derivative as $\partial_x f = \frac{\alpha}{x} f$.

(a) Limited point-source diffusion. In spherical polar coordinates, see Section A.3, we have without angular dependence that $\nabla^2 c = \partial_r^2 c + \frac{2}{r}\partial_r c$. From Eq. (4.28) we find

$\partial_r c = -\frac{r}{2Dt}c$, and thus $\partial_r^2 c = \left(-\frac{1}{2Dt} + \frac{r^2}{4D^2t^2}\right)c$, as well as $\partial_t c = \left(-\frac{3}{2}\frac{1}{t} + \frac{r^2}{4Dt^2}\right)c$. Hence $\partial_t c = D\left(\partial_r^2 + \frac{2}{r}\partial_r\right)c$. The initial condition Eq. (4.27) is fulfilled if $c(\mathbf{r} \neq 0, 0) = 0$ and $\int d\mathbf{r}\, c(\mathbf{r}, 0) = N_0$. Now, for $\mathbf{r} \neq 0$ Eq. (4.28) gives $c(\mathbf{r}, t) \to 0$ exponentially fast for $t \to 0$, while for any t we have $\int d\mathbf{r}\, c(\mathbf{r}, 0) = N_0(4\pi Dt)^{-\frac{3}{2}} \int_0^\infty dr\, 4\pi r^2 \exp\left(-\frac{r^2}{4Dt}\right) = N_0\frac{4}{\sqrt{\pi}}\int_0^\infty du\, u^2 e^{-u^2} = N_0\frac{4}{\sqrt{\pi}}\Gamma\left(\frac{3}{2}\right) = N_0$.

(b) Limited planar-source diffusion. From Eq. (4.30) we find $\partial_x c = -\frac{x}{2Dt}c$, and thus $\partial_x^2 c = \left(-\frac{1}{2Dt} + \frac{x^2}{4D^2t^2}\right)c$, as well as $\partial_t c = \left(-\frac{1}{2}\frac{1}{t} + \frac{x^2}{4Dt^2}\right)c$. Hence $\partial_t c = D\partial_x^2 c$. The initial condition Eq. (4.29) is fulfilled if $c(x > 0, 0) = 0$ and $\int_0^\infty dx\, c(x, 0) = n_0$. Now, for $x > 0$ Eq. (4.30) gives $c(x, t) \to 0$ exponentially fast for $t \to 0$, while for any t we have $\int_0^\infty dx\, c(x, 0) = n_0(\pi Dt)^{-\frac{1}{2}} \int_0^\infty dx\, \exp\left(-\frac{x^2}{4Dt}\right) = n_0\frac{2}{\sqrt{\pi}}\int_0^\infty du\, e^{-u^2} = n_0\frac{2}{\sqrt{\pi}}\Gamma\left(\frac{1}{2}\right) = n_0$.

(c) Constant planar-source diffusion. From Eq. (4.32) and the associated footnote for $\mathrm{erfc}(s)$ we find $\partial_x c = -c_0\frac{1}{\sqrt{\pi D}}t^{-\frac{1}{2}}\exp\left(-\frac{x^2}{4Dt}\right)$, and thus $\partial_x^2 c = c_0\frac{1}{\sqrt{\pi D}}\frac{x}{2D}t^{-\frac{3}{2}}\exp\left(-\frac{x^2}{4Dt}\right)$, as well as $\partial_t c = c_0\frac{x}{2\sqrt{\pi D}}t^{-\frac{3}{2}}\exp\left(-\frac{x^2}{4Dt}\right)$. Hence $\partial_t c = D\partial_x^2 c$. The boundary condition Eq. (4.31) is fulfilled by Eq. (4.32) since $c(0, t) = c_0\frac{2}{\sqrt{\pi}}\int_0^\infty du\, e^{-u^2} = c_0\frac{2}{\sqrt{\pi}}\Gamma\left(\frac{1}{2}\right) = c_0$.

Solution 4.5
The Einstein relation linking diffusion to viscosity
We use $k_B T = 4.14 \times 10^{-21}$ J and $\eta = 10^{-3}$ Pa s in the Einstein relation (4.78).

(a) For a hydrated ion we take the radius $a = 0.1$ nm and arrive at $D = 2.2 \times 10^{-9}$ m²/s. According to Eq. (4.25a) this is very close to the experimental value.

(b) Taking $a = 0.5$ μm we find $D = 4.4 \times 10^{-13}$ m²/s. With this diffusion constant the time it takes to diffuse $L = 100$ μm is $\tau_{\mathrm{diff}} = \sqrt{L^2/D} = 2.3 \times 10^4$ s = 6.3 h.

Solution 4.6
Thermally induced jump rates for molecules in water
The rate for successful jumps is the product of the attempt rate f with the probability of success $\exp(-\Delta E/k_B T)$, i.e., $\Gamma = f\exp(-\Delta E/k_B T)$. So we just need to determine f, which is given by the oscillation frequency $f = \frac{1}{2\pi}\omega = \frac{1}{2\pi}\sqrt{K/M}$, where K is the force constant of the harmonic potential in which the molecule of mass M is moving. From the energy estimate we have $\frac{1}{2}\Delta E = V\left(\frac{1}{2}d\right) = \frac{1}{2}K\left(\frac{1}{4}d\right)^2$, which leads to $K = 16\frac{\Delta E}{d^2}$ and thus $f = \frac{2}{\pi d}\sqrt{\frac{\Delta E}{M}}$. Consequently $\Gamma = \frac{2}{\pi d}\sqrt{\frac{\Delta E}{M}}\exp(-\Delta E/k_B T)$.

Solution 4.7
The current density from thermally induced molecular jumping
The surface density of molecules in one molecular layer of thickness d is ρd.

(a) The jumping rate Γ gives an estimate of how often a molecule jumps to one side, and consequently the current density is $J_x = \rho d\,\Gamma$.

(b) The total molecular current density in a plane between two neighboring molecular layers is given by the difference of the current densities coming from the two sides, i.e., $J_x^{\mathrm{tot}} = J_x(0) - J_x(d) = [\rho(0) - \rho(d)]\,d\,\Gamma = -\frac{1}{d}[\rho(d) - \rho(0)]\,d^2\Gamma \approx -\partial_x\rho\,d^2\Gamma$.

(c) Applying Fick's law, $J_x = -D\partial_x\rho$, to the previous result gives $D = d^2\Gamma$.

Solution 4.8
A theoretical expression for the viscosity
The Einstein relation and the previous analysis of the diffusion constant yields

$$\eta = \frac{k_{\mathrm{B}}T}{6\pi Da} = \frac{k_{\mathrm{B}}T}{6\pi d^2\Gamma a} = \frac{k_{\mathrm{B}}T}{6\pi d^2\Gamma a} = \frac{k_{\mathrm{B}}T}{12ad}\sqrt{\frac{M}{\Delta E}}\,e^{\Delta E/k_{\mathrm{B}}T}. \tag{4.83}$$

Inserting into this expression the parameters listed in the exercise as well as the mass of a water molecule, $M = 18 \times 1.67 \times 10^{-27}$ kg yields $\eta = 0.7$ mPa s at room temperature.

Solution 4.9
Starting a Poiseuille flow in a circular channel
The Navier–Stokes equation becomes a inhomogeneous, linear partial differential equation

$$\rho\,\partial_t u_x(r,t) - \eta\left[\partial_r^2 + \frac{1}{r}\,\partial_r\right]u_x(r,t) = \frac{\Delta p}{L}. \tag{4.84}$$

A particular solution to this equation fulfilling the no-slip boundary conditions is of course the well-known steady-state solution, $u_\infty(r) = \frac{\Delta p}{4\eta L}\big(a^2 - r^2\big)$. Moreover, $v_x(r,t)$ of Eq. (4.71) is a solution of the corresponding homogeneous equation, Eq. (4.59), with the initial condition $v_x(r,0) = u_\infty(r)$. Therefore, $u_x(r,t) = u_\infty - v_x(r,t)$ is a solution to our problem Eq. (4.84) with the appropriate boundary/initial conditions $u_x(a,t) = 0$, $\partial_r u_x(0,t) = 0$, $u_x(r,0) = 0$, and $u_x(r,\infty) = u_\infty$. The explicit expression for $u_x(r,t)$ is

$$u_x(r,t) = \frac{a^2\Delta p}{4\eta L}\left[1 - \frac{r^2}{a^2} - \sum_{n=1}^{\infty}\frac{8}{\gamma_n^3\,J_1(\gamma_n)}\,J_0\!\left(\gamma_n\,\frac{r}{a}\right)\,\exp\left(-\gamma_n^2\,\frac{\nu}{a^2}\,t\right)\right]. \tag{4.85}$$

In the figure below are shown the time-evolution of the velocity profile from rest to the fully developed paraboloid flow.
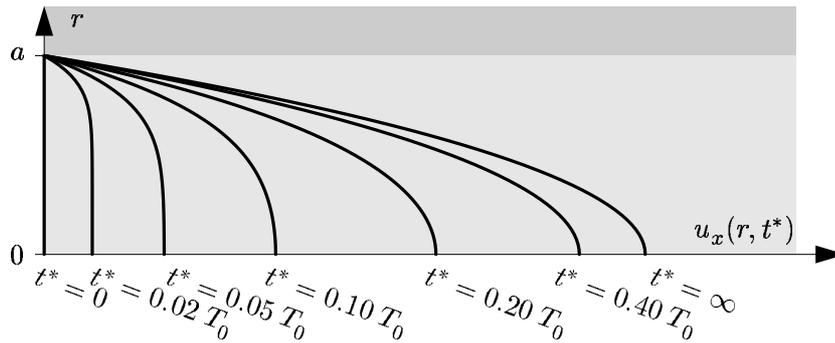
Figure 4.7: The evolution in time of the velocity profile $u_x(z,t)$ in a circular channel with radius a for a Poiseuille flow under acceleration due to the abrupt appearance of the driving pressure Δp at $t = 0$. The time is expressed in units of the momentum diffusion time $T_0 = a^2/\nu$. The velocity profile is shown at seven different times t^* spanning from the zero-velocity profile at $t^* = 0$ to the fully developed paraboloid shape at $t^* = \infty$.

Solution 4.10
Starting Poiseuille flow in a parallel-plate channel
The analysis of the time evolution of a Poiseuille flow for an infinite parallel-plate channel begins with the Navier–Stokes equation analogous to Eq. (4.84),

$$\rho\,\partial_t u_x(z,t) - \eta\,\partial_z^2 v_x(z,t) = \frac{\Delta p}{L}. \tag{4.86}$$

The boundary conditions for $u_x(z,t)$ are

$$u_x(h,t) = 0, \qquad u_x(0,t) = 0, \qquad u_x(z,0) = 0, \qquad u_x(z,\infty) = \frac{\Delta p}{2\eta L}\,\big(h-z\big)z, \quad (4.87)$$

where we have utilized that the steady-state solution Eq. (2.52) will be reached in the limit $t \to \infty$. In analogy with the previous exercise the full solution $u_x(z,t)$ can therefore be written as a sum

$$u_x(z,t) \equiv u_x(z,\infty) - v_x(z,t) \tag{4.88}$$

of the particular solution $u_x(z,\infty)$ and a general solution $v_x(z,t)$ to the corresponding homogeneous equation. When inserting Eq. (4.88) into Eq. (4.86) we obtain the homogeneous differential equation which $v_x(z,t)$ has to satisfy, compare with Eq. (4.59),

$$\partial_t v_x(z,t) - \nu\,\partial_z^2 v_x(z,t) = 0, \tag{4.89}$$

with $\nu = \eta/\rho$. The boundary conditions for $v_x(z,t)$ follow from Eqs. (4.87) and (4.88),

$$v_x(h,t) = 0, \qquad v_x(0,t) = 0, \qquad v_x(z,0) = \frac{\Delta p}{2\eta L}\,\big(h-z\big)z, \qquad v_x(z,\infty) = 0. \tag{4.90}$$

To proceed, we do not set out to find the solution $v_x(z,t)$ directly, but instead we seek some simpler solutions $u_n(z,t)$, which can be used in a Fourier-like expansion

$$v_x(z,t) = \sum_n \tilde{c}_n\, u_n(z,t), \tag{4.91}$$

where $\tilde{c}_n$ are some expansion coefficients. One particular class of solutions $u_n(z,t)$ to Eq. (4.89) can be found by separation of the variables using the following trial solution,

$$u_n(z,t) \equiv T_n(t)\,\tilde{u}_n(z). \tag{4.92}$$

Inserting this into Eq. (4.89) and dividing by $T_n(t)\,\tilde{u}_n(z)$ yields

$$\frac{1}{T_n(t)}\,\partial_t T_n(t) = \frac{\nu}{\tilde{u}_n(z)}\,\partial_z^2 \tilde{u}_n(z). \tag{4.93}$$

The t-dependent left-hand side can only equal the z-dependent right-hand side if the two sides equal the same constant $-\lambda_n$. Thus we arrive at

$$\partial_t T_n(t) = -\lambda_n\, T_n(t), \tag{4.94a}$$

$$\partial_z^2 \tilde{u}_n(z) = -\frac{\lambda_n}{\nu}\, \tilde{u}_n(z). \tag{4.94b}$$

The solutions to these standard differential equations are

$$T_n(t) = \exp\left(-\lambda_n t\right), \tag{4.95a}$$

$$\tilde{u}_n(z) = \tilde{c}_n^{(0)} \sin\left(\sqrt{\tfrac{\lambda_n}{\nu}}\,z\right) + \tilde{c}_n^{(1)} \cos\left(\sqrt{\tfrac{\lambda_n}{\nu}}\,z\right) \tag{4.95b}$$

where $\tilde{c}_n^{(0)}$ and $\tilde{c}_n^{(1)}$ are constants.

To narrow down the possible solutions we use three of the four boundary conditions Eq. (4.90). From $v_x(z,\infty) = 0$ follows $T_n(\infty) = 0$ and thus $\lambda_n > 0$. The sine-term is identical zero for $z = 0$, so no-slip $v_x(0,t) = 0$ at $z = 0$ can only be maintained if the cosine-term is excluded by putting $\tilde{c}_n^{(1)} = 0$. Further, no-slip at $z = h$ imposes the following constraint on the argument of the sine-term,

$$\sqrt{\tfrac{\lambda_n}{\nu}}\,h = n\pi, \quad n = 1, 2, 3, \ldots \tag{4.96}$$

Here $n\pi$ is the countable number of roots of the sine function. This provides us with a complete set of basis functions which can be used to express any solution of Eq. (4.89) in the form of a Fourier-sine series

$$v_x(z,t) = \sum_{n=1}^{\infty} \tilde{c}_n^{(0)} \sin\left(n\pi\,\tfrac{z}{h}\right) \exp\left(-n^2\pi^2\,\tfrac{\nu}{h^2}\,t\right). \tag{4.97}$$

The unknown coefficients $\tilde{c}_n^{(0)}$ are determined by the third boundary condition in Eq. (4.90) for $v_x(z,0)$,

$$v_x(z,0) = \sum_{n=1}^{\infty} \tilde{c}_n^{(0)} \sin\left(n\pi\tfrac{z}{h}\right) \equiv \frac{\Delta p}{2\eta L}\left(h - z\right)z. \tag{4.98}$$

Introducing the dimensionless coordinate $\zeta = z/h$, multiplying Eq. (4.98) by $\sin\left(m\pi\,\zeta\right)$, integrating over ζ, and using the orthogonality relation

$$\int_0^1 d\zeta\,\sin\left(m\pi\,\zeta\right)\sin\left(n\pi\,\zeta\right) = \tfrac{1}{2}\,\delta_{mn} \tag{4.99}$$

for the sine functions $\sin(n\pi\zeta)$, we can calculate coefficient $\tilde{c}_m^{(0)}$,

$$\tilde{c}_m^{(0)} = \frac{h^2\Delta p}{\eta L} \int_0^1 d\zeta\,\left(\zeta - \zeta^2\right)\sin\left(m\pi\,\zeta\right) = \frac{4h^2\Delta p}{\eta L}\,\frac{1}{(m\pi)^3}, \quad m \text{ odd, } 0 \text{ otherwise.} \tag{4.100}$$

Note that only odd values of m yield non-zero contributions.[6]

The final result for the velocity field $u_x(z,t)$ of a starting Poiseuille flow can now be obtained by combining Eqs. (4.88), (4.97), and (4.100),

$$u_x(z,t) = \frac{h^2\Delta p}{2\eta L}\left[\left(1 - \tfrac{z}{h}\right)\tfrac{z}{h} - \sum_{n,\text{odd}}^{\infty} \frac{8}{(n\pi)^3}\,\sin\left(n\pi\,\tfrac{z}{h}\right)\exp\left(-n^2\pi^2\,\tfrac{\nu}{h^2}\,t\right)\right]. \tag{4.101}$$

The velocity profile at different times during the evolution of the full parabolic Poiseuille flow is shown in Fig. 4.8.

---

[6]The integral in Eq. (4.100) is calculated by using $\int dx\,x\sin x = \sin x - x\cos x$ and $\int dx\,x^2\sin x = 2x\sin x + \left(2 - x^2\right)\cos x$.
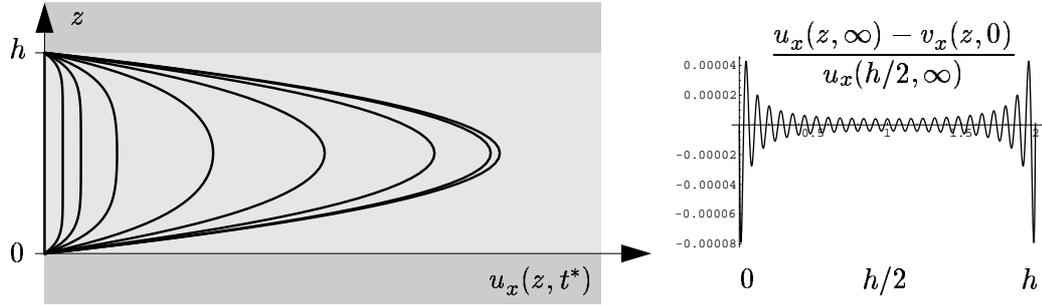
Figure 4.8: The evolution in time of the velocity profile $u_x(z,t)$ in a infinite parallel-plate channel with height h for a Poiseuille flow under acceleration due to the abrupt appearance of the driving pressure Δp at $t = 0$. The time is expressed in units of the momentum diffusion time $T_0 = h^2/\nu$. The velocity profile is shown at seven different times t^* spanning from the zero-velocity profile at $t^* = 0$, through $t^*/T_0 = 0.005, 0.01, 0.02, 0.05, 0.1, 0.2$, and 0.4 to the fully developed parabolic shape at $t^* = \infty$. To the right is shown the relative difference between the full parabolic velocity field $u_x(z,\infty)$, taking into account only the terms in Eq. (4.97) with $n < 50$, and $v_x(z,0) = \frac{\Delta p}{2\eta L}(h-z)z$.

Chapter 5

Capillary effects

One of the characteristic features of microfluidics is the dominance of surface effects due to the large surface to bulk ratio on the micrometer scale. A prominent class of surface effects are known as capillary effects, named so after the latin word *capillus* for hair, since, as we shall see, they are particularly strong in microchannels having bore diameters equal to or less than the width of a human hair, which is about 50 μm.

The capillary effects can be understood by studying Gibbs free energy $\mathcal{G}$, the energy of systems where the thermodynamic control parameters are pressure p, temperature T, and particle number N. In particular we shall be interested in equilibrium or quasi-equilibrium situations, where the Gibbs free energy per definition is at a minimum. As an example, let the system under consideration consist of two sub-systems divided by a free surface at equilibrium. The total Gibbs energy $\mathcal{G}$ of the system is then given as a sum of several energy contributions $\mathcal{G}_i$ such as the free energy of each of the two sub-systems and the free energy of the surface. Let the free surface of the system be given in terms of some variable ξ such as position, volume, or geometrical shape, and let the equilibrium value be given by $\xi = \xi_0$. Variations $\xi = \xi_0 + \delta\xi$ away from the equilibrium value ξ_0 must result in a vanishing variation $\delta\mathcal{G}$ of the free energy, because if $\mathcal{G}$ could vary, the system would spontaneously change ξ_0 to obtain a lower free energy contradicting the assumption that ξ_0 is the equilibrium value. This can be formulated mathematically as

$$\delta\mathcal{G} = \partial_\xi \mathcal{G}\, \delta\xi = \left(\sum_i \partial_\xi \mathcal{G}_i\right)\delta\xi = 0. \tag{5.1}$$

This expression will be used in the following to establish the governing equations for capillary effects.

5.1 Surface tension

A central concept in the theory of surfaces is the surface tension. The surface tension depends on the two materials on each side of the surface, and whether they are solids, fluids, or gases.
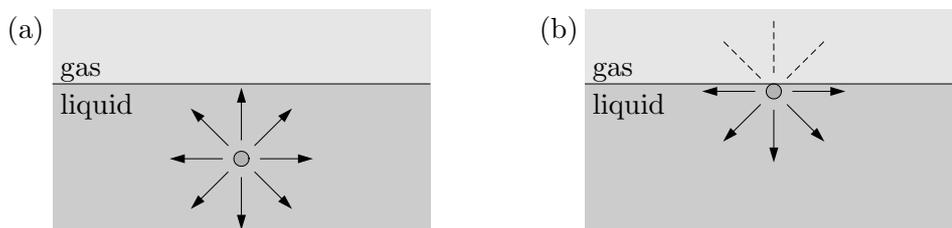
Figure 5.1: The origin of surface tension for a liquid-gas interface. (a) A molecule in the bulk of the liquid forms chemical bonds (arrows) with the neighboring molecules surrounding it. (b) A molecule at the surface of the liquid misses the chemical bonds in the direction of the surface (dashed lines). Consequently, the energy of surface molecules is higher than that of bulk molecules, and the formation of such an interface costs energy.

5.1.1   Definition of surface tension

The surface tension γ of an interface[1] is defined as the Gibbs free energy per area for fixed pressure and temperature,

$$\gamma \equiv \left(\frac{\partial \mathcal{G}}{\partial \mathcal{A}}\right)_{p,T}. \tag{5.2}$$

The SI-unit of γ is therefore

$$\left[\gamma\right] = \mathrm{J\,m^{-2}} = \mathrm{N\,m^{-1}} = \mathrm{Pa\,m}. \tag{5.3}$$

A microscopic model for surface tension between a liquid and a gas is sketched in Fig. 5.1. A molecule in the bulk forms chemical bonds with the neighboring thus gaining a certain amount of binding energy. A molecule at the surface cannot form as many bonds since there are almost no molecules in the gas. This lack of chemical bonds results in a higher energy for the surface molecules. This is exactly the surface tension: it costs energy to form a surface. Using this model it is easy to estimate the order of magnitude of surface tension for a liquid-gas interface. A molecule in the bulk has roughly six nearest neighbors (think of a cubic geometry). A surface molecule has only five missing the one above it in the gas. The area covered by a single molecule is roughly $\mathcal{A} \approx (0.3\ \mathrm{nm})^2$, see Fig. 1.2, while a typical inter-molecular bond ΔE in a liquid is of the order a couple of thermal energies, $\Delta E \approx 2k_{\mathrm{B}}T \approx 50$ meV. This yields

$$\gamma \approx \frac{2k_{\mathrm{B}}T}{\mathcal{A}} = \frac{50\ \mathrm{meV}}{(0.3\ \mathrm{nm})^2} = 90\ \mathrm{mJ\,m^{-2}}. \tag{5.4}$$

The measured value for the water-air interface at 20°C is 70 mJ/m^2, see Table 5.1.

Surface tension can also be interpreted as a force per length having the unit N/m = J/m^2. This can be seen by considering a flat rectangular surface of length L and width

---

[1]In the literature surface tension is normally denoted γ or σ. To avoid confusion with the stress tensor, γ will be used throughout these notes.
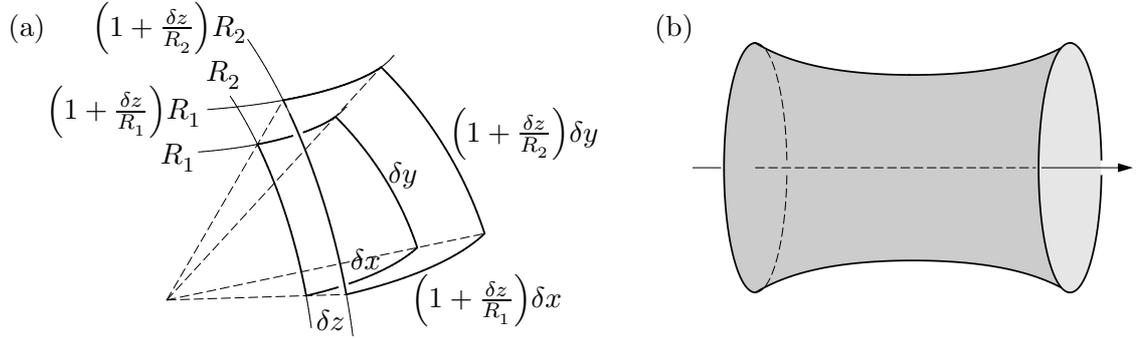
Figure 5.2: (a) The displacement by the amount δz of a small section of a curved surface with area $\mathcal{A} = \delta x\,\delta y$. The local radii of curvature changes from R_i to $R_i + \delta z = (1 + \delta z/R_i)R_i$, $i = 1, 2$ thus changing the area from $\mathcal{A}$ to $(1+\delta z/R_1)(1+\delta z/R_2)\mathcal{A}$. (b) A sketch of a soap film suspended by two circular frames with open ends. The pressure inside and outside are equal, so $\Delta p_{\mathrm{surf}} = 0$ implying $1/R_1 + 1/R_2 = 0$. Here the radius of curvature is positive in the azimuthal direction and negative in the axial direction.

w. If we keep the width constant while stretching the surface the amount ΔL from L to $L + \Delta L$, an external force F must act to supply the work $\Delta \mathcal{G} = F\Delta L$ necessary for creating the new surface area $w\Delta L$ containing the energy $\Delta \mathcal{G} = \gamma w\Delta L$,

$$\frac{F}{w} = \frac{1}{w}\frac{\Delta\mathcal{G}}{\Delta L} = \frac{1}{w}\frac{\gamma\,w\Delta L}{\Delta L} = \gamma. \tag{5.5}$$

5.1.2 The Young–Laplace pressure across curved interfaces

An important consequence of a non-zero surface tension is the presence of the so-called Young–Laplace pressure drop Δp_{surf} across a curved interface in thermodynamical equilibrium. The expression for Δp_{surf} is derived using the energy minimum condition Eq. (5.1).

Consider a small piece of the curved surface with the area $\mathcal{A} = \delta x\,\delta y$ in equilibrium as sketched in Fig. 5.2(a). We now study the consequences of expanding the area through a small displacement δz in the direction parallel to the local normal-vector of the surface. The two local radii of curvature in the x and the y direction thus changes from R_i to $R_i + \delta z = (1 + \delta z/R_i)R_i$, $i = 1, 2$. The side lengths δx and δy are changed similarly, leading to a change in area form $\mathcal{A}$ to $(1+\delta z/R_1)(1+\delta z/R_2)\mathcal{A}$. Neglecting terms of order $(\delta z)^2$ the area has therefore been enlarged by the amount $\delta\mathcal{A}$ given by

$$\delta\mathcal{A} \approx \left(\frac{\delta z}{R_1} + \frac{\delta z}{R_2}\right)\mathcal{A}. \tag{5.6}$$

If we disregard any influence of gravity there will only be two contributions to the change $\delta\mathcal{G}$ of the free energy of the system: an increase in surface energy $\mathcal{G}_{\mathrm{surf}}$ due to an increased area, and a decrease in pressure-volume energy $\mathcal{G}_{\mathrm{pV}}$ due to the increase in volume. In this case Eq. (5.1) becomes

$$\delta\mathcal{G} = \delta\mathcal{G}_{\mathrm{surf}} + \delta\mathcal{G}_{\mathrm{pV}} = \gamma\,\delta\mathcal{A} - \left[\mathcal{A}\,\delta z\right]\Delta p_{\mathrm{surf}} = 0. \tag{5.7}$$

liquid	γ [mJ/m^2]		liquid	solid	θ
water	72.9		water	SiO$_2$	52.3°
mercury	486.5		water	glass	25.0°
benzene	28.9		water	Au	0.0°
methanol	22.5		water	Pt	40.0°
blood	$\sim$60.0		water	PMMA	73.7°
			mercury	glass	140.0°

Table 5.1: Measured values of the surface tension γ at liquid-vapor interfaces and of the contact angle θ at liquid-solid-air contact lines. All values are at 20 °C.

Inserting Eq. (5.6) in this expression and isolating the pressure drop yields the Young–Laplace equation

$$\Delta p_{\text{surf}} = \left(\frac{1}{R_1} + \frac{1}{R_2} \right) \gamma. \tag{5.8}$$

It is important to note the sign convention used here: the pressure is highest in the convex medium, i.e., the medium where the centers of the curvature circles are placed. An example illustrating more complex signs of the curvatures is shown in Fig. 5.2(b), where a thin soap film supported by two co-axial, circular frames with open ends is analyzed. The open ends result in equal pressures inside and outside, whence the Young–Laplace pressure drop is zero, $\Delta p_{\text{surf}} = 0$, which by Eq. (5.8) implies a vanishing mean curvature, $1/R_1 + 1/R_2$. The solution is a film with a positive curvature in the azimuthal direction and a negative curvature in the axial direction.

When using the Navier–Stokes equation to analyze the flow of two immiscible fluids, 1 and 2, the Young–Laplace appears as a boundary condition at the interface between the two fluids. In the direction of the surface normal $\mathbf{n}$ the difference between the stresses $\sigma^{(1)}$ and $\sigma^{(2)}$ of the two fluids, see Eq. (1.44), must equal Δp_{surf} to avoid the existence of un-physical forces of infinite magnitude,

$$-\left(p^{(1)} - p^{(2)} \right) n_i + \left(\sigma_{ik}^{(1)} - \sigma_{ik}^{(2)} \right) n_k = \left(\frac{1}{R_1} + \frac{1}{R_2} \right) \gamma^{(12)}. \tag{5.9}$$

5.2   Contact angle

Another fundamental concept in the theory of surface effects in microfluidics is the contact angle that appears at the contact line between three different phases, typically the solid wall of a channel and two immiscible fluids inside that channel. The two concepts, contact angle and surface tension, allow for understanding the capillary forces that act on two-fluid flows inside microchannels in lab-on-a-chip systems.

5.2.1   Definition of the contact angle

The contact angle θ is defined as the angle between the solid-liquid and the liquid-gas interface at the contact line where three immiscible phases meet, as illustrated in Fig. 5.3(a).
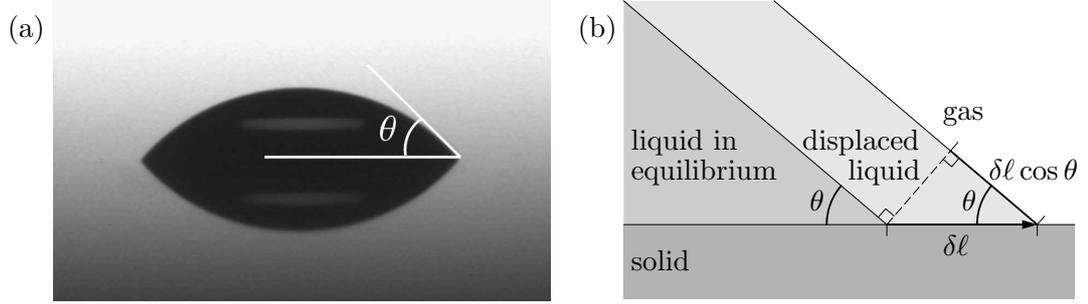
Figure 5.3: (a) The contact angle θ is defined as the angle between the solid-liquid and the liquid-gas interface at the contact line. The picture is taken from a measurement of the contact angle of a water drop on a pure (and reflecting) silicon dioxide substrate in air showing $\theta = 52.3°$, courtesy the groups of Kristensen and Bruus at MIC. (b) A sketch of the small displacement $\delta\ell$ of the contact line away from the equilibrium position. The change of the interface areas are proportional to $+\delta\ell$, $+\delta\ell\cos\theta$, and $-\delta\ell$ for the solid-liquid, liquid-gas, and solid-gas interface, respectively.

In equilibrium θ is determined by the three surface tensions γ_{sl}, γ_{lg}, and γ_{sg} for the solid-liquid, liquid-gas and solid-gas interfaces by Young's equation to be discussed in the following subsection. Some typical values for contact angles θ are listed in Table 5.1.

Whereas the contact angle is well-defined in equilibrium it turns out to depend in a complicated way on the dynamical state of a moving contact line. One can for example observe that the contact angle at the advancing edge of a moving liquid drop on a substrate is different from that at the receding edge.

5.2.2 Young's equation; surface tensions and contact angle

To derive an expression for the contact angle in equilibrium we again use the free energy minimum condition Eq. (5.1). We consider the system sketched in Fig. 5.3(b), where in equilibrium a flat interface between a liquid and a gas forms the angle θ with the surface of a solid substrate. Imagine now that the liquid-gas interface is tilted an infinitesimal angle around an axis parallel to the contact line and placed far away from the substrate interface. As a result the contact line is moved the distance $\delta\ell$ while keeping the contact angle θ. To order $\delta\ell$ the only change in free energy comes from the changes in interface areas near the contact line. It is easy to see from Fig. 5.3(b) that the change of the interface areas are proportional to $+\delta\ell$, $+\delta\ell\cos\theta$, and $-\delta\ell$ for the solid-liquid, liquid-gas, and solid-gas interface, respectively. The energy balance at equilibrium Eq. (5.1) for the Gibbs energy per unit length $\frac{1}{w}\delta\mathcal{G}$ along the contact line becomes,

$$\frac{1}{w}\delta\mathcal{G} = \gamma_{\mathrm{sl}}\delta\ell + \gamma_{\mathrm{lg}}\delta\ell\cos\theta - \gamma_{\mathrm{sg}}\delta\ell = 0, \tag{5.10}$$

which after simple rearrangements gives Young's equation for the contact angle θ,

$$\cos\theta = \frac{\gamma_{\mathrm{sg}} - \gamma_{\mathrm{sl}}}{\gamma_{\mathrm{lg}}}. \tag{5.11}$$

(a)

(b)
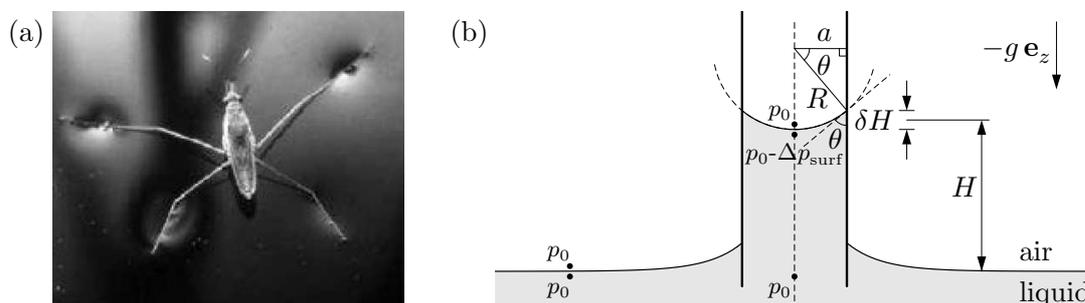
Figure 5.4: (a) The importance of surface tension for microsystems illustrated by an insect able to walk on water. The gravitational force is balanced by the surface tension of the water-air interface. (b) Capillary rise in a vertically standing cylindrical microchannel.

Systems with contact angles $\theta < 90°$ are called hydrophilic (water loving), while those with $\theta > 90°$ are called hydrophobic (water fearing).

5.3 Capillary rise

In the previous discussion we have neglected gravity, an approximation that turns out to be very good in many cases for various microfluidic systems. Consider for example an incompressible liquid of volume Ω with a free liquid-air interface $\partial\Omega$. The equilibrium shape of the liquid will be determined by minimizing the free energy $\mathcal{G}$ consisting of the surface energy and the gravitational potential energy of the bulk,

$$\mathcal{G}_{\min} = \min_{\Omega} \left\{ \gamma \int_{\partial\Omega} \mathrm{d}a \ + \ \rho\,g \int_{\Omega} \mathrm{d}\mathbf{r}\, z \right\}, \tag{5.12}$$

under the constant volume constraint $\int_{\Omega} \mathrm{d}\mathbf{r} = \mathrm{const}$. Here the gravitational acceleration is taken in the negative z direction, $\mathbf{g} = -g\,\mathbf{e}_z$. The equilibrium shape for a free liquid drop in zero gravity is a sphere, since the sphere has the minimal area for a given volume.

   We see from Eq. (5.12) that the shape problem is governed by a characteristic length, the so-called capillary length ℓ_{cap},

$$\ell_{\mathrm{cap}} \equiv \sqrt{\frac{\gamma}{\rho\,g}}, \tag{5.13}$$

which for the water-air interface at 20°C takes the value

$$\ell_{\mathrm{cap}}^{\mathrm{water\text{-}air}} = \sqrt{\frac{0.073 \ \mathrm{J/m^2}}{1000 \ \mathrm{kg/m^3} \ 9.81 \ \mathrm{m/s^2}}} = 2.7 \ \mathrm{mm}. \tag{5.14}$$

Since $a \ll \ell_{\mathrm{cap}} \Rightarrow \rho\,g \ll \gamma/a^2$, gravity does not influence the shape of free water-air interfaces in microfluidic systems of sizes a well below 1 mm. This insight can be used to analyze the so-called capillary rise that happens in narrow, vertically standing microchannels.

Capillary rise can be observed as sketched in Fig. 5.4(b) by dipping one end of a narrow open-ended tube into some liquid. The liquid will rise inside the tube until it reaches equilibrium at some height H above the zero level $z = 0$ defined as the flat liquid level far away from the tube. The task is to determine H.

5.3.1 Capillary rise height

For simplicity we consider a vertically placed micro-tube with a circular cross section of radius $a \ll \ell_{\text{cap}}$. The vertical direction is denoted $\mathbf{e}_z$ and gravity is $\mathbf{g} = -g\,\mathbf{e}_z$. The contact angle of the tube-liquid-air system is denoted θ and the surface tension of the liquid-air interface is called γ. Because $a \ll \ell_{\text{cap}}$ and because the tube is circular the liquid-air surface of minimal energy inside the tube will be spherical. Thus the two radii of curvature are identical, and from the geometry of Fig. 5.4(b) we find

$$R_1 = R_2 \equiv R = \frac{a}{\cos\theta}. \tag{5.15}$$

Because the liquid-air interface is curved, a Young–Laplace pressure drop Δp_{surf} will be present across it. Following the sign convention of Eq. (5.8) the pressure is higher in the convex air volume just above the interface as compared to the pressure $p_{\text{liq}}(H)$ in the concave liquid volume just below the interface (we neglect the finite width δH of the meniscus). Since the pressure of the air is standard atmospheric pressure p_0, we find

$$p_{\text{liq}}(H) = p_0 - \Delta p_{\text{surf}} = p_0 - \frac{2\gamma}{R} = p_0 - \frac{2\gamma}{a}\,\cos\theta. \tag{5.16}$$

The pressure $p_{\text{liq}}(0)$ at $z = 0$ inside the liquid far away from the tube is p_0 because the Young–Laplace pressure across a flat surface is zero, but according to Eq. (2.3) it is also given in terms of the hydrostatic pressure generated by the liquid above $z = 0$,

$$p_0 = p_{\text{liq}}(0) = p_{\text{liq}}(H) + \rho g H. \tag{5.17}$$

Combining Eqs. (5.16) and (5.17) yields the equilibrium height H of the capillary rise,

$$H = \frac{2\gamma}{\rho g a}\,\cos\theta = 2\,\frac{\ell_{\text{cap}}^2}{a}\,\cos\theta = \frac{2}{\rho g a}\,(\gamma_{\text{sg}} - \gamma_{\text{sl}}). \tag{5.18}$$

Quite significant rise heights can be obtained in microchannels. From Table 5.1 we find $H = 4.2$ cm for water in a 100 μm radius PMMA polymer channel, and $H = 42$ cm for $a = 10$ μm.

Because it is relatively easy to measure accurately the geometrical quantities a, H, and $\cos\theta$, Eq. (5.18) is one of the most accurate ways to measure surface tension,

$$\gamma = \frac{\rho g}{2}\,\frac{aH}{\cos\theta}. \tag{5.19}$$

5.3.2 Capillary rise time

After having established the equilibrium height H that the meniscus of the liquid reaches by capillary rise inside a vertically placed tube with circular cross-section, we shall now calculate the approximate rise time. Let $L(t)$ be the height of the liquid column inside the tube at time t. Equilibrium is reached as $t \to \infty$ so $L(\infty) = H$. By mass conservation the speed $\mathrm{d}L/\mathrm{d}t$ by which the liquid rises must be given by the average velocity $V_0 = Q/(\pi a^2)$ of the vertical liquid flow inside the tube of radius a. If for simplicity we assume that the liquid flow is a fully developed Poiseuille flow, we can express the flow rate Q by Eq. (2.30b) and obtain

$$\frac{\mathrm{d}L(t)}{\mathrm{d}t} = V_0 = \frac{Q}{\pi a^2} \approx \frac{a^2 \Delta p(t)}{8\eta} \frac{1}{L(t)}. \tag{5.20}$$

The pressure drop $\Delta p(t)$ between $z = 0$ and $z = L(t)$ induced by viscous friction in the rising liquid column must equal the Young–Laplace pressure drop across the meniscus minus the decreasing hydrostatic pressure of the liquid column,

$$\Delta p(t) = \Delta p_{\mathrm{surf}} - \rho\, g\, L(t). \tag{5.21}$$

When inserting this into Eq. (5.20) with the explicit expression Eq. (5.16) for Δp_{surf} we obtain a first-order ordinary differential equation for the rise height $L(t)$,

$$\frac{\mathrm{d}L(t)}{\mathrm{d}t} = \frac{\gamma}{8\eta} \left[2a\cos\theta\, \frac{1}{L(t)} - \frac{\rho\, ga^2}{\gamma} \right] = \frac{\rho ga^2}{8\eta} \left[\frac{H}{L(t)} - 1 \right]. \tag{5.22}$$

To facilitate the analysis the differential equation is made dimensionless,

$$t = \tau_{\mathrm{cap}}\, \tilde{t}, \qquad \text{where} \quad \tau_{\mathrm{cap}} \equiv \frac{8\eta H}{\rho ga^2}, \tag{5.23a}$$

$$L = H\, \tilde{L}, \tag{5.23b}$$

$$\frac{\mathrm{d}\tilde{L}(\tilde{t})}{\mathrm{d}\tilde{t}} = \frac{1}{\tilde{L}(\tilde{t})} - 1, \quad \tilde{L}(0) = 0, \quad \tilde{L}(\infty) = 1. \tag{5.23c}$$

At small times $\tilde{t} \ll 1$ we have $\tilde{L} \ll 1$, so $d\tilde{L}/d\tilde{t} \approx 1/\tilde{L}$. This is easily integrated to give

$$\tilde{L}(\tilde{t}) = \sqrt{2\tilde{t}}, \qquad \tilde{t} \ll 1. \tag{5.24}$$

For large times $\tilde{t} \to \infty$ we have $\tilde{L} \to 1$ from below. Thus we can write $\tilde{L} = 1 - \delta\tilde{L}$, where $0 \le \delta\tilde{L} \ll 1$. Inserting this in Eq. (5.23c) we get $-d(\delta\tilde{L})/d\tilde{t} = 1/(1-\delta\tilde{L}) - 1 \approx \delta\tilde{L}$, which implies $\delta\tilde{L} \propto \exp(-\tilde{t})$. We therefore arrive at

$$\tilde{L}(\tilde{t}) = 1 - \exp\left(-\tilde{t} \right), \qquad \tilde{t} \gg 1. \tag{5.25}$$

Going back to physical dimensions we can conclude that the meniscus in capillary rise initially advances as the square root of time, but on the time scale τ_{cap} it crosses over

to approach the equilibrium height H asymptotically as an exponential saturation with the same time scale τ_{cap} as the characteristic time in the exponent. Recalling from the discussion of Eq. (5.18) that for water in a PMMA tube of radius $a = 100\ \mu$m we have $H = 4.2$ cm, the value for τ_{cap} in this case becomes

$$\tau_{\mathrm{cap}}^{\text{water-air}} = 3.4 \text{ s.} \tag{5.26}$$

This value is good news, because the whole calculation of the capillary rise time was made under the assumption that the Poiseuille flow profile was fully developed, and as we know from Eq. (4.72) this profile is established on the much smaller time scale of 2 ms. The result for the capillary rise time is thus consistent with the assumption of the calculation.

5.3.3 Capillary rise and dimensionless numbers

We end the section on capillary rise by mentioning three dimensionless numbers that often are used to characterize the phenomenon.

When some characteristic length scale a is established for a system, the Bond number Bo of the system can be introduced,

$$Bo = \frac{\text{gravitational force}}{\text{surface tension force}} = \frac{\rho g a^2}{\gamma} = \frac{a^2}{\ell_{\mathrm{cap}}^2}. \tag{5.27}$$

Note that $Bo = 1$ if the characteristic length scale equals the capillary length, $a = \ell_{\mathrm{cap}}$. Surface tension dominates over gravitation when $Bo \ll 1$ or equivalently, when the characteristic size a of the system is much smaller than the capillary length, $a \ll \ell_{\mathrm{cap}}$.

When some characteristic velocity V_0 is imposed on the system, the capillary number Ca can be introduced,

$$Ca = \frac{\text{viscous force}}{\text{surface tension force}} = \frac{\eta V_0}{\gamma}. \tag{5.28}$$

Note that $Ca = 1$ if the imposed velocity equals the intrinsic viscosity-surface velocity, $V_0 = \gamma/\eta$.

Finally, given two dimensionless numbers their ratio will also be a dimensionless number. The ratio of Ca and Bo is denoted the Stokes number N_{St}, and it can be introduced when both a length scale and a velocity scale is given,

$$N_{\mathrm{St}} = \frac{\text{viscous force}}{\text{gravitational force}} = \frac{Ca}{Bo} = \frac{\eta V_0}{\rho g a^2}. \tag{5.29}$$

5.4 Capillary pumps

If a microchannel is placed horizontally along the x axis as shown in Fig. 5.5, the gravitational force cannot balance the capillary forces, so the capillary "rise" or capillary flow will continue as long as there is a channel for the liquid to propagate in. The theory for the position $L(t)$ of the meniscus in this case is analogous to the theory of capillary rise treated in the previous section, except that gravity now drops out of the equations. The position $L(t) = 0$ is defined as the entrance of the microchannel at the input reservoir, which is is so wide that no Young–Laplace pressure drop is present there, i.e., $p(x = 0) = p_0$.
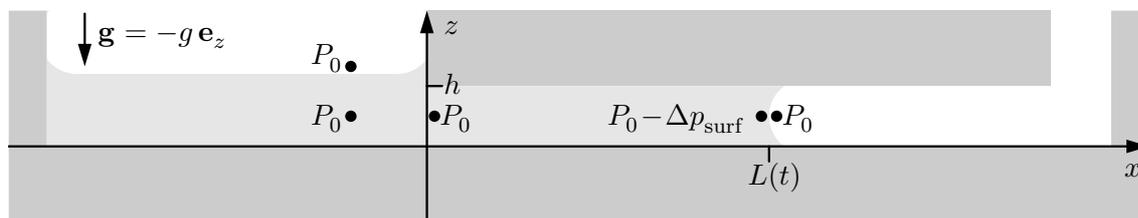
Figure 5.5: A sketch of the principle of a capillary pump (dark gray). The curved meniscus at position $L(t)$ results in an uncompensated Young–Laplace under-pressure $-\Delta p_{\text{surf}}$ that drives the liquid (light gray) to the right in the microchannel . Notice all the points where the pressure is (approximately) equal to the atmospheric pressure p_0 of the air (white).

5.4.1   Capillary pump advancement times

We are going to apply the capillary pump analysis for microfluidic channels with flat rectangular cross-sections of width w and height $h \ll w$. Hence we shall use the Hagen–Poiseuille result $Q = h^3 w \Delta p / (12\eta L)$ of Eq. (2.53). The pressure drop Δp between the entrance at $x = 0$ and the advancing meniscus at $x = L(t)$ is constant and simply given by the Young–Laplace pressure drop,

$$\Delta p = \Delta p_{\text{surf}} = \frac{2\gamma}{h} \cos\theta. \tag{5.30}$$

In analogy with Eq. (5.20) the speed $\mathrm{d}L(t)/\mathrm{d}t$ by which the front of the liquid is advancing through the microchannel is determined by mass conservation of the flow in the tube. Assuming a full developed Poiseuille flow profile at $x = 0$, we find at $x = L(t)$ that

$$\frac{\mathrm{d}L(t)}{\mathrm{d}t} = V_0 = \frac{Q}{wh} \approx \frac{h^2 \Delta p_{\text{surf}}}{12\eta} \frac{1}{L(t)}. \tag{5.31}$$

This differential equation is easily integrated by separation of $L\,\mathrm{d}L$ and $\mathrm{d}t$. Introducing the characteristic time τ_{adv} for the capillary advancement of the meniscus,

$$\tau_{\text{adv}} \equiv \frac{6\eta}{\Delta p_{\text{surf}}} = \frac{3\eta h}{\gamma \cos\theta} \quad \text{(parallel-plate channel)}, \tag{5.32}$$

the solution can be written as

$$L(t) = h \sqrt{\frac{t}{\tau_{\text{adv}}}}. \tag{5.33}$$

This result is analogous to the small-time behavior Eq. (5.24) of capillary rise.

The above analysis is easily redone for a circular channel of radius a, and as result Eq. (5.33) and τ_{adv} are slightly changed,

$$L(t) = a \sqrt{\frac{t}{\tau_{\text{adv}}}}, \quad \tau_{\text{adv}} \equiv \frac{4\eta}{\Delta p_{\text{surf}}} = \frac{2\eta a}{\gamma \cos\theta} \quad \text{(circular channel)}. \tag{5.34}$$
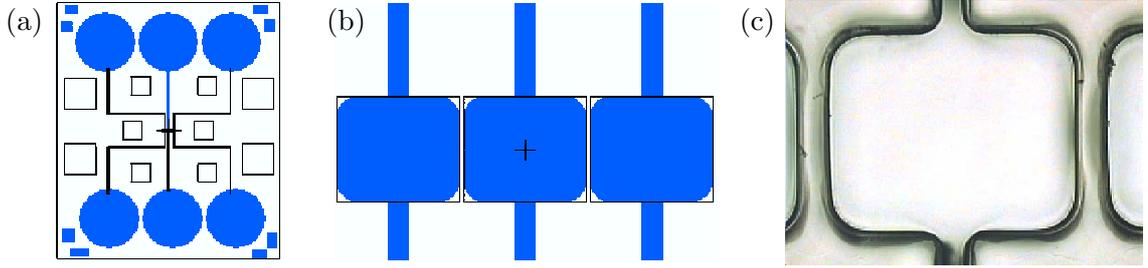
Figure 5.6: A bio-sensor with a capillary-force pump fabricated in 20 μm thick PMMA by the group of Boisen at MIC. (a) The design of the 35 mm $\times$ 30 mm chip, which contains six circular reservoirs of radius $r = 4$ mm and three channels of width $w = 200$ μm connecting them pair-wise. (b) The center of the chip where each of the three channels widens into a 1.2 mm $\times$ 1.0 mm rectangular measuring site, and where the bio-sensing is done by use of cantilevers dipped into the liquid. (c) A microscope picture of the central detection site in the actual device.

5.4.2 A bio-sensor chip with a capillary-force pump

As an example of the use of capillary pumps in lab-on-a-chip systems we shall study the bio-sensor chip developed by the group of Boisen at MIC, see Fig. 5.6.

The core of the system is the use of micrometer scale cantilevers which have been coated with specific bio-molecules. Such cantilevers can be used as a bio-sensors when they are immersed into a liquid biochemical solution. The principle of operation is simple: When biochemical reactions take place at the surface of the cantilever mechanical surface stresses are induced. The cantilever bends due to these stresses, and the bending can be detected by a piezo-resistive read-out built into the cantilever. By careful selection of the bio-coating, the cantilever can be designed to respond selectively to certain bio-molecules.

The chip is constructed by spinning a polymer layer, here PMMA of height $h = 20$ μm, onto a glass plate. By photolithography six circular reservoirs of radius $r = 4$ mm are etched into the PMMA-layer and three channels with rectangular cross-sections of width $w = 200$ μm and height $h = 20$ μm are connecting them pair-wise. The mask design of the chip is shown in Fig. 5.6(a). At the center of the chip each of the three channels widens into a 1.2 mm $\times$ 1.0 mm rectangular measuring site, see Fig. 5.6(b), where the cantilever probes are going to be dipped into the liquid. The whole chip is covered by a second glass plate to close off the microfluidic channels, but holes are provided for liquid handling at the six reservoirs and at the three measuring sites. In Fig. 5.6(c) is shown a microscope picture of one of the measuring sites. Using a simple pipette the biochemical liquid is injected into one of the large reservoirs. By capillary forces the liquid is sucked into the microchannel leading from the reservoir to the measuring site.

To apply Eqs. (5.32) and (5.33) we define the beginning of the capillary channel, $x = 0$, at the reservoir inlet reservoir. The distance from a center reservoir or a corner reservoir to the corresponding measuring site is $L_1 = 8$ mm and $L_2 = 15$ mm, respectively. Using the physical parameter values in Table 5.1 for a water-PMMA-air system we find the time

t_{arriv} it takes the liquid to arrive at the measuring sites to be

$$t_{\text{arriv}} \approx 1 \text{ s.} \tag{5.35}$$

The "power-less" capillary pump systems is thus both adequate and handy for the task of delivering liquids at specific points on the chip.

5.5 Marangoni effect; surface tension gradients

In establishing Eq. (5.9) for the matching condition for Navier–Stokes equation at the interface between two immiscible fluids, we have assumed that the surface tension is a constant. However, there are many cases where the surface tension in fact is varying in space. Especially gradients in the concentration of surfactants (such as soap) at the interface and temperature gradients implies gradients in the surface tension γ.

Just as gradients in the pressure field implies a gradient force per volume, $-\boldsymbol{\nabla} p$, so does a gradient in the surface tension imply a gradient force per area, $+\boldsymbol{\nabla}\gamma$. The difference in sign between the two gradient forces is due to the fact that pressure forces tend to maximize volume, whereas surface-tension forces tend to minimize area. The surface-tension gradient force is known as the Marangoni force,

$$\mathbf{f}_{\text{Maran}} \equiv \boldsymbol{\nabla}\gamma. \tag{5.36}$$

Adding the Marangoni force to Eq. (5.9) yields a more general matching condition,

$$-\left(p^{(1)} - p^{(2)}\right) n_i + \left(\sigma_{ik}^{(1)} - \sigma_{ik}^{(2)}\right) n_k = \left(\frac{1}{R_1} + \frac{1}{R_2}\right)\gamma^{(12)} + \partial_i \gamma^{(12)}. \tag{5.37}$$

One can get an idea of the size of temperature induced Marangoni forces by noting that the heating up a water-air interface by 5 °C from 20 °C to 25 °C will lower the surface tension by 0.8 mJ/m^2 from 72.9 mJ/m^2 to 72.1 mJ/m^2. The shorter a distance over which one can maintain this temperature gradient the stronger the Marangoni force; but in all cases only in microsystems one can hope for a sufficiently large effect compared to other forces.

The Marangoni force can be used as a micro propulsion system, as some bacteria actually do in Nature. The principle is simple: If one emits some surfactant that lowers the surface tension behind a little body then the body will be pushed forward, as the interface tries to minimize the region of high surface tension (without surfactant) while maximizing the region of low surface tension (with surfactant). One can build a little boat illustrating this principle by attaching a piece of soap at the end of a stick. As the soap dissolves the stick moves forward.

5.6 Exercises

Exercise 5.1
Surface tension interpreted as force per length
Make a sketch clarifying the geometry of the stretched-surface argument, which in Section 5.1.1 led to Eq. (5.5). Derive this equation carefully using your sketch.

Exercise 5.2
The Young–Laplace pressure in a flat channel with equal contact angles
Argue why the Young–Laplace pressure drop indeed is given by Eq. (5.30) for a liquid-gas interface inside a flat and very wide rectangular channel with the same contact angle for the top and bottom plate.

Exercise 5.3
The Young–Laplace pressure in a flat channel with different contact angles
Find the expression for the Young–Laplace pressure drop across a liquid-gas interface with surface tension γ inside a flat and very wide rectangular channel of height h, where the contact angle for the bottom and top plate are given by θ_1 and θ_2, respectively.

Exercise 5.4
Droplets on substrates with various contact angles
Consider liquid droplets on a solid substrate in air for the following three cases: water on gold, water on platinum, and mercury on glass. Use the values of the physical parameters given in Table 5.1 and make a sketch of the resulting shapes assuming small droplets $a \ll \ell_{\mathrm{cap}}$ in all three cases.

Exercise 5.5
Capillary rise for mercury
Consider mercury (Hg) as the liquid in a capillary rise experiment using a glass tube of radius $a = 100$ μm. The relevant physical parameters for Hg and glass are $\rho = 1.36 \times 10^4$ kg/m^3, $\theta = 140°$, and $\gamma = 0.487$ J/m^2.

(a) Go through the arguments leading to the expression Eq. (5.18) for the capillary rise height H. Hint: make a sketch like Fig. 5.4(b) and be careful with the sign of $\cos\theta$.

(b) Determine the value of H for the mercury-glass system.

Exercise 5.6
Alternative formula for the capillary rise height
Consider the expression Eq. (5.18) for the capillary rise height H.

(a) Use Young's equation to show the second expression for H,

$$H = \frac{2}{\rho g a} \left(\gamma_{\mathrm{sg}} - \gamma_{\mathrm{sl}} \right). \tag{5.38}$$

(b) Use the constant energy argument, $\delta\mathcal{G} = 0$, at equilibrium to prove Eq. (5.38) considering a displacement δH away from the equilibrium position H and the corresponding change $\delta\mathcal{G}_{\mathrm{grav}}$ in gravitational energy and $\delta\mathcal{G}_{\mathrm{surf}}$ in surface energy. Hint: Note that the shape of the meniscus remains unchanged during the displacement and hence does not contribute to any change in the Gibb's free energy.

Exercise 5.7
The expressions for the capillary rise time
Consider Section 5.3.2, where the dynamics of the capillary rise is treated.

(a) Derive the dimensionless differential equation Eq. (5.23c) for the position $\tilde{L}(\tilde{t})$ of the rising meniscus during capillary rise.

(b) Verify that the solutions Eqs. (5.24) and (5.25) are correct.

Exercise 5.8
Dimensionless numbers for capillary rise
Consider Section 5.3.3, where the three dimensionless numbers Bo, Ca, and N_{St} are defined.

(a) Calculate the values of these three dimensionless numbers for the same physical parameter values that led to the estimate for $\tau_{\text{cap}}^{\text{water-air}}$ in Eq. (5.26), and use $V_0 = H/\tau_{\text{cap}}$.

(b) Discuss the significance of the obtained values.

Exercise 5.9
Liquids advancing by capillary forces in horizontal microchannels
Consider Section 5.4.1, where the the capillary pump advancement times are discussed.

(a) State the assumptions leading to Eq. (5.33) for the position of the advancing meniscus in a capillary pump.

(b) Check that solution Eq. (5.33) is consistent with the assumptions.

Exercise 5.10
Capillary pump with circular cross section
In Section 5.4.1 the capillary pump with rectangular cross section is analyzed. Redo the analysis for a capillary pump with a circular cross section and prove Eq. (5.34) for the advancement time τ_{adv}.

Exercise 5.11
Advancement times in the capillary pump
Apply the results of Section 5.4 to the following problems.

(a) Calculate more precisely the arrival times $t_{\text{arriv}}^{(1)}$ and $t_{\text{arriv}}^{(2)}$ for the liquids advancing from a corner reservoir and a center reservoir, respectively, in the bio-sensor chip described in Section 5.4.2.

(b) Use Table 5.1 to predict how the advancement times would alter if the walls of the capillary pump were changed from PMMA to gold and to platinum.

(c) Discuss the consequences for the functionality of a capillary pump if $\theta = 90°$ and if $\theta > 90°$.

Exercise 5.12
The sign of the Marangoni force
Make a sketch of a surface with a varying surface tension γ. Argue why the sign in the Marangoni force, $\mathbf{f}_{\text{Maran}} \equiv +\boldsymbol{\nabla}\gamma$, is positive.

5.7 Solutions

Solution 5.1
Surface tension interpreted as force per length
During the stretch the force F acts over the distance ΔL thus performing the work $\Delta W = F\Delta L$ on the surface. Assuming that energy is not dissipated all external work is transformed into surface energy $\Delta \mathcal{G}_{\mathrm{surf}} = \gamma w \Delta L$. Thus $W = \Delta \mathcal{G}_{\mathrm{surf}}$, which implies $\gamma = F/w$.

Solution 5.2
The Young–Laplace pressure in a flat channel with equal contact angles
The curvature in the wide transverse direction of the flat channel is of the order $2/w$, so inclusion of the radii of curvature in both directions leads to a the Young–Laplace pressure of the form $\Delta p_{\mathrm{surf}} = \gamma(2/h+2/w)\cos\theta = (2\gamma/h)(1+h/w)\cos\theta \approx (2\gamma/h)\cos\theta$, for $h \gg w$.

Solution 5.3
The Young–Laplace pressure in a flat channel with different contact angles
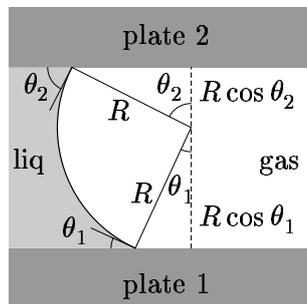
The distance between the bottom and top plate of the flat channel is denoted h. Let θ_1 and θ_2 be the contact angle at the bottom and top plate, respectively, then, as shown to the left, $h = R\cos\theta_1 + R\cos\theta_2$. Assuming that the only non-zero radius of curvature R is perpendicular to the plates, the Young–Laplace pressure is given by

$$\Delta p_{\mathrm{surf}} = \frac{\gamma}{R} = \frac{\gamma}{h}(\cos\theta_1 + \cos\theta_2) = \frac{2\gamma}{h}\frac{\cos\theta_1 + \cos\theta_2}{2}. \quad (5.39)$$

Solution 5.4
Droplets on substrates with various contact angles
For $a \ll \ell_{\mathrm{cap}}$ gravity does not matter, and all shapes are sections of spheres.
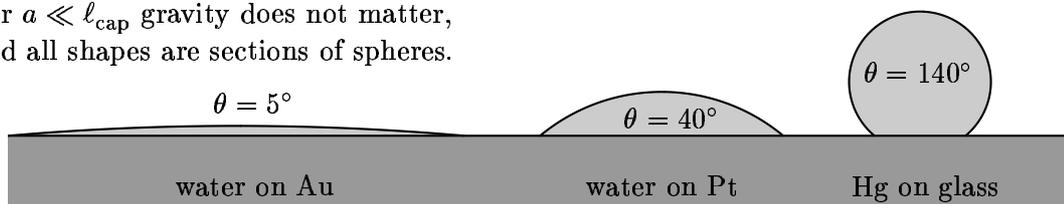
Solution 5.5
Capillary rise for mercury
For mercury $\theta = 140° > 90°$. As a consequence the liquid surface in a sketch corresponding to Fig. 5.4(b) will curve the other way, and Δp_{surf} changes sign. So the under-pressure

becomes an over-pressure leading to capillary fall instead of rise. The arguments leading to Eq. (5.18) still holds, so $H = 2\gamma\cos\theta/(\rho g a) = -55.7$ mm.

Solution 5.6
Alternative formula for the capillary rise height
The second expression for H in Eq. (5.18) clearly shows that capillary rise is due to gain in energy obtained when liquid covers an area of a solid previously covered by gas.

(a) Young's equation states that $\gamma\cos\theta = \gamma_{\mathrm{sg}} - \gamma_{\mathrm{sl}}$, hence the desired result follows by simple substitution.

(b) A vertical displacement δH changes the gravitational energy by the amount $\delta\mathcal{G}_{\mathrm{grav}} = mg\delta H = (\rho\pi a^2 H)g\delta H$, while the corresponding change in surface energy is $\delta\mathcal{G}_{\mathrm{surf}} = (\gamma_{\mathrm{sl}} - \gamma_{\mathrm{sg}})\mathcal{A} = (\gamma_{\mathrm{sl}} - \gamma_{\mathrm{sg}})2\pi a\delta H$. From $\delta\mathcal{G}_{\mathrm{grav}} + \delta\mathcal{G}_{\mathrm{surf}} = 0$ follows the desired result, $2(\gamma_{\mathrm{sl}} - \gamma_{\mathrm{sg}}) = \rho g a H$.

Solution 5.7
The expressions for the capillary rise time
Eq. (5.22) follows directly from the assumption of a fully developed quasi-stationary Poiseuille flow Eq. (5.20) driven by the constant Young–Laplace pressure minus the time-dependent hydrostatic pressure Eq. (5.21).

(a) The dimensionless form of Eq. (5.22) is obtained by multiplying the equation by $8\eta/(\rho g a^2)$ and substituting L by $H\tilde{L}$. This yields $\tau_{\mathrm{cap}}\mathrm{d}\tilde{L}/\mathrm{d}t = \tilde{L}^{-1} - 1$. Finally, substituting t by $\tau_{\mathrm{cap}}\tilde{t}$ leads to the result $\mathrm{d}\tilde{L}/\mathrm{d}\tilde{t} = \tilde{L}^{-1} - 1$, Eq. (5.23c).

(b) For $\tilde{t} \ll 1$ we have $\tilde{L} \approx \sqrt{2\tilde{t}} \ll 1$, Eq. (5.24). Hence $\mathrm{d}\tilde{L}/\mathrm{d}\tilde{t} = \sqrt{2}\frac{1}{2}/\sqrt{\tilde{t}} = 1/\sqrt{2\tilde{t}} = 1/\sqrt{\tilde{L}} \approx 1/\sqrt{\tilde{L}} - 1$.

For $\tilde{t} \gg 1$ we have $\tilde{L} \approx 1 - \exp(-\tilde{t})$ and $\exp(-\tilde{t}) \ll 1$, Eq. (5.25). Consequently, $\mathrm{d}\tilde{L}/\mathrm{d}\tilde{t} = \exp(-\tilde{t}) = [1 + \exp(-\tilde{t})] - 1 \approx 1/[1 - \exp(-\tilde{t})] - 1 = 1/\tilde{L} - 1$.

Solution 5.8
Dimensionless numbers for capillary rise
The parameters used in Eq. (5.26) are $a = 100~\mu\mathrm{m}$, $\rho = 10^3$ kg/m^3, $g = 9,81$ m/s, $\eta = 10^{-3}$ Pa s, and $\gamma = 0.073$ J/m^2. Moreover, $V_0 = H/\tau_{\mathrm{cap}} \approx 1$ cm/s.

(a) From the parameter values follow $Bo = 1.3\times10^{-3}$, $Ca = 1.4\times10^{-5}$, and $N_{\mathrm{St}} = 0.1$.

(b) Since $Bo \ll 1$ and $Ca \ll 1$ surface tension dominates over both gravity and viscosity. And since $N_{\mathrm{St}} \ll 1$ gravity dominates over viscosity.

Solution 5.9
Liquids advancing by capillary forces in horizontal microchannels
We discuss the consistency of Eq. (5.33) with the underlying assumptions.

(a) The main assumptions are (i) translation invariance along the x axis, (ii) quasi-stationary Poiseuille flow, i.e., the acceleration term $\rho\partial_t v_x$ is negligible in the Navier–Stokes eqation, and (iii) the circulation rolls in the front of the liquid string have a negligible influence on the flow. These rolls must exist to ensure a smooth transition from the Poiseuille flow parabola in the bulk of the liquid and the curved meniscus at the front moving at constant speed.

(b) Assuming that Eq. (5.33), stating $L \propto t^{1/2}$, is correct, we find $v = \partial_t L = \frac{1}{2} L/t$ and $\partial_t v = -\frac{1}{2} L/t^2 = -v/t$. Moreover, if Poiseuille flow is present in the majority of the liquid string, $\eta \partial_z^2 v = \Delta p/L = [12\eta L/(wh^3)]Q/L = (12\eta/h^2)v$. So the acceleration term can be neglected if $|\rho \partial_t v| \ll |\eta \partial_z^2 v|$, i.e., if $\rho v/t \ll (12\eta/h^2)v$ or $h^2/(12\nu) \ll t$, where ν is the kinematic viscosity. For $h = 100$ μm and $\nu = 10^{-6}$ m^2/s we find it necessary to demand that $t \gg 0.8$ ms to ensure that the solution is consistent with assumption (ii).

Since hydrodynamics do not contain an intrinsic length scale, the circulation rolls in the front of the liquid string must have the size h. Hence, they can be neglected if they are must smaller than the entire liquid string, $h \ll L$, which means $1 \ll \sqrt{t/\tau_{\text{adv}}}$ or $t \gg \tau_{\text{adv}}$. Using in Eq. (5.32) the usual parameters for water as well as $h = 100$ μm, we find $\tau_{\text{adv}} \approx 10$ μs. Thus the solution is consistent with assumption (iii) if $t \gg 10$ μs, but this is already ensured if assumption (ii) holds.

Solution 5.10
Capillary pump with circular cross section
For a circular cross section with radius a, Eq. (5.30) becomes $\Delta p_{\text{surf}} = 2\gamma \cos \theta/a$ while Eq. (5.31) changes to $dL/dt = a^2 \Delta p_{\text{surf}}/(8\eta L)$. This in turn modifies Eq. (5.32) to $\tau_{\text{adv}} = 4\eta/\Delta p_{\text{surf}} = 2\eta a/\gamma \cos \theta$ as stated in Eq. (5.34).

Solution 5.11
Advancement times in the capillary pump
The channels under consideration have $h = 20$ μm and $w = 200$ μm and thus an aspect ratio $h/w = 0.1$. The correction factor for the hydraulic resistance becomes

$$1 - 0.630\frac{h}{w} = 0.937. \tag{5.40}$$

Since this correction factor according to Eq. (2.49) appears opposite the viscosity η it is natural to define an effective viscosity η_{eff} by

$$\eta_{\text{eff}} \equiv \frac{\eta}{1 - 0.630\frac{h}{w}} = 1.067\eta. \tag{5.41}$$

The finite width of the channel implies an apparent increase in the viscosity (or in reality in the hydraulic resistance).

(a) The capillary advancement time τ_{adv} for the PMMA-water-air system can now be estimated from Eq. (5.32) as

$$\tau_{\text{adv}} = \frac{3\eta_{\text{eff}}h}{\gamma \cos \theta} \tag{5.42}$$

$$= \frac{3\left(1.067 \times 10^{-3}\right)\left(2 \times 10^{-5}\right)}{0.0729 \cos(73.7°)} \text{ s} \tag{5.43}$$

$$= 3.129 \times 10^{-6} \text{ s}. \tag{5.44}$$

From Eq. (5.33) follows

$$t = \left(\frac{L}{h}\right)^2 \tau_{\text{adv}}. \tag{5.45}$$

With $L_1 = 8$ mm and $L_2 = 15$ mm the advancement times t_1 and t_2 become

$$t_1 = 0.500 \text{ s}, \qquad t_2 = 1.760 \text{ s}. \tag{5.46}$$

(b) Changing from PMMA to platinum or gold leads to a lowering of the contact angle θ. This increases $\cos\theta$ and thus decreases $\tau_{\text{adv}} \propto 1/\cos\theta$. The pump becomes more efficient by this change in material with the gold being the best choice if fast pumping is wanted.

(c) In the limit $\theta \to 90°$ we obtain $\cos\theta \to 0$, and consequently $\tau_{\text{adv}} \to \infty$. The pump ceases to work. For $\theta > 90°$ it costs surface energy for the liquid to enter the pump, so in fact the pump will force out liquid initially present in the channels. It thus acts as a pump in the reverse direction.

Solution 5.12
The sign of the Marangoni force
Consider the sketch to the right shown in Solution 5.1, and assume that the surface tension γ varies as a function of x (the L-direction). The external force F acting at $x = L$ is shown, $F(L) = \gamma(L)w$. Similarly, an anti-parallel external force in must act at $x = 0$ given by $F(0) = -\gamma(0)w$, hence the total surface tension force acting on the area is $F_{\text{tot}} = F(L) - F(0) = [\gamma(L) - \gamma(0)]w$. Thus the surface tension force per area, the Marangoni force, becomes $f_{\text{Maran}} = F_{\text{tot}}/wL = [\gamma(L) - \gamma(0)]/L \to +\partial_x\gamma$, for $L \to 0$.

Chapter 6

Numerical simulations

In the previous chapters we have studied some analytical solutions to the Navier–Stokes equation and the convection-diffusion equation. Although these solutions are very important they are in fact also very special: only in a few and highly symmetric cases is it possible to find analytical solutions. In the vast majority of cases we are forced to perform numerical simulations to get the solutions to the complicated set of partial differential equations that appears in theoretical microfluidics.

There are many ways to find the solutions to partial differential equations numerically. Most methods rely on some sort of discretization and transformation of the continuous equations into a matrix problem, which then can be solved by one of the many existing matrix solvers. The computer code to handle the problem can be written from scratch using general purpose software like Fortran, C, MATLAB or Mathematica, or by employing a specialized software for solving partial differential equations like ANSYS, Coventer, CFDACE, or COMSOL Multiphysics.

In this course we shall use COMSOL Multiphysics to illustrate how to solve problems in microfluidics numerically. COMSOL is designed to solve a wide range of partial differential equations comprising most of the equations appearing in physics and chemistry such as the Navier–Stokes equation, the Poisson equation, the Schrödinger equation, the convection-diffusion equation, the Maxwell equations, and problems combining these equations. COMSOL allows the unexperienced user to quickly get started and solve fairly complex microfluidics problems, while it remains a powerful tool for the experienced user.

The basic numerical method used in COMSOL is the so-called finite element method (FEM). While this method perhaps is not the first choice for fluidic problems exhibiting turbulence, it is very good for the low Reynolds number problems encountered in microfluidics. In the following we shall take a brief look at the idea of FEM, and then move on to a short introduction to COMSOL including some examples. Once started on COMSOL the user can with the help of the on-line user guides and user manuals launch into a self-study and progress on his own.

A good account of the theory of FEM is the M.Sc.-thesis *Computational fluid dynamics in microfluidic systems* by Laurits Højgaard Olesen (July, 2003) available at the web-page www.mic.dtu.dk/research/MIFTS of the group of Bruus at MIC.
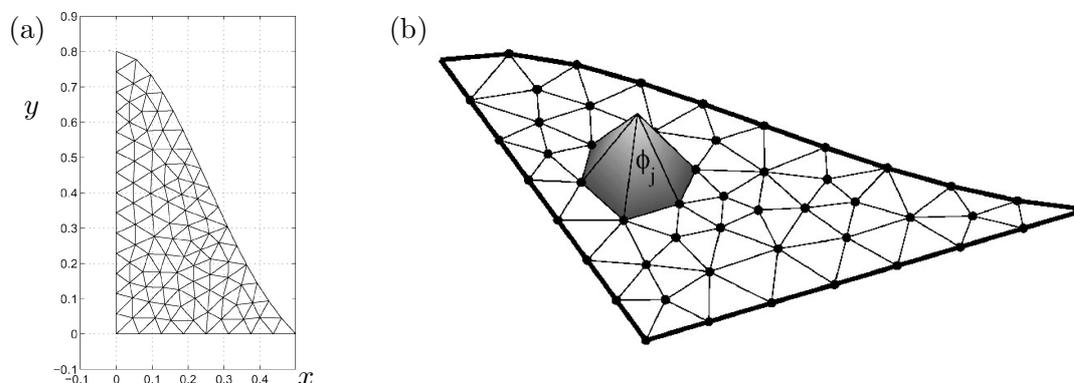
Figure 6.1: (a) The FEM mesh for half of the cross-section of the Gaussian-shaped microfluidic channel of Fig. 2.4(b). (b) The corresponding FEM domain showing one of the linearly interpolating basis function ϕ_j.

6.1   The finite element method (FEM)

Consider a vector field $\mathbf{v}(\mathbf{r}, t)$ for which we want to solve a partial differential equation in some domain Ω,

$$\mathcal{D}\mathbf{v}(\mathbf{r}, t) = \mathbf{f}(\mathbf{r}, t), \quad \text{for } \mathbf{r} \in \Omega, \tag{6.1}$$

where $\mathcal{D}$ is some differential operator and where $\mathbf{f}(\mathbf{r}, t)$ is the source or forcing term. The solution must typically respect some boundary conditions of the Dirichlet or the Neumann type (or a combination of the two),

$$v_i(\mathbf{r}, t) = a(\mathbf{r}), \quad \text{for } \mathbf{r} \in \partial\Omega, \quad \text{(Diriclet boundary condition)}, \tag{6.2a}$$

$$(\mathbf{n} \cdot \boldsymbol{\nabla}) v_i(\mathbf{r}, t) = b(\mathbf{r}), \quad \text{for } \mathbf{r} \in \partial\Omega, \quad \text{(Neumann boundary condition)}, \tag{6.2b}$$

where $\mathbf{n}$ as usual is the outward-pointing normal vector of the surface. Solutions to the problem in the form of Eqs. (6.1) and (6.2) are called strong solutions.

6.1.1   Discretization using finite elements

Normally, it is not possible to obtain strong solutions for the problem at hand. Instead one usually discretize the otherwise continuous problem and obtain so-called weak solutions; weak in the sense of approximate.

A typical discretization of a 2D computational domain Ω is shown in Fig. 6.1(a) in the form of a mesh containing a finite number of finite-sized triangular elements. These elements are the origin of the name FEM. Each element in the 2D mesh consists of a number of straight edges, and a number of corners denoted nodes.

It is now possible to introduce a finite set of N basis functions ϕ_j. As sketched in Fig. 6.1(b) the jth basis function is only non-zero in the neighboring elements containing the jth node $\mathbf{r}_j$. At $\mathbf{r}_j$ itself the basis function becomes unity, $\phi_j(\mathbf{r}_j) \equiv 1$, while it decays
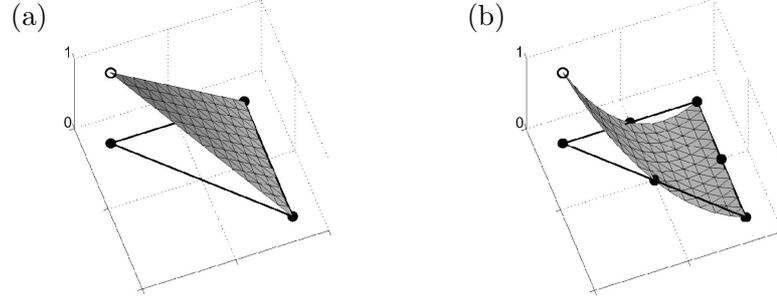
Figure 6.2: (a) A basis function corresponding to linear interpolation within an element. (b) A basis function corresponding to quadratic interpolation within an element.

continuously to zero on the edges connecting the neighboring nodes. Using these basis functions the solutions to the differential equation is sought on the following discrete form

$$v_i(\mathbf{r}) \approx \sum_{j=1}^{N} v_j^{(i)} \, \phi_j(\mathbf{r}), \tag{6.3}$$

where the coefficients $v_j^{(i)}$ are to be determined.

There are many choices for the specific form of the basis functions ϕ_j. Two commonly used forms are the linear and the quadratic interpolating functions shown in Fig. 6.2.

6.1.2 Weak solutions

In the theory of partial differential equations it has been shown that there are no conditions that ensures the existence of a unique solution to the problem Eqs. (6.1) and (6.2). However, such a existence and uniqueness theorem does in fact exist for the so-called weak solution to the problem. A weak solution is defined in the following by the introduction of the inner product in function space.

Consider the set $\mathcal{F}_\Omega$ of "well-behaved", real functions on Ω. The inner product $\langle u, v \rangle$ for any pair of functions $u, v \in \mathcal{F}_\Omega$ is defined by

$$\langle u, v \rangle \equiv \int_\Omega \mathrm{d}\mathbf{r} \, u(\mathbf{r}) v(\mathbf{r}). \tag{6.4}$$

If we let $\mathbf{v}$ be a strong solution to Eq. (6.1), then $\mathcal{D}\mathbf{v} - \mathbf{f} = 0$. It is therefore natural to define the defect $d(\mathbf{w})$ for any function $\mathbf{w}$ as

$$d(\mathbf{w}) \equiv \mathcal{D}\mathbf{w} - \mathbf{f}. \tag{6.5}$$

A weak solution $\mathbf{w}$ to Eq. (6.1) is defined as a function with a defect $d(\mathbf{w})$ that has a vanishing inner product with any function v within the function space $\mathcal{F}_\Omega$,

$$\langle v_i, [d(\mathbf{w})]_i \rangle \equiv 0, \quad \text{for all } v_i \in \mathcal{F}_\Omega. \tag{6.6}$$

Clearly, a strong solution is also a weak solution, but the converse is not necessarily true.

The introduction of weak solutions relaxes the constraints that we must put on the functions belonging to $\mathcal{F}_\Omega$. The differential operators $\mathcal{D}$ in all of the partial differential equations we shall work with contain only up to second order derivatives. For strong solutions this implies that the functions should have at least continuous first derivatives to avoid infinite second derivatives. However, for weak solutions it suffices to deal with continuous functions which are only piecewise differentiable. This can be seen by partial integration of the inner product of a function v with the term $\nabla^2 w$ contained in $\mathcal{D}w$ of Eq. (6.5) as follows,

$$\int_\Omega \mathrm{d}\mathbf{r}\, v\nabla^2 w = \int_{\partial\Omega} \mathrm{d}a\, v(\mathbf{n}\cdot\boldsymbol{\nabla})w - \int_\Omega \mathrm{d}\mathbf{r}\, (\boldsymbol{\nabla}v)\cdot(\boldsymbol{\nabla}w). \tag{6.7}$$

The surface integral is handled by invoking the boundary conditions Eq. (6.2) while the volume integral is well-defined as long as v and w are just piecewise differentiable.

6.1.3   The Galerkin method

In the Galerkin method a weak solution $w_i(\mathbf{r}) = \sum_{j=1}^N w_j^{(i)}\, \phi_j(\mathbf{r})$ written in terms of the basis functions is obtained by demanding that its defect $d(w_i)$ has a zero inner product with all basis functions,

$$\langle \phi_k,\, \mathcal{D}w_i - f_i \rangle = 0, \quad k = 1, 2, \ldots, N. \tag{6.8}$$

This condition can be written as a finite matrix equation,

$$\sum_{j=1}^N \langle \phi_k,\, \mathcal{D}\phi_j \rangle\, w_j^{(i)} = \langle \phi_k,\, f_i \rangle. \tag{6.9}$$

The matrix problem of the Galerkin method is not simple to tackle numerically. To obtain an accurate solution it is often necessary to employ a fine mesh containing many elements. The $N \times N$ matrix of Eq. (6.9) thus becomes very large. However, since each basis function is non-zero in only one element, the matrix is sparse. This sparsity is utilized fully when implementing good computer codes for the finite element method. The sparsity leads to a significant reduction in memory requirements since only the non-zero matrix elements need to be stored together with an index of where they are stored. Moreover, the sparsity implies a huge reduction in the number of arithmetic operations needed to solve the problem. For a full matrix problem this number is proportional to N^3 for standard Gauss elimination, but by using direct banded matrix schemes, or iterative methods like conjugate gradient methods or multi-grid methods, it can be reduced to becoming proportional to N^2 or even N.

6.1.4   The Navier–Stokes equation in FEM

Using the Galerkin finite element method the Navier–Stokes equation

$$\rho\Big[\partial_t \mathbf{v} + (\mathbf{v}\cdot\boldsymbol{\nabla})\mathbf{v}\Big] = -\boldsymbol{\nabla}p + \eta\nabla^2\mathbf{v} + \mathbf{f} \tag{6.10}$$

is rewritten in the spirit of Eq. (6.9) as

$$\rho\Big[\langle\phi_j,\partial_t\mathbf{v}\rangle + \langle\phi_j,(\mathbf{v}\cdot\boldsymbol{\nabla})\mathbf{v}\rangle\Big] + \eta\langle\boldsymbol{\nabla}\phi_j,\boldsymbol{\nabla}\mathbf{v}\rangle - \langle\boldsymbol{\nabla}\phi_j,p\rangle = \langle\boldsymbol{\nabla}\phi_j,\mathbf{f}\rangle - \int_{\partial\Omega}\mathrm{d}a\Big[\mathbf{n}p - \eta(\mathbf{n}\cdot\boldsymbol{\nabla})\mathbf{v}\Big]. \tag{6.11}$$

Here partial integrations have been performed to get rid of the Laplace operator ∇^2 and the pressure gradient $\boldsymbol{\nabla}p$. The Navier–Stokes equation is as usual supplemented by the continuity equation $\boldsymbol{\nabla}\cdot\mathbf{v} = 0$ for incompressible fluids,

$$\langle\phi_j,\boldsymbol{\nabla}\cdot\mathbf{v}\rangle = 0. \tag{6.12}$$

When expanding the velocity components v_x and v_y as well as the pressure p in terms of the basis functions ϕ_j we obtain the following system of matrix equations

$$\rho\big[\mathbf{M}\dot{\mathbf{v}}_x + \mathbf{C}\mathbf{v}_x\big] + \eta\mathbf{K}\mathbf{v}_x - \mathbf{Q}_x^T\mathbf{p} = \mathbf{f}_x, \tag{6.13a}$$

$$\rho\big[\mathbf{M}\dot{\mathbf{v}}_y + \mathbf{C}\mathbf{v}_y\big] + \eta\mathbf{K}\mathbf{v}_y - \mathbf{Q}_y^T\mathbf{p} = \mathbf{f}_y, \tag{6.13b}$$

$$\mathbf{Q}_x\mathbf{v}_x + \mathbf{Q}_y\mathbf{v}_y = \mathbf{0}, \tag{6.13c}$$

where the column vectors $\mathbf{v}_x$, $\mathbf{v}_y$, and $\mathbf{p}$ contain the expansion coefficients for the velocity and pressure fields. The other matrices appearing are the mass matrix

$$\mathbf{M}_{jk} = \langle\phi_j,\phi_k\rangle, \tag{6.14}$$

the stiffness matrix

$$\mathbf{K}_{jk} = \langle\boldsymbol{\nabla}\phi_j,\boldsymbol{\nabla}\phi_k\rangle, \tag{6.15}$$

the convection matrix

$$\mathbf{C}_{jk} = \Big\langle\phi_j,\Big[\sum_m\phi_m v_x^{(m)}\Big]\partial_x\phi_k + \Big[\sum_m\phi_m v_y^{(m)}\Big]\partial_y\phi_k\Big\rangle, \tag{6.16}$$

and the divergence matrices

$$\mathbf{Q}_{x,jk} = \langle\phi_j,\partial_x\phi_k\rangle, \tag{6.17a}$$

$$\mathbf{Q}_{y,jk} = \langle\phi_j,\partial_y\phi_k\rangle. \tag{6.17b}$$

Finally, the force vectors $\mathbf{f}_x$ and $\mathbf{f}_y$ on the right-hand side include both the body force and the boundary integral from the partial integrations,

$$\mathbf{f}_{x,j} = \langle\phi_j,f_x\rangle - \int_{\partial\Omega}\mathrm{d}a\,\phi_k\big[n_x p - \eta(\mathbf{n}\cdot\boldsymbol{\nabla})v_x\big], \tag{6.18a}$$

$$\mathbf{f}_{y,j} = \langle\phi_j,f_y\rangle - \int_{\partial\Omega}\mathrm{d}a\,\phi_k\big[n_y p - \eta(\mathbf{n}\cdot\boldsymbol{\nabla})v_y\big]. \tag{6.18b}$$

With this we end the very brief and superficial treatment of the general theory and move on to discuss the use of the software package COMSOL in solving microfluidic problems.

6.2   A short introduction to COMSOL

COMSOL can be considered as a high-level computer-language implementation of the finite element method for solving general partial differential equations. COMSOL can be run as a stand-alone platform or together with MATLAB. It can be run in two basic modes of operation: either through the graphical user interface (GUI) or by running scripts. The former is easier for the beginner or for simple or single tasks, whereas the latter is more powerful and can be used to solve more complicated problems.

COMSOL contains a large number of convenient, predefined subroutines and tools, but at the same time it allows the user to write his own subroutines.

6.2.1   The structure of problem-solving in COMSOL

The typical steps used when solving a problem using COMSOL are: (1) definition of the geometry or domain of the problem, (2) definition of the partial differential equation and boundary conditions to be solved, (3) meshing of the domain, (4) solution of the problem, and (5) post-processing of the results to generate various graphs. For further help on running COMSOL the built-in COMSOL manuals and users guide can be found by clicking

$$\text{"Start"} \rightarrow \text{"Programs"} \rightarrow \text{COMSOL 3.2} \rightarrow \text{"Documentation"} \rightarrow \text{"COMSOL"}. \quad (6.19)$$

This results in the appearance of a list with seven pdf-files. One of these is the "Quick Start" for beginners.

6.2.2   Solving a problem using the COMSOL graphical user interface

In the following is given one simple example for solving a flow problem with COMSOL using the graphical user interface, namely the Poiseuille flow in the parallel infinite-plate channel.

Naturally, we begin by launching COMSOL. We choose the option to run it together with MATLAB as follows:

$$\text{Start} \rightarrow \text{Programs} \rightarrow \text{COMSOL 3.2} \rightarrow \text{COMSOL with MATLAB.} \quad (6.20)$$

Wait a little while for the "Model Navigator" window to appear. When it appears it is set to run a 2D problem. Do not change this, but continue by clicking the following sequence:

$$\text{Fluid Dynamics} \rightarrow \text{Incompressible Navier–Stokes} \rightarrow \text{Steady-state analysis.} \quad (6.21)$$

After entering the last item click "OK", which results in the opening of the geometry window. Choose the "rectangle"-bottom in the top-left corner of the menu that appeared to the left. Make a long rectangle by click-and-drag inside the geometry window.

Having established a rectangular domain move on to define the differential equation by clicking on "Physics" on the top menu-bar followed by "Subdomain settings". Choose subdomain 1 (there is only one). Fill in the desired values for ρ, η, and the components of
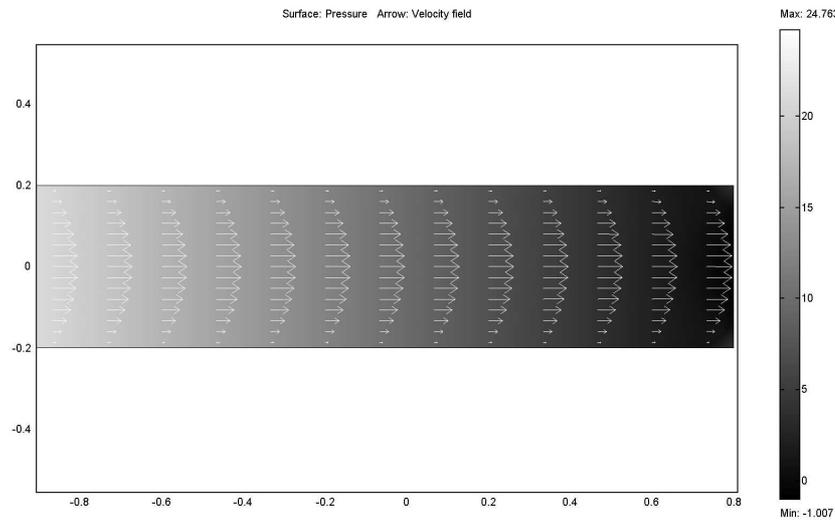
Figure 6.3: The output from COMSOL on the simple Poiseuille flow problem studied in Section 6.2.

the body-force. Click "OK". Since we have already chosen to work with the Navier–Stokes equation it suffices just to define these parameters.

To define some proper boundary conditions click "Physics" followed by "Boundary settings". Select boundary 1 followed by "Boundary condition: Inflow/Outflow velocity". Enter the parabolic velocity profile of the inlet in the form "$s*(1-s)$" in the x component (here denoted u_0. Notice that s going from zero to unity is always used as the natural parameter of the curve that has been selected. Finish the boundary settings by choosing boundary 4 to have the boundary condition Outflow/Pressure. Choose the predefined value $p_0 = 0$. Boundary 2 and 3 need not be set since the are already assigned the default no-slip boundary condition.

Continue along the top menu-bar and press "Mesh" just next to "Physics". Select first "Initialize Mesh" followed by "Refine Mesh". This will generate a mesh with sufficient resolution for the problem at hand.

Finally, click on "Solve" just to the right of "Physics" on the top menu-bar. After a few seconds a beautifully colored plot appears showing the velocity component v_x.

To change the plot click on "Postprocessing" $\rightarrow$ "surface". Select "Predefined quantities" to be pressure. Then click on "Arrow" and once the arrow-window appears mark the field "Arrow plot" in the top left corner. Choose the arrows to mark the velocity field. Click "OK" and obtain the plot shown in Fig. 6.3.

6.3 Some COMSOL scripts for microfluidics

We end this section by giving two explicit COMSOL scripts, one for computation of the flow in the backstep geometry of Fig. 3.6 and the other for the shape-perturbed Poiseuille flow of Section 2.5.

To launch the scripts the ascii files containing the scripts must be available on the computer. Go to the MATLAB window that was opened together with COMSOL and click

$$\text{File} \rightarrow \text{Run Script} \ldots \rightarrow \text{Browse.} \tag{6.22}$$

In the browse-window the relevant script-file is located and activated.

6.3.1   Incompressible flow in a backstep geometry

```
% INCOMPRESSIBLE FLOW IN A BACKSTEP GEOMETRY AS IN FIG. 3.5
% Laurits H. Olesen (2004 06 03)

clear fem

% GEOMETRY
fem.geom = rect2(0,10,0,2) - rect2(0,3,0,1);
fem.mesh = meshinit(fem);

% SPACE DIMENSION
fem.sdim = {'x' 'y'};

% DEPENDENT VARIABLES
fem.dim = {'u' 'v' 'p'};
fem.shape = [2 2 1];

% PHYSCICAL CONSTANTS
fem.const.rho = 1;   % Density
fem.const.eta = 1;   % Viscosity
fem.const.u0 = 1;    % Velocity

% DEFINING THE STRESS TENSOR BY EXPRESSIONS
fem.expr = {'sigmaxx' '-p+2*eta*ux' ...
            'sigmaxy' 'eta*(uy+vx)' ...
            'sigmayy' '-p+2*eta*vy'};

% GOVERNING EQUATIONS
fem.form = 'general';
fem.equ.da = {{{'-rho'} {'-rho'} {'0'}}};
fem.equ.ga = {{{'sigmaxx' 'sigmaxy'} {'sigmaxy' 'sigmayy'} {'0' '0'}}};
fem.equ.f = {{{'rho*(u*ux+v*uy)'} {'rho*(u*vx+v*vy)'} {'ux+vy'}}};

% GROUP THE BOUNDARY INTO THREE GROUPS
fem.bnd.ind = {[2:5] [1] [6]};
```

```
% BOUNDARY CONDITIONS
fem.bnd.r = {{{'u'} {'v'} {'0'}} ...                 % walls
            {{'u-u0*4*s*(1-s)'} {'v'} {'0'}} ... % inlet
            {{'0'} {'v'} {'0'}}};                 % outlet
% PERFORM SYMBOLIC DIFFERENTIATION OF fem.equ AND fem.bnd FIELDS
fem = femdiff(fem);

% CREATE EXTENDED MESH STRUCTURE
fem.xmesh = meshextend(fem);

% SOLVE FOR STEADY STATE FLOW
fem.sol = femnlin(fem,'report','on');

% PLOT SOLUTION
postplot(fem,'tridata','p','arrowdata',{'u' 'v'},'axisequal','on')
```

6.3.2 Multipolar deformations and Poiseuille flows

```
% THE MULTIPOLAR-DEFORMED POISEUILLE FLOW OF SEC. 2.5
% Henrik Bruus (2004 07 28)

% INITIALIZATION
clear all;
close all;
name = 'ShapePert.dat';                       % Name of output file
[fil,OpenMessage] = fopen(name,'wat');        % Open output file
disp(['Open file message: ',OpenMessage]);  % Print status of output file
fprintf(fil,'%s\n','a  R_hyd  Area  Perim');% Headline in output file

% ACQUIRE THE NUMBER OF PLOTS FROM THE USER
n = input('How many plots? ');
switch (n)
    case {1,2,3}              % arranging the plots in rows and columns
        spR = 1; spC = n;
    case {4,5,6}
        spR = 2; spC = 3;
    case {7,8,9}
        spR = 3; spC = 3;
    otherwise
        spR = 3; spC = 4;
end;
```

```matlab
% THE MAIN LOOP
for i = 1:n,
disp(['i = ' num2str(i)]);  % Print a counter
if (i==1)
    fig1 = figure;          % Prepare the first figure and call it fig1
end;

% GEOMETRY
a = 0.02*(i-1);      % perturbation parameter
t = 0:pi/50:2*pi;    % a vector holding all angles theta
k = 3;               % the order of the multipolar deformation
p = [(1+a*sin(k*t)).*cos(t); (1+a*sin(k*t)).*sin(t)];
                     % the perimeter

% PRINT A FIGURE WITH THE GEOMETRY OF THE POISEUILLE FLOW CROSS-SECTION
figure(fig1);
subplot(spR,spC,i);

% LET THE BOUNDARY C BE GIVEN BY THE PERIMETER P DEFINED ABOVE
c = geomspline(p,'splinemethod','uniform','closed','on');
geomplot(c,'pointmode','off');  % plot the geometry
axis equal;
title(['a = ' sprintf('%4.2f',a)]);
shg;        % show the graphics
drawnow;    % draw the graphics now

% SETTING UP THE COMSOL CALCULATION
clear fem;              % clear the fem-structure
fem.geom = solid2(c);   % the domain is the area with the boundary c

% SETTING THE EQUATIONS AND BOUNDARY CONDITIONS
fem.dim = 'u';   % call the variable for u
fem.equ.f = 1;   % Set up a normalized Poiseuille problem
fem.equ.c = 1;
fem.bnd.h = 1;

% LAGRANGE ELEMENTS AND MESH
fem.shape = 2;
fem.mesh = meshinit(fem);
fem.xmesh = meshextend(fem);
```

```
% PREPARE THE PLOTS OF THE SOLUTION
if (i==1)
    fig2 = figure;
end;
figure(fig2);
subplot(spR,spC,i);
% Solve the Poiseulle flow problem
fem.sol = femlin(fem);

% PLOT THE SOLUTION
postplot(fem,'tridata', 'u', 'axis', [-1.2 1.2 -1.2 1.2]);
title(['a = ' sprintf('%4.2f',a)]);
axis equal;
shg;
drawnow;

% CALCULATE FLOW RATE, HYDRAULIC RESISTANCE, AREA AND PERIMETER
Q = postint(fem,'u','edim',2);  % Flow rate
R = 1/Q;                         % Hydraulic resistance
A = postint(fem,'1','edim',2);  % Area
L = postint(fem,'1','edim',1);  % Perimeter
% Write the result in the output file
fprintf(fil,'%4.2f % 7.4f % 7.4f % 7.4f\n',[a,R/(8/pi),A/pi,L/(2*pi)]);

end;  % End for-loop-i

fclose(fil);                     % close the output file
disp('End of calculation');  % print final message
```

6.4 Exercises

Exercise 6.1
Hydraulic resistance for straight channels with different cross sectional shapes
Solve Eq. (2.18a) numerically by aid of COMSOL and verify the analytical results in
Table 3.1. Take advantage of the graphical user interface in COMSOL and the Poisson
equation module, located in the model navigator among the classical PDE modes.

Exercise 6.2
The influence of the boundary form
From the previous exercise it is clear that the velocity field approaches zero at the boundary
of the channel, Eq. (2.18b), but what is the asymptotic form and what is the influence of

the boundary form? Contrast your observations with the velocity field for the equilateral triangle which can be obtained analytically, see Section 2.4.4.

Exercise 6.3
Two hydraulic resistors connected in series

The aim is to reproduce Fig. 3.6 for different Reynolds numbers, see Eq. (3.44). You should take advantage of the graphical user interface in COMSOL and the 2D Navier–Stokes module for steady-state analysis. For the fluid properties you can for simplicity use $\rho = 1$ and $\eta = 1$. For the height h_1 and length L_1 of R_1 it is convenient to use $h_1 = 1$ and $L_1 = 4$ and, e.g., $h_2 = 2$ and $L_2 = 8$ for R_2. Furthermore, consider a parabolic velocity profile at the inflow which is conveniently specified by $v_x = V_0 4s(1-s)$ and $v_y = 0$ where $s \in [0; 1]$ on the inflow boundary. Choose "normal flow/pressure" for the out-flow boundary ($p_0 = 0$ for convenience) and no-slip boundary elsewhere. By changing the maximal velocity V_0 you vary the Reynolds number, see Eq. (3.44).

Exercise 6.4
The Hagen–Poiseuille law

Use the geometry from the previous exercise to examine the break-down of the Hagen–Poiseuille law when the Reynolds number is increased, i.e., compare the true pressure drop Δp to the Hagen–Poiseuille law $\Delta p = (R_1 + R_2)Q$. Hint: use

$$Q = w \int_0^{h_1} \mathrm{d}y \, v_x = wV_0 h_1 \int_0^1 \mathrm{d}s \, 4s(1-s) = \frac{2}{3} wh_1 V_0, \qquad (6.23)$$

$R_1 = 12\eta L_1/(h_1^3 w)$ and $R_2 = 12\eta L_2/(h_2^3 w)$, see Table 3.1, to show that

$$\Delta p = 8\eta \left(\frac{L_1}{h_1^3} + \frac{L_2}{h_2^3} \right) h_1 V_0. \qquad (6.24)$$

Exercise 6.5
The hydraulic resistance of a rectangular bend

Create a microchannel with a rectangular (90°) bend, a so-called L-shaped channel. In analogy with Exercise 6.3 and Exercise 6.4 study the hydraulic resistance of this channel and compare with the predictions of equivalent circuit theory.

Exercise 6.6
The hydraulic resistance of non-trivial geometries

Create microchannels with non-trivial geometries of your own choice, but keep the concept "microfluidcs" in mind. Consider pure water as the liquid. Study the hydraulic resistance as a function of velocity or Reynolds number, and observe the onset of non-linearities (deviations from the Hagen–Poiseuille law). Is the inertial term in the Navier–Stokes equation important in microfluidics?

Exercise 6.7
Diffusion in 1D

Consider a 1D tank of length L into which N_0 particles are injected at one end, $x = 0$, at time $t = 0$. Use the 1D diffusion model (transient analysis) in the COMSOL model navigator to solve numerically the diffusion equation

$$\partial_t c(x,t) = D\,\partial_x^2 c(x,t), \quad \text{for } 0 < x < L. \tag{6.25}$$

The initial condition should mimic $c(x, t\!=\!0) \approx N_0\delta(x)$. What is the characteristic time T_0 it takes to form a spatially uniform concentration $c(x, t = T_0) \simeq N_0/L$? How does it compare to the result obtained by dimensional analysis of the diffusion equation?

Exercise 6.8
Diffusion of a drop of ink in a circular 2D tank

Consider a circular tank of radius R in 2D. A tiny drop of ink with radius $a \ll R$ is injected at the center at time $t = 0$. Use the 2D diffusion model (transient analysis) in the COMSOL model navigator to solve numerically the diffusion equation

$$\partial_t c(\mathbf{r},t) = D\,\nabla^2 c(\mathbf{r},t), \quad \text{for } 0 < r < R. \tag{6.26}$$

The initial condition should mimic $c(\mathbf{r}, t\!=\!0) \approx N_0\delta(\mathbf{r})$. What is the characteristic time T_0 it takes to form a spatially uniform concentration $c(\mathbf{r}, t = T_0) \simeq N_0/(\pi R^2)$? How does it compare to the result obtained by dimensional analysis of the diffusion equation?

Exercise 6.9
Diffusion of a drop of ink in an arbitrarily shaped 2D tank

Repeat Exercise 6.8 but choose an arbitrary shape for the 2D tank. Furthermore, choose any position $\mathbf{r}_0$ for the initial ink drop, $c(\mathbf{r}, t\!=\!0) \approx N_0\delta(\mathbf{r} - \mathbf{r}_0)$. Try first to estimate the characteristic time-scale T_0 for reaching a spatially uniform concentration, and then compare this with numerics. Consider a general way to estimate T_0 for an arbitrary geometry Ω with a boundary $\partial\Omega$.

6.5 Solutions

Solution 6.1
To be added

In the next edition solutions to the exercises will be added.

Chapter 7

Electrohydrodynamics

In many lab-on-a-chip applications the motion of the liquids or the solutes are controlled electrically. Therefore it is highly relevant to study electrohydrodynamics, i.e., the coupling of electromagnetism and hydrodynamics. Using this wide definition, electrohydrodynamics comprises a wide range of phenomena such as the electrical properties of liquids *per se*, electrochemistry, and electrokinetics.

One obvious way to couple electromagnetism to hydrodynamics is through the body force $\rho_{el}\mathbf{E}$ in the Navier–Stokes equation, as we have seen in Eq. (1.49),

$$\rho\Big(\partial_t \mathbf{v} + (\mathbf{v}\cdot\boldsymbol{\nabla})\mathbf{v}\Big) = -\boldsymbol{\nabla}p + \eta\nabla^2\mathbf{v} + \rho\,\mathbf{g} + \rho_{el}\mathbf{E}, \tag{7.1}$$

for a liquid with a non-zero charge density ρ_{el} in an external electric field $\mathbf{E}$.

We shall only deal with electromagnetic phenomena in the electro-static regime, i.e., we are disregarding any magnetic and radiative effects. In accordance with the continuum hypothesis of Section 1.1.2 the governing equations are the Maxwell equations for continuous media, where the electric field $\mathbf{E}$, the displacement field $\mathbf{D}$, the polarization field $\mathbf{P}$, the electrical current density $\mathbf{J}_{el}$, and the electrical potential ϕ all have been averaged locally over their microscopic counterparts. The fundamental equations are:

$$\boldsymbol{\nabla}\times\mathbf{E} = \mathbf{0}, \tag{7.2a}$$

$$\boldsymbol{\nabla}\cdot\mathbf{D} = \boldsymbol{\nabla}\cdot(\epsilon\mathbf{E}) = \rho_{el}, \tag{7.2b}$$

$$\mathbf{D} = \epsilon_0\mathbf{E} + \mathbf{P} = \epsilon\mathbf{E}, \tag{7.2c}$$

$$\mathbf{J}_{el} = \sigma_{el}\mathbf{E}. \tag{7.2d}$$

Due to Eq. (7.2a) the $\mathbf{E}$-field can be written as (minus) the gradient of a potential ϕ. If ϵ is constant this gradient leads to the Poisson equation when inserted into Eq. (7.2b),

$$\mathbf{E} = -\boldsymbol{\nabla}\phi, \tag{7.3a}$$

$$\nabla^2\phi(\mathbf{r}) = -\frac{1}{\epsilon}\,\rho_{el}(\mathbf{r}). \tag{7.3b}$$

These equations will be used in the following analysis of electrohydrodynamic phenomena in microfluidics.

7.1   Polarization and dipole moments

Polarization effects play an important role in microfluidics, so it seems appropriate to review the basic theory of polarization. Consider a little particle, i.e., a biological cell or a small part of some liquid, having the electric charge density ρ_{el} which occupies the region Ω in space centered around the point $\mathbf{r}_0$. General positions inside the particle are denoted $\mathbf{r}_0 + \mathbf{r}$. If an external electrical field $\mathbf{E}$ is imposed on the system the ith component F_i of electrical force $\mathbf{F}_{\mathrm{el}}$ acting on the particle is given by

$$F_i = \int_\Omega \mathrm{d}\mathbf{r}\, \rho_{\mathrm{el}}(\mathbf{r}_0+\mathbf{r}) E_i(\mathbf{r}_0+\mathbf{r}) \approx \int_\Omega \mathrm{d}\mathbf{r}\, \rho_{\mathrm{el}}(\mathbf{r}_0+\mathbf{r}) \Big[E_i(\mathbf{r}_0) + r_j \partial_j E_i(\mathbf{r}_0) \Big] = Q E_i(\mathbf{r}_0) + p_j \partial_j E_i(\mathbf{r}_0),$$

(7.4)

where we have introduced the charge Q and electric dipole moment $\mathbf{p}$ of the particle as

$$Q \equiv \int_\Omega \mathrm{d}\mathbf{r}\, \rho_{\mathrm{el}}(\mathbf{r}_0 + \mathbf{r}), \tag{7.5a}$$

$$\mathbf{p} \equiv \int_\Omega \mathrm{d}\mathbf{r}\, \rho_{\mathrm{el}}(\mathbf{r}_0 + \mathbf{r})\, \mathbf{r}. \tag{7.5b}$$

As expected there is an electrical force when the charge Q of the region Ω is non-zero, but note that a force is also present even when $Q = 0$ if both the dipole moment $\mathbf{p}$ and the electric field gradient tensor $\boldsymbol{\nabla}\mathbf{E}$ are non-zero. The forces in the latter case are denoted dielectric forces, and they will play the central role when in a later chapter we are discussing dielectrophoresis.

A particularly simple example of a dipole moment is the two-point-charge dipole, or in short the point dipole, sketched in Fig. 7.1(a). It is defined by the charge distribution

$$\rho_{\mathrm{el}}(\mathbf{r}_0 + \mathbf{r}) = +q\,\delta\big(+\tfrac{1}{2}\mathbf{d} - \mathbf{r} \big) - q\,\delta\big(-\tfrac{1}{2}\mathbf{d} - \mathbf{r} \big), \tag{7.6}$$

which, when inserted into Eq. (7.5b), results in the dipole moment

$$\mathbf{p} = q\mathbf{d}. \tag{7.7}$$

The polarization vector $\mathbf{P}(\mathbf{r}_0)$ appearing in Eq. (7.2c) is defined as the dipole moment density in a small region Ω^* surrounding $\mathbf{r}_0$ as the volume $\mathrm{Vol}(\Omega^*)$ is taken to zero,

$$\mathbf{P}(\mathbf{r}_0) = \lim_{\mathrm{Vol}(\Omega^*)\to 0} \left[\frac{1}{\mathrm{Vol}(\Omega^*)} \int_{\Omega^*} \mathrm{d}\mathbf{r}\, \rho_{\mathrm{el}}(\mathbf{r}_0 + \mathbf{r})\, \mathbf{r} \right]. \tag{7.8}$$

The divergence $\boldsymbol{\nabla}\!\cdot\!\mathbf{P}$ of the polarization can be interpreted as the polarization charge density. This is shown by considering the arbitrarily shaped body Ω sketched in Fig. 7.1(b), which contains a number of dipoles in the polarizable medium as well as some external charges not part of the medium. In the bulk of the body the charges from the dipole moments cancel each other, but at the surface part of the dipole charges goes outside the body. Since $\mathbf{d}\!\cdot\!\mathbf{n}\mathrm{d}a$ describes the volume of a dipole $q\mathbf{d}$ sticking out of the surface element

(a)

$\mathbf{p} = q\,\mathbf{d}$

$\mathbf{r}_0 + \frac{1}{2}\mathbf{d}$

$+q$

$\mathbf{r}_0$

$\mathbf{d}$

$\mathbf{r}_0 - \frac{1}{2}\mathbf{d}$

$-q$

(b)

$\mathbf{E}$
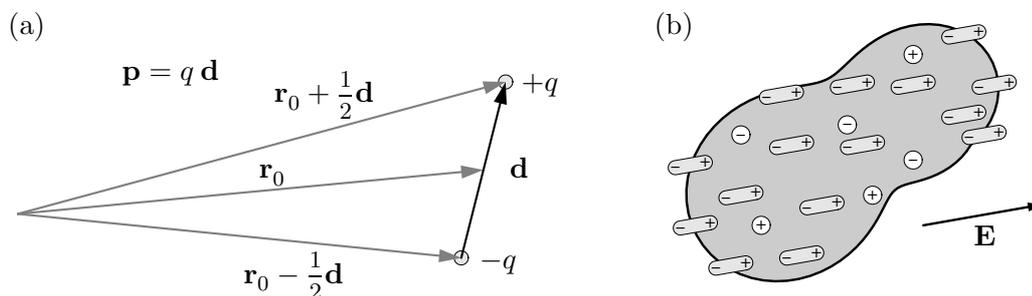
Figure 7.1: (a) The simple point dipole consisting of a charge $+q$ separated from a charge $-q$ by the distance $\mathbf{d}$. (b) The dipole moments (light gray ovals) and external charges (white circles) inside a body Ω (dark gray). Polarization charge is left behind in the body when the dipole moments sticks out at the surface of the body.

dda with unit normal vector $\mathbf{n}$ the amount of polarization charge Q_{pol} left behind in the body is given by

$$Q_{\mathrm{pol}} = -\int_{\partial\Omega} \mathrm{d}a\,\mathbf{n}\cdot\left(\frac{q\mathbf{d}}{\mathrm{Vol}(\Omega^*)}\right) = -\int_{\partial\Omega} \mathrm{d}a\,\mathbf{n}\cdot\mathbf{P} = -\int_{\Omega} \mathrm{d}\mathbf{r}\,\boldsymbol{\nabla}\cdot\mathbf{P}. \tag{7.9}$$

This results holds for any region Ω so the polarization charge density ρ_{pol} can be defined as

$$\rho_{\mathrm{pol}} \equiv -\boldsymbol{\nabla}\cdot\mathbf{P}, \tag{7.10}$$

but this allows for a simple expression for the density ρ_{ext} of the external charges:

$$\rho_{\mathrm{ext}} = \rho_{\mathrm{tot}} - \rho_{\mathrm{pol}} = \epsilon_0\boldsymbol{\nabla}\cdot\mathbf{E} + \boldsymbol{\nabla}\cdot\mathbf{P} = \boldsymbol{\nabla}\cdot\left(\epsilon_0\mathbf{E} + \mathbf{P}\right). \tag{7.11}$$

Thus by defining the displacement field as $\mathbf{D} \equiv \epsilon_0\mathbf{E} + \mathbf{P}$ leads to Eq. (7.2b), and we have learned that ρ_{el} should not comprise the polarization charge density ρ_{pol}. For liquids and isotropic solids the polarization is proportional to the electrical field, and the following expressions introducing the susceptibility χ and the relative dielectric constant ϵ_r can be used:

$$\mathbf{D} = \epsilon_0\mathbf{E} + \mathbf{P} = \epsilon_0\mathbf{E} + \epsilon_0\chi\mathbf{E} = \epsilon_0(1 + \chi)\mathbf{E} = \epsilon_0\epsilon_r\mathbf{E} = \epsilon\mathbf{E}. \tag{7.12}$$

We let the topic of electric dipoles, polarization, and dielectric effects rest for now, but shall return to it in a later chapter, when we study dielectrophoretic handling of charge-neutral particles. In the following we shall instead focus on the electric effects related to electric monopoles.

7.2 Electrokinetic effects

Having established the fundamental equations for electrohydrodynamics we move on to the first example, electrophoresis. This is one of four electrokinetic phenomena that are important in microfluidics. They all involve the motion of liquids relative to charged surfaces. The terminology in use is
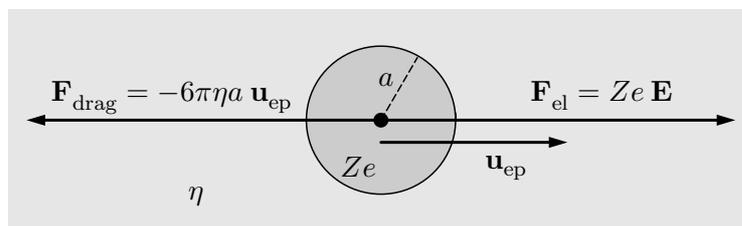
Figure 7.2: The principle of electrophoresis. A spherical particle of charge Ze and radius a moves in a low-conductivity liquid with viscosity η under the influence of an applied electrical field $\mathbf{E}$. The motion becomes stationary at the velocity $\mathbf{u}_{\text{ep}}$, when the Stokes drag force $\mathbf{F}_{\text{drag}}$ balances the electrical driving force $\mathbf{F}_{\text{el}}$.

1. **Electrophoresis** — the movement of a charged surface (of say dissolved or suspended material) relative to a stationary liquid induced by an applied electric field.

2. **Electroosmosis** — the movement of liquid relative to a stationary charged surface (of say a capillary tube) induced by an applied electric field.

3. **Sedimentation potential** — the electric potential created when charged particles are made to move relative to a stationary liquid.

4. **Streaming potential** — the electric potential created when a liquid is made to move relative to a charged surface.

7.2.1   Electrophoresis

In the following we study how an applied electrical field $\mathbf{E}$ influences a spherical particle of charge Ze and radius a in a stationary liquid of low electrical conductivity, say de-ionized water. This is a particularly simple case of electrophoresis. The low conductivity of the liquid implies the lack of ions that otherwise would have accumulated around the charged particle and partly neutralized its charge, an effect known as electrical screening. Therefore, as sketched in Fig. 7.2, the electric force is simply $\mathbf{F}_{\text{el}} = Ze\mathbf{E}$. From Section 4.7.1 we know that on the short time-scale of a few μs, the charged particle reaches steady-state motion, here the electrophoretic velocity $\mathbf{u}_{\text{ep}}$, due to viscous drag. In this situation the Stokes drag force Eq. (2.65), $\mathbf{F}_{\text{drag}} = -6\pi\eta a\,\mathbf{u}_{\text{ep}}$, balances $\mathbf{F}_{\text{el}}$,

$$\mathbf{F}_{\text{tot}} = \mathbf{F}_{\text{el}} + \mathbf{F}_{\text{drag}} = 0 \quad \Rightarrow \quad \mathbf{u}_{\text{ep}} = \frac{Ze}{6\pi\eta a}\,\mathbf{E} \equiv \mu_{\text{ion}}\,\mathbf{E}. \tag{7.13}$$

The dependence of the resulting drift velocity $\mathbf{u}_{\text{ep}}$ on particle charge and size makes electrophoresis usable in biochemistry for sorting of proteins and DNA fragments. The sample under consideration is dissolved in water and inserted in one end of a tube with electrodes at each end. A voltage difference is applied to the electrodes, and the part of the sample that arrives first at the other end of the tube contains the smallest and most charged particles.

ions at $T = 25°C$	H^+	Ag^+	K^+	Li^+	Na^+	Br^-	Cl^-	F^-	I^-	OH^-
mobility μ_{ion} $\left[10^{-8} \text{ m}^2 \text{ (V s)}^{-1}\right]$	36.2	6.42	7.62	4.01	5.19	8.09	7.91	5.70	7.96	20.6
diffusivity D_{ion} $\left[10^{-9} \text{ m}^2 \text{ s}^{-1}\right]$	9.31	-	1.96	1.03	1.33	2.08	2.03	1.46	2.05	5.30

Table 7.1: Experimental values for ionic mobility and diffusivity for small ions in aqueous solutions at small concentrations. Note how H^+ and OH^- have significantly different values due to their special modes of propagation by exchange of electrons with the neutral water molecules.

7.2.2 Ionic mobility and conductivity

From Eq. (7.13) we see that the terminal velocity $\mathbf{u}_{ep}$ is proportional to the applied electrical field $\mathbf{E}$. The proportionality constant is called the ionic mobility μ_{ion},

$$\mu_{ion} \equiv \frac{Ze}{6\pi\eta a}. \tag{7.14}$$

This simple theoretical estimate based on a macroscopic continuum model is in remarkable agreement with measured values of the ionic mobility of ions having a radius in the sub-nm range and moving in water. The radius a, however, is not the bare ionic radius $a \approx 0.05$ nm but instead the somewhat larger so-called hydrated radius $a \approx 0.2$ nm. This is due to the fact that ions in aqueous solutions accumulates approximately one atomic layer of water molecules. For $Z = 1$, $\eta = 1$ mPa s, and $a = 0.2$ nm we get

$$\mu_{ion} \approx 4 \times 10^{-8} \text{ m}^2 \text{ (V s)}^{-1}. \tag{7.15}$$

The experimental values for μ_{ion} are shown in Table 7.1.

The ionic mobility μ_{ion} is directly related to the ionic conductivity σ_{ion} as seen by combining Eqs. (7.2d) and (7.14),

$$\mu_{ion}\mathbf{E} = \mathbf{u}_{ep} = \frac{1}{Zec_{ion}} \mathbf{J}_{el} = \frac{\sigma_{ion}}{Zec_{ion}} \mathbf{E}, \tag{7.16}$$

so

$$\sigma_{ion} = Zec_{ion}\mu_{ion} \approx 10^{-3} \text{ S m}^{-1}, \tag{7.17}$$

where the ionic concentration in the numerical example has been set to $c_{ion} = 1$ mM. The numerical result is in good agreement with experimental values for σ_{ion}.

7.3 The Debye layer near charged surfaces

The next electrohydrodynamic topic is a study of the electric potential and charge distribution in an electrolyte, i.e., an aqueous solution of ions, in equilibrium near a charged surface. The results obtained in this section will form the basis for our analysis in the
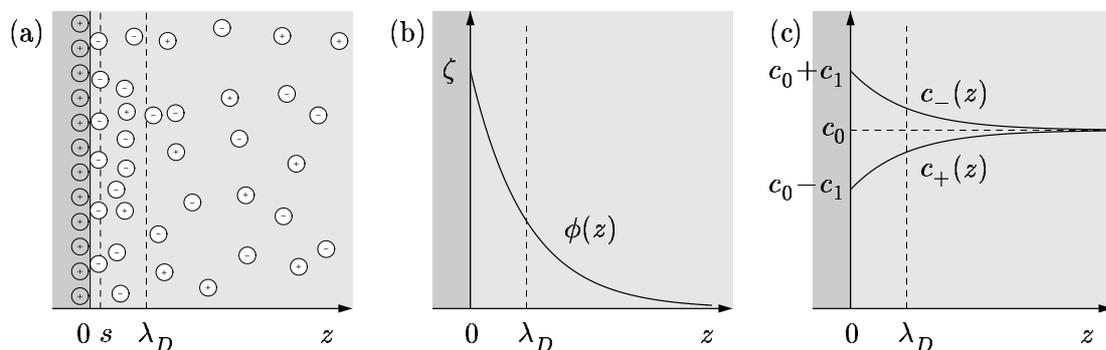
Figure 7.3: (a) The ionic structure in thermal equilibrium of the Debye layer in an electrolyte (light gray, $x > 0$) near a solid surface in the xy plane after charge transfer between the solid (dark gray, $z < 0$) and the electrolyte has taken place. For $0 < z < s$ lies the single-layer of immobile counter-ions, the Stern layer. For $s < z < \lambda_D$ follows the diffuse mobile layer of predominantly counter-ions. For $z > \lambda_D$ the electrolyte is charge neutral. (b) The simple continuous field model for the electric potential $\phi(z)$ in the Debye layer. The potential at the Stern layer next to the surface takes the value $\phi(0) = \zeta$, while it decays to zero in the bulk on the length scale given by the Debye length λ_D. (c) The corresponding ionic densities $c_+(z)$ and $c_-(z)$ in the Debye layer.

following chapter of the electrokinetic effect called electroosmosis and its applications to micropumps.

Consider an electrolyte in contact with a solid surface, either in the form of the walls of the microfluidic channel in which the liquid flows or in the form of a particle suspended in the liquid. Depending on the chemical composition of the solid and of the electrolyte chemical processes at the surface will result in a charge transfer between the electrolyte and the wall. As a result the wall and the electrolyte gets oppositely charged while maintaining global charge neutrality. In Fig. 7.3(a) is sketched how the ions are distributed in the electrolyte after the charge transfer has taken place.

7.3.1 The continuum model of the Debye layer

The basic physics is simple. The ions having the opposite charge of the solid, the counterions, are attracted to the solid, while the other ions, the co-ions, are repelled. In case of zero temperature a complete charge cancellation, i.e., perfect electric shielding, would occur at the surface, however, at finite temperature thermal motion counteracts this behavior. The governing equation for the continuum description of the co- and counter-ionic concentrations $c_\pm(\mathbf{r})$ comes from the thermodynamic expression for the chemical potential $\mu(\mathbf{r})$, the free energy of the last added ion,

$$\mu(\mathbf{r}) = \mu_0 + k_B T \ln\left(\frac{c_\pm(\mathbf{r})}{c_0}\right) \pm Ze\phi(\mathbf{r}), \tag{7.18}$$

where μ_0 and c_0 is the chemical potential and ionic density, respectively, in the absence of the electric potential. Note, that for simplicity that the ionic valences are opposite, $\pm Z$.

Thermodynamic equilibrium implies that the chemical potential is constant throughout the system, because if it were varying the system could gain energy by reorganizing its constituents. We therefore have

$$\mu(\mathbf{r}) = \text{const} \quad \Rightarrow \quad \boldsymbol{\nabla}\mu(\mathbf{r}) \equiv 0 \quad \Rightarrow \quad k_{\text{B}}T\boldsymbol{\nabla}\ln\left(\frac{c_{\pm}(\mathbf{r})}{c_0}\right) = \mp Ze\boldsymbol{\nabla}\phi(\mathbf{r}). \tag{7.19}$$

In the following we assume, as indicated in Fig. 7.3, that infinitely far away from the surface the two ionic concentrations approaches the same unperturbed value c_0 and the electrical potential goes to zero, while at the surface the potential takes the value ζ, known in the literature as the zeta potential:

$$c_{\pm}(\infty) = c_0, \qquad \phi(\infty) = 0, \qquad \phi(\text{surf}) = \zeta. \tag{7.20}$$

With these boundary conditions Eq. (7.19) is easily integrated,

$$c_{\pm}(\mathbf{r}) = c_0 \, \exp\left[\mp \frac{Ze}{k_{\text{B}}T} \, \phi(\mathbf{r})\right], \tag{7.21}$$

which results in the charge density ρ_{el},

$$\rho_{\text{el}}(\mathbf{r}) = Ze\big[c_+(\mathbf{r}) - c_-(\mathbf{r})\big] = -2Zec_0 \, \sinh\left[\frac{Ze}{k_{\text{B}}T} \, \phi(\mathbf{r})\right]. \tag{7.22}$$

Expressing the charge density in terms of the potential using the Poisson equation (7.3b) leads to a differential equation, the so-called Poisson–Boltzmann equation, for the electrical potential,

$$\nabla^2\phi(\mathbf{r}) = 2\frac{Zec_0}{\epsilon} \, \sinh\left[\frac{Ze}{k_{\text{B}}T} \, \phi(\mathbf{r})\right], \tag{7.23}$$

which can be solved numerically or in some special cases analytically. One analytical solution can be obtained in the case of a planar surface in the xy plane at $z = 0$ and the electrolyte occupying the $z > 0$ half-space. Due to translation symmetry in the xy plane the problem becomes one dimensional and ϕ depends only on z, the direction perpendicular to the surface plane. The resulting, so-called Gouy–Chapman solution, is

$$\phi(z) = \frac{4k_{\text{B}}T}{Ze} \, \text{arctanh}\left[\tanh\left(\frac{Ze\zeta}{4k_{\text{B}}T}\right) \, \exp\left(-\frac{z}{\lambda_D}\right)\right], \tag{7.24}$$

where

$$\lambda_D \equiv \sqrt{\frac{\epsilon k_{\text{B}}T}{2(Ze)^2 c_0}} \tag{7.25}$$

is the so-called Debye length to be derived in the next section. In Exercise 7.2 we prove that Eq. (7.24) indeed is a solution to the Debye layer problem Eq. (7.23). For a standard electrolyte with an ionic concentration of 1 mM = 1 mol/m^3 and a dielectric constant equal that of water, $\epsilon = 78\epsilon_0$ we find the following value of λ_D at room temperature:

$$\lambda_D \approx 9.5 \text{ nm}. \tag{7.26}$$

7.3.2   The Debye–Hückel approximation for the Debye layer

To gain insight into the physics of the Debye layer and to build up our intuition, we shall now study the so-called Debye–Hückel approximation. The approximation is valid when the electrical energy is small compared to the thermal energy, i.e., in the

$$\text{Debye–Hückel limit} \quad Ze\zeta \ll k_\mathrm{B}T. \tag{7.27}$$

In this limit, i.e., for zeta potentials much less than 26 mV at room temperature, we can employ the Taylor expansion $\sinh(u) \approx u$ in Eq. (7.23) and obtain the simple equation.

$$\nabla^2 \phi(\mathbf{r}) = 2\frac{(Ze)^2 c_0}{\epsilon k_\mathrm{B}T}\,\phi(\mathbf{r}) \equiv \frac{1}{\lambda_D^2}\,\phi(\mathbf{r}), \tag{7.28}$$

which explains why λ_D, given by Eq. (7.25), is introduced.

   A planar surface in the xy plane at $z = 0$ is a the first special case that we solve analytical. Eq. (7.28) becomes the simple second order ordinary differential equation,

$$\partial_z^2 \phi(z) = \frac{1}{\lambda_D^2}\,\phi(z), \tag{7.29}$$

which, given the boundary conditions Eq. (7.20), has the exponential solution,

$$\phi(z) = \zeta\,\exp\left[-\frac{z}{\lambda_D}\right] \quad (z > 0, \text{ single plate wall}). \tag{7.30}$$

The charge density ρ_el in the Debye layer corresponding to the potential Eq. (7.30) is found by using the Poisson equation (7.3b),

$$\rho_\mathrm{el}(z) = -\epsilon\partial_z^2 \phi(z) = -\frac{\epsilon\zeta}{\lambda_D^2}\,\exp\left[-\frac{z}{\lambda_D}\right] \quad (z > 0, \text{ single plate wall}), \tag{7.31}$$

The ionic densities $c_-(z)$ and $c_+(z)$ are found directly from Eq. (7.21) in the Debye–Hückel approximation by Taylor-expanding the exponential function,

$$c_\pm(z) = c_0\left[1 \mp \frac{Ze\zeta}{k_\mathrm{B}T}\,\exp\left[-\frac{z}{\lambda_D}\right]\right] \quad (z > 0, \text{ single plate wall}). \tag{7.32}$$

It is seen how the density of co-ions is suppressed near the surface while that of the counter-ions are enhanced. This result is sketched in Fig. 7.3(c). Note that Eq. (7.32) has been derived under the assumption limit $Ze\zeta \ll k_\mathrm{B}T$, so the ionic densities are always positive.

   The infinite parallel-plate channel with surfaces at $z = \pm h/2$ is the second special case that we solve analytical. As before the potential ϕ only depends on z and the Poisson–Boltzmann equation is given by Eq. (7.29), but now the boundary conditions are

$\phi(\pm h/2) = \zeta$. As this problem is symmetric about $z = 0$ the solution involves $\cosh(x/\lambda_D)$ rather than $\exp(-x/\lambda_D)$, and the resulting potential is seen to be

$$\phi(z) = \zeta \, \frac{\cosh\left(\frac{z}{\lambda_D}\right)}{\cosh\left(\frac{h}{2\lambda_D}\right)} \quad (-\frac{h}{2} < z < \frac{h}{2}, \text{ parallel-plate channel}). \tag{7.33}$$

As above the charge density ρ_{el}, see Fig. 8.1, follows from the Poisson equation,

$$\rho_{\text{el}}(z) = -\frac{\epsilon\zeta}{\lambda_D^2} \, \frac{\cosh\left(\frac{z}{\lambda_D}\right)}{\cosh\left(\frac{h}{2\lambda_D}\right)} \quad (-\frac{h}{2} < z < \frac{h}{2}, \text{ parallel-plate channel}). \tag{7.34}$$

The circular-shaped channel with surfaces at radius $r = a$ is the third and last analytical solution presented here. Employing the boundary condition $\phi(a) = \zeta$, the symmetry of the problem, as in Eq. (2.32), dictates the use of cylindrical coordinates without angular dependences. The Poisson–Boltzmann equation becomes

$$\left[\partial_r^2 + \frac{1}{r}\,\partial_r\right]\phi(r) = \frac{1}{\lambda_D^2}\,\phi(r) \quad (0 < r < a, \text{ circular channel}). \tag{7.35}$$

This is recognized as the modified Bessel differential equation of order zero, so the solution involves the modified Bessel function of order 0,

$$\phi(r) = \zeta \, \frac{I_0\left(\frac{r}{\lambda_D}\right)}{I_0\left(\frac{a}{\lambda_D}\right)} \quad (0 < r < a, \text{ circular channel}). \tag{7.36}$$

The charge density $\rho_{\text{el}}(r)$ follows from the Poisson and Poisson–Boltzmann equation as

$$\rho_{\text{el}}(r) = -\epsilon\nabla^2\phi(r) = -\frac{\epsilon}{\lambda_D^2}\,\phi(r) = -\frac{\epsilon\zeta}{\lambda_D^2}\,\frac{I_0\left(\frac{r}{\lambda_D}\right)}{I_0\left(\frac{a}{\lambda_D}\right)} \quad (0 < r < a, \text{ circular channel}). \tag{7.37}$$

7.3.3 Surface charge and the Debye layer capacitance

The Debye layer acts as an electrical capacitor since it accumulates electrical charge as a response to the electrical potential difference ζ between the surface and the bulk. In the following we study this property.

One way to obtain the capacitance of the Debye layer is by integrating the charge density $\rho_{\text{el}}(x)$ of Eq. (7.31) along the z direction from the surface at $z = 0$ to infinity, $x = \infty$. The result q_{liq} is the charge per area $\mathcal{A}$ that is contained in the liquid in the direction perpendicular to any small area $\mathcal{A}$ on the surface,

$$q_{\text{liq}} = \int_0^\infty dz\,\rho_{\text{el}}(z) = \int_0^\infty dz\left[-\frac{\epsilon\zeta}{\lambda_D^2}\,\exp\left[-\frac{z}{\lambda_D}\right]\right] = -\frac{\epsilon}{\lambda_D}\,\zeta. \tag{7.38}$$
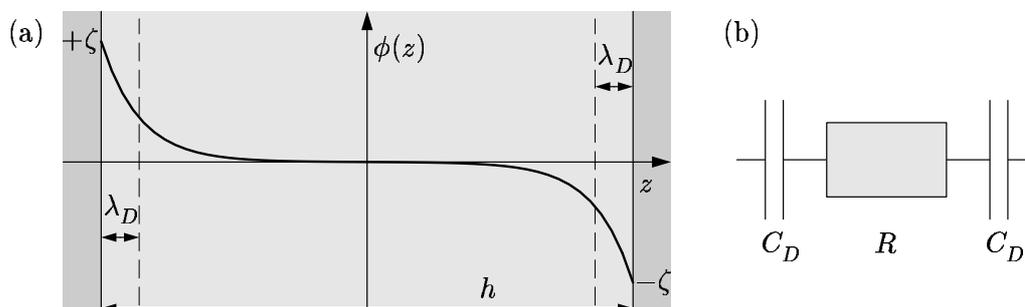
Figure 7.4: (a) An electrolyte (light gray) occupying the space of height h between a set of parallel-plate metallic electrodes (dark gray) . When applying a voltage difference 2ζ between the two electrodes, a Debye layer of width λ_D builds up on each of them. (b) The electrical equivalent diagram of the system shown in panel (a) consisting of one capacitor C_D for each Debye layer and one resistor R for the bulk electrolyte.

From this linear relation between charge per area and applied potential difference we can immediately read off the capacitance per area C_D of the Debye layer in thermal equilibrium,

$$C_D \equiv \frac{\epsilon}{\lambda_D}. \tag{7.39}$$

Using $\lambda_D = 9.6$ nm and $\epsilon = 78\epsilon_0$ we find the value

$$C_D \approx 0.073 \ \mathrm{F \ m}^{-2}. \tag{7.40}$$

We can check the above result by calculating the surface charge per area q_{surf} that is accumulated on the surface. This is done by using a standard Gauss box argument. Imagine a flat box of surface area $\mathcal{A}$ and a vanishingly small thickness placed parallel to the surface such that the surface lies inside the box. The symmetry of the problem dictates that there are only a non-zero electric field through the area $\mathcal{A}$ on the liquid side of the surface and, moreover, the electric field is perpendicular to this surface. Thus the total charge inside the box is $\mathcal{A}q_{\mathrm{surf}} = \epsilon E \mathcal{A}$, and we have

$$q_{\mathrm{surf}} = \epsilon E = -\epsilon \partial_z \phi(0) = \frac{\epsilon}{\lambda_D} \ \zeta. \tag{7.41}$$

As expected, this result is exactly the opposite of charge per area in the liquid, so indeed the Debye layer acts as a charge neutral capacitor, where the solid surface and the electrolyte are the two "plates" of the capacitor.

Since the Debye layer acts as a capacitor and since the electrolyte has a finite conductivity σ_{el} or resistivity $1/\sigma_{\mathrm{el}}$ we should be able to ascribe a characteristic RC time τ_{RC} to the system. We can get an estimate of this time scale by considering the setup sketched in Fig. 7.4.

We consider an electrolyte sandwiched between a set of parallel-plate metallic electrodes. The distance between the electrodes is denoted h. When one electrode is biased
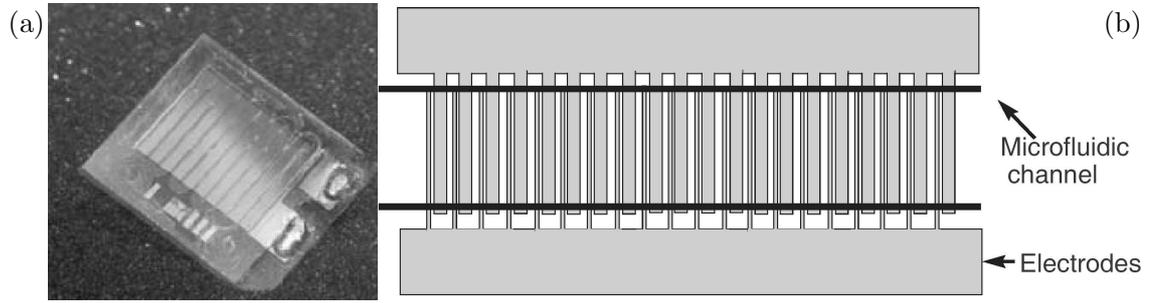
Figure 7.5: (a) A picture of a polymer-based microfluidic channel. The channel forms a meander with ten turns. A pair of intercalating gold electrodes are placed at the bottom of the channel. The two contact pads are seen on the right-hand edge of the chip. (b) The design of the electrode pair. One set of the electrodes are wide and the other narrow. This spatially asymmetric design should induce a pumping effect when an AC voltage bias is applied to the electrode pair. Courtesy the group of Bruus at MIC (2004).

by the voltage $+\zeta$ and the other by $-\zeta$ a Debye layer builds up on each of them. The equivalent diagram of the system consist of a series coupling of one capacitor for each Debye layer and one resistor for the bulk electrolyte. The RC time for this system is now found as

$$\tau_{RC} = RC = \left(\frac{h}{\sigma_{\text{el}} \mathcal{A}} \right) \left(\frac{1}{2} \frac{\epsilon}{\lambda_D} \mathcal{A} \right) = \frac{\epsilon}{2\sigma_{\text{el}}} \frac{h}{\lambda_D}. \tag{7.42}$$

The value of the RC time is found by using our standard values for the parameters: $\lambda_D = 9.6$ nm, $h = 100$ μm, $\epsilon = 78\epsilon_0$, and $\sigma_{\text{el}} = 10^{-3}$ S/m,

$$\tau_{RC} = 3.6 \text{ ms.} \tag{7.43}$$

For processes slower than 3.6 ms enough time is available for establishing the Debye layer. However, the Debye layer cannot follow faster processes. In AC experiments this translates into a characteristic frequency ω_{D} of the Debye layer,

$$\omega_{\text{D}} = \frac{2\pi}{\tau_{RC}} = 1.7 \times 10^3 \text{ rad/s.} \tag{7.44}$$

For frequencies higher than a few kHz the Debye layer is not established. In Fig. 7.5 is shown a microfluidic channel fabricated at MIC with surface electrodes to study and to utilize the RC time effects of the Debye layer in electrolytes. The hope is to design an electrode system that can pump the electrolyte when an AC bias voltage is applied.

7.3.4 Electrophoresis and Debye layer screening

In Section 7.2.1 we studied electrophoresis in the case of a non-conducting liquid. This case was simple since the charge of the particle suspended in the liquid did not suffer any electrical screening. The opposite limit, where the liquid is a highly conducting electrolyte,

is also a simple case. Here the particle charge is completely screened by the ions of the electrolyte within a distance of the Debye screening length λ_D. Since the effective charge of the particle in this case is zero it cannot move by electrophoresis, but only by dielectric forces, a process called dielectrophoresis.

Let us solve the Debye layer problem for a charged spherical particle of radius a. The problem is spherical symmetric, so the potential due to the particle can only depend on the radial coordinate r, $\phi(\mathbf{r}) = \phi(r)$. The boundary conditions for $\phi(r)$ are

$$\phi(a) = \zeta, \qquad \phi(\infty) = 0. \tag{7.45}$$

After employing the Debye–Hückel approximation, the Poisson–Boltzmann equation (7.23) becomes

$$\frac{1}{r^2}\,\partial_r\left(r^2\,\partial_r\phi\right) = \frac{1}{\lambda_D^2}\,\phi \quad \text{(spherical polar coordinates)}, \tag{7.46}$$

where the Laplace operator in spherical coordinates is simplified due to the lack of angular dependence in the problem. This differential equation is solved by the standard substitution $\psi(r) \equiv r\,\phi(r)$, since Eq. (7.46) then is transformed into the simpler equation

$$\partial_r^2\psi = \frac{1}{\lambda_D^2}\,\psi \quad \text{(spherical symmetry)}, \tag{7.47}$$

with the straightforward exponential solutions $\psi(r) \propto \exp(\pm r/\lambda_D)$. Going back from $\psi(r)$ to $\phi(r)$ and employing the boundary conditions Eq. (7.45) yields the solution

$$\phi(r) = \zeta\,\frac{a}{r}\,\exp\left[\frac{a-r}{\lambda_D}\right] \quad (r > a, \text{ spherical symmetry}). \tag{7.48}$$

This solution, which has the form of a modified or screened Coulomb potential, corresponds to a collection of counter-ions around the charged particle. This charge collection is known as a screening cloud. Just a few times the Debye length λ_D away for the particle, its charge cannot be observed, it is completely screened. For strong electrolytes, where λ_D is very small, the originally charged particle becomes charge-neutral for all practical purposes.

In the intermediate case of moderate Debye length, the electrophoresis problem becomes complicated. The motion of the particle distorts the screening cloud, which becomes asymmetric, resulting in very complex interactions between the electrolyte, the screening cloud and the particle. This topic is beyond the scope of these lecture notes.

In the case of very long Debye lengths, i.e., for non-conducting liquids, we recover the simple un-screened charged particle studied in Section 7.2.1.

7.4 Exercises

Exercise 7.1
The dielectric force and the point dipole
Consider the electric force $\mathbf{F}_{\text{el}}$ on a particle.

(a) Write the dielectrophoretic force in vector notation instead of the index notation employed in Eq. (7.4).

(b) Verify the expression $\mathbf{p} = q\mathbf{d}$ Eq. (7.7) for the point dipole, and write in vector notation the dielectric force acting on it.

Exercise 7.2
The analytic solution for the Debye layer potential in 1D

In this exercise we prove that $\phi(x)$ given in Eq. (7.24) indeed is a solution to the Debye layer problem for a planar charged surface.

(a) Use the following substitutions $x \equiv \lambda_D \tilde{x}$, $\phi \equiv \zeta \tilde{\phi}$ and $\alpha \equiv Ze\zeta/(k_B T)$ to show that the Poisson–Boltzmann equation (7.23) can be written in the dimensionless form

$$\partial_{\tilde{x}}^2 \tilde{\phi}(\tilde{x}) = \frac{1}{\alpha} \sinh\left[\alpha\tilde{\phi}(\tilde{x})\right]. \tag{7.49}$$

(b) Show that Eq. (7.49) can be rewritten by use of the substitution $u(\tilde{x}) \equiv \alpha\tilde{\phi}(\tilde{x})$ to the form

$$u'' = \sinh(u) \quad \Rightarrow \quad \left(\tfrac{1}{2}\left[u'\right]^2\right)' = \left(\cosh(u)\right)', \quad u = \alpha\tilde{\phi}, \tag{7.50}$$

where prime means derivative with respect to $\tilde{x}$.

(c) Use the boundary condition $u(\infty) = u'(\infty) = 0$ and the physical insight $u'(\tilde{x}) < 0$ to argue that Eq. (7.50) can be integrated once to yield the result

$$u' = -\sqrt{2\cosh(u) - 2} = -2\sinh\left(\tfrac{1}{2}u\right), \quad u = \alpha\tilde{\phi}, \tag{7.51}$$

where the hyperbolic relation $\cosh(u) = 2\sinh^2(u/2) + 1$ has been used.

(d) Now introduce the new function $v(\tilde{x}) = u(\tilde{x})/2 = \alpha\tilde{\phi}(\tilde{x})/2$ with the boundary conditions $v(0) = \alpha/2$ and $v(\infty) = 0$. Show that Eq. (7.51) can be rewritten and integrated by separation of the variables v and $\tilde{x}$ as follows:

$$\int_{\frac{\alpha}{2}}^{v(\tilde{x})} \frac{dv}{\sinh(v)} = -\int_0^{\tilde{x}} d\tilde{x} \quad \Rightarrow \quad \left[\log\left[\tanh\left(\frac{v}{2}\right)\right]\right]_{\frac{\alpha}{2}}^{v(\tilde{x})} = -\tilde{x}, \quad v = \frac{\alpha}{2}\tilde{\phi}. \tag{7.52}$$

(e) Show that Eq. (7.52) leads to following form of the final expression for $\tilde{\phi}(\tilde{x})$,

$$\tilde{\phi}(\tilde{x}) = \frac{4}{\alpha}\tanh^{-1}\left[\tanh\left(\frac{\alpha}{4}\right)e^{-\tilde{x}}\right]. \tag{7.53}$$

Exercise 7.3
The low-voltage limit of the Debye layer potential in 1D

Consider the Debye–Hückel approximation in the 1D case of Section 7.3.2.

(a) Show by Taylor expansion of Eq. (7.24) that the exact solution and the Debye–Hückel approximation Eq. (7.30) agrees in the low-voltage limit $Ze\zeta \ll k_B T$.

(b) At which value of ζ is the relative error made in the Debye–Hückel approximation 10% of the exact result?

Exercise 7.4
The analytic solution for the Debye layer potential inside a cylindrical channel
Prove that $\phi(r)$ given in Eq. (7.36) is the solution to the Poisson–Boltzmann equation
(7.35) for the straight channel with circular cross-section of radius a given the boundary
conditions $\phi(a) = \zeta$ and $\partial_r \phi(0) = 0$ (no cusps in the potential along the center axis).

Exercise 7.5
Surface charge in the Debye layer of the parallel-plate channel
Determine within the Debye–Hückel approximation the surface charge density q_{surf} of
the parallel-plate channel of height h, and verify in analogy with the single-wall results
Eqs. (7.38) and (7.41) that q_{surf} is opposite to the charge density per area q_{liq} in the
electrolyte.

Exercise 7.6
The simple model for the *RC* time of the Debye layer
Consider the equivalent circuit diagram in Fig. 7.4(b).
    (a) Express the resulting capacitance in terms of C_D.
Let $V_{\mathrm{ext}}(t)$ be some externally applied voltage driving current $I(t)$ from one wall to the
other. We assume that the intrinsic zeta potential is zero.
    (b) Find the differential equation for $I(t)$ and discuss the role of the RC-time $\tau_{RC} = RC$ in the solution.
    (c) Derive Eq. (7.42) and discuss the physical assumptions made and how the various
parameters influence τ_{RC}.

Exercise 7.7
The Debye layer potential of a charged sphere
Consider the charged sphere of radius a immersed in an electrolyte as described in Section 7.3.4.
    (a) Check that the Laplace operator in spherical coordinates, when no angular dependence is present, is the one employed in Eq. (7.46).
    (b) Verify that the substitution $\psi(r) = r\,\phi(r)$ indeed transforms Eq. (7.46) into
Eq. (7.47).
    (c) Prove that the solution Eq. (7.48) is correct, and calculate the charge density $\rho_{\mathrm{el}}(r)$
of the screening cloud surrounding the sphere.
    (d) Compare the physical implications of the form of $\phi(r)$ in Eq. (7.48) with the case
of an un-screened charged particle.

7.5   Solutions

Solution 7.1
The dielectric force and the point dipole
Consider the electric force $\mathbf{F}_{\mathrm{el}}$ on a particle.
    (a) In vector notation Eq. (7.4) becomes $\mathbf{F}_{\mathrm{el}} = Q\mathbf{E} + (\mathbf{p} \cdot \boldsymbol{\nabla})\mathbf{E}$.
    (b) We first note that $\int d\mathbf{r}\, f(\mathbf{r})\delta(\mathbf{r}^* - \mathbf{r}) = f(\mathbf{r}^*)$. Hence, inserting Eq. (7.6) into
Eq. (7.5b) yields $\mathbf{p} = q\frac{1}{2}\mathbf{d} - q\left(-\frac{1}{2}\right)\mathbf{d} = q\mathbf{d}$. From (a) we then obtain $\mathbf{F}_{\mathrm{el}} = q(\mathbf{d} \cdot \boldsymbol{\nabla})\mathbf{E}$.

Solution 7.2
The analytic solution for the Debye layer potential in 1D
Only a few details needs to be filled in solving this exercise concerning Eq. (7.24).

(a) Using the substitutions $x \equiv \lambda_D \tilde{x}$, $\phi \equiv \zeta \tilde{\phi}$ and $\alpha \equiv Ze\zeta/(k_BT)$ is straightforward. It remains to note the $\partial_x = (\partial_x \tilde{x})\partial_{\tilde{x}} = \lambda_D^{-1}\partial_{\tilde{x}}$, and thus $\partial_x^2 = \lambda_D^{-2}\partial_{\tilde{x}}^2$.

(b) Using $u(\tilde{x}) \equiv \alpha\tilde{\phi}(\tilde{x})$ gives $u'' = \sinh(u)$. Moreover $\left(\frac{1}{2}[u']^2\right)' = u'u''$, while $[\cosh(u)]' = \sinh(u)\,u'$, which upon division by u' proves the implication in Eq. (7.50).

(c) Integration of Eq. (7.50) gives $[u']^2 = 2\cosh(u) + \text{const}$. At $\tilde{x} = \infty$ this reads $[u'(\infty)]^2 = 2\cosh[\alpha\tilde{\phi}(\infty)] + \text{const} = 2 + \text{const}$, so the boundary condition $u'(\infty) = 0$ requires $\text{const} = -2$. When isolating u' the negative sign must be used to ensure $u' < 0$.

(d) Using $v = u/2$, Eq. (7.51) becomes $v' = -\sinh(v)$ or $dv/d\tilde{x} = \sinh(v)$. Separation of the variables leads to $dv/\sinh(v) = d\tilde{x}$, and employing the boundary condition $v(0) = \alpha/2$ leads to the integral Eq. (7.52). We note that $\big[\log[\tanh(v/2)]\big]' = [1/\tanh(v/2)][1/\cosh^2(v/2)]v'/2 = 1/[2\sinh(v/2)\cosh(v/2)]v' = v'/\sinh(v)$, so Eq. (7.52) is integrated correctly.

(e) Since $\Big[\log(z)\Big]_a^b = \log(a) - \log(b) = \log(a/b)$, Eq. (7.52) becomes $\log\big[\tanh(\alpha\tilde{\phi}/4)/\tanh(\alpha/4)\big] = -\tilde{x}$, and Eq. (7.53) results once $\tilde{\phi}$ is isolated.

Solution 7.3
The low-voltage limit of the Debye layer potential in 1D
For $s = Ze\zeta/(4k_BT) \ll 1$ we have the following Taylor expansions: $\tanh(s) \approx s - s^3/s$ and $\text{arctanh}(s) \approx s + s^3/s$.

(a) Given the above, and noting that $0 < \exp(-z/\lambda_D) < 1$ for $z > 0$, a Taylor expansion of Eq. (7.24) to lowest order in s becomes $\phi(z) \approx \frac{4k_BT}{Ze}\frac{Ze\zeta}{4k_BT}e^{-z/\lambda_D} = \zeta\,e^{-z/\lambda_D}$.

(b) There is not a unique answer to the question, as the error of an approximating function is not well defined. One possibility is to note that the Gouy–Chapman and the Debye–Hückel solutions agree at $z = 0$ and $z = \infty$, so it is natural to study the function values at $z = \lambda_D$, which is the only distinctive length scale of the problem, and here e^{-z/λ_D} is just $\frac{1}{e}$. The Taylor expansion to third order in s becomes $\text{arctanh}[\tanh(s)/e] \approx [\tanh(s)/e] + [\tanh(s)/e]^3/3 \approx [s - s^3/3]/e + [s^3/e^3]/3 = [1 - s^2(1 - 1/e^2)/3]\,s/e$. The relative error is approximately below 10% when the first correction to the leading term is below 10%, i.e., when $s^2(1 - 1/e^2)/3 < 0.1$ or $s < 0.6$, implying $\zeta < 2.4\frac{k_BT}{Ze} = 61$ mV$/Z$.

Solution 7.4
The analytic solution for the Debye layer potential inside a cylindrical channel
If we introduce the dimensionless radial coordinate $s = r/\lambda_D$ and thus $\partial_s = \lambda_D\partial_r$, the Poisson–Boltzmann equation (7.35) straightforwardly rewritten to Bessel's modified differential equation of order zero: $s^2\partial_s^2\psi + s\partial_s\psi - s^2\psi = 0$, where $\psi(s) \equiv \phi(\lambda_D s)$. The general solution is the linear combination of the modified Bessel functions of order zero, I_0 and K_0, of the first and second kind, respectively: $\psi(s) = c_1 I_0(s) + c_2 K_0(s)$. Since $K_0(s) \to \infty$ for $s \to 0$, its derivative is also diverging, and this function must be discarded due to the second boundary condition $\partial_s\psi(0) = 0$, i.e., $c_2 = 0$. The first boundary condition requires

$\zeta = \phi(a) = \psi(a/\lambda_D) = c_1 I_0(a/\lambda_D)$, and consequently $c_1 = \zeta/I_0(a/\lambda_D)$. In conclusion $\psi(s) = \zeta I_0(s)/I_0(a/\lambda_D)$.

Solution 7.5
Surface charge in the Debye layer of the parallel-plate channel
Due to symmetry the two plates at $z = \pm h/2$ have the same surface charge density, but when using the Gauss box argument involving $q_{\mathrm{surf}} = \epsilon \mathbf{E} \cdot \mathbf{n}$, the electric field $\mathbf{E} = -\partial_z \phi \mathbf{e}_z$ is multiplied with the surface normal $\mathbf{n}(-h/2) = +\mathbf{e}_z$ or $\mathbf{n}(h/2) = -\mathbf{e}_z$. Using this and $\partial_s \cosh(s) = \sinh(s)$ we find

$$q_{\mathrm{surf}}\left(\pm\frac{h}{2}\right) = \pm\epsilon\partial_z\phi\left(\pm\frac{h}{2}\right) = \pm\frac{\sinh\left(\pm\frac{h}{2\lambda_D}\right)}{\cosh\left(\frac{h}{2\lambda_D}\right)}\frac{\epsilon\zeta}{\lambda_D} = \tanh\left(\frac{h}{2\lambda_D}\right)\frac{\epsilon\zeta}{\lambda_D}. \qquad (7.54)$$

The charge per area q_{liq} in the liquid is found to balance the surface charges by using the Poisson equation,

$$q_{\mathrm{liq}} = -\epsilon\int_{-\frac{h}{2}}^{\frac{h}{2}} \mathrm{d}z\,\partial_z\phi = -\epsilon\partial_z\phi\left(\frac{h}{2}\right) - (-\epsilon)\partial_z\phi\left(-\frac{h}{2}\right) = -\left[q_{\mathrm{surf}}\left(\frac{h}{2}\right) + q_{\mathrm{surf}}\left(-\frac{h}{2}\right)\right]. \quad (7.55)$$

Solution 7.6
The simple model for the RC time of the Debye layer
Consider the equivalent circuit diagram in Fig. 7.4(b).

(a) The resulting capacitance per area $\mathcal{A}$ is given by the two Debye layer capacitors in series, i.e., $C/\mathcal{A} = (1/C_D + 1/C_D)^{-1} = C_D/2$. So $C = \mathcal{A}C_D/2$.

(b) Let $V_{\mathrm{ext}}(t)$ be the total voltage drop across the series coupling from left to right, which also defines the positive direction of the current $I(t)$. Using the capacitor equation $V_D = q_{\mathrm{surf}}/C_D$ for the voltage drop across one Debye layer, and Ohm's law $V_R = RI$ for the voltage drop across the resistor, we find $V_{\mathrm{ext}} = 2q_{\mathrm{surf}}/C_D + RI$. Dividing by R and taking the time-derivative we arrive at $\partial_t I + \frac{1}{\tau_{RC}}I = \partial_t V_{\mathrm{ext}}/R$, where we have used $I = \mathcal{A}\partial_t q_{\mathrm{surf}}$ and introduced $\tau_{RC} \equiv RC = R\mathcal{A}C_D/2$. It is seen that τ_{RC} is the characteristic time scale for charging the Debye layers.

(c) We just found $\tau_{RC} = R\mathcal{A}C_D/2$. Since $R = h/(\mathcal{A}\sigma_{\mathrm{el}})$ for a resistor of length h, area $\mathcal{A}$, and resistivity $1/\sigma_{\mathrm{el}}$, and since $C_D = \epsilon/\lambda_D$ we obtain $\tau_{RC} = [h/(\mathcal{A}\sigma_{\mathrm{el}})][\mathcal{A}\epsilon/(2\lambda_D)] = \epsilon h/(2\sigma_{\mathrm{el}}\lambda_D)$. We see that fast charging occurs for small channel heights h, large Debye lengths λ_D, and large conductivity σ_{el}. As was explicitly stated when discussing the basic equation for the chemical potential Eq. (7.19), the main assumption leading to the RC-model is that at each moment during the charging the Debye layer is close to thermodynamic equilibrium.

Solution 7.7
The Debye layer potential of a charged sphere
Spherical polar coordinates are treated in Section A.3.2.

(a) For spherical symmetric scalar fields, where no angular dependence is present, only the first term in Eq. (A.33) is non-zero, i.e., $\nabla^2\phi = \frac{1}{r^2}\partial_r(r^2\partial_r\phi)$ as used in Eq. (7.46).

(b) First we write Eq. (7.46) as $\frac{1}{r}\partial_r(r^2\partial_r\phi) = r\phi/\lambda_D^2 = \psi/\lambda_D^2$, where $\phi(r) = \psi(r)/r$ is used on the right-hand side. For the left-hand side we get $r^2\partial_r\phi = r^2(\partial_r\psi/r - \psi/r^2) = r\partial_r\psi - \psi$. So $\frac{1}{r}\partial_r(r\partial_r\psi - \psi) = \frac{1}{r}(r\partial_r^2\psi + \partial_r\psi - \partial_r\psi) = \partial_r^2\psi$. In conclusion $\partial_r^2\psi = \psi/\lambda_D^2$.

(c) Eq. (7.48) yields $\phi(a) = \zeta$ and $\phi(\infty) = 0$, thus fulfilling the required boundary conditions. Moreover, multiplying the equation by r leads to $\psi(r) = c\exp(-r/\lambda_D)$, where the constant is $c = a\zeta\exp(a/\lambda_D)$, which clearly is a solution to the Poisson-Boltzmann equation (7.47). The charge density is given by

$$\rho_{\text{el}}(r) = -\epsilon\nabla^2\phi = -\frac{\epsilon}{\lambda_D^2}\phi = -\frac{\epsilon\zeta}{\lambda_D^2}\frac{a}{r}\exp\left[\frac{a-r}{\lambda_D}\right]. \tag{7.56}$$

(d) The potential around and un-screen charged particle is the well-known long range Coulomb potential $\zeta a/r$. For the screened charged particle the range of the Coulomb potential has been shortened by the appearance of the exponential factor $\exp[(a-r)/\lambda_D]$ having the characteristic screening length λ_D.

Chapter 8

Electroosmosis

Electroosmosis is a non-equilibrium effect, where a liquid is brought to move relative to a charged surface by an applied external potential gradient $\boldsymbol{\nabla}\phi_{\text{ext}}$. Therefore, to obtain a complete electrohydrodynamical transport theory, we need to supplement the diffusion-convection equation (4.16) with an electrically induced current density $\mathbf{J}^{\text{el}}$.

8.1   Electrohydrodynamic transport theory

The symbol $\mathbf{J}_\alpha^{\text{el}}$ usually refers to the electrical current density of ion α, so we introduce the symbol $\tilde{\mathbf{J}}_\alpha^{\text{el}} = \mathbf{J}_\alpha^{\text{el}}/(Z_\alpha e)$ for the particle current density of ion α having the valence Z_α. Likewise, the particle current densities due to convection and diffusion are the usual mass current densities divided by the ionic mass m_α, $\tilde{\mathbf{J}}_\alpha^{\text{conv}} = \mathbf{J}_\alpha^{\text{conv}}/m_\alpha$ and $\tilde{\mathbf{J}}_\alpha^{\text{diff}} = \mathbf{J}_\alpha^{\text{diff}}/m_\alpha$. Combining Eqs. (4.16) and (7.2d) we obtain one of the governing equation for transport in electrohydrodynamics, the so-called Nernst–Planck equation for the current density $\tilde{\mathbf{J}}_\alpha$,

$$\tilde{\mathbf{J}}_\alpha \equiv \tilde{\mathbf{J}}_\alpha^{\text{conv}} + \tilde{\mathbf{J}}_\alpha^{\text{diff}} + \tilde{\mathbf{J}}_\alpha^{\text{el}} = c_\alpha \mathbf{v} - D_\alpha \boldsymbol{\nabla} c_\alpha - \frac{\sigma_\alpha^{\text{el}}}{Z_\alpha e}\,\boldsymbol{\nabla}\phi, \tag{8.1}$$

where c_α is the particle density, or concentration, of ion α. Naturally, in the spirit of linear response theory, the gradients appearing in this equation (note that $\mathbf{v}$ can be thought of arising from pressure gradients) relate only to pressure p_{ext}, concentration c_{ext}, and potential ϕ_{ext} applied externally on top of the equilibrium fields p_{eq}, c_{eq}, and ϕ_{eq},

$$p = p_{\text{eq}} + p_{\text{ext}}, \tag{8.2a}$$

$$c = c_{\text{eq}} + c_{\text{ext}}, \tag{8.2b}$$

$$\phi = \phi_{\text{eq}} + \phi_{\text{ext}}. \tag{8.2c}$$

The reason is that in equilibrium (in the center-of-mass system) there are no current densities, even though the fields themselves may be non-zero. We have already used this fact implicitly in Section 2.4.1, where for a horizontally placed channel the gravitational force was balanced by minus the gradient of the hydrostatic pressure $p_{\text{eq}}(z) = -\rho g z$, and
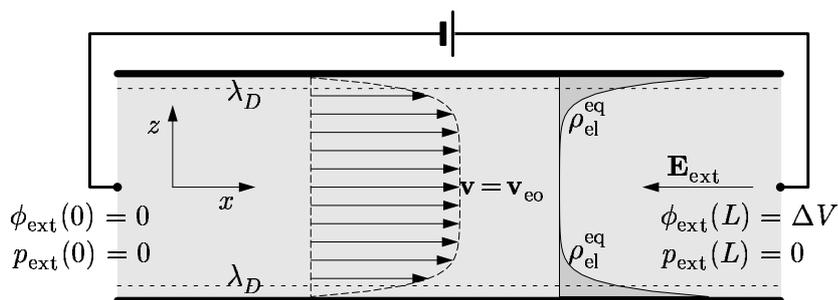
Figure 8.1: The velocity profile $\mathbf{v}$ (dashed line and arrows) and the negative Debye layer charge density profile $\rho_{\mathrm{el}}^{\mathrm{eq}}$ (dark gray and full line) in an ideal electroosmotic (EO) flow inside a cylindrical channel of radius a and positively charged walls (thick horizontal lines). The EO flow is induced by the external potential difference $\Delta\phi_{\mathrm{ext}} = \Delta V$ resulting in the homogeneous electric field $\mathbf{E}_{\mathrm{ext}}$. Note how the velocity profile reaches the constant value v_{eo} at a distance of a few times the Debye length λ_D from the walls. No pressure drop is present along the channel in this ideal case.

in Section 7.3.1, where the electrical force in the Debye layer was balanced by minus the gradient of a concentration-dependent pressure, see Eq. (7.19).

These considerations will be used in the following when analyzing the electroosmotic effect, which is based on moving the ions in the Debye layer by external potential.

8.2   Ideal electroosmotic flow

The principle of electroosmotic (EO) flow is shown in Fig. 8.1. Two metallic electrodes are situated at each end of a channel, in which charge separation at the walls has led to the formation of an equilibrium Debye layer. When a DC potential difference $\Delta V = \Delta\phi_{\mathrm{ext}}$ is applied over the electrodes the resulting electrical field $\mathbf{E}_{\mathrm{ext}}$,

$$\mathbf{E}_{\mathrm{ext}} \equiv -\boldsymbol{\nabla}\phi_{\mathrm{ext}}, \tag{8.3}$$

exerts a body force $\rho_{\mathrm{el}}^{\mathrm{eq}}\mathbf{E}_{\mathrm{ext}}$ on the Debye layer, which begins to move and then by viscous drag pulls the charge neutral bulk liquid along. If no electrochemical processes occur at the electrodes the motion stops after a very short time (of the order μs) when the electrodes are screened by the formation of a Debye layer around them. If, however, electrochemical processes, e.g., electrolysis, can take place at the electrodes such a charge build-up is prevented, and electrical currents can flow in the system and thus move the liquid by viscous drag. In the following we derive an expression for the resulting electroosmotic velocity field in the liquid.

Given the equilibrium charge density $\rho_{\mathrm{el}}^{\mathrm{eq}}(\mathbf{r})$ of the Debye layer the Navier–Stokes equation to be used for analyzing EO flows is

$$\rho\Big(\partial_t\mathbf{v} + (\mathbf{v}\cdot\boldsymbol{\nabla})\mathbf{v}\Big) = -\boldsymbol{\nabla}p_{\mathrm{ext}} + \eta\nabla^2\mathbf{v} - \rho_{\mathrm{el}}^{\mathrm{eq}}\boldsymbol{\nabla}\phi_{\mathrm{ext}}. \tag{8.4}$$

Note that by assumption the external potential does not introduce any changes in the charge density.

We define an ideal EO flow by the following four conditions: (i) the ζ potential is constant along the wall, (ii) the electrical field is homogeneous, (iii) the flow is in steady-state, and (iv) the Debye length is much smaller than the radius or half-width a of the channel, $\lambda_D \ll a$.

As the first explicit example we study the infinite parallel-plate channel with the positively charged walls placed parallel to the xy plane at $z = -h/2$ and $z = h/2$. The external electrical field is applied in the negative x direction, $\mathbf{E} = -E\mathbf{e}_x$, and the external pressure gradient is put to zero. The symmetry of this ideal EO flow setup dictates the following structure of the fields,

$$\boldsymbol{\nabla}\phi_{\text{ext}}(\mathbf{r}) = -\mathbf{E} = E\,\mathbf{e}_x, \tag{8.5a}$$

$$\boldsymbol{\nabla}p_{\text{ext}}(\mathbf{r}) = \mathbf{0}, \tag{8.5b}$$

$$\mathbf{v}(\mathbf{r}) = v_x(z)\,\mathbf{e}_x, \tag{8.5c}$$

and only the x component of the steady-state Navier–Stokes equation is non-trivial,

$$0 = \eta\partial_z^2\,v_x(z) + \left[\epsilon\partial_z^2\phi_{\text{eq}}(z)\right]E. \tag{8.6}$$

The solution almost presents itself by rewriting this equation as

$$\partial_z^2\left[v_x(z) + \frac{\epsilon E}{\eta}\,\phi_{\text{eq}}(z)\right] = 0. \tag{8.7}$$

Employing the boundary conditions

$$v_x\left(\pm\frac{h}{2}\right) = 0, \tag{8.8}$$

we obtain the solution

$$v_x(z) = \left[\zeta - \phi_{\text{eq}}(z)\right]\frac{\epsilon E}{\eta}. \tag{8.9}$$

The two-wall potential $\phi_{\text{eq}}(z)$ is given by Eq. (7.33), which combined with Eq. (8.9) gives

$$v_x(z) = \left[1 - \frac{\cosh\left(\dfrac{z}{\lambda_D}\right)}{\cosh\left(\dfrac{h}{2\lambda_D}\right)}\right]v_{\text{eo}}, \tag{8.10}$$

where we have introduced the EO velocity v_{eo} defined as

$$v_{\text{eo}} \equiv \frac{\epsilon\zeta}{\eta}\,E. \tag{8.11}$$

This expression is analogous to electrophoresis and ionic mobility Eq. (7.13), and we quite naturally define the EO mobility μ_{eo} as

$$\mu_{\text{eo}} \equiv \frac{v_{\text{eo}}}{E} = \frac{\epsilon\zeta}{\eta}. \tag{8.12}$$

Typical values for EO flow are

$$\zeta \approx 100 \text{ mV}, \qquad \mu_{\text{eo}} \approx 7 \times 10^{-8} \text{ m}^2 \text{ (Vs)}^{-1}, \qquad v_{\text{eo}} \approx 1 \text{ mm s}^{-1}. \tag{8.13}$$

For the ideal EO flow we obtain the simple velocity profile

$$\mathbf{v}(\mathbf{r}) \approx v_{\text{eo}} \, \mathbf{e}_x = -\mu_{\text{eo}} \, \mathbf{E}, \quad \text{for } \lambda_D \ll \frac{1}{2} h. \tag{8.14}$$

The corresponding flow rate, the so-called free EO flow rate Q_{eo}, for a section of width w is given by

$$Q_{\text{eo}} = \int_{-h/2}^{h/2} \mathrm{d}y \int_0^w \mathrm{d}z \, v_x(y, z) = v_{\text{eo}} \, wh, \quad \text{for } \lambda_D \ll \frac{1}{2} h. \tag{8.15}$$

The exact expression (still within the Debye-Hückel approximation) valid for any value of λ_D is left as an exercise for the reader.

Analytical results for an ideal EO flow within the Debye-Hückel approximation can also be given for a cylindrical channel of circular cross-section with radius a. The equilibrium potential $\phi_{\text{eq}}(r)$ is given by Eq. (7.36), and the velocity field has the structure $\mathbf{v} = v_x(r) \, \mathbf{e}_x$ and obeys the boundary conditions

$$\partial_r v_x(0) = 0, \qquad v_x(a) = 0. \tag{8.16}$$

Otherwise, the analysis carries through exactly as for the infinite parallel-plate geometry and we arrive at the result

$$v_x(r) = \left[1 - \frac{I_0\left(\frac{r}{\lambda_D}\right)}{I_0\left(\frac{a}{\lambda_D}\right)} \right] v_{\text{eo}}. \tag{8.17}$$

Also here $\mathbf{v} \approx v_{\text{eo}} \, \mathbf{e}_x$ for $\lambda_D \ll a$, so the free EO flow rate becomes

$$Q_{\text{eo}} = \int_0^{2\pi} \mathrm{d}\theta \int_0^a \mathrm{d}r \, r v_x(r, \theta) = v_{\text{eo}} \, \pi a^2, \quad \text{for } \lambda_D \ll a. \tag{8.18}$$

8.3   Debye layer overlap

Although we in the following mostly are dealing with ideal EO flow in the limit $\lambda_D \ll a$, we shall in this section briefly discuss what happens if the Debye length λ_D becomes comparable with the transverse length scale a, and the Debye layers from various part of the wall overlap at the center of the channel. According to our standard value Eq. (7.26) for λ_D this will happen for a cylindrical channel with radius a of the order 10 nm. With modern nanotechnology it is in fact possible to make such channels intentionally, and for some fine-masked porous materials such dimensions actually occur in nature.

In Fig. 8.2(a) are shown three normalized EO flow profiles obtained by plotting $v_x(r)/v_{\text{eo}}$ of Eq. (8.17) with the value $\lambda_D/a = 0.01$, 0.1, and 1. It is seen how, for small values of λ_D/a, a flat nearly constant velocity profile is obtained as stated in the previous section.
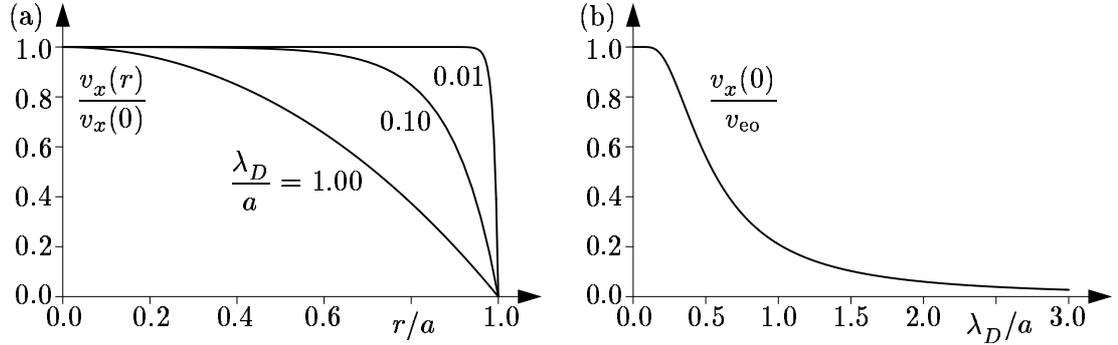
Figure 8.2: (a) The normalized EO flow profile $v_x(r)/v_x(0)$ for a cylindrical channel of radius a with three different values of the Debye length: nearly constant ($\lambda_D/a = 0.01a$), rounded ($\lambda_D/a = 0.1$), and parabolic ($\lambda_D/a = 1$). (b) The maximal velocity in the channel, $v_x(0)$ in units of v_{eo} as a function of λ_D/a. Note that $v_x(0)/v_{eo} \approx 1$ for $\lambda_D/a < 0.1$ while $v_x(0)/v_{eo} \approx a^2/(4\lambda_D^2)$ for $\lambda_D/a \gg 1$.

As λ_D/a increases to 0.1, a rounded profile results still being flat near the center of the channel. When λ_D becomes comparable to a the profile has changed into a paraboloid shape. The latter result is easily verified by Taylor expanding Eq. (8.17) in a/λ_D, which gives

$$v_x(r) \approx \frac{a^2}{4\lambda_D^2} \left[1 - \frac{r^2}{a^2} \right] v_{eo} + \mathcal{O}\Big((a/\lambda_D)^2\Big). \tag{8.19}$$

The expansion also shows that the EO flow profile gets heavily suppressed as λ_D is increased beyond a as is evident from the pre-factor a^2/λ_D^2, see Fig. 8.2(b).

In conclusion, when the Debye screening length is large compared to the transverse dimension of the channel, the screening of the charges on the wall becomes incomplete, and the electrical potential does not vary much across the channel. In this case the Debye layers reaching out from the wall overlap in the center preventing the maintenance of a charge neutral bulk liquid. Together with the Navier–Stokes equation this further implies that the velocity profile likewise does not vary much, and as a result the no-slip boundary condition is felt strongly even at the center of the channel. The electroosmotic flow is therefore strongly suppressed in the limit of Debye layer overlap, i.e., when $\lambda_D \geq a$.

8.4 Ideal EO flow with back-pressure

In Section 8.2 we have seen how a non-equilibrium EO flow can be generated by applying an electrical potential difference $\Delta\phi_{ext}$ along a channel where an equilibrium Debye exists. For an ideal EO flow without any external pressure the flow rate Q_{eo} is given in Eq. (8.18). In this section we study how the flow rate depends on an externally applied pressure difference Δp_{ext}, i.e., we study the capability of an EO microchannel to work as a micropump.

The setup is sketched in Fig. 8.3. A cylindrical channel of radius a and length L is oriented along the x axis between $x = 0$ and $x = L$. As before the walls and the Debye
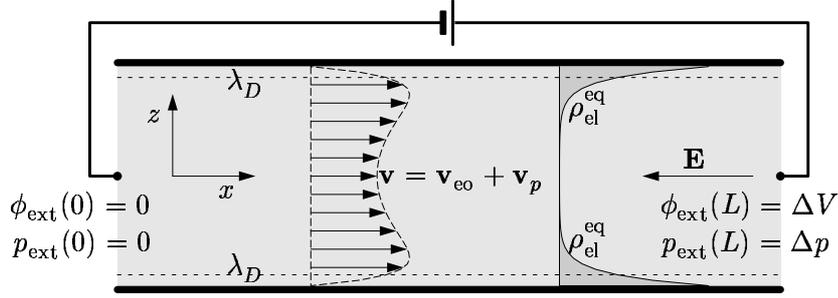
Figure 8.3: The velocity profile $\mathbf{v}$ (dashed line and arrows) and the negative Debye layer charge density profile $\rho_{\text{el}}^{\text{eq}}$ (dark gray and full line) in an ideal electroosmotic (EO) flow with back-pressure $\Delta p_{\text{ext}} = \Delta p$ inside a cylindrical channel of radius a with positively charged walls (thick horizontal lines). The EO flow is induced by the external potential difference $\Delta\phi_{\text{ext}} = \Delta V$. Note how the flat EO flow profile $\mathbf{v}_{\text{eo}}$ from Fig. 8.1 now has a parabolic dent from the superimposed back-pressure driven Poiseuille flow profile $\mathbf{v}_p$.

layer are positively and negatively charged, respectively. The external electrical potential ϕ_{ext} and pressure p_{ext}, both assumed to depend linearly on x, are applied as follows:

$$\phi_{\text{ext}}(x = 0) = 0 \qquad \phi_{\text{ext}}(x = L) = \Delta V \qquad -\boldsymbol{\nabla}\phi_{\text{ext}} = \mathbf{E} = -\frac{\Delta V}{L}\,\mathbf{e}_x \qquad (8.20a)$$

$$p_{\text{ext}}(x = 0) = 0 \qquad p_{\text{ext}}(x = L) = \Delta p \qquad -\boldsymbol{\nabla}p_{\text{ext}} = -\frac{\Delta p}{L}\,\mathbf{e}_x \qquad (8.20b)$$

The Navier–Stokes equation for this highly symmetric problem, where $\mathbf{v}(\mathbf{r}) = v_x(r)\mathbf{e}_x$, reduces to the following linear differential equation for the x component:

$$0 = \eta\nabla^2\,v_x(r) + \left[\epsilon\nabla^2\phi_{\text{eq}}(r)\right]\frac{\Delta V}{L} - \frac{\Delta p}{L}, \qquad (8.21)$$

with the boundary conditions

$$v_x(a) = 0, \qquad \partial_r v_x(0) = 0. \qquad (8.22)$$

The equation is solved by superimposing an EO flow $v_{x,\text{eo}}(r)$, Eq. (8.17), and a standard Poiseuille flow $v_{x,p}(r)$, Eq. (2.33a) with opposite sign for Δp,

$$v_x(r) = v_{x,p}(r) + v_{x,\text{eo}}(r) \qquad (8.23a)$$

$$0 = \eta\nabla^2\,v_{x,\text{eo}}(r) - \rho_{\text{el}}^{\text{ext}}(r)\frac{\Delta V}{L}, \qquad v_{x,\text{eo}}(a) = 0, \qquad \partial_r v_{x,\text{eo}}(0) = 0, \qquad (8.23b)$$

$$0 = \eta\nabla^2\,v_{x,p}(r) - \frac{\Delta p}{L}, \qquad v_{x,p}(a) = 0, \qquad \partial_r v_{x,p}(0) = 0. \qquad (8.23c)$$

The resulting velocity field of EO flow with back-pressure is therefore

$$v_x(r) = \left[1 - \frac{I_0\left(\frac{r}{\lambda_D}\right)}{I_0\left(\frac{a}{\lambda_D}\right)}\right]\frac{\epsilon\zeta}{\eta}\frac{\Delta V}{L} - \left[a^2 - r^2\right]\frac{1}{4\eta}\frac{\Delta p}{L}. \qquad (8.24)$$
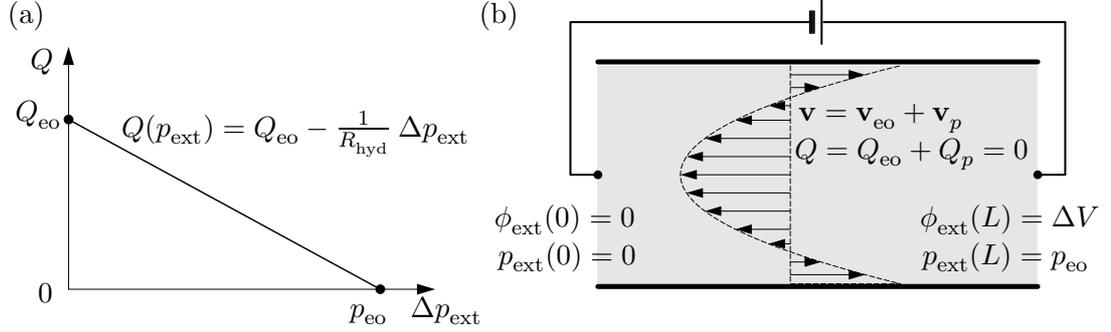
Figure 8.4: (a) The flow rate-pressure characteristic Q–p for an ideal EO flow with back-pressure Δp_{ext}. (b) The flow profile $\mathbf{v}$ in a cylindrical microchannel at maximal back-pressure, the electroosmotic pressure p_{eo}, where the net flow rate is zero, $Q = 0$.

Note that the superposition procedure works because the high symmetry has rendered the Navier–Stokes equation linear by removing the inertial term $(\mathbf{v}\cdot\boldsymbol{\nabla})\mathbf{v}$.

For an ideal EO flow, i.e., in the limit $\lambda_D \ll a$, the flow rate derived from Eq. (8.24) is

$$Q = Q_{\text{eo}} + Q_p = \pi a^2 v_{\text{eo}} - \frac{1}{R_{\text{hyd}}} \Delta p = \frac{\pi a^2 \epsilon \zeta}{\eta L} \Delta V - \frac{\pi a^4}{8\eta L} \Delta p. \tag{8.25}$$

This yields the linear flow rate-pressure characteristic Q–p shown in Fig. 8.4(a). Two points on the Q–p graph characterizes the capability of the EO microchannel to work as a micropump. One is the free EO flow rate, $(Q, p) = (Q_{\text{eo}}, 0)$, obtained at zero back-pressure, $\Delta p_{\text{ext}} = 0$. The other is the zero-flow pressure, or electroosmotic pressure, $(Q, p) = (0, p_{\text{eo}})$, defined as the back-pressure needed to exactly cancel the EO flow, i.e., $R_{\text{hyd}} p_{\text{eo}} \equiv Q_{\text{eo}}$,

$$Q_{\text{eo}} \equiv \frac{\pi a^2 \epsilon \zeta}{\eta L} \Delta V \qquad \text{at free flow } (Q, p) = (Q_{\text{eo}}, 0), \tag{8.26a}$$

$$p_{\text{eo}} \equiv \frac{Q_{\text{eo}}}{R_{\text{hyd}}} = \frac{8\epsilon \zeta}{a^2} \Delta V \quad \text{at zero flow } (Q, p) = (0, p_{\text{eo}}). \tag{8.26b}$$

The flow profile when running the EO micropump at zero-flow is sketched in Fig. 8.4(b).

Typical values for Q_{eo} and p_{eo} are found by using $\zeta = 0.1$ V, $a = 10$ μm, $L = 100$ μm, $\eta = 1$ mPa and $\epsilon = 78\epsilon_0$,

$$\frac{Q_{\text{eo}}}{\Delta V} = 0.21 \text{ nL s}^{-1} \text{ V}^{-1}, \tag{8.27a}$$

$$\frac{p_{\text{eo}}}{\Delta V} = 5.52 \text{ Pa V}^{-1}. \tag{8.27b}$$

These numbers are not very high. It is clear from Eq. (8.26a) that a high flow rate in a single-channel EO micropump is obtained with a high voltage drop ΔV, a high zeta-potential ζ, a large radius a and a short channel length L. However, Eq. (8.26b) reveals

that the pressure capability of a single channel scales as a^{-2}. If a is chosen to be large to secure a decent flow rate then the pressure capability is low and *vice versa*. A single EO channel can therefore mainly be used in the free flow case, where, e.g., the flat EO flow profile can be utilized to move concentration profiles in an undistorted manner along a channel. If one is to construct a micropump based on EO flow more elaborate designs are needed. This is discussed in the following sections.

8.5   The many-channel EO pump

An EO-based micropump with decent flow rate and pressure capabilities can be constructed by using a large number of narrow channels in a parallel coupling. Consider a large number N of identical cylindrical channels of radius a, length L, and zeta-potential ζ. When coupled in parallel all these channels experience the same external pressure p_{ext}, so the pressure capability $p_{\text{eo},N}$ for the ensemble of channels is the same as for each individual channel, while the free EO flow rate $Q_{\text{eo},N}$ scales with the number of channels,

$$Q_{\text{eo},N} = N Q_{\text{eo}} = N \frac{\pi a^2 \epsilon \zeta}{\eta L} \, \Delta V \quad \text{at free flow } (Q,p) = (Q_{\text{eo},N}, 0), \qquad (8.28\text{a})$$

$$p_{\text{eo},N} = p_{\text{eo}} \quad = \frac{8 \epsilon \zeta}{a^2} \, \Delta V \qquad \text{at zero flow } (Q,p) = (0, p_{\text{eo},N}). \qquad (8.28\text{b})$$

Now, only the EO pressure $p_{\text{eo},N}$ depends on the radius a while the EO flow rate $Q_{\text{eo},N}$ depends on the total open area $\mathcal{A}_{\text{open}} = N \pi a^2$. The area is of the same order of magnitude as the total cross sectional area $\mathcal{A}_{\text{tot}}$ occupied with the channels including walls a voids between the channels. For a closed packed hexagonal array of parallel cylindrical channels of inner radius a and outer radius $a + w$, i.e., channels with a wall thickness of w, the total area $\mathcal{A}_{\text{tot}}$ of the ensemble of channels is given by

$$\mathcal{A}_{\text{tot}} = \frac{2\sqrt{3}}{\pi} \left(1 + \frac{w}{a}\right)^2 N \pi a^2 = \frac{2\sqrt{3}}{\pi} \left(1 + \frac{w}{a}\right)^2 \mathcal{A}_{\text{open}}. \qquad (8.29)$$

Although in principle it is possible to fabricate a many-channel EO pump by using microtechnology, it is in practice not easy to fabricate a sufficiently high number of parallel channels. But by using the so-called frits there is a way around this problem. A frit consists of closely packed, sintered glass spheres with a diameter of the order 1 μm, which makes it a porous material due to the voids between the spheres. Frits are widely used as filters so they are produced commercially.

A frit can also be used as a many-channel EO pump. Instead of a regular array of cylindrical channels, the frit contains a high number of channels of irregular shape and size forming a percolation pattern through the frit. Despite the irregularities of the frit channels they can still serve as EO flow channels.

In Fig. 8.5 is shown a frit-based EO micropump designed and fabricated in the group of Bruus at MIC. The pump achieves $Q_{\text{eo}} \approx 0.8$ μL/s and $p_{\text{eo}} \approx 4$ kPa when running at a voltage of $\Delta V = 30$ V. To stabilize the pump the electrodes have been separated from the liquid flow by anion exchange membranes. These membranes only allow the passage of
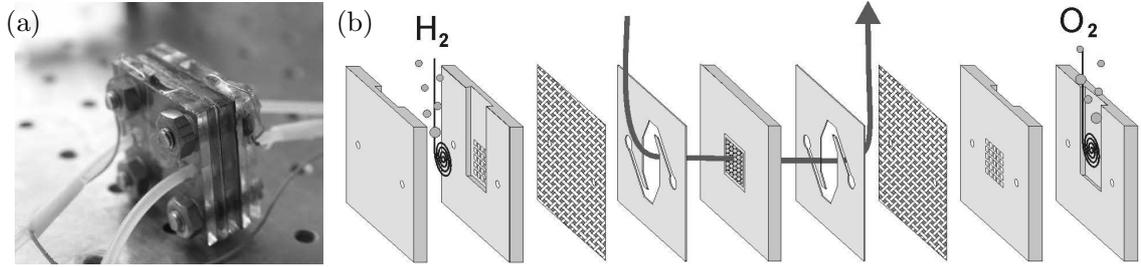
Figure 8.5: (a) A frit-based EO micropump designed and built in the group of Bruus at MIC. For $\Delta V = 30$ V, the pump has $Q_{\mathrm{eo}} \approx 0.8$ μL/s and $p_{\mathrm{eo}} \approx 4$ kPa, and it can run steadily for hours. (b) The pump consists of layers of polymer sheets micromachined using the laser ablation technique described in Fig. 2.4. The glass frit (gray hatched square) is situated in the central layer. The platinum electrodes (spirals), where gas bubbles are generated by electrolysis, are separated from the liquid flow (the arrow) by anion exchange membranes (white and gray hatched layers), which only allow the passage of OH^- ions.

OH^{-1} ions, and thus prevent the electrolytic gases generated at the electrodes to interfere with the liquid flow. With the design the pump can run steadily for hours.

The shown prototype of the frit-based EO pump has the dimensions $20 \times 20 \times 10$ mm^3, the size mainly being set by the commercially available frits, which are cylindrical with a radius of 1.8 mm and a thickness of 2 mm, and the size of the screws holding it together. It is of course the plan to integrate the pump directly in a lab-on-a-chip system, now that the prototype has been tested successfully.

8.6   The cascade EO pump

While the many-channel EO pump solved the problem of obtaining a high pressure capability, we still have not gotten around the problem of the low nL/s flow rate indicated by Eq. (8.27a). In many microfluidic applications a flow rate of μL/s is needed. With a simple EO pump this can be achieved by applying high voltages of the order 1 kV. This is of course doable but not very practical.

A solution to this problem is a so-called cascade EO pump, which consists of several EO pump stages in series each with a zero voltage drop. A single zero-voltage EO pump stage can be realized by breaking the translation symmetry along the flow direction. A particularly simple example of this principle is shown in Fig. 8.6(a).

Consider two cylindrical channels of radius a_1 and a_2, respectively, but with the same length L and zeta potential ζ. These two channels are joined together in series to form one long channel of length $2L$. All effects induced by the transition from the wide to the narrow part of the resulting channel are neglected. The three positions of interest are $x = 0$, L and $2L$. The applied voltage $\phi_{\mathrm{ext}}(x)$ is going from 0 to ΔV and back to zero at these three points, respectively. The pressure is $p_{\mathrm{ext}}(0) = 0$, $p_{\mathrm{ext}}(L) = p_c$, and $p_{\mathrm{ext}}(2L) = \Delta p$.

We introduce the size ratio $\alpha \equiv a_1/a_2$ and use channel 2 as our reference,

$$\alpha \equiv \frac{a_1}{a_2}, \qquad R^*_{\text{hyd}} \equiv \frac{8\eta L}{\pi a_2^4}, \qquad Q^*_{\text{eo}} \equiv \frac{\pi a_2^2 \epsilon \zeta}{\eta L} \, \Delta V \qquad (8.30)$$

so that the hydraulic resistances and EO flow rates become

$$Q_{\text{eo},1} = \alpha^2 Q^*_{\text{eo}}, \qquad R_{\text{hyd},1} = \alpha^{-4} R^*_{\text{hyd}}, \qquad (8.31\text{a})$$

$$Q_{\text{eo},2} = -Q^*_{\text{eo}}, \qquad R_{\text{hyd},2} = R^*_{\text{hyd}}. \qquad (8.31\text{b})$$

Note the minus sign for $Q_{\text{eo},2}$ due to the direction of the voltage drop. The Q–p characteristic of the single-stage EO pump is found by noting that the flow rate Q in the two sections must be identical due to mass conservation,

$$Q = Q_{\text{eo},1} + \frac{0 - p_c}{R_{\text{hyd},1}} \quad = \alpha^2 Q^*_{\text{eo}} - \alpha^4 \frac{p_c}{R^*_{\text{hyd}}}, \qquad (8.32\text{a})$$

$$Q = Q_{\text{eo},2} + \frac{p_c - \Delta p}{R_{\text{hyd},2}} = -Q^*_{\text{eo}} + \frac{p_c - \Delta p}{R^*_{\text{hyd}}}. \qquad (8.32\text{b})$$

Solving these equations with respect to the unknown flow rate Q and the central pressure p_c at $x = L$ we get

$$p_c = \frac{1 + \alpha^2}{1 + \alpha^4} \, R^*_{\text{hyd}} Q^*_{\text{eo}} + \frac{1}{1 + \alpha^4} \, \Delta p, \qquad (8.33\text{a})$$

$$Q = \frac{\alpha^2 - \alpha^4}{1 + \alpha^4} \, Q^*_{\text{eo}} - \frac{\alpha^4}{1 + \alpha^4} \, \frac{\Delta p}{R^*_{\text{hyd}}}. \qquad (8.33\text{b})$$

From this we readily find the zero-flow pressure capability p_{eo} and the zero-pressure free EO flow rate Q_{eo},

$$p_{\text{eo}} = \left(\frac{1}{\alpha^2} - 1\right) R^*_{\text{hyd}} Q^*_{\text{eo}}, \qquad (8.34\text{a})$$

$$Q_{\text{eo}} = \frac{\alpha^2 - \alpha^4}{1 + \alpha^4} \, Q^*_{\text{eo}}. \qquad (8.34\text{b})$$

This result implies that despite the zero total voltage drop along the single-stage EO channel it nevertheless functions as an EO pump. The larger the difference is between the two parts of the single-stage channel, i.e., the more the size ration α deviates from unity, the larger is the EO effect.

In the special case $\alpha = 1$ where the two parts of the single-stage EO pump are identical, the pressure capability is zero simply because the EO flows in the two parts of the single-stage channel are equal in size but opposite in direction. In the limit $\alpha \gg 1$ the narrow part 2 dominates the pump characteristic and we retrieve the results from the ideal EO pump with a reversal of direction due to the reverse voltage drop. Likewise in the opposite limit, $\alpha \ll 1$, the narrow part 1 dominate, but now without a reversal of flow direction.
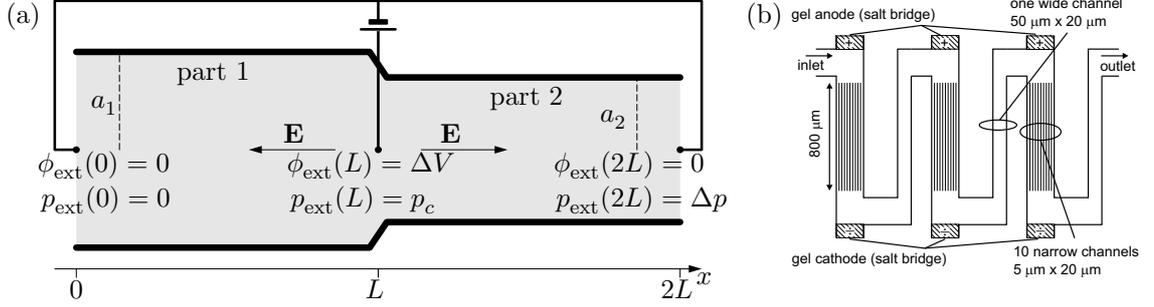
Figure 8.6: (a) A single stage (with two parts) in a cascade EO pump, which yields a finite EO flow although the total voltage drop along the channel is zero. (b) The cascade EO pump from Fig. 3.11(a) containing three identical stages. Each stage consists of ten narrow channels in series with one wide channel, and the total voltage drop per stage is zero.

A zero-voltage EO pump stage can also be constructed by letting channel 1 be a many-channel EO pump and channel 2 a single-channel EO pump, as shown in Fig. 8.6(b). Let us take N^2 narrow channels of radius $a_1 = a_2/N$, and as before use channel 2 as our reference:

$$\alpha \equiv \frac{a_1}{a_2} = \frac{1}{N}, \qquad R_{\text{hyd}}^* \equiv \frac{8\eta L}{\pi a_2^4}, \qquad Q_{\text{eo}}^* \equiv \frac{\pi a_2^2 \epsilon \zeta}{\eta L} \Delta V. \tag{8.35}$$

With this choice of geometry the two parts of the EO pump stage have the same area available for flow, $\mathcal{A} = N^2 \pi a_1^2 = \pi a_2^2$, and the hydraulic resistances and EO flow rates become

$$Q_{\text{eo},1} = \frac{1}{N^2} Q_{\text{eo}}^*, \qquad R_{\text{hyd},1} = N^4 R_{\text{hyd}}^*, \tag{8.36a}$$

$$Q_{\text{eo},N} = Q_{\text{eo}}^*, \qquad R_{\text{hyd},N} = N^2 R_{\text{hyd}}^*, \tag{8.36b}$$

$$Q_{\text{eo},2} = -Q_{\text{eo}}^*, \qquad R_{\text{hyd},2} = R_{\text{hyd}}^*. \tag{8.36c}$$

Here subscript N refers to the ensemble of N^2 parallel channels in section 1, while a single channel here carries the subscript 1. The flow rate in the two sections now become

$$Q = Q_{\text{eo},N} + \frac{0 - p_c}{R_{\text{hyd},N}} = Q_{\text{eo}}^* - \frac{1}{N^2} \frac{p_c}{R_{\text{hyd}}^*}, \tag{8.37a}$$

$$Q = Q_{\text{eo},2} + \frac{p_c - \Delta p}{R_{\text{hyd},2}} = -Q_{\text{eo}}^* + \frac{p_c - \Delta p}{R_{\text{hyd}}^*}. \tag{8.37b}$$

From this we find in analogy with Eq. (8.33) that the central pressure p_c and the flow rate Q depend linearly on Q_{eo}^* and the back-pressure Δp,

$$p_c = \frac{2N^2}{N^2 + 1} R_{\text{hyd}}^* Q_{\text{eo}}^* + \frac{N^2}{N^2 + 1} \Delta p \tag{8.38a}$$

$$Q = \frac{N^2 - 1}{N^2 + 1} Q_{\text{eo}}^* - \frac{1}{N^2 + 1} \frac{\Delta p}{R_{\text{hyd}}^*}. \tag{8.38b}$$

The zero-flow pressure capability p_{eo} and the zero-pressure free EO flow rate Q_{eo} becomes,

$$p_{\mathrm{eo}} = \left(N^2 - 1\right) R_{\mathrm{hyd}}^* Q_{\mathrm{eo}}^* = \left(1 - \frac{1}{N^2}\right) R_{\mathrm{hyd},1} Q_{\mathrm{eo},1}, \qquad (8.39\mathrm{a})$$

$$Q_{\mathrm{eo}} = \frac{N^2 - 1}{N^2 + 1} Q_{\mathrm{eo}}^* \qquad = \frac{1 - \frac{1}{N^2}}{1 + \frac{1}{N^2}} Q_{\mathrm{eo},2}. \qquad (8.39\mathrm{b})$$

It is thus seen that as the number of sub-channels in section 1 grows, the pressure capability of the zero-voltage EO pump stage approaches that of a single narrow sub-channel in section 1, while the free EO flow rate approaches that of the wide channel in section 2.

Regardless of how a single zero-voltage EO pump stage with a pressure capability of Δp is realized, it is possible to join several such stages in series thus ended with a so-called cascade EO pump, where the pressure capability is augmented by Δp for each stage added, while the free EO flow rate remains unchanged. Thus very efficient EO pumps can be fabricated which only requires the same low voltage applied to the center of each zero-voltage stage, see Exercises 8.6 and 8.7.

8.7 Exercises

Exercise 8.1
EO flow in an infinite parallel-plate channel
Consider the infinite parallel-plate channel of height h studied in Section 8.2 with the zeta potential ζ on both walls, $\phi_{\mathrm{eq}}(\pm h/2) = \zeta$. Check that the flow field $v_x(z)$ Eq. (8.10) is a solution to the steady-state Navier–Stokes equation (8.6) fulfilling the no-slip boundary conditions.

Exercise 8.2
The flow rate and pressure capability of an infinite parallel-plate EO pump
Consider an infinite parallel-plate EO pump of length L, width w and height h with the zeta potential ζ on the top and bottom walls. The pumping liquid has the viscosity η. The applied voltage drop along the pump driving the EO flow is ΔV, and it is assumed to give rise to an homogeneous electrical field.
   (a) Derive an expression for the zero-pressure free EO flow rate Q_{eo}.
   (b) Derive an expression for the zero-flow pressure capability p_{eo}.

Exercise 8.3
EO flow in a cylindrical channel with circular cross-section
Consider the cylindrical channel with circular cross-section of radius a studied in Section 8.2 with the zeta potential ζ on the wall, $\phi_{\mathrm{eq}}(a) = \zeta$. Write down the relevant component of the Navier–Stokes equation and check that the flow field $v_x(r)$ Eq. (8.17) is a solution to this equation fulfilling the no-slip boundary condition.

Exercise 8.4
The internal pressure in a single-stage zero-voltage EO pump
Consider the single-stage zero-voltage EO pump studied in the first half of Section 8.6.

(a) Derive Eqs. (8.32a) and (8.32b) and show that they imply the expression for the internal pressure p_c Eq. (8.33a).

(b) Discuss p_c in the free-flow case $\Delta p = 0$ and in the zero-EO-flow case $Q_{eo}^* = 0$. Try to relate the discussion to other known cases.

Exercise 8.5
The geometry of the many-channel EO pump
Consider the ensemble of N identical, parallel cylindrical channels of inner radius a and wall thickness w forming a closed packed hexagonal lattice. Prove Eq. (8.29) relating the open area $\mathcal{A}_{open}$ available for fluid flow to the total cross-sectional area $\mathcal{A}_{tot}$ of the ensemble.

Exercise 8.6
A multi-stage EO cascade pump with a total voltage drop of zero
Consider as in Section 8.6 a multi-stage EO cascade pump consisting of M identical copies of a single-stage zero-voltage EO pump coupled in series. The multi-stage pump is placed between $x = 0$ and $x = M\,2L$. The j-th stage lies between $x = (j-1)\,2L$ and $x = j\,2L$. Each stage has the voltages zero at its ends and V at the center $x = (j - \frac{1}{2})\,2L$. The corresponding pressures are denoted p_{j-1} and p_j at the ends and p_j^c in the center.

(a) Find the pressure-flow rate characteristic of this multi-stage, porous EO pump, i.e., express flow rate Q as a function of the total pressure drop $\Delta p = p_M - p_0$ and the parameters R_{hyd}^*, Q_{eo}^*, N, and M.

(b) Determine the EO pressure p_{eo}, i.e., $p_M - p_0$ when $Q = 0$, and the flow rate Q_{eo} in the case of free EO flow, i.e., when $p_M - p_0 = 0$.

Exercise 8.7
Experimental realization of a multi-stage EO cascade pump
Multi-stage EO pumps with 6 and 15 stages has been developed by Takamura et al., Electrophoresis **24**, 185-192 (2003), see the figure below. Each stage consists of a ten-channel EO pump followed by a single-channel EO pump as described in the second half of Section 8.6.
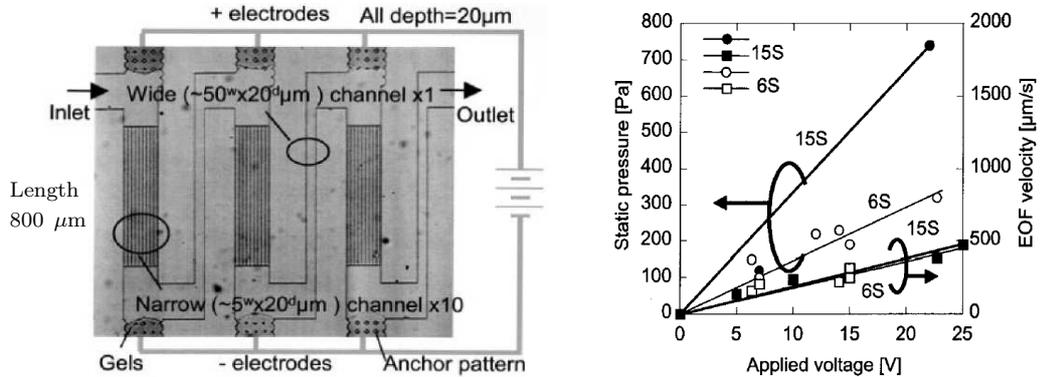
(a) Use the experimental results to estimate the values of the EO mobility μ_{eo} and the zeta potential ζ assuming that the liquid is pure water.

(b) Write down the values of the parameters L, N, M, R_{hyd}^*.

(c) Calculate p_{eo} and Q_{eo} (for a 6 and a 15 stage pump) and compare with the experimental results.

8.8   Solutions

Solution 8.1
EO flow in an infinite parallel-plate channel
Using $\phi(z)$ from Eq. (7.33) as the equilibrium potential we can rewrite the velocity field v_x given in Eq. (8.10) as $v_x(z) = [1 - \phi_{eq}(z)/\zeta]\, v_{eo} = v_{eo} - (\epsilon E/\eta)\phi_{eq}(z)$. When this is inserted into the Navier–Stokes equation (8.6) the two terms containing $\phi_{eq}(z)$ cancel and we arrive at $\partial_z^2 v_{eo} = 0$, which is true as v_{eo} is a constant. Moreover, the boundary conditions are fulfilled since $v_x(\pm h/2) = [1 - \phi_{eq}(\pm h/2)/\zeta]\, v_{eo} = [1 - \zeta/\zeta]\, v_{eo} = 0$.

Solution 8.2
The flow rate and pressure capability of an infinite parallel-plate EO pump
The magnitude of the electric field is given by $E = \Delta V/L$.
    (a) From Eq. (8.15) follows $Q_{eo} = v_{eo} wh = \frac{\epsilon \zeta wh}{\eta L}\Delta V$.
    (b) From Eq. (8.26b) follows $p_{eo} = R_{hyd} Q_{eo} = \frac{12\eta L}{wh^3}\frac{\epsilon \zeta wh}{\eta L}\Delta V = \frac{12\epsilon \zeta}{h^2}\Delta V$.

Solution 8.3
EO flow in a cylindrical channel with circular cross-section
In analogy with Eq. (8.7) the non-linear term vanishes and only the x-component of the Navier–Stokes equation is non-zero, $(\partial_r^2 + \frac{1}{r}\partial_r)[v_x(r) + (\epsilon E/\eta)\phi_{eq}(r)] = 0$. Using $\phi(r)$ from Eq. (7.36) as the equilibrium potential we can rewrite the velocity field v_x given in Eq. (8.17) as $v_x(r) = [1 - \phi_{eq}(r)/\zeta]\, v_{eo} = v_{eo} - (\epsilon E/\eta)\phi_{eq}(r)$. When this is inserted into the Navier–Stokes equation above, the two terms containing $\phi_{eq}(z)$ cancel and we arrive at $(\partial_r^2 + \frac{1}{r}\partial_r)v_{eo} = 0$, which is true as v_{eo} is a constant. Moreover, the boundary condition is fulfilled since $v_x(a) = [1 - \phi_{eq}(a)/\zeta]\, v_{eo} = [1 - \zeta/\zeta]\, v_{eo} = 0$.

Solution 8.4
The internal pressure in a single-stage zero-voltage EO pump
    (a) This is done by straightforward algebra, no tricks is envolved.
    (b) For $\Delta p = 0$ we discuss three cases. (i) The two sections are identical, $\alpha = 1$, which makes $Q = 0$ and $p_c = R_{hyd}^* Q_{eo}^* = R_{hyd,1} Q_{eo,1} = R_{hyd,2} Q_{eo,2}$; both sections enters on equal footing. (ii) Section 2 has a vanishing hydraulic resistance, $\alpha \ll 1$, which makes $Q = \alpha^2 Q_{eo}^* = Q_{eo,1}$ and $p_c = \alpha^2 R_{hyd}^* Q_{eo}^* = R_{hyd,2} Q_{eo,2}$; section 1 delivers the flow rate, while section 2 creates the pressure. (iii) Section 1 has a vanishing hydraulic resistance, $\alpha \gg 1$, which makes $Q = -Q_{eo}^* = Q_{eo,2}$ and $p_c = \alpha^{-2} R_{hyd}^* Q_{eo}^* = R_{hyd,1} Q_{eo,2}$; section 2 delivers the flow rate, while section 1 creates the pressure.

    For $Q_{eo}^* = 0$ the circuit is just a normal series coupling of $R_{hyd,1}$ and $R_{hyd,2}$. The total resistance is $R_{hyd} = R_{hyd,1} + R_{hyd,2} = (1 + \alpha^{-4})R_{hyd}^*$ so that $Q = \Delta p/R_{hyd} = \frac{1}{1+\alpha^{-4}}\Delta p/R_{hyd}^* = \frac{\alpha^4}{1+\alpha^4}\Delta p/R_{hyd}^*$ in accordance with Eq. (8.33b). The central pressure is then $p_c = R_{hyd,1}Q = \alpha^{-4}R_{hyd}^* \times \frac{\alpha^4}{1+\alpha^4}\Delta p/R_{hyd}^* = \frac{1}{1+\alpha^4}\Delta p$ in agreement with Eq. (8.33a).

Solution 8.5
The geometry of the many-channel EO pump
When close packing N circular disks of radius $a + w$ we note that each disk has six neighbors. The centers of the central disk and any two neighbors that touches each other form an equilateral triangle with side-length $2(a+w)$ and area $\sqrt{3}(a+w)^2$. One third of this area is designated to each of the three disks, and since the central disk participates in six such areas, it takes up an area of $6 \times \frac{1}{3} \times \sqrt{3}(a+w)^2 = 2\sqrt{3}(a+w)^2$. Thus in total the N disks take up an area $\mathcal{A}_{\text{tot}} = 2\sqrt{3}(a+w)^2 N = (2\sqrt{3}/\pi)(1+w/a)^2 \times N\pi a^2 = (2\sqrt{3}/\pi)(1+w/a)^2 \mathcal{A}_{\text{open}}$, since the open area of each disk is πa^2.

Solution 8.6
A multi-stage EO cascade pump with a total voltage drop of zero
Due to mass conservation the flow rate Q is the same in each of the M stages of the pump.

(a) Using the single-stage result Eq. (8.38b), we can write the flow through the jth stage of the multi-stage EO pump as $Q = \frac{N^2-1}{N^2+1}Q_{\text{eo}}^* - \frac{1}{N^2+1}(p_j - p_{j-1})/R_{\text{hyd}}^*$. Adding these M equations, utilizing $\sum_{j=1}^{M}(p_j - p_{j-1}) = p_M - p_0 = \Delta p$, $\sum_{j=1}^{M} Q = MQ$, and $\sum_{j=1}^{M} Q_{\text{eo}}^* = MQ_{\text{eo}}^*$, and finally dividing by M, we arrive at the $Q - p$ characteristics,

$$Q = \frac{N^2 - 1}{N^2 + 1} Q_{\text{eo}}^* - \frac{1}{M(N^2 + 1)} \frac{\Delta p}{R_{\text{hyd}}^*}. \tag{8.40}$$

(b) From the result above we easily find the EO pressure cabability at $Q = 0$ to be $p_{\text{eo}} = M(N^2 - 1)R_{\text{hyd}}^* Q_{\text{eo}}^* \rightarrow MR_{\text{hyd},1}Q_{\text{eo},1}$, for $N \rightarrow \infty$. Likewise, the free EO flow rate at $\Delta p = 0$ becomes $Q_{\text{eo}} = \frac{N^2-1}{N^2+1} Q_{\text{eo}}^* \rightarrow Q_{\text{eo},2}$, for $N \rightarrow \infty$.

Solution 8.7
Experimental realization of a multi-stage EO cascade pump
The experimental results of the pump is given in panel (b) of the figure in Exercise 8.7. Note that the ordinate axis to the left is the zero-flow pressure capability p_{eo}, while the axis to the right is the EO velocity v_{eo}.

(a) At the figure we read off $(\Delta V, v_{\text{eo}}) = (25 \text{ V}, 500 \text{ } \mu\text{m/s})$ while $L = 800$ μm, and thus from Eq. (8.12)

$$\mu_{\text{eo}} \equiv \frac{v_{\text{eo}}}{E} = \frac{v_{\text{eo}}}{\Delta V/L} = \frac{5 \times 10^{-4} \text{ m/s} \times 8 \times 10^{-4} \text{ m}}{25 \text{ V}} = 1.6 \times 10^{-8} \text{ m}^2/(\text{V s}). \tag{8.41}$$

From Eq. (8.12) we also get

$$\zeta = \frac{\eta \mu_{\text{eo}}}{\epsilon} = \frac{10^{-3} \text{ Pa s} \times 1.6 \times 10^{-8} \text{ m}^2/(\text{V s})}{78.0 \times 8.85 \times 10^{-12} \text{ F/m}} = 23.2 \text{ mV}. \tag{8.42}$$

(b) The parameters are: $L = 800$ μm, $N = \sqrt{10}$, $M = 6$ or 15, and with $\eta = 10^{-3}$ Pas, $w = 5 \times 10^{-5}$, and $h = 2 \times 10^{-5}$m we obtain

$$R_{\text{hyd}}^* = \frac{12\eta L}{wh^3(1 - 0.63h/w)} = 3.21 \times 10^{13} \text{ Pa s/m}^3 = 32.1 \text{ Pa s/nL}. \tag{8.43}$$

(c) At $\Delta V = 10$ V the EO flow Q_{eo} rate is found by multiplying the cross sectional area with the observed EO velocity read from the graph:

$$Q_{eo} = v_{eo}wh = 2 \times 10^{-4} \text{ m/s} \times 5 \times 10^{-5} \text{ m} \times 2 \times 10^{-5} \text{ m} = 0.2 \text{ nL/s}. \tag{8.44}$$

At the same voltage the pressure per stage is given by Eq. (8.39a) as

$$p_{eo} = \left(N^2 - 1\right) R_{hyd}^* Q_{eo} = 9 \times 3.21 \times 10^{13} \times 2 \times 10^{-13} \text{ Pa} = 58 \text{ Pa}. \tag{8.45}$$

For the 6-stage and 15-stage pump the predicted pressures are

$$p_{eo}(6) = \ 6 \times 58 \text{ Pa} = 348 \text{ Pa}, \tag{8.46a}$$
$$p_{eo}(15) = 15 \times 58 \text{ Pa} = 870 \text{ Pa}. \tag{8.46b}$$

The measured pressures are 150 Pa and 350 Pa, i.e., a factor of 2.5 lower than predicted. It may be due to a hydraulic leak or an uneven distribution of voltage drops that the pump cannot sustain as high a pressure as predicted.

Chapter 9

Dielectrophoresis

Dielectrophoresis (DEP) is the movement of a charge neutral particle in a dielectric fluid induced by an inhomogeneous electric field. This driving field can be either DC or AC.

We begin our analysis by considering a DC field $\mathbf{E}$. Moreover, we shall exclusively work with linear media such that the polarization $\mathbf{P}$ of the dielectric fluid is given by Eq. (7.12)

$$\mathbf{P} = \epsilon_0 \chi \, \mathbf{E}, \tag{9.1}$$

where χ is the susceptibility, and such that the induced dipole moment $\mathbf{p}$ of the dielectric particle is

$$\mathbf{p} = \alpha \, \mathbf{E}, \tag{9.2}$$

where α is the polarizability.

According to Eq. (7.4) a dielectric force $\mathbf{F}_{\mathrm{dip}}$ acts on a dipole moment $\mathbf{p}$ situated in an inhomogeneous electric field $\mathbf{E}$, i.e., a field with a non-zero gradient tensor $\boldsymbol{\nabla}\mathbf{E}$,

$$\mathbf{F}_{\mathrm{dip}} = (\mathbf{p}\cdot\boldsymbol{\nabla})\mathbf{E}. \tag{9.3}$$

Before launching a rigorous analysis we shall build our intuition regarding induced polarization by presenting some heuristic arguments.

9.1   Induced polarization and dielectric forces; heuristically

As sketched in Fig. 9.1 we consider a dielectric sphere with dielectric constant ϵ_2 placed in a dielectric fluid with dielectric constant ϵ_1. An inhomogeneous electric field $\mathbf{E}$ is imposed by charging a spherical electrode to the left and a planar electrode to the right.

From Eq. (7.12),

$$\mathbf{D} = \epsilon_0\mathbf{E} + \mathbf{P} = \epsilon_0(1 + \chi)\mathbf{E} = \epsilon\mathbf{E}, \tag{9.4}$$

follows that when an electric field $\mathbf{E}$ is applied to a medium with a large dielectric constant ϵ, the medium will acquire a large polarization $\mathbf{P}$ and consequently contain many dipoles $\mathbf{p}$. This is sketched in Fig. 9.1(a1), where the medium (light gray) with the smaller dielectric constant ϵ_1 contains a few polarization charges at its surfaces, while the sphere (dark gray) with the larger dielectric constant $\epsilon_2 > \epsilon_1$ contains more charges at its surface.
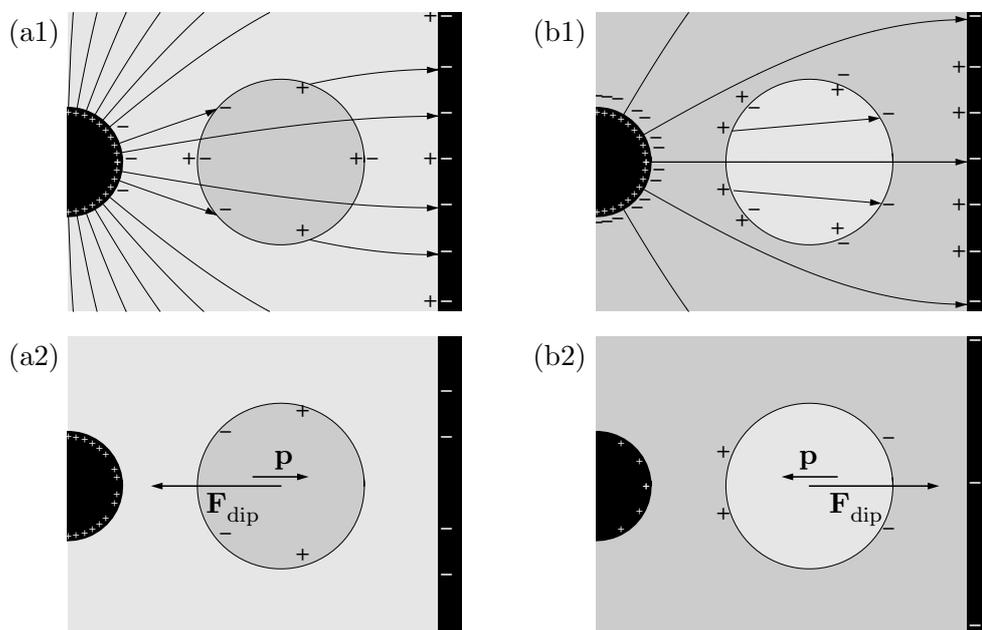
Figure 9.1: Sketch supporting the heuristic argument for the direction of the electric dipole moment $\mathbf{p}$ induced in a dielectric sphere with dielectric constant ϵ_2 by the inhomogeneous electrical field $\mathbf{E}$. The sphere is placed in a dielectric fluid with dielectric constant ϵ_1 and the dielectric force acting on the sphere is denoted $\mathbf{F}_{\mathrm{dip}}$. (a1) The particle is more polarizable than the fluid, i.e., $\epsilon_2 > \epsilon_1$. Here the fluid could be vacuum. (b1) The particle is less polarizable than the fluid, i.e., $\epsilon_2 < \epsilon_1$. (a2) and (b2) The effective charges and directions of $\mathbf{p}$ and $\mathbf{F}_{\mathrm{dip}}$ corresponding to (a1) and (b1), respectively.

In Fig. 9.1(b1), the situation is reversed. Now the the medium (dark gray) has the larger dielectric constant ϵ_1 and many polarization charges at its surfaces, while the sphere (light gray) has the smaller dielectric constant $\epsilon_2 < \epsilon_1$ and fewer polarization charges.

In Fig. 9.1(a2) and (b2) only the un-paired surface charges of panel (a1) and (b1) are shown, which makes it easy to draw the direction of the dipole moment $\mathbf{p}$ of the dielectric sphere. Since by construction the gradient of the electric field points to the region with highest density of electrical field lines, i.e., to the left, it is also easy by use of Eq. (9.3) to deduce the direction of the dielectric force $\mathbf{F}_{\mathrm{dip}}$.

For $\epsilon_1 < \epsilon_2$ the dielectric force pulls the dielectric particle towards the region of strong $\mathbf{E}$-field (to the left), while for $\epsilon_1 > \epsilon_2$ the particle is pushed away from this region (towards the right).

9.2   A point dipole in a dielectric fluid

The first step in our more rigorous analysis is to determine the electrical potential $\phi_{\mathrm{dip}}(\mathbf{r})$ arising from a point dipole $\mathbf{p} = q\mathbf{d}$ placed at the center of the coordinate system in a

dielectric fluid with dielectric constant ϵ.

$$\mathbf{p} = q\mathbf{d}, \quad \begin{cases} +q \text{ at } +\frac{1}{2}\mathbf{d}, \\ -q \text{ at } -\frac{1}{2}\mathbf{d}. \end{cases} \tag{9.5}$$

From an observation point $\mathbf{r}$ the distance to the dipole charges $+q$ and $-q$ are $|\mathbf{r}-\mathbf{d}/2|$ and $|\mathbf{r}+\mathbf{d}/2|$, respectively. The potential $\phi_{\mathrm{dip}}(\mathbf{r})$ from a point dipole, where $d \ll r$, therefore becomes

$$\phi_{\mathrm{dip}}(\mathbf{r}) = \frac{+q}{4\pi\epsilon} \frac{1}{|\mathbf{r}-\mathbf{d}/2|} + \frac{-q}{4\pi\epsilon} \frac{1}{|\mathbf{r}+\mathbf{d}/2|} \approx \frac{1}{4\pi\epsilon} \frac{\mathbf{p}\cdot\mathbf{r}}{r^3} = \frac{p}{4\pi\epsilon} \frac{\cos\theta}{r^2}, \tag{9.6}$$

where θ is the angle between the dipole $\mathbf{p}$ and the observation point vector $\mathbf{r}$. If a given potential $\phi_{\mathrm{tot}}(\mathbf{r})$ contains a component of the form $B\cos\theta/r^2$,

$$\phi_{\mathrm{tot}}(\mathbf{r}) = B \frac{\cos\theta}{r^2} + \phi_{\mathrm{rest}}(\mathbf{r}), \tag{9.7}$$

it implies that a dipole of strength

$$p = 4\pi\epsilon\, B \tag{9.8}$$

is located at the center of the coordinate system. This result will be used in the following when calculating the induced dipole moment of a dielectric sphere placed in a dielectric fluid.

9.3   A dielectric sphere in a dielectric fluid; induced dipole

In Fig. 9.2(a) is shown a dielectric fluid with dielectric constant ϵ_1, which is penetrated by a homogeneous electric field $\mathbf{E}_0 = -\boldsymbol{\nabla}\phi_0$ generated by charging some capacitor plates at $x = \pm\infty$. In spherical polar coordinates (r, θ, φ), using the x-axis and not the z-axis as polar axis, the unperturbed potential ϕ_0 is given by

$$\phi_0(r, \theta, \varphi) = -E_0\, x(r, \theta, \varphi) = -E_0\, r\cos\theta. \tag{9.9}$$

A dielectric sphere of radius a and dielectric constant ϵ_2 is then placed in the fluid as shown in Fig. 9.2(b). The electric field polarizes the sphere resulting in a distortion of the electrical field, which now becomes $\mathbf{E} = -\boldsymbol{\nabla}\phi$, where the potential ϕ is given by one function ϕ_1 outside the sphere and another function ϕ_2 inside,

$$\phi(r, \theta, \varphi) = \begin{cases} \phi_1(r, \theta), & \text{for } r > a, \\ \phi_2(r, \theta), & \text{for } r < a. \end{cases} \tag{9.10}$$

where we notice that the system is rotation symmetric around the x axis so that $\phi(\mathbf{r}) = \phi(r, \theta)$ does not depend on the azimuthal angle φ.

The boundary conditions at the surface of the sphere, $r = a$, are the usual ones for electrostatics: the normal component $\mathbf{D}\cdot\mathbf{e}_r$ of $\mathbf{D}$ and the tangential component $\mathbf{E}\cdot\mathbf{e}_\theta$ of
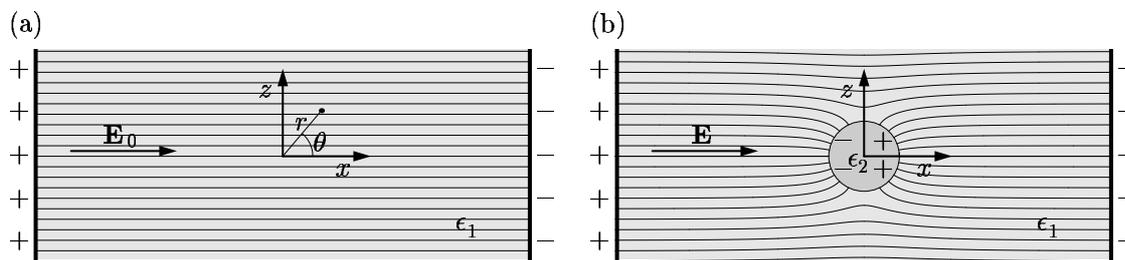
Figure 9.2: (a) A dielectric fluid with a dielectric constant ϵ_1 penetrated by an unperturbed homogeneous electric field $\mathbf{E}_0 = -\boldsymbol{\nabla}\phi_0$, where $\phi_0(r, \theta, \varphi) = -E_0 x = -E_0 r \cos\theta$. (b) A dielectric sphere of radius a and dielectric constant $\epsilon_2 > \epsilon_1$ placed in the dielectric fluid . The electric field polarizes the sphere and a perturbed electric field $\mathbf{E} = -\boldsymbol{\nabla}\phi$ results.

$\mathbf{E}$ must be continuous across the surface of the sphere at $r = a$. So at $r = 0$, $r = a$, and $r = \infty$ we have in total four boundary conditions:

$$\phi_2(0, \theta) \text{ is finite,} \tag{9.11a}$$

$$\phi_1(a, \theta) = \phi_2(a, \theta), \tag{9.11b}$$

$$\epsilon_1 \partial_r \phi_1(a, \theta) = \epsilon_2 \partial_r \phi_2(a, \theta), \tag{9.11c}$$

$$\phi_1(r, \theta) \underset{r \to \infty}{\longrightarrow} -E_0 r \cos\theta. \tag{9.11d}$$

Both the fluid and the sphere are dielectric media without external charges, hence $\rho_{\mathrm{el}} = 0$ in Eq. (7.3b) and the potential obeys the Laplace equation

$$\nabla^2 \phi(\mathbf{r}) = 0. \tag{9.12}$$

The general solution to the Laplace equation in spherical coordinates with no dependence on the azimuthal angle φ can be expressed in terms of the Legendre polynomials P_l as

$$\phi(r, \theta) = \sum_{l=0}^{\infty} \left[A_l r^l + B_l r^{-(l+1)} \right] P_l(\cos\theta). \tag{9.13}$$

Because of the boundary condition Eq. (9.11d), which forces $\phi(\mathbf{r})$ to be proportional to the first Legendre polynomial $P_1(\cos\theta) = \cos\theta$ it is reasonable to employ a trial solution containing only the $l = 1$ terms in Eq. (9.13). Thus using boundary conditions Eqs. (9.11a) and (9.11d) we arrive at a trial solution of the form

$$\phi_1(r, \theta) = -E_0 r \cos\theta + B \frac{\cos\theta}{r^2}, \text{ for } r > a, \tag{9.14a}$$

$$\phi_2(r, \theta) = A r \cos\theta, \text{ for } r < a. \tag{9.14b}$$

The remaining two boundary conditions Eqs. (9.11b) and (9.11c) yield two equations for

the two unknown coefficients A and B,

$$-E_0 a + \frac{1}{a^2} B = a\, A, \tag{9.15a}$$

$$-E_0 - \frac{2}{a^3} B = \frac{\epsilon_2}{\epsilon_1}\, A, \tag{9.15b}$$

which are easily solved to give

$$A = \frac{-3\epsilon_1}{\epsilon_2 + 2\epsilon_1}\, E_0, \tag{9.16a}$$

$$B = \frac{\epsilon_2 - \epsilon_1}{\epsilon_2 + 2\epsilon_1} a^3\, E_0. \tag{9.16b}$$

In conclusion, the trial solution works and results in the following solutions for the electrical potentials ϕ_1 and ϕ_2:

$$\phi_1(\mathbf{r}) = -E_0 r \cos\theta + \frac{\epsilon_2 - \epsilon_1}{\epsilon_2 + 2\epsilon_1} a^3 E_0 \frac{\cos\theta}{r^2} = \phi_0(\mathbf{r}) + \phi_{\mathrm{dip}}(\mathbf{r}), \text{ for } r > a, \tag{9.17a}$$

$$\phi_2(\mathbf{r}) = \frac{-3\epsilon_1}{\epsilon_2 + 2\epsilon_1} E_0 r \cos\theta \qquad\qquad = \frac{3\epsilon_1}{\epsilon_2 + 2\epsilon_1} \phi_0(\mathbf{r}), \text{ for } r < a. \tag{9.17b}$$

Eq. (9.17b) shows that the potential ϕ_2 inside the sphere is merely proportional to the unperturbed potential ϕ_0. However, Eq. (9.17a) reveals a more rich structure in the potential outside the sphere in dielectric fluid: here the unperturbed potential has been supplemented with a dipole potential ϕ_{dip}. In an applied electric field the dielectric sphere acquires an induced dipole moment $\mathbf{p}$, which according to Eqs. (9.7) and (9.8) has the value

$$\mathbf{p} = 4\pi\epsilon_1 \frac{\epsilon_2 - \epsilon_1}{\epsilon_2 + 2\epsilon_1} a^3 \mathbf{E}_0. \tag{9.18}$$

The fraction in the pre-factor plays a significant role, and it has therefore been given a name, the Clausius–Mossotti factor $K(\epsilon_1, \epsilon_2)$,

$$K(\epsilon_1, \epsilon_2) \equiv \frac{\epsilon_2 - \epsilon_1}{\epsilon_2 + 2\epsilon_1}. \tag{9.19}$$

Note how the exact result in Eq. (9.18) confirms the heuristic picture: when the sphere is more dielectric than the liquid, $\epsilon_2 > \epsilon_1$, the induced dipole moment $\mathbf{p}$ and the unperturbed field $\mathbf{E}_0$ are parallel, while they become anti-parallel when the sphere is less dielectric than the liquid, $\epsilon_2 < \epsilon_1$. We also see that the induced dipole moment vanishes if the sphere and the fluid has the same dielectric constant $\epsilon_2 = \epsilon_1$.

This result Eq. (9.18) is very useful, since it provides us with a simple way to calculate the dielectric forces acting on a dielectric sphere immersed in a dielectric fluid.

9.4   The dielectrophoretic force on a dielectric sphere

The exact theory for the dielectric force $\mathbf{F}_{\mathrm{dip}}$ on a dielectric sphere of finite radius a is complicated. The reason is that while it is straightforward to calculate the induced dipole moment $\mathbf{p}$ in an homogeneous external electrical field $\mathbf{E}_0$, as shown in the previous section, the calculation becomes more involved in an inhomogeneous. In technical terms we need to take higher multi-pole moments into account besides the dipole moment. If, however, the radius a of the sphere is much smaller than the distance ℓ over which the external electrical field varies we can still use Eq. (9.18) for the induced dipole. As shown below, this follows from a Taylor expansion (here just taken to first order) of the external electrical field $\mathbf{E}_0(\mathbf{r})$ around the center coordinate $\mathbf{r}_0$ of the sphere,

$$\mathbf{E}_0(\mathbf{r}) \approx \mathbf{E}_0(\mathbf{r}_0) + \big[(\mathbf{r} - \mathbf{r}_0)\cdot\boldsymbol{\nabla}\big]\,\mathbf{E}_0(\mathbf{r}_0) = \mathbf{E}_0(\mathbf{r}_0) + \mathcal{O}(a/\ell). \tag{9.20}$$

In this expression the value of the gradient term is of the order a/ℓ since $|\mathbf{r} - \mathbf{r}_0| < a$ and $\boldsymbol{\nabla}\mathbf{E}_0(\mathbf{r}_0) \approx (1/\ell)\mathbf{E}_0(\mathbf{r}_0)$. Clearly, the induced dipole moment $\mathbf{p}$ could also depend on the gradient $\boldsymbol{\nabla}\mathbf{E}_0(\mathbf{r}_0)$, but this correction would also be suppressed by the same factor of a/ℓ, so Eq. (9.18) for the dipole moment is generalized to

$$\mathbf{p} \approx a^3 4\pi\epsilon_1 K(\epsilon_1,\epsilon_2)\mathbf{E}_0(\mathbf{r}_0) + a^4\big[\mathbf{f}_1(\epsilon_1,\epsilon_2)\cdot\boldsymbol{\nabla}\big]\mathbf{E}_0(\mathbf{r}_0) = a^3 4\pi\epsilon_1 K(\epsilon_1,\epsilon_2)\mathbf{E}_0(\mathbf{r}_0) + \mathcal{O}(a/\ell). \tag{9.21}$$

The vector function $\mathbf{f}_1(\epsilon_1,\epsilon_2)$ appearing above is a generalized Clausius–Mossotti function. Combining Eqs. (9.3), (9.20), and (9.21) we arrive at

$$\mathbf{F}_{\mathrm{dip}}(\mathbf{r}_0) = \big[\mathbf{p}(\mathbf{r}_0)\cdot\boldsymbol{\nabla}\big]\mathbf{E}_0(\mathbf{r}_0) + \mathcal{O}(a/\ell)$$

$$= 4\pi\epsilon_1\,\frac{\epsilon_2 - \epsilon_1}{\epsilon_2 + 2\epsilon_1}\,a^3\big[\mathbf{E}_0(\mathbf{r}_0)\cdot\boldsymbol{\nabla}\big]\mathbf{E}_0(\mathbf{r}_0) + \mathcal{O}(a/\ell)$$

$$= 2\pi\epsilon_1\,\frac{\epsilon_2 - \epsilon_1}{\epsilon_2 + 2\epsilon_1}\,a^3\boldsymbol{\nabla}\big[\mathbf{E}_0(\mathbf{r}_0)^2\big] + \mathcal{O}(a/\ell). \tag{9.22}$$

In the last equality we have used $\boldsymbol{\nabla}\big[\mathbf{E}^2\big] = 2\mathbf{E}\cdot\boldsymbol{\nabla}\mathbf{E}$, which is valid in electrostatics where $\boldsymbol{\nabla}\times\mathbf{E} = \mathbf{0}$ (see Exercise 9.1), valid also in AC if $\ell \ll c/\omega$.

   We shall use Eq. (9.22) in the following. This kind of dipole force is often called a dielectrophoretic force $\mathbf{F}_{\mathrm{DEP}}$, and using the Clausius–Mossotti factor it is written as

$$\mathbf{F}_{\mathrm{DEP}}(\mathbf{r}_0) = 2\pi\epsilon_1\,K(\epsilon_1,\epsilon_2)\,a^3\boldsymbol{\nabla}\big[\mathbf{E}_0(\mathbf{r}_0)^2\big]. \tag{9.23}$$

The direction of the DEP force is governed by the direction of the gradient of the square of the electrical field. Since $\mathbf{E}_0$ only appears as $\mathbf{E}_0^2$ the sign of the DEP force is independent of the sign of $\mathbf{E}_0$ but is given by the sign of the Clausius–Mossotti factor $K(\epsilon_1,\epsilon_2)$.

9.5   Dielectrophoretic particle trapping in microfluidics

The dielectrophoretic (DEP) force $\mathbf{F}_{\mathrm{DEP}}$ can be used to trap dielectric particles suspended in microfluidic channel. The principle is quite simple. An inhomogeneous electric field is
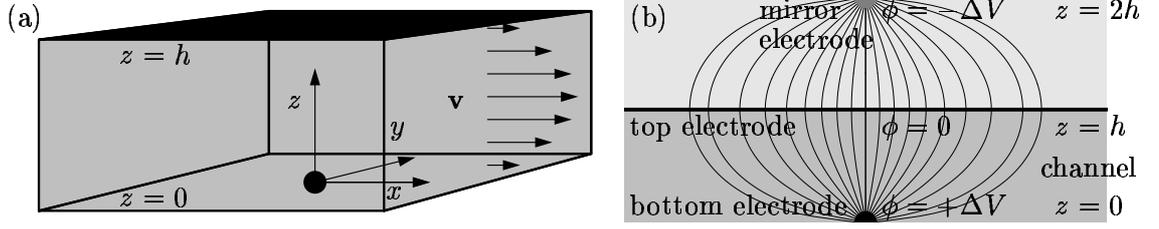
Figure 9.3: (a) An example of DEP trap in a rectangular microfluidic channel of dimensions $L \times w \times h$ to catch dielectric particle suspended in a liquid flow with velocity profile $\mathbf{v}$. An inhomogeneous electric field $\mathbf{E}$ is created by applying a voltage difference ΔV between the (semi-)spherical electrode at the bottom of the microchannel and the planar electrode covering the top. Through the DEP force the bottom electrode will attract the suspended dielectric particles. (b) The electrical field lines calculated by the method of image charges for the potential $\phi(\mathbf{r})$. The spherical bottom electrode at $\mathbf{r} = \mathbf{0}$ has the potential $\phi(\mathbf{0}) = \Delta V$. The planar top electrode of potential $\phi(h\mathbf{e}_z) = 0$ can be realized by placing a mirror electrode with the potential $\phi(2h\mathbf{e}_z) = -\Delta V$ at $\mathbf{r} = 2h\mathbf{e}_z$.

created in a microchannel by charging carefully shaped metal electrodes at the walls of the channel. Dielectric particles suspended in the liquid flowing through the microchannel will be attracted to the electrodes, and if the DEP force $\mathbf{F}_{\mathrm{DEP}}$ is stronger than the viscous drag force $\mathbf{F}_{\mathrm{drag}}$,

$$|\mathbf{F}_{\mathrm{DEP}}| > |\mathbf{F}_{\mathrm{drag}}|, \tag{9.24}$$

the particles will get trapped by the electrodes.

To exemplify the technique and get some analytical expressions for the forces involved we shall study the particularly simple geometry shown in Fig. 9.3.

The microfluidic channel is rectangular with length L, width w, and height h as in Section 2.4.5, which in the flat and wide channel limit $h \ll w$ can be approximated by the infinite parallel-plate channel of Section 2.4.6. The origin of the coordinate system is placed at the center of the floor wall such that $-L/2 < x < L/2$, $-w/2 < y < w/2$, and $0 < z < h$. A pressure drop of Δp along the channel results in the flow profile $\mathbf{v} = v_x(z)\mathbf{e}_x$ Eq. (2.52),

$$v_x(z) = \frac{\Delta p}{2\eta L}(h-z)z = 6\left(1 - \frac{z}{h}\right)\frac{z}{h}v_0, \tag{9.25}$$

where v_0 is the average flow velocity, such that the flow rate is given by $Q = v_0\, wh$.

The dielectric particles suspended in the liquid has radius a. Neglecting finite-size effects from the channel walls we can therefore approximate the drag force acting on a sphere trapped at the position $\mathbf{r}$ by Eq. (2.65)

$$\mathbf{F}_{\mathrm{drag}} \approx 6\pi\eta\, a\, \mathbf{v}(\mathbf{r}). \tag{9.26}$$

The inhomogeneous electric field is created by applying a potential $\phi = \Delta V$ to a (semi-)spherical metallic electrode of radius r_0 situated at the floor at $\mathbf{r} = \mathbf{0}$ and the potential $\phi = 0$ to a planar metallic electrode covering the ceiling at the plane $\mathbf{r} = h\,\mathbf{e}_z$,

see Fig. 9.3(a). We assume the liquid has a vanishing conductivity so that we can disregard the formation of Debye screening layers near the electrodes. By the mirror image charge method it is easy to construct the electrical potential $\phi(\mathbf{r})$ of this configuration,

$$\phi(\mathbf{r}) = \frac{r_0}{|\mathbf{r}|}\,\Delta V - \frac{r_0}{|\mathbf{r} - 2h\mathbf{e}_z|}\,\Delta V, \tag{9.27}$$

which clearly by symmetry has $\phi(\mathbf{r} = h\mathbf{e}_z) \equiv 0$. The trapping of particles takes place close to the spherical electrode, i.e., $|\mathbf{r}| \ll h$. In this region the electrical field is given approximately as

$$\mathbf{E}(\mathbf{r}) = -\boldsymbol{\nabla}\phi(\mathbf{r}) \approx \frac{r_0\Delta V}{r^2}\,\mathbf{e}_r, \text{ for } r_0 < |\mathbf{r}| \ll h. \tag{9.28}$$

where $\mathbf{e}_r$ is the radial vector pointing away from the spherical electrode.

With the electrical field Eq. (9.28) at hand it is an easy task to derive an expression for the DEP force Eq. (9.23)

$$\mathbf{F}_{\text{DEP}}(\mathbf{r}) = 2\pi\epsilon_1\,\frac{\epsilon_2 - \epsilon_1}{\epsilon_2 + 2\epsilon_1}\,a^3\boldsymbol{\nabla}\left[\frac{(\Delta V)^2 r_0^2}{r^4}\right] = -8\pi\,\frac{\epsilon_2 - \epsilon_1}{\epsilon_2 + 2\epsilon_1}\,\frac{a^3 r_0^2}{r^5}\,\epsilon_1(\Delta V)^2\,\mathbf{e}_r. \tag{9.29}$$

The maximal DEP force $F_{\text{DEP}}^{\max}$ is achieved when the particle is as close to the spherical electrode as possible, $r = r_{\min} = r_0 + a$. If we denote the electrode radius by $r_0 = \Gamma a$, we obtain the minimal distance

$$r_{\min} = (1 + \Gamma)a, \quad \Gamma \equiv \frac{r_0}{a}. \tag{9.30}$$

From this follows an estimate for the maximal DEP force:

$$F_{\text{DEP}}^{\max} \equiv |\mathbf{F}_{\text{DEP}}(r_{\min})| = 8\pi\,\frac{\epsilon_2 - \epsilon_1}{\epsilon_2 + 2\epsilon_1}\,\frac{\Gamma^2}{(1 + \Gamma)^5}\,\epsilon_1(\Delta V)^2. \tag{9.31}$$

The average flow velocity at the position $z = r_0 + a = (1 + \Gamma)a$ follows from Eq. (9.25)

$$v_x(r_0 + a) = 6\left(1 - (1 + \Gamma)\frac{a}{h}\right)(1 + \Gamma)\frac{a}{h}\,v_0 \approx 6(1 + \Gamma)\frac{a}{h}\,v_0. \tag{9.32}$$

The drag force on a particle placed at $r = r_{\min} = r_0 + a$ follows from Eqs. (9.26) and (9.32),

$$|\mathbf{F}_{\text{drag}}(r_0 + a)| \approx 6\pi\eta\,a\,v_x(r_0 + a) = 36\pi(1 + \Gamma)\frac{\eta a^2}{h}\,v_0. \tag{9.33}$$

The largest average velocity $v_0^{\max}$ which still allows for trapping of particles at the spherical electrode is found from the condition $F_{\text{drag}} = F_{\text{DEP}}^{\max}$, which results in

$$v_0^{\max} = \frac{4}{9}\,\frac{\epsilon_2 - \epsilon_1}{\epsilon_2 + 2\epsilon_1}\,\frac{\Gamma^2}{(1 + \Gamma)^6}\,\frac{h\epsilon_1(\Delta V)^2}{\eta a^2}. \tag{9.34}$$

To obtain trapping we need a liquid with a dielectric constant smaller than that of the particle. Let us therefore use the liquid benzene with $\epsilon_1 = 2.28\,\epsilon_0$ and $\eta = 0.65\text{ mPa s}$
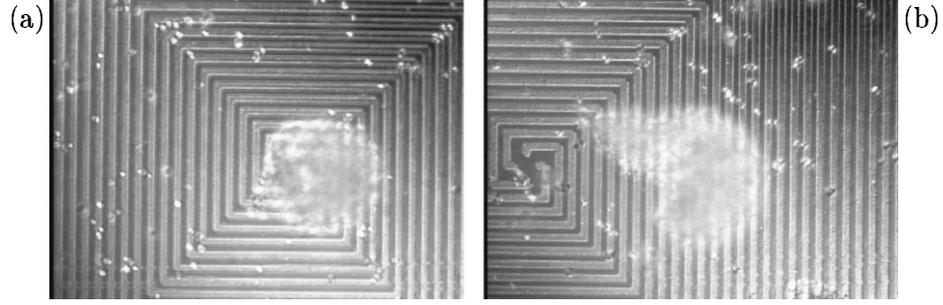
Figure 9.4: An actual DEP trap for biological cells designed at MIC in the group of Wolff. (a) A cloud of yeast cells are caught at the center of the spiral electrode, where the gradients are largest. (b) The cells are carried away by the liquid flow after being released by removing the applied voltage on the electrodes.

and pyrex glass particles with $\epsilon_2 = 6.0\,\epsilon_0$. The length scales are set to $a = r_0 = 5\ \mu$m and $h = 100\ \mu$m, while the applied voltage drop is $\Delta V = 10$ V. With these parameters we find

$$v_0^{\mathrm{max}} = 3.0 \text{ cm/s}. \tag{9.35}$$

It is encouraging that this value is so high. From a theoretical point of view it ought to be possible to design DEP traps for dielectric particles, and indeed this turns out to be the case experimentally. In Fig. 9.4 is shown an actual DEP trap for biological cells designed at MIC in the group of Wolff.

9.6 The AC dielectrophoretic force on a dielectric sphere

So far we have only considered DC voltages driving the DEP trap. There are, however, many advantages in using AC voltage bias instead. One advantage is that any charge monopoles (ions) in the system will not change their mean position being influenced by AC electric fields. Another and related advantage is that the creation of permanent Debye screening layers at the electrodes is avoided. A third advantage is that in the AC mode the DEP trap will also work even if the liquid and the particle have non-zero conductivities, $\sigma_{\mathrm{el},1}$ and $\sigma_{\mathrm{el},2}$. Finally, as we shall see, under AC drive the Clausius–Mossotti factor depends on the driving frequency ω and it can even change its sign, which allow us to control *in situ* whether the DEP force should be attractive or repulsive.

In the following we shall study a simple harmonic time-variation $\exp(-i\omega t)$ (meaning that we must take the real part at the end). In that case the applied potential $\phi(\mathbf{r}, t)$ and the associated electrical field $\mathbf{E}(\mathbf{r}, t) = -\boldsymbol{\nabla}\phi(\mathbf{r}, t)$ have the forms

$$\phi(\mathbf{r}, t) \equiv \phi(\mathbf{r})\, e^{-i\omega t}, \tag{9.36a}$$

$$\mathbf{E}(\mathbf{r}, t) \equiv \mathbf{E}(\mathbf{r})\, e^{-i\omega t}. \tag{9.36b}$$

When dealing with such harmonic time-dependencies, say,

$$A(t) = \text{Re}\left[A_0 e^{-i\omega t}\right], \tag{9.37a}$$

$$B(t) = \text{Re}\left[B_0 e^{-i\omega t}\right], \tag{9.37b}$$

where A_0 and B_0 are constant complex amplitudes, it is useful to know how to calculate the time-average $\langle A(t)B(t)\rangle$ over one full period τ:

$$\langle A(t)B(t)\rangle \equiv \frac{1}{\tau}\int_0^\tau \mathrm{d}t\, A(t)B(t) = \frac{1}{2}\,\text{Re}\left[A_0 B_0^*\right]. \tag{9.38}$$

The proof of this expression, where B_0^* denotes the complex conjugate of B_0, is left as an exercise for the reader.

We now move on to generalize the expression for the DEP force taking AC fields and conductivity into account. The starting point is the general boundary condition for the radial component $E_r(r,\theta) = -\partial_r \phi(a,\theta)$ at the surface of the dielectric sphere,

$$\epsilon_1 E_{r,1}(a,\theta,t) - \epsilon_2 E_{r,2}(a,\theta,t) = q_{\text{surf}}. \tag{9.39}$$

For perfect dielectrics the surface charge density q_{surf} is zero, as stated in Eq. (9.11c), but now with non-zero conductivities and AC fields it becomes non-zero and in fact time-dependent. The time-derivative of q_{surf} is given by charge conservation and Ohm's law,

$$\partial_t q_{\text{surf}}(t) = J_{r,1}(a,\theta,t) - J_{r,2}(a,\theta,t) = \sigma_{\text{el},1}E_{r,1}(a,\theta,t) - \sigma_{\text{el},2}E_{r,2}(a,\theta,t). \tag{9.40}$$

Taking the time-derivative of Eq. (9.39) using **E**-fields on the form Eq. (9.36b), substituting Eq. (9.40) into the result, and multiplying with i/ω, we arrive at

$$\left(\epsilon_1 - i\frac{\sigma_{\text{el},1}}{\omega}\right)E_{r,1}(a,\theta) = \left(\epsilon_2 - i\frac{\sigma_{\text{el},2}}{\omega}\right)E_{r,2}(a,\theta). \tag{9.41}$$

We see that if we define a complex dielectric function $\epsilon(\omega)$ as

$$\epsilon(\omega) \equiv \epsilon - i\frac{\sigma}{\omega}, \tag{9.42}$$

then the boundary condition in the AC case Eq. (9.41) is seen to have the same mathematical form as the boundary condition Eq. (9.11c) in the DC case. We can therefore use the result Eq. (9.23) directly just using the complex dielectric functions in the Clausius–Mossotti factor, which is where the boundary condition has been used,

$$\mathbf{F}_{\text{DEP}}(\mathbf{r}_0,t) = 2\pi\epsilon_1\,\frac{\epsilon_2(\omega)-\epsilon_1(\omega)}{\epsilon_2(\omega)+2\epsilon_1(\omega)}\,a^3\nabla\Big[\mathbf{E}(\mathbf{r}_0,t)^2\Big]. \tag{9.43}$$

Note that the ϵ_1 in the prefactor is the dielectric constant and not the dielectric function. To obtain the real time-averaged DEP force $\langle \mathbf{F}_{\text{DEP}}\rangle$ for the complex result Eq. (9.43) we use Eq. (9.38) with $A(t) = K\big[\epsilon_1(\omega),\epsilon_2(\omega)\big]\mathbf{E}(\mathbf{r}_0,t)$ and $B(t) = \mathbf{E}(\mathbf{r}_0,t)$. The result is

$$\langle \mathbf{F}_{\text{DEP}}(\mathbf{r}_0,\omega)\rangle = 2\pi\epsilon_1\,\text{Re}\left[\frac{\epsilon_2(\omega)-\epsilon_1(\omega)}{\epsilon_2(\omega)+2\epsilon_1(\omega)}\right]a^3\nabla\Big[\mathbf{E}_{\text{rms}}(\mathbf{r}_0)^2\Big]. \tag{9.44}$$

Here we have introduced the usual root-mean-square value $\mathbf{E}_{\text{rms}} = \mathbf{E}/\sqrt{2}$.

The expression Eq. (9.44) can be used to get a good first insight into the dielectrophoretic forces in the AC mode. One interesting result is to find the critical frequency ω_{c} at which the sign of $\langle \mathbf{F}_{\text{DEP}}(\mathbf{r}_0, \omega) \rangle$ changes. This is found from Clausius–Mossotti function by demanding $\text{Re}\left\{[\epsilon_2(\omega_{\text{c}}) - \epsilon_1(\omega_{\text{c}})][\epsilon_2(\omega_{\text{c}}) + 2\epsilon_1(\omega_{\text{c}})]^*\right\} = 0$, which yields

$$\omega_{\text{c}} = \sqrt{\frac{(\sigma_{\text{el},1} - \sigma_{\text{el},2})(\sigma_{\text{el},2} + 2\sigma_{\text{el},1})}{(\epsilon_2 - \epsilon_1)(\epsilon_2 + 2\epsilon_1)}}. \tag{9.45}$$

Let us calculate a characteristic value for ω_{c} for a biological cell, consisting mainly of the cytoplasm, in water. We use the following parameters: $\sigma_{\text{el},2} = 0.1$ S/m and $\epsilon_2 = 60.0\epsilon_0$ for the cell, and $\sigma_{\text{el},1} = 0.01$ S/m and $\epsilon_1 = 78.0\epsilon_0$ for water. The value obtained is

$$\omega_{\text{c}} = 1.88 \times 10^8 \text{ rad/s}. \tag{9.46}$$

The frequency dependent DEP can be used to separate, e.g., living cells from dead cells and cancer cells from normal cells. The different cells have different electrical properties, and consequently they have different critical frequencies ω_{c} determining at which frequencies ω they are caught by the DEP electrode and at which they are expelled by it.

9.7 Exercises

Exercise 9.1
The gradient of $\mathbf{E}^2$ in electrostatics
In electrostatics $\boldsymbol{\nabla} \times \mathbf{E} = \mathbf{0}$. Show that this leads to

$$\boldsymbol{\nabla}\left[\mathbf{E}^2\right] = 2(\mathbf{E}\cdot\boldsymbol{\nabla})\mathbf{E}. \tag{9.47}$$

Hint: write the ith component of $\boldsymbol{\nabla}\left[\mathbf{E}^2\right]$ in index notation as $\partial_i E_j E_j$ and use that $\boldsymbol{\nabla}\times\mathbf{E}=\mathbf{0}$ implies $\partial_i E_j = \partial_j E_i$ for $i \neq j$.

Exercise 9.2
The potential arising from a point dipole
Consider the point dipole $\mathbf{p} = q\mathbf{d}$ located at the origin of the coordinate system as defined in Eq. (9.5). Prove Eq. (9.6) expressing the far-field potential $\phi_{\text{dip}}(\mathbf{r})$ due to this dipole. Hint: perform a Taylor expansion using that $d \ll r$.

Exercise 9.3
Two particular solutions to the Laplace equation
In case of a zero charge density the electrical potential $\phi(\mathbf{r})$ fulfills the Laplace equation $\nabla^2\phi = 0$. Prove that $\phi_1(\mathbf{r}) = Ar\cos\theta$ and $\phi_2(\mathbf{r}) = B\cos\theta/r^2$ are solutions to this equation in spherical coordinates (r, θ, φ), see Eq. (A.33).

Exercise 9.4
A dielectric sphere in a dielectric fluid
Consider the dielectric sphere in a dielectric fluid as defined in Section 9.3.

(a) Prove that for the trial solution Eqs. (9.14a) and (9.14b), the boundary conditions Eqs. (9.11b) and (9.11c) result in Eqs. (9.15a) and (9.15b) for the coefficients A and B.

(b) Prove that Eqs. (9.17a) and (9.17b) indeed provide a solution to the charge-free electrostatic problem of a perfect dielectric sphere placed in a perfect dielectric fluid.

(c) Use the solution for $\phi_2(\mathbf{r})$ to draw the electrical field lines *inside* the dielectric sphere of Fig. 9.2(b) (where $\epsilon_1 < \epsilon_2$).

Exercise 9.5
A sphere with a small dielectric constant placed in a fluid
In Fig. 9.2(b) is shown the electric field lines in the case of a sphere with a dielectric constant ϵ_2 placed in a dielectric fluid with a smaller dielectric constant $\epsilon_1 < \epsilon_2$. Sketch the electrical field lines in the opposite case $\epsilon_1 > \epsilon_2$.

Exercise 9.6
The simple dielectrophoretic (DEP) trap
Consider the simple DEP trap sketched in Fig. 9.3 and reproduced below.

(a) Discuss to which extend Eq. (9.27) in fact gives is a potential satisfying the boundary conditions $\phi(r = r_0) = \Delta V$ and $\phi(z = h) = 0$.

(b) Make a sketch of a sphere trapped near the spherical electrode. Include the forces acting on the sphere, and discuss the validity of Eq. (9.34).

(c) Check the units in Eq. (9.34) and the value $v_0^{\mathrm{max}} = 3.0$ cm/s quoted in Eq. (9.35).
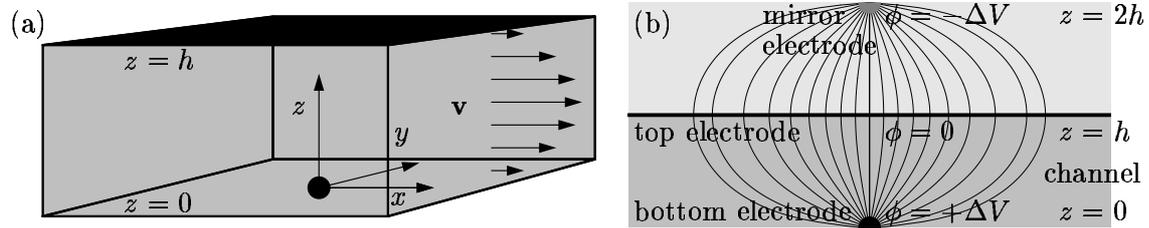
Exercise 9.7
The time average of a product of time-dependent functions
Consider the real physical quantities $A(t)$ and $B(t)$ with harmonic time-variation,

$$A(t) = \mathrm{Re}\left[A_0 e^{-i\omega t}\right], \qquad B(t) = \mathrm{Re}\left[B_0 e^{-i\omega t}\right], \tag{9.48}$$

where A_0 and B_0 are complex amplitudes. Prove that the time-average $\langle A(t)B(t)\rangle$ over one full period τ is given by

$$\langle A(t)B(t)\rangle \equiv \frac{1}{\tau}\int_0^\tau \mathrm{d}t\, A(t)B(t) = \frac{1}{2}\mathrm{Re}\left[A_0 B_0^*\right]. \tag{9.49}$$

Hint: rewrite $A(t)B(t)$ using that $\mathrm{Re}\left[Z\right] = \frac{1}{2}\left[Z + Z^*\right]$ for any complex number Z.

Exercise 9.8
The AC DEP force on a dielectric sphere
Consider the dielectric sphere in an AC electric field presented in Section 9.6.

(a) Show how Eqs. (9.39) and (9.40) lead to the AC boundary condition Eq. (9.41) at the surface of the sphere for the normal component of the electric field.

(b) Prove that the frequency-dependent Clausius–Mossotti factor becomes zero at the critical frequency $\omega = \omega_c$ given in Eq. (9.45). Hint: rewrite the complex fraction so that its denominator becomes real.

(c) Plot the frequency-dependent Clausius–Mossotti factor

$$K(\omega) = \text{Re}\left[\frac{\epsilon_2(\omega) - \epsilon_1(\omega)}{\epsilon_2(\omega) + 2\epsilon_1(\omega)}\right] \qquad (9.50)$$

in the interval $0 < \omega < 3\omega_c$. Use the parameter values given after Eq. (9.45) for a biological cell, consisting mainly of the cytoplasm, in water.

9.8 Solutions

Solution 9.1
The gradient of $\mathbf{E}^2$ in electrostatics
Using index notation we get $\left(\boldsymbol{\nabla}[\mathbf{E}^2]\right)_i = \partial_i(E_j E_j) = 2E_j \partial_i E_j$. We would like to exchange the i and j indices on the last two terms. If $i = j$ this is trivially true, but it is also true for $i \neq j$ if $\boldsymbol{\nabla} \times \mathbf{E} = \mathbf{0}$, since, e.g., $0 = (\boldsymbol{\nabla} \times \mathbf{E})_x = \partial_y E_z - \partial_z E_y = 0$. Thus we get

$$\left(\boldsymbol{\nabla}[\mathbf{E}^2]\right)_i = \partial_i(E_j E_j) = 2E_j \partial_i E_j = 2E_j \partial_j E_i = \left[2(\mathbf{E}\cdot\boldsymbol{\nabla})\mathbf{E}\right]_i. \qquad (9.51)$$

Solution 9.2
The potential arising from a point dipole
We introduce the function $f(\mathbf{s}) = \frac{1}{|\mathbf{r}+\mathbf{s}|} = \left[(\mathbf{r}+\mathbf{s})\cdot(\mathbf{r}+\mathbf{s})\right]^{-\frac{1}{2}}$, where $\mathbf{r}$ is some constant vector and $s \ll r$. A first order Taylor expansion of $f(\mathbf{s})$ around $\mathbf{s} = \mathbf{0}$ becomes $f(\mathbf{s}) \approx f(\mathbf{0}) + \mathbf{s}\cdot\boldsymbol{\nabla}_{\mathbf{s}} f(\mathbf{0})$. Since $\boldsymbol{\nabla}_{\mathbf{s}} f(\mathbf{s}) = -\frac{1}{2}\frac{1}{|\mathbf{r}+\mathbf{s}|^3} 2(\mathbf{r}+\mathbf{s})$ we get $f(\mathbf{s}) \approx = \frac{1}{r} - \frac{\mathbf{s}\cdot\mathbf{r}}{r^3}$. In terms of f the dipole potential can be written as $\phi_{\text{dip}} = \frac{+q}{4\pi\epsilon} f\left(-\frac{\mathbf{d}}{2}\right) + \frac{-q}{4\pi\epsilon} f\left(\frac{\mathbf{d}}{2}\right)$, which upon insertion of the Taylor expansion for f becomes $\phi_{\text{dip}} \approx \frac{+q}{4\pi\epsilon}\left[\frac{1}{r} - \frac{-\mathbf{d}\cdot\mathbf{r}}{2r^3}\right] + \frac{-q}{4\pi\epsilon}\left[\frac{1}{r} - \frac{\mathbf{d}\cdot\mathbf{r}}{2r^3}\right] = \frac{1}{4\pi\epsilon}\frac{(q\mathbf{d})\cdot\mathbf{r}}{r^3}$.

Solution 9.3
Two particular solutions to the Laplace equation
For $S(r,\theta,\phi) = r\cos\theta$ Eq. (A.33) gives

$$\nabla^2(r\cos\theta) = \frac{1}{r^2}\partial_r(r^2\cos\theta) + \frac{1}{r^2\sin\theta}\partial_\theta(-r\sin^2\theta) = \frac{2}{r}\cos\theta - \frac{2\sin\theta\cos\theta}{r\sin\theta} = 0. \quad (9.52)$$

For $S(r,\theta,\phi) = \cos\theta/r^2$ Eq. (A.33) gives

$$\nabla^2\left(\frac{\cos\theta}{r^2}\right) = \frac{1}{r^2}\partial_r\left(\frac{-2\cos\theta}{r}\right) + \frac{1}{\sin\theta r^2}\partial_\theta\left(\frac{-\sin^2\theta}{r^2}\right) = \frac{2\cos\theta}{r^4} - \frac{2\cos\theta}{r^4} = 0. \quad (9.53)$$

Solution 9.4
A dielectric sphere in a dielectric fluid
   (a) Using the trial solution Eqs. (9.14a) and (9.14b), in which all terms contain the factor $\cos\theta$, the boundary conditions Eqs. (9.11b) and (9.11c) does not affect the angular dependence. Thus all $\cos\theta$-factors are cancelled out, and we obtain Eq. (9.15a) by inserting $r = a$. Eq. (9.15b) is obtained after taking the partial derivatives ∂_r, which brings down the powers 1 and -2, and then inserting $r = a$.
   (b) Eqs. (9.17a) and (9.17b) are superpositions of functions ϕ that in Exercise 9.3 were shown to be solutions of the Laplace equation $\nabla^2\phi = 0$. Hence they describe a charge-free electrostatic situation. The boundary conditions were checked in (a) above.
   (c) Eq. (9.17b) shows that the potential ϕ_2 inside the sphere is proportional to the unperturbed potential ϕ_0, and thus from $\mathbf{E} = -\nabla\phi$ follows $\mathbf{E}_2 = [3/(2+\epsilon_2/\epsilon_1)]\mathbf{E}_0$. Since $\epsilon_1 < \epsilon_2$ the density of the resulting homogeneous field lines is smaller than that of $\mathbf{E}_0$.

Solution 9.5
A sphere with a small dielectric constant placed in a fluid
For $\epsilon_1 > \epsilon_2$ the liquid is more polarizable than the sphere and the field lines tend to avoid entering the sphere, see the figure below. This could be a polymer sphere in water.
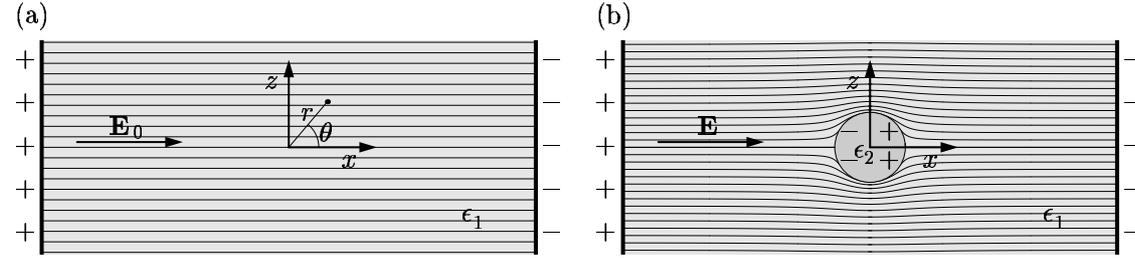
Solution 9.6
The simple dielectrophoretic (DEP) trap
In the following we use the parameter values given after Eq. (9.34).
   (a) Putting $\mathbf{r} = r_0\mathbf{e}$ and Taylor expanding in r_0/h in the second term of Eq. (9.27) yields

$$\phi(r_0\mathbf{e}) = \frac{r_0\Delta V}{|r_0\mathbf{e}|} - \frac{r_0\Delta V}{|r_0\mathbf{e} - 2h\mathbf{e}_z|} = \Delta V - \frac{\Delta V}{|\mathbf{e} - 2(h/r_0)\mathbf{e}_z|} \approx \left[1 + \mathcal{O}\left(\frac{r_0}{h}\right)\right]\Delta V. \quad (9.54)$$

With $r_0 = 5~\mu$m and $h = 100~\mu$m we estimate the relative error to be $r_0/h = 5\%$.
   (b) Consider a configuration where the sphere is lying on the bottom of the channel to the right of the electrode and touching it. The DEP-force is then $\mathbf{F}_{\text{DEP}} = -F_{\text{DEP}}^{\text{max}}\mathbf{e}_r$, where $\mathbf{e}_r$ is the unit vector pointing from the center of the electrode to the center of the sphere. The drag force is $\mathbf{F}_{\text{drag}} = F_{\text{drag}}\mathbf{e}_x$, while the normal force from the bottom of the channel is $\mathbf{F}_N = -F_N\mathbf{e}_z$. In the x-direction the force balance become $F_{\text{drag}} = F_{\text{DEP}}^{\text{max}}\cos\theta$.
   With $a = r_0 = 5~\mu$m we find from Eq. (9.28) that the electric field varies from $\Delta V/r_0$ to $\Delta V/(9r_0)$ across the sphere. Thus the electric field varies significantly on a length scale corresponding to the diameter of the sphere, $\ell = 2r_0$, and the correction term $a/\ell = 1/2$ in Eq. (9.20) is in fact not small. If the Stokes drag law is valid the assumption for the

drag force is not bad: With minor deviations of order $r_0/h = 5\%$ the velocity field varies linearly across the sphere, and the resulting drag force in well estimated by the average value evaluated at center position of the sphere. However, as the sphere is close to the wall, the assumptions of the walls being far away, see Section 2.6, is violated, and the Stokes drag law is not valid. In conclusion, the estimate for the v_0^{max} can only be trusted as an order-of-magnitude estimate.

(c) From $[\epsilon_1] = \mathrm{F/m}$ follows $[\epsilon_1(\Delta V)^2] = (\mathrm{F/m})\,\mathrm{V}^2 = (\mathrm{FV})\,\mathrm{V/m} = \mathrm{CV/m} = \mathrm{J/m} = \mathrm{N}$, and since $[\eta a^2] = \mathrm{Pa\,s\,m}^2 = \mathrm{N\,s}$, we arrive at

$$[v_0^{\mathrm{max}}] = \frac{\mathrm{m\,N}}{\mathrm{N\,s}} = \frac{\mathrm{m}}{\mathrm{s}}. \tag{9.55}$$

Solution 9.7
The time average of a product of time-dependent functions
Rewriting $A(t) = \frac{1}{2}[A_0 e^{-i\omega t} + A_0^* e^{i\omega t}]$ and $B(t) = \frac{1}{2}[B_0 e^{-i\omega t} + B_0^* e^{i\omega t}]$ we find

$$\langle A(t)B(t)\rangle = \frac{1}{4\tau}\int_0^\tau \mathrm{d}t \left[A_0 e^{-i\omega t} + A_0^* e^{i\omega t}\right]\left[B_0 e^{-i\omega t} + B_0^* e^{i\omega t}\right] \tag{9.56a}$$

$$= \frac{1}{4\tau}\int_0^\tau \mathrm{d}t \left[A_0 B_0^* + A_0^* B_0 + A_0 B_0 e^{-i2\omega t} + A_0^* B_0^* e^{i2\omega t}\right] \tag{9.56b}$$

$$= \frac{1}{4}\left[A_0 B_0^* + A_0^* B_0\right] = \frac{1}{2}\,\mathrm{Re}\left[A_0 B_0^*\right]. \tag{9.56c}$$

Solution 9.8
The AC DEP force on a dielectric sphere
(a) A Gauss box argument at the surface of the sphere gives $\epsilon_1 \mathbf{E}_1 \cdot \mathbf{n}_1 + \epsilon_2 \mathbf{E}_2 \cdot \mathbf{n}_2 = q_{\mathrm{surf}}$. Here $\mathbf{n}_1$ and $\mathbf{n}_2$ are unit vectors pointing away from the surface into the liquid and the sphere, respectively. Since the radial unit vector points from the sphere out into the liquid, we get Eq. (9.39) with the proper signs. Taking the time-derivative of this equation yields $-i\omega\epsilon_1 E_{r,1} + i\omega\epsilon_2 E_{r,2} = \partial_t q_{\mathrm{surf}}$. Combining this with Eq. (9.40) gives $-i\omega\epsilon_1 E_{r,1} + i\omega\epsilon_2 E_{r,2} = \sigma_{\mathrm{el},1} E_{r,1} - \sigma_{\mathrm{el},2} E_{r,2}$. Separation of 1-terms and 2-terms followed by multiplication by i/ω leads to Eq. (9.41).

(b) The DEP-force is zero if the real part of the Clausius–Mossotti factor is zero.

$$\mathrm{Re}\left[\frac{\epsilon_2(\omega_c) - \epsilon_1(\omega_c)}{\epsilon_2(\omega_c) + 2\epsilon_1(\omega_c)}\right] = \mathrm{Re}\left[\frac{[\epsilon_2(\omega_c) - \epsilon_1(\omega_c)][\epsilon_2(\omega_c) + 2\epsilon_1(\omega_c)]^*}{[\epsilon_2(\omega_c) + 2\epsilon_1(\omega_c)][\epsilon_2(\omega_c) + 2\epsilon_1(\omega_c)]^*}\right] = 0. \tag{9.57}$$

Using $\epsilon(\omega_c) = \epsilon - i\sigma/\omega_c$, the real part of the enumerator becomes,

$$(\epsilon_2 - \epsilon_1)(\epsilon_2 + 2\epsilon_1) + \frac{1}{\omega_c^2}(\sigma_{\mathrm{el},2} - \sigma_{\mathrm{el},1})(\sigma_{\mathrm{el},2} + 2\sigma_{\mathrm{el},1}) = 0, \tag{9.58}$$

from which Eq. (9.45) follows.

(c) The Clausius–Mossotti function $K(\omega)$ for the parameter values corresponding to a biological cell, $\epsilon_2 = 60.0\epsilon_0$ and $\sigma_{\mathrm{el},2} = 0.1$ S/m, in water, $\epsilon_1 = 78.0\epsilon_0$ and $\sigma_{\mathrm{el},1} = 0.01$ S/m. The characteristic frequency is $\omega_c = 1.88\times10^8$ rad/s.
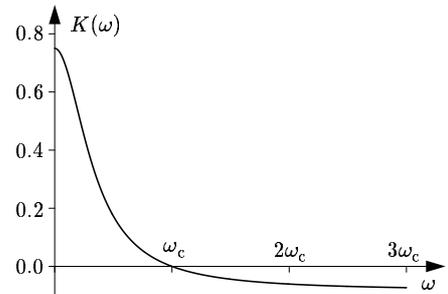
Chapter 10

Magnetophoresis

Magnetophoresis (MAP) is the magnetic analogue to dielectrophoresis (DEP). Particles possessing either an induced or a permanent magnetization $\mathbf{M}$ can be moved around inside a microfluidic channel by applying an external, inhomogeneous magnetic field $\mathbf{H}$. Whereas the dielectric response of virtually all materials is strong enough to allow for dielectrophoretic effects, the magnetic response is often too weak for most materials to make magnetophoresis happen. In fact, one must often carefully prepare a given sample by attaching magnetic particles before launching it into a MAP device. However, this seemingly annoying feature is actually the strength of MAP, because it ensures full control over which part of a sample is subject to MAP. In DEP devices the strong dielectric response of both target and auxiliary particles can clutter the functionality of the device and make the DEP device difficult to operate.

10.1 Magnetophoresis and bioanalysis

Magnetophoresis in microsystems is currently undergoing a rapid development and is already a strong tool especially for bioanalysis. On one hand, most biological samples are non-magnetic and are not affected or destroyed by the relatively weak magnetic fields employed in MAP, and on the other hand, it is possible to label cells or biomolecules specifically with magnetic microbeads. This provides a versatile physical handle for manipulation and handling of biological samples.

A sketch of a typical bio-coated, magnetic microbead is shown in Fig. 10.1. The main body is a non-magnetic polymer sphere, often made of polystyrene, containing a large number of magnetic nanoparticles. The diameter of the polymer sphere is of the order 1 μm to make it practical for handling, while the magnetic particles preferably have a diameter near 10 nm. In magnetic particles of such small size all atomic magnetic moments are aligned, but the direction of this total magnetic moment can rotate freely under the influence of thermal fluctuations at room temperature, see Exercise 10.1. This is known as superparamagnetism. The advantage of using superparamagnetic microbeads is twofold. Firstly, such particles are have a vanishing average magnetic moment in the absence of an external magnetic field, and secondly, they exhibit only a tiny hysteresis
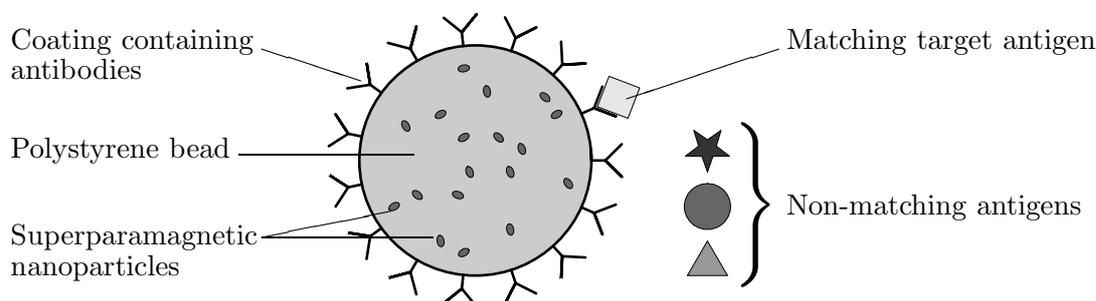
Figure 10.1: A typical polystyrene microbead used for magnetic separation in lab-on-a-chip systems. The bead has a radius of about 1 μm contains inclusions in the form of paramagnetic nanoparticles. The surface is coated with a specific antibody chosen to capture a given target antigen (white square) and not to interact with any other antigens (triangle, pentagram, and circle).

effect, meaning the average magnetic moment returns to the value zero after removing any applied external magnetic field. Consequently, such particles are ideal for capturing by turning on an external magnetic field, and for releasing by turning off the magnetic field.

The advantage of using polymers as the main body is that it allows for coating the microbead with specific biomolecules. Through well-controlled biochemical processes the surface can by coated with carefully chosen antibodies, DNA strings or RNA. Once coated with such biomolecules the microbead can act as a highly specific capture probe for specific target molecules. An example of this capture selectivity is sketched in Fig. 10.1, where a surface coating of a specific antibody allows for capturing a specific target antigen, leaving all non-matching antigens untouched.

Magnetic separation of biomolecules can be implemented in lab-on-a-chip systems as the one sketched in Fig. 10.2. Imagine a microfluidic channel with magnetic elements placed at the bottom wall. These elements can either be on-chip electromagnets or magnetic material, magnetized by external electrical currents or magnetic fields, respectively. When superparamagnetic, bio-coated microbeads are flushed through the channel they will be attracted by magnetophoretic forces to the magnetic elements if these are turned on. Once reaching the magnetic elements the beads are immobilized and the antibodies on their surfaces will form a layer of capture probes ready to bind with the proper antigen. If a sample containing many different antigens then is flowing through the microchannel, only the specific antigen matching the antibody on the microbeads will be captured. If the channel is flushed with a rising buffer after the capturing, we have achieved an up-concentration of the target antigen. This target sample can be released by turning off the magnetic elements, flushing out the sample and collecting it at the outlet.
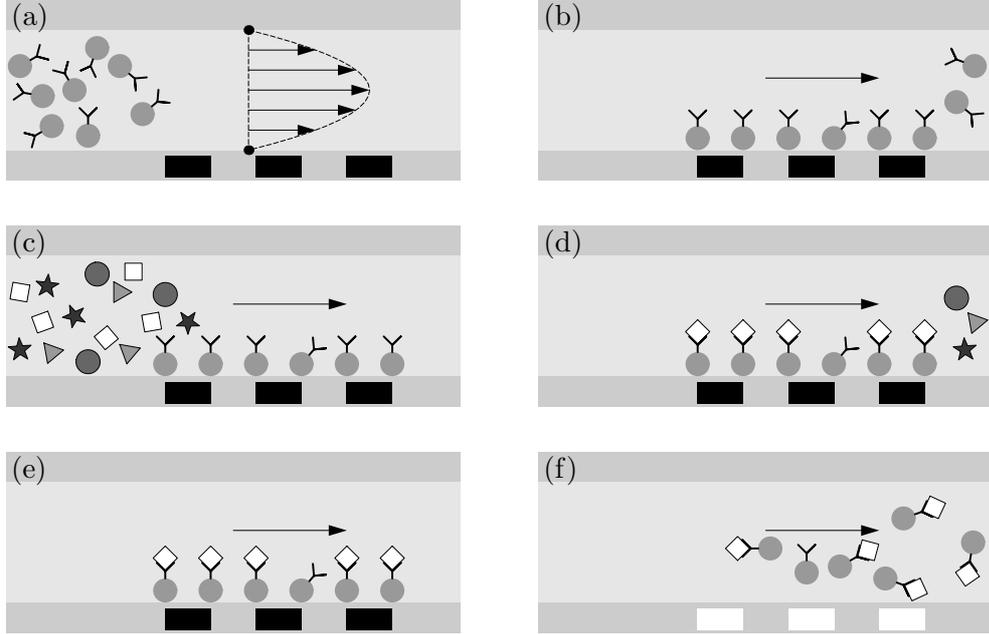
Figure 10.2: The principle in magnetic separation for bio-sampling using magnetic beads flowing in a microfluidic channel. (a) A Poiseuille flow (light gray) carrying magnetic microbeads (dark circles) coated with suitable antibodies (attached Y-shapes). (b) Immobilization of the magnetic antibody-beads by activating magnets (black rectangles) placed in the bottom wall (gray). (c) Introduction of sample containing the target antigen (white squares) and a number of other antigens (triangles, circles and pentagrams). (d) Capture of the target antigen by the immobilized antibody-beads. (e) Thorough rinsing. (f) Release of the target sample by de-activating the magnets (now white rectangles) followed by collection at the microchannel outlet to the right.

10.2 Magnetostatics

The theory of magnetophoresis has many similarities with that of dielectrophoresis. The starting point is the magnetostatic part of Maxwell's equations, i.e., assuming only stationary current densities and neglecting all time derivatives otherwise appearing. The two magnetostatic Maxwell equations are

$$\boldsymbol{\nabla} \cdot \mathbf{B} = 0, \tag{10.1a}$$

$$\boldsymbol{\nabla} \times \mathbf{B} = \mu_0 \mathbf{J}_{\text{tot}} = \mu_0 \mathbf{J}_{\text{ext}} + \mu_0 \mathbf{J}_{\text{mag}}, \tag{10.1b}$$

where $\mu_0 = 4\pi \times 10^{-7}$ H/m is the magnetic permeability of vacuum, and where $\mathbf{J}_{\text{tot}}$, $\mathbf{J}_{\text{ext}}$ and $\mathbf{J}_{\text{mag}}$ all are stationary current densities; $\mathbf{J}_{\text{tot}}$ the total current density, $\mathbf{J}_{\text{ext}}$ all external transport current densities running in conductors, and $\mathbf{J}_{\text{mag}}$ the current densities bound to magnetic material in the form of atomic/molecular current loops and quantum mechanical spins. This division of the total current density is analogous to the division of the total charge density into external and polarization charge densities, see Eq. (7.11).

In analogy with the dipole moment $\mathbf{p} = q\mathbf{d}$ of equation Eq. (7.7) the magnetic dipole moment $\mathbf{m}$ for a circulating magnetization current I_{mag} enclosing a flat area $\mathcal{A}$ with the surface normal $\mathbf{n}$ is given by

$$\mathbf{m} = I_{\mathrm{mag}}\mathcal{A}\,\mathbf{n}. \tag{10.2}$$

In analogy with the polarization $\mathbf{P}$ of Eq. (7.8) the magnetization $\mathbf{M}$ is defined as the magnetic moment density,

$$\mathbf{M}(\mathbf{r}_0) \;=\; \lim_{\mathrm{Vol}(\Omega^*)\to 0}\left[\frac{1}{\mathrm{Vol}(\Omega^*)}\int_{\Omega^*}\mathrm{d}\mathbf{r}\,\mathbf{m}(\mathbf{r}_0 + \mathbf{r})\right]. \tag{10.3}$$

A careful mathematical analysis shows that the magnitization $\mathbf{M}$ is related to the density $\mathbf{J}_{\mathrm{mag}}$ of the circulating magnetization current as

$$\mathbf{J}_{\mathrm{mag}} = \boldsymbol{\nabla} \times \mathbf{M}; \tag{10.4}$$

an expression which is the magnetic analogue of the relation Eq. (7.10) between the electric polarization $\mathbf{P}$ and the polarization charge density ρ_{pol}. Note that the analogy between magnetization and electric polarization is not perfect, as the source to $\mathbf{M}$ is the vector $\mathbf{J}_{\mathrm{mag}}$, while the source to $\mathbf{P}$ is the scalar ρ_{pol}. But we nevertheless continue to point our the similarities between the magnetic and the electric theory. Just as $\mathbf{E}$ and $\mathbf{P}$ could be combined to give the useful concept of the $\mathbf{D}$ field, it is beneficial to combine the magnetic induction $\mathbf{B}$ and the magnetization $\mathbf{M}$ in the definition of the magnetic field $\mathbf{H}$ as

$$\mathbf{H} = \frac{1}{\mu_0}\,\mathbf{B} - \mathbf{M}. \tag{10.5}$$

By inserting Eq. (10.4) into Eq. (10.1b) we finally obtain

$$\boldsymbol{\nabla} \times \mathbf{H} = \mathbf{J}_{\mathrm{ext}}, \tag{10.6}$$

which states that the source of the $\mathbf{H}$ field is the external current densities.

The last fundamental concept to be introduced here in connection with magnetostatics is the magnetic susceptibility tensor χ defined as

$$\chi \equiv \left(\frac{\partial \mathbf{M}}{\partial \mathbf{H}}\right)_{V,T}. \tag{10.7}$$

For isotropic materials $\mathbf{M}$ and $\mathbf{H}$ are parallel, and χ becomes a scalar. Furthermore, in some cases the relation between $\mathbf{M}$ and $\mathbf{H}$ is linear, and we get the most simple expressions, which are analogous to Eq. (7.12),

$$\mathbf{M} = \chi\,\mathbf{H}, \tag{10.8a}$$

$$\mathbf{B} = \mu_0\Big(\mathbf{H} + \mathbf{M}\Big) = \mu_0\Big(1 + \chi\Big)\mathbf{H} \equiv \mu_0\mu_r\mathbf{H} \equiv \mu\,\mathbf{H}. \tag{10.8b}$$

Here the coefficients μ and μ_r are called the permeability and relative permeability, respectively.

10.3 Basic equations for magnetophoresis

We are going to study which magnetic forces act on a magnetizable body when this is placed in an external magnetic field. Consider a given external magnetic field characterized by $\mathbf{H}_{\text{ext}}$ before the magnetizable object enters. When the object then is placed in the magnetic field, it acquires an magnetization $\mathbf{M}$, and this in turn generates extra contributions to the magnetic field, which therefore changes from $\mathbf{H}_{\text{ext}}$ to $\mathbf{H}$.

To find the magnetic force $\mathbf{F}$ on the magnetizable object is not entirely simple. We shall not go through the derivation here, but just mention that a safe way to proceed is to consider the free energy of the system. The differential of the free energy density is generally given by $-\mathbf{B}\cdot\text{d}\mathbf{H}$. From this the change $\delta\mathcal{F}$ in total free energy $\mathcal{F}$ upon a small spatial displacement $\delta\mathbf{r}$ in the system can be calculated. Now, free energy and force are in general related by the differential relation

$$\delta\mathcal{F} = -\mathbf{F}\cdot\delta\mathbf{r}. \tag{10.9}$$

Carrying out this analysis results in the following expression for the force $\mathbf{F}$ on the magnetizable object, valid if the fields are static, $\boldsymbol{\nabla} \times \mathbf{H}_{\text{ext}} = 0$, and the body is non-conducting:

$$\mathbf{F} = \mu_0 \int_{\text{body}} \text{d}\mathbf{r}\,(\mathbf{M}\cdot\boldsymbol{\nabla})\mathbf{H}_{\text{ext}}, \text{for}\ \ \boldsymbol{\nabla} \times \mathbf{H}_{\text{ext}} = 0. \tag{10.10}$$

This expression with its underlying assumptions is the basis for understanding magnetophoresis.

To be a little more specific we consider, in analogy with the dielectric treatment in Section 9.3, a homogeneous, isotropic, and non-conducting sphere of radius a and permeability μ. As $\boldsymbol{\nabla} \times \mathbf{H}_{\text{ext}} = 0$ it is possible like in Eqs. (7.2a) and (7.3a) to introduce a magnetic potential ϕ_m such that

$$\mathbf{H}_{\text{ext}} = -\boldsymbol{\nabla}\phi_m. \tag{10.11}$$

The analogy to the dielectric case is now very close, and the resulting expression for the magnetization $\mathbf{M}$ of the sphere after being placed in the homogeneous field $\mathbf{H}_{\text{ext}}$ is given by

$$\mathbf{M} = 3\frac{\mu - \mu_0}{\mu + \mu_0}\,\mathbf{H}_{\text{ext}}. \tag{10.12}$$

Note how closely this expression resembles Eq. (9.18) for the induced dipole moment in electrostatics. The analogy is perfect when we consider the resulting MAP-force $\mathbf{F}_{\text{MAP}}$,

$$\mathbf{F}_{\text{MAP}}(\mathbf{r}_0) = 2\pi\mu_0\,K(\mu_0, \mu)\,a^3\nabla\Big[\mathbf{H}_{\text{ext}}(\mathbf{r}_0)^2\Big], \tag{10.13}$$

where even the Clausius–Mossotti factor from Eq. (9.19) reappears. Note how the MAP-force is dependent on the gradient of the square of the magnetic field, just as the DEP-force.

In conclusion we can say, that force expressions applying to magnetophoresis and dielectrophoresis can be very similar or even in special cases identical. However, it is important to bear in mind that often there will be substantial deviations between the two descriptions, primarily due to the intrinsic non-linear nature of magnetic materials.
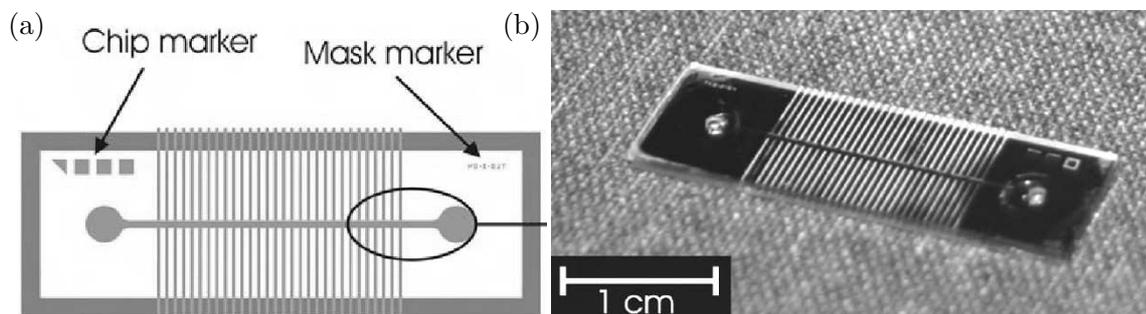
Figure 10.3: (a) Design mask for a 400 μm wide and 14 mm long channel with 30 magnetic elements along each side of the channel. (b) The silicon-based lab-on-a-chip system with the magnetic permalloy elements at the side and a pyrex lid for sealing. The 2 mm wide inlet and outlet is seen at each end of the device. Courtesy the group of Fougt Hansen at MIC.

10.4   Magnetophoretic lab-on-a-chip systems

We end this short introduction to magnetophoresis by showing one explicit example of a magnetophoretic lab-on-a-chip system fabricated in the group of Fougt Hansen at MIC.

In Fig. 10.3(a) is shown the the design mask for fabricating a magnetic microfluidic separation chip. The core of the design is the 14 mm long, 400 μm wide and 80 μm high channel with 30 magnetic element placed along each side. At each end of the channels are placed an inlet and an outlet reservoir with diameters of 2 mm.

The finished device is seen on the picture in Fig. 10.3(b). The main structure is fabricated in silicon. The magnetic elements are filled with permalloy (20% Fe and 80% Ni) by electroplating before sealing the channel with a pyrex lid.

To operate the device it is placed in the middle of the gap of an electromagnet and a syringe pump is attached by teflon tubes. When the electromagnet is turned on the permalloy elements are magnetized and strong field gradients are created in the channel.

Through an inlet valve solutions of superparamagnetic beads with a diameter of 1 μm are led through the channel in a Poiseuille flow with a maximum speed around 1 mm/s. The MAP-force drags the beads to the side of the channel and capture them at the edges of the magnetic elements.

In Fig. 10.4 is seen a micrograph of the first 10 elements (top panel) and the next 10 elements (bottom channel). The captured beads are seen as a dark gray shadow at the end of the magnetic elements (light gray rectangles). The number of beads being caught decreases along the channel. The largest amount of captured beads are seen on element number 1.

So far the system has mainly been run with magnetic beads without any bio-coating. The system has now been successfully tested and is ready to be applied for more bio-related investigations.
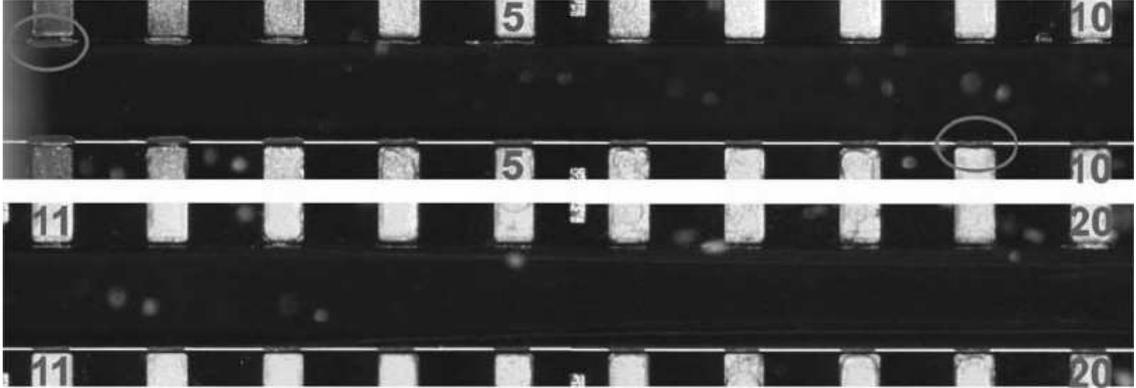
Figure 10.4: Micrograph of magnetic bead capture by magnetophoresis in a 400 μm wide and 80 μm high silicon-based microchannel with a pyrex lid. The magnetic elements (light rectangles) are made of permalloy. Courtesy the group of Fougt Hansen at MIC.

10.5 Exercises

Exercise 10.1
Superparamagnetic nanoparticles
In the simplest cases the relaxation time τ for the net magnetization of a superparamagnetic particle follows an activation law,

$$\tau = \tau_0 \, \exp\left(\frac{KV}{k_{\mathrm{B}}T}\right), \tag{10.14}$$

where the pre-exponential factor is $\tau_0 = 10^{-12} - 10^{-10}$ s, V is the volume of the particle, and $K \approx 10^4$ J/m^3 is the so-called anisotropy energy density.

Argue why particles need to have a radius of about 10 nm or smaller to exhibit superparamagnetism at room temperature.

Exercise 10.2
The magnetic moment of a square current loop
Prove that the mechanical torque $\boldsymbol{\tau}$ is given by

$$\boldsymbol{\tau} = I\mathcal{A}\,\mathbf{n} \times \mathbf{B} \tag{10.15}$$

for a thin wire formed as a square closed loop of side length L in the positive direction, carrying a circulating current I, and placed in the horizontal xy plane, when a magnetic field $\mathbf{B}$ is present inclined an angle θ relative to the surface normal of the area $\mathcal{A} = L^2$ enclosed by the loop. Hint: use that the force $\mathbf{F}$ on a thin wire of length L carrying a current I is given by $\mathbf{F} = BIL\,\mathbf{e}_L \times \mathbf{e}_B$, where $\mathbf{e}_L$ and $\mathbf{e}_B$ are unit vectors indicating the direction along the wire and magnetic field, respectively.

Exercise 10.3
The rotation of M
Prove Eq. (10.6) from the preceding part of Section 10.2.

10.6   Solutions

Solution 10.1
To be added
In the next edition solutions to the exercises will be added.

Chapter 11

Two-phase flow

In the previous chapters we have been concerned with the microfluidic properties of a single liquid. In Section 4.2 we went beyond the case of a pure liquid and studied the convection-diffusion equation for solutes in a solvent. This theme was extended in Section 7.3, where we analyzed the influence of dissolved ions on the electrohydrodynamic properties of electrolytes. The topic of the present chapter is the behavior of two different fluids flowing simultaneously in a microchannel; a situation denoted two-phase flow. We will treat examples of flow involving either one liquid and one gas phase, or two different liquid phases.

Two-phase flow is very important in lab-on-a-chip systems, where it is often desirable to bring together two liquids to prepare for further treatment, to obtain certain chemical reactions, or to perform chemical analysis. The presence of gas bubbles in microchannels is another major two-phase flow issue in microfluidics, either because the mechanical properties of the bubbles are used for some functionality of the devise, or because unwanted bubbles appear as a consequence of the introduction of some liquid or as the result of electrolysis.

In the following we will study some basic theoretical aspects of simple two-phase flow in microfluidic systems. By keeping the examples simple we can gain some insight in a topic for which the mathematical formalism otherwise easily can grow to an almost intractable level of complexity.

11.1   Two-phase Poiseuille flow

Consider the infinite parallel-plate geometry analyzed in Section 2.4.6 for basic Poiseuille flow, but assume now that we have managed to establish a steady-state flow of two different liquids with a flat interface situated at $z = h^*$ as shown in Fig. 11.1. The flow is driven by a pressure drop Δp over the distance L along the x axis. The bottom layer $0 < z < h^*$ is liquid 1 with viscosity η_1, while the top layer $h^* < z < h$ is liquid 2 with viscosity η_2. As in Section 2.4.6 the system is translation invariant along the x and the y axis, so as
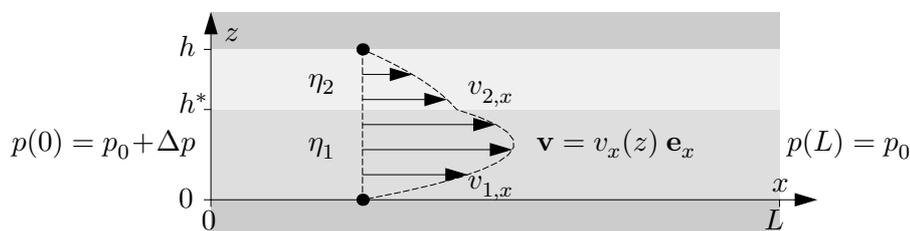
Figure 11.1: An example of two-phase Poiseuille flow. Fluid 1 of viscosity η_1 (light gray) and fluid 2 of viscosity η_2 (gray) occupying the space of height h between two horizontally placed, parallel, infinite planar plates (dark gray). The interface situated at $z = h^*$ is assumed to be planar and stable. A constant pressure drop Δp along the x axis drives a Poiseuille flow $\mathbf{v} = v_x(z)\,\mathbf{e}_x$. The boundary conditions are no slip at the walls and continuous velocity v_x and shear stress σ_{xz} at the interface $z = h^*$. Note the discontinuity in the derivative of the velocity at the interface. Here we have used the parameter values $\eta_2 = 4\eta_1$ and $h^* = 0.6h$.

before the velocity field $\mathbf{v}$ and the pressure field p must be of the form

$$\mathbf{v} = v_x(z)\,\mathbf{e}_x, \quad 0 < z < h, \tag{11.1a}$$

$$p(x) = p_0 + \left(1 - \frac{x}{L}\right)\Delta p. \tag{11.1b}$$

Note that because we have assumed a flat interface no Young-Laplace pressure arises and the pressure field is as simple as in the case of a single-phase Poiseuille flow.

It is natural to piece the full velocity field $v_x(z)$ together from to piecewise differentiable fields $v_{1,x}(z)$ and $v_{2,x}(z)$:

$$v_x(z) = \begin{cases} v_{2,x}(z), & \text{for} \quad h^* < z < h, \\ v_{1,x}(z), & \text{for} \quad 0 < z < h^*. \end{cases} \tag{11.2}$$

The boundary conditions for the velocity field are no slip at the walls and continuous velocity v_x and shear stress σ_{xz} at the interface $z = h^*$,

$$v_{2,x}(h) = 0, \tag{11.3a}$$

$$v_{1,x}(0) = 0, \tag{11.3b}$$

$$v_{1,x}(h^*) = v_{2,x}(h^*), \tag{11.3c}$$

$$\sigma_{1,x}(h^*) = \sigma_{2,x}(h^*). \tag{11.3d}$$

If the shear stress were not continuous, infinite and thus unphysical forces would be present at the interface. A straightforward generalization of Eq. (2.52) for the single-phase Poiseuille flow velocity field yields the following expressions for $v_{1,x}(z)$ and $v_{1,x}(z)$

that satisfies the first two boundary conditions Eqs. (11.3b) and (11.3a),

$$v_{2,x}(z) = \frac{\Delta p}{4\eta_2 L}\,(h - z)(z - h_2), \tag{11.4a}$$

$$v_{1,x}(z) = \frac{\Delta p}{4\eta_1 L}\,(h_1 - z)z. \tag{11.4b}$$

Here h_1 and h_2 are two constants to be determined by use of the last two boundary conditions Eqs. (11.3c) and (11.3d). Using the fact that in the setup with the given symmetries $\sigma_{xz}(z) = \eta\partial_z v_x(z)$, the two boundary conditions results in two linear equations for the two unknown h_1 and h_2, which are easily solved to yield

$$h_2 = \frac{\left(\frac{\eta_1}{\eta_2} - 1\right)\left(1 - \frac{h^*}{h}\right)}{\frac{\eta_1}{\eta_2}\left(1 - \frac{h^*}{h}\right) + \frac{h^*}{h}}\,h^*, \tag{11.5a}$$

$$h_1 = h + h_2. \tag{11.5b}$$

In Fig. 11.1 is shown an explicit example of a velocity profile in a two-phase Poiseuille flow with a flat interface. Note the discontinuity in the derivative of the velocity field at the interface $z = h^*$. This discontinuity arises from the different values of the viscosities η_1 and η_2 and the demand for a continuous shear stress at the interface.

11.2 Capillary and gravity waves

It might be of interest to study under which conditions the interface of a two-phase Poiseuille flow is stable. The full analysis of this simple question turns out to be very difficult and is beyond the scope of these lecture notes. Therefore, to shed some light on the issue we are forced to consider some simplified cases, namely the so-called capillary and gravity waves where the effect of viscosity can be neglected.

11.2.1 Gravity waves of short wavelength

Gravity waves of small amplitude and short wavelengths on a water-air surface is arguably the most simple example of interface waves where viscosity can be neglected. This is also known as gravity waves on an inviscid liquid with a free surface. During the calculations we make certain assumptions to progress at ease; at the end of the calculation we check the obtained solution for consistency with these assumptions. If viscosity indeed can be neglected then according to Eq. (11.61) in Exercise 11.2 the flow of the incompressible water is a potential flow,

$$\mathbf{v} = \boldsymbol{\nabla}\phi, \tag{11.6}$$

where ϕ is a scalar potential function to be determined. Assume that the body of water is infinite in the xy plane and sustained by a solid base plane placed at $z = -h$. When at rest the water-air surface is flat and given by $z = \zeta(x, y, t) \equiv 0$. Starting from rest a small-amplitude plane wave running in the x direction is gradually established. Under these

circumstances the potential function does not depend on y, thus $\phi = \phi(x, z, t)$. Neglecting the non-linear term due to the smallness of $\mathbf{v}$, the incompressible Navier–Stokes equation takes the form

$$\rho \partial_t \mathbf{v} = -\boldsymbol{\nabla} p + \rho \mathbf{g} \quad \Rightarrow \quad \rho \boldsymbol{\nabla}(\partial_t \phi) = -\boldsymbol{\nabla}(p + \rho g z). \tag{11.7}$$

We evaluate this expression at $z = \zeta$, which is assumed small. The pressure of air at the interface is the constant p_0. Moreover, keeping only first order terms in ϕ and ζ, we find that $\phi(\zeta) \approx \phi(0) + \partial_z \phi(0)\zeta \approx \phi(0)$, thus ϕ needs only to be evaluated at the equilibrium position $z = 0$. Eq. (11.7) is now easily integrated and evaluated at $z = \zeta$ to give

$$\rho\big(\partial_t \phi + g\,\zeta\big) = p_0, \tag{11.8}$$

which can be interpreted as continuity of the pressure going from the liquid to air across the interface. Differentiating this equation with respect to time yields

$$\partial_t^2 \phi + g\,\partial_t \zeta = 0. \tag{11.9}$$

We now note that on one hand $v_z = \partial_z \phi$ and on the other hand, since $\mathbf{v}$ and ζ are both small, $v_z = \mathrm{d}\zeta/\mathrm{d}t = \partial_t \zeta + (\mathbf{v}\cdot\boldsymbol{\nabla})\zeta \approx \partial_t \zeta$. Thus inserting $\partial_t \zeta = v_z = \partial_z \phi$ into Eq. (11.9) and rearranging the two terms leads to

$$-\partial_t^2 \phi = g\,\partial_z \phi. \tag{11.10}$$

The continuity equation $\boldsymbol{\nabla}\cdot\mathbf{v} = 0$ must also be fulfilled. Combining this equation with the potential form $\mathbf{v} = \boldsymbol{\nabla}\phi$ yields the Laplace equation for ϕ,

$$\boldsymbol{\nabla}\cdot\mathbf{v} = 0 \quad \Rightarrow \quad \nabla^2 \phi = 0. \tag{11.11}$$

Consequently, it is natural to seek plane-wave solutions of the form

$$\phi(x, z, t) = f(z)\,\cos(kx - \omega t), \tag{11.12}$$

where $k = 2\pi/\lambda$ is the wavenumber and ω the angular frequency. Inserting this into the continuity equation Eq. (11.11) yields, after removal of the common cosine-factor

$$\partial_z^2 f - k^2 f = 0 \quad \Rightarrow \quad f(z) = \frac{A}{\sinh(kh)}\,\cosh\big[k(z + h)\big], \tag{11.13}$$

where the argument of the cosine hyperbolic function is chosen to ensure $v_z = \partial_z \phi = 0$ for $z = -h$, so that no liquid is allowed to flow through the solid base plane at $z = -h$. In conclusion, the potential function ϕ and the velocity field $\mathbf{v}$ becomes

$$\phi(x, z, t) = \frac{A}{\sinh(kh)}\,\cosh\big[k(z + h)\big]\,\cos(kx - \omega t), \tag{11.14a}$$

$$\mathbf{v}(x, z, t) = \frac{A}{\sinh(kh)} \begin{pmatrix} -k\cosh\big[k(z + h)\big]\,\sin(kx - \omega t) \\ 0 \\ +k\sinh\big[k(z + h)\big]\,\cos(kx - \omega t) \end{pmatrix}. \tag{11.14b}$$
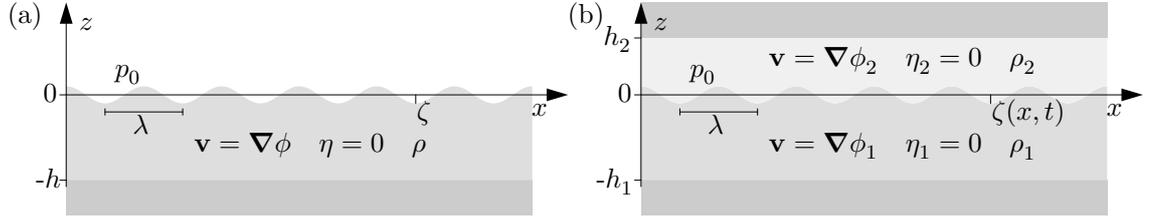
Figure 11.2: (a) A free-surface gravity wave on an inviscid liquid with a density ρ and of depth h. The surface is displaced by the amount $\zeta(x,t)$ from the equilibrium position given by $z \equiv 0$, and the resulting wave has the wavelength λ. (b) A gravity wave at the interface between two confined liquid layers of densities ρ_1 and ρ_2 and of layer depths h_1 and h_2, respectively.

At the interface, $z = 0$, we obtain the velocity

$$
\mathbf{v}(x,0,t) = A \begin{pmatrix} -k \tanh\big[kh\big]\ \sin(kx - \omega t) \\ 0 \\ +k \cos(kx - \omega t) \end{pmatrix} \xrightarrow[kh\to\infty]{} A \begin{pmatrix} -k \sin(kx - \omega t) \\ 0 \\ +k \cos(kx - \omega t) \end{pmatrix},
\tag{11.15}
$$

while at the base plane, $z = -h$, we get

$$
\mathbf{v}(x,-h,t) = \frac{A}{\sinh(kh)} \begin{pmatrix} -k \sin(kx - \omega t) \\ 0 \\ 0 \end{pmatrix} \xrightarrow[kh\to\infty]{} \begin{pmatrix} 0 \\ 0 \\ 0 \end{pmatrix}.
\tag{11.16}
$$

Note that in general the no-slip boundary condition is not fulfilled by the velocity field given in Eq. (11.16). This is not a big surprise; as we have neglected viscosity there is no reason for $v_x = 0$ at the solid wall. We can only insist that no liquid can penetrate the wall, i.e., $v_z = 0$ for $z = -h$. The free-surface gravity wave is sketched in Fig. 11.2(a).

With the solution for $\phi(x,z,t)$ at hand we can use Eq. (11.10) to obtain the dispersion relation $\omega = \omega(k)$ for the gravity waves. Inserting Eq. (11.14a) we arrive at the following after removal of the common function

$$
\omega^2 = gk \quad \Rightarrow \quad \omega = \sqrt{gk} = \sqrt{2\pi\,\frac{g}{\lambda}},
\tag{11.17}
$$

thus the frequency increases as the wavelength decreases.

We end this treatment by assessing the validity of omitting the viscosity. To establish when $|\eta \nabla^2 \mathbf{v}| \ll |\rho \partial_t \mathbf{v}|$ we note that $\boldsymbol{\nabla} \to k$ and $\partial_t \to \omega = \sqrt{gk}$. So we get

$$
|\eta \nabla^2 \mathbf{v}| \ll |\rho \partial_t \mathbf{v}| \quad \Rightarrow \quad \eta k^2 \ll \rho \sqrt{gk} \quad \Rightarrow \quad k^3 \ll \frac{\rho^2 g}{\eta^2} \quad \Rightarrow \quad \lambda \gg 2\pi \Big(\frac{\eta^2}{\rho^2 g}\Big)^{\frac{1}{3}}.
\tag{11.18}
$$

Inserting the values for water we obtain $\lambda \gg 60\ \mu m$. Likewise, to establish when the non-linear term can be neglected we use again $\boldsymbol{\nabla} \to k$, $\partial_t \to \omega$, and $\mathbf{v} \to \omega\zeta$:

$$
|\rho(\mathbf{v}\cdot\boldsymbol{\nabla})\mathbf{v}| \ll |\rho \partial_t \mathbf{v}| \quad \Rightarrow \quad k\omega\zeta \ll \omega \quad \Rightarrow \quad \lambda \gg 2\pi\zeta.
\tag{11.19}
$$

Finally, the no-slip condition is only approximately fulfilled for $kh \gg 1$ or $\lambda \ll 2\pi\,h$, so the range of validity of the treatment is given by

$$\max\left\{60\ \mu\text{m},\ 2\pi\,\zeta\right\} \ll \lambda \ll 2\pi\,h. \tag{11.20}$$

Based on the solution for free-surface gravity waves we can easily analyze the gravity waves at the interface between two confined liquid layers 1 and 2 as sketched in Fig. 11.2(b). We simply try to match solutions for the potential function ϕ_1 and ϕ_2, for each layer, of the form given by ϕ in Eq. (11.14a):

$$\phi(x,z,t) = \begin{cases} \phi_2(x,z,t) = A_2 \cosh\left[k(z-h_2)\right]\,\cos(kx - \omega t), & \text{for} \quad 0 < z < h_2, \\ \phi_1(x,z,t) = A_1 \cosh\left[k(z+h_1)\right]\,\cos(kx - \omega t), & \text{for} \quad -h_1 < z < 0. \end{cases}$$
$$\tag{11.21}$$

Here A_1 and A_2 are constants to be determined by the boundary conditions at the interface, $z = 0$. One boundary condition is the continuity of the pressure at the interface. In analogy with Eq. (11.8), but now with the liquid pressures on both sides of the equation we obtain

$$\rho_1\big(\partial_t\phi_1 + g\,\zeta\big) = \rho_2\big(\partial_t\phi_2 + g\,\zeta\big),\ \text{for } z = 0, \tag{11.22}$$

which can be solved with respect to ζ to yield

$$\zeta = \frac{1}{(\rho_1 - \rho_2)g}\left(\rho_2\partial_t\phi_2 - \rho_1\partial_t\phi_1\right),\ \text{for } z = 0. \tag{11.23}$$

The other boundary condition simply states that the vertical velocity component $v_z = \partial_z\phi$ must be the same on either side of the interface,

$$\partial_z\phi_1 = \partial_z\phi_2,\ \text{for } z = 0. \tag{11.24}$$

Now, by differentiation of Eq. (11.23) with respect to time and utilizing $v_z = \partial_z\phi = \partial_t\zeta$ we arrive at

$$(\rho_1 - \rho_2)g\partial_z\phi_1 = \rho_2\partial_t^2\phi_2 - \rho_1\partial_t^2\phi_1,\ \text{for } z = 0. \tag{11.25}$$

Insertion of the wave functions Eq. (11.21) leads to the following forms of Eqs. (11.24) and (11.25), after appropriate algebraic reductions,

$$A_1 \sinh\left(kh_1\right) = -A_2 \sinh\left(kh_2\right), \tag{11.26a}$$

$$(\rho_1 - \rho_2)gkA_1 \sinh\left(kh_1\right) = \left[\rho_1 A_1 \cosh\left(kh_1\right) - A_2 \cosh\left(kh_2\right)\right]\omega^2. \tag{11.26b}$$

Solving for ω we find the dispersion relation

$$\omega = \sqrt{\frac{(\rho_1 - \rho_2)gk}{\rho_1\coth\left(kh_1\right) + \rho_2\coth\left(kh_2\right)}}. \tag{11.27}$$

When both liquids are very deep, $kh_1 \gg 1$ and $kh_2 \gg 1$ the result is simply

$$\omega = \sqrt{gk\,\frac{\rho_1 - \rho_2}{\rho_1 + \rho_2}}. \tag{11.28}$$

The discussion of the physical interpretation of this expression for $\rho_1 > \rho_2$ and for $\rho_1 < \rho_2$ is left as an exercise for the reader.

11.2.2   Capillary waves

So far the role of surface tension between the fluids in the two-phase flow has been neglected, but to add it is not too difficult, at least conceptually. We have already in connection with Eq. (5.9) discussed how surface tension must be included as a Young–Laplace pressure-drop discontinuity in the boundary condition at the interface for the stress tensor projected along the surface normal. Since the Young–Laplace pressure-drop Δp_{surf} is given by the surface tension γ times the curvature κ of the interface,

$$\Delta p_{\mathrm{surf}} = \gamma \, \kappa, \tag{11.29}$$

we choose to study the influence of surface tension for the gravity waves in the limit of small wavelengths, see Section 11.2.1, as the curvature increases as the wavelength decreases.

   From differential geometry it is known that for a curve $\mathbf{r}(s)$ described by the parameter s, the curvature κ is given by

$$\kappa(s) = \frac{|\mathbf{r}'(s) \times \mathbf{r}''(s)|}{|\mathbf{r}'(s)|^3}, \tag{11.30}$$

where the prime denotes differentiation with respect to s. If one interprets s as time, the expression for the curvature can by understood from a physical point of view, since $\mathbf{r}'$ and $\mathbf{r}''$ can be identified with the instantaneous velocity $\mathbf{v}$ and acceleration $\mathbf{a}$, respectively. For a particle in a circular orbit of radius $\mathbf{r}$ we know from classical mechanics that $|\mathbf{a}| = |\mathbf{v}|^2/r$ or $1/r = |\mathbf{a}|/|\mathbf{v}|^2$, but $1/r$ is exactly the curvature, so Eq. (11.30) really states that $\kappa = |\mathbf{e}_v \times \mathbf{a}|/|\mathbf{v}|^2$, where $\mathbf{e}_v \equiv \mathbf{v}/|\mathbf{v}|$ is a unit vector in the tangential direction.

   If we as in Section 11.2.1 study waves only propagating along the x direction, then the x coordinate can serve as a parameter to define the shape $\mathbf{r}(x)$ of the interface at any given time t and y coordinate,

$$\mathbf{r} = \begin{pmatrix} x \\ y \\ \zeta(x) \end{pmatrix}, \quad \mathbf{r}' = \begin{pmatrix} 1 \\ 0 \\ \zeta'(x) \end{pmatrix}, \quad \mathbf{r}'' = \begin{pmatrix} 0 \\ 0 \\ \zeta''(x) \end{pmatrix}, \tag{11.31}$$

where ζ is the displacement along the z axis of the interface away from the equilibrium position at $z = 0$. Keeping terms of linear order in ζ gives the curvature

$$\kappa(x) = \zeta''(x) + \mathcal{O}(\zeta^2). \tag{11.32}$$

   Using the potential description of the velocity field, $\mathbf{v} = \boldsymbol{\nabla}\phi$ from Section 11.2.1 we obtain by combining Eqs. (5.9) and (11.8) the following partial differential equation for ϕ and ζ:

$$\rho\big(\partial_t \phi + g\,\zeta\big) = p_0 + \gamma \partial_x^2 \zeta. \tag{11.33}$$

In analogy with the derivation of Eq. (11.10), we differentiate Eq. (11.33) with respect to time and utilize $\partial_t \zeta = \partial_z \phi$ to obtain

$$-\partial_t^2 \phi = g\,\partial_z \phi - \frac{\gamma}{\rho}\,\partial_x^2 \partial_z \phi, \text{ for } z = 0. \tag{11.34}$$

Moreover, the incompressibility condition $\boldsymbol{\nabla}\mathbf{v} = \nabla^2\phi$ still holds, so ϕ still takes the form of Eq. (11.14a),

$$\phi(x, z, t) = A \cosh\left[k(z + h)\right] \cos(kx - \omega t). \tag{11.35}$$

Inserting this into Eq. (11.34) leads, in analogy with Eq. (11.17), to the dispersion relation $\omega(k)$ for capillary waves,

$$\omega^2 = gk + \frac{\gamma}{\rho}\,k^3 \quad \Rightarrow \quad \omega = \sqrt{gk + \frac{\gamma}{\rho}\,k^3}. \tag{11.36}$$

As expected, the effect of surface tension becomes more dominant at shorter wavelength where the wavenumber is big. Surface tension dominates in the square root of the dispersion relation when

$$\frac{\gamma}{\rho}\,k^3 \gg gk \quad \Rightarrow \quad k \gg \sqrt{\frac{\rho g}{\gamma}} = \frac{1}{\ell_{\mathrm{cap}}} \quad \Rightarrow \quad \lambda \ll 2\pi\ell_{\mathrm{cap}}, \tag{11.37}$$

where the capillary length ℓ_{cap}, introduced in Eq. (5.13) for characterizing capillary rise, now reappears.

11.3   Gas bubbles in microfluidic channels

Many microfluidic networks on modern lab-on-a-chip devices contain channel contractions. These tend to become problematic if, as often is the case, gas bubbles are introduced into the liquid at the inlets or by electrochemical processes. Due to the small channel dimensions gas bubbles can easily be big enough to span the entire channel cross-section. Such "large" bubbles are prone to get stuck at the channel contraction, whereby they can clog the flow and disturb measurements or functionality of the system in an uncontrolled manner. To clear the clogged channel an external pressure, the so-called clogging pressure, has to be applied to push the clogging bubble out of the system.

A complete analysis of the motion of a large bubble through a microchannel contraction involves many different physical effects, some which are not completely understood. Any comprehensive analysis would at least require detailed modelling of the liquid-gas, liquid-solid, and solid-gas interfaces as well as the dynamics in the bulk fluids. But also more complicated processes near the contact lines need to be addressed, e.g., wetting, contact line pinning and hysteresis, dynamic contact angles and contact lines, and static and dynamic friction. We will, however, restrict our analysis to the simple quasi-static motion of bubbles. By this we mean that the velocity of the bubble is nearly zero and that the entire model system remains arbitrarily close to equilibrium for all bubble positions. All dynamic aspects are thus neglected, and basically the model involves only the free energy of the internal interfaces of the system and external pressures. This is motivated by the fact that it is difficult experimentally to control surface related properties. We thus only study geometry related effects. We also choose to work with axisymmetric channels of smooth (but otherwise arbitrary) contraction geometries free from any sharp corners and other singularities. With these simplifications the forces or pressures needed to push
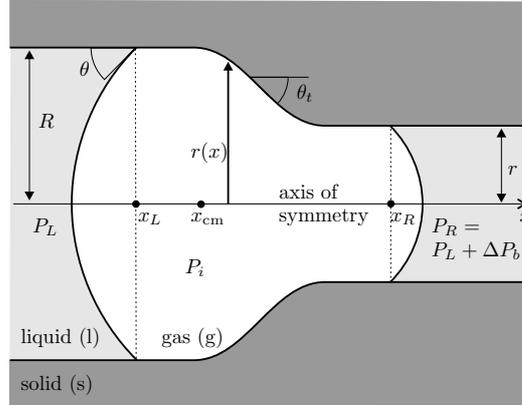
Figure 11.3: A bubble with internal pressure P_i and center of mass x_{cm} in a hydrophilic axisymmetric channel. The left (right) contact line has the coordinate x_L (x_R) and contact angle θ. The channel is contracting from a straight part of radius R to one of radius r. The specific channel profile is defined by some function $r(x)$. Throughout this paper we have chosen $r(x)$ to be a sloped straight line joined to the straight parts by two circle arcs. The tapering angle θ_t is given by $\tan \theta_t = -r'(x)$. The pressure left (right) of the bubble is denoted P_L (P_R) and the pressure difference across the bubble is ΔP_b.

a bubble through the system can be calculated accurately without losing the essential physics of the problem. This in turn enables us to formulate design rules for microchannel contractions to prevent or reduce clogging. The treatment given in the following is an excerpt from Jensen, Goranović, and Bruus, J. Micromech. Microeng. **14**, 876 (2004).

11.3.1 The model and basic physical assumptions

Consider a hydrophilic microfluidic channel or capillary, such as the one depicted in Fig. 11.3, which is axisymmetric about the x axis with a position dependent channel radius $r(x)$. The channel is filled with a liquid. A large bubble of some other fluid, we think mainly of a gas such as air, is present in the liquid. By large we mean that the volume of the bubble is larger than the volume $V_{\mathrm{sph}}^{\mathrm{max}}$ of the largest inscribed sphere that can be placed anywhere in the microchannel. A large bubble divides the liquid in two disconnected parts, left and right of the bubble, respectively. The bubble itself consists of a bulk part in direct contact with the walls of the channel and of two menisci, in contact with the liquid, capping the ends of the bubble.

The bubble is assumed to be in quasi-static equilibrium. In that case it is relatively simple to combine mass conservation with geometric constraints to determine, as a function of the bubble position, the pressure drops over the two menisci needed to maintain this equilibrium. We define our central concept, the clogging pressure, as the maximum of the position dependent pressure drop across the bubble, i.e., the minimal external pressure that must be supplied to push the bubble through the microchannel.

Our model system consists of a solid channel containing a liquid and one large gas

bubble. Therefore, the essential physical parameters are the three surface tensions (surface free energy per area) γ_{lg}, γ_{sl}, and γ_{sg} for the liquid-gas, solid-liquid, and solid-gas interfaces, respectively. In equilibrium the contact angle θ is determined by the surface tensions through the Young equation Eq. (5.11),

$$\gamma_{\text{sg}} - \gamma_{\text{sl}} = \gamma_{\text{lg}} \cos \theta. \tag{11.38}$$

The contact angle is in the following taken as the equilibrium angle or rather as an average contact angle. Because contact angle hysteresis is very sensible to surface effects we do not address these questions in this work.

To sustain a curved interface with the main radii of curvature R_1^c and R_2^c between a gas of pressure P_g and a liquid of pressure P_l, the pressure difference $\Delta P = P_g - P_l$ must obey the Young-Laplace equation Eq. (5.8)

$$\Delta P = \gamma_{\text{lg}} \left(\frac{1}{R_1^c} + \frac{1}{R_2^c} \right) = 2\gamma_{\text{lg}} \frac{\cos \theta}{r}, \tag{11.39}$$

where the last equation is applicable for a constant circular cross-section of radius r. We use the standard convention that these radii are taken as positive if the interface is concave when seen from the gas.

In the rest of the paper we consider a "large" bubble having the initial position '1' in the widest part of the channel. The initial volume is $V_1 = \gamma V_{\text{sph}}^{\text{max}}$, where $\gamma > 1$ and $V_{\text{sph}}^{\text{max}} = 4\pi r_1^3/3$, and the corresponding internal pressure is $P_{i,1}$. At a later stage the bubble is moved to a position '2', where the volume is V_2 and the internal pressure $P_{i,2}$. In the quasi-static case the bubble motion is isothermal and hence the compressibility condition applies,

$$P_{i,1} V_1 = P_{i,2} V_2. \tag{11.40}$$

The pressure P_i within the bubble is given as the external pressure P_0 plus the pressure change ΔP across the curved interface, given by Eq. (11.39).

The most extreme compression is obtained by pressing a large bubble, which floats without geometrical constraints in a bulk liquid of pressure P_0, into a narrow circular channel of radius r. Combining Eqs. (11.39) and (11.40) yields

$$\frac{V_1}{V_2} = \frac{P_{i,2}}{P_{i,1}} \approx \frac{P_{i,2}}{P_0} = 1 + \frac{2\gamma_{\text{lg}} \cos \theta}{r P_0}. \tag{11.41}$$

For example, moving a large spherical air bubble in water ($\gamma_{\text{lg}} = 0.0725 \text{ J m}^{-2}$) at the ambient pressure $P_0 = 10^5$ Pa into a channel of radius $r = 25$ μm leads to $V_1/V_2 \approx 1.06$, i.e., a volume compression of 6%. Moving, as in Sec. VI, a bubble from a 300 μm to a 190 μm wide channel yields a compression of about 0.2%.

In the case of laser ablated microchannels in plastic chips compressibility effects are negligible as the smallest dimensions typically are greater than 100 μm. However, for silicon based micro- or nanofluidic devices compressibility may play a significant role.

For a bubble positioned in a microchannel contraction the total internal energy E_{tot} is the sum of the surface free energy, gravitational energy, kinetic energy, and frictional

energy. We regard the surrounding pressures as external energy. By our definition quasi-static motion of an incompressible bubble imply that the kinetic energy is zero and that friction is zero because of hydrostatic and thermodynamic equilibrium. Finally, we treat channels of characteristic dimensions $2r$ less than 300 μm, which is significantly smaller than the capillary length of water, $\ell_{\text{cap}} \approx 2700$ μm, Eq. (5.13). So the gravitational energy can also be neglected, which ensures that the menisci may be approximated by spherical caps.

The total internal energy E_{tot} of the microchannel containing a quasi-statically moving bubble is given only by the surface free energy, i.e., the sum of interfacial energies γ_i times interfacial areas A_i,

$$E_{\text{tot}} = \sum_i \gamma_i A_i = \gamma_{\text{lg}} A_{\text{lg}} + \gamma_{\text{sg}} A_{\text{sg}} + \gamma_{\text{sl}} A_{\text{sl}}. \tag{11.42}$$

The pressure-related applied external force F needed to balance the bubble is given by the gradient of the total internal energy with respect to the center of mass coordinate of the bubble x_{cm}. Hence

$$F = \frac{\mathrm{d}E_{\text{tot}}}{\mathrm{d}x_{\text{cm}}}, \tag{11.43}$$

which thus depends on the bubble position x_{cm} and, through the areas A_i, on the geometry of the channel.

The Young-Laplace pressure drops, c.f. Eq. (11.39), at the menisci are given by,

$$\Delta P_L \quad = P_i - P_L, \tag{11.44a}$$
$$\Delta P_R \quad = P_i - P_R. \tag{11.44b}$$

The total pressure drop $\Delta P_b(x_{\text{cm}})$ over the bubble as a function of its center of mass x_{cm} is given by

$$\Delta P_b(x_{\text{cm}}) = P_R - P_L = \Delta P_L(x_{\text{cm}}) - \Delta P_R(x_{\text{cm}}). \tag{11.45}$$

The clogging pressure P_{clog} is defined as the maximal position dependent pressure drop across the bubble,

$$P_{\text{clog}} = \max\left\{-\Delta P_b(x_{\text{cm}})\right\}. \tag{11.46}$$

The clogging pressure expresses the minimal amount by which the left-side pressure P_L must exceed the right-side pressure P_R to push the bubble through the contraction quasi-statically from left to right.

11.3.2 General energy considerations for axisymmetric microchannels

Consider a bubble placed in a cylindrical channel of radius R. We want to determine the change in energy resulting from moving it into a smaller channel of radius $r < R$, e.g., by moving it from left to right in the channel depicted in Fig. 11.3. Intuitively, we would expect the energy to increase as a result of the move. In most cases this intuition is correct, however, we shall see that in some cases the system gains energy by the move, solely due to geometric conditions.
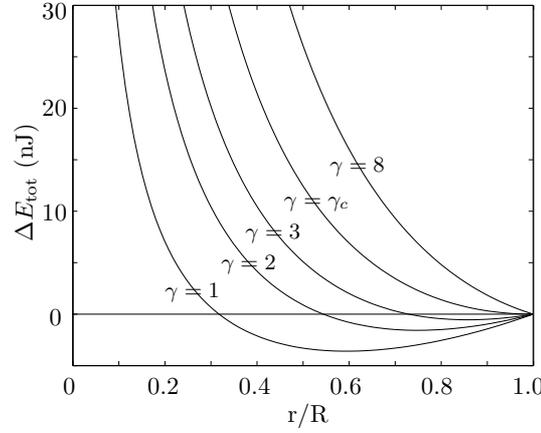
Figure 11.4: Plot of the energy change ΔE_{tot} as a function of the ratio r/R. The bubble is moved from a wide channel of radius $R = 150\ \mu$m to a narrow channel of radius r. Five curves are shown corresponding to the volume ratio $\gamma = 1$, 2, 3, γ_c, and 8, respectively, $\gamma_c \approx 4.75$. For "small" volumes $1 \leq \gamma < \gamma_c$ the system can gain energy by moving the bubble to the narrow channel, if the latter is not too narrow. For $\gamma > \gamma_c$ the move costs energy in all cases.

The bubble has the initial volume $V_1 = \gamma V_{\text{sph}}^{\max}$, where $\gamma > 1$ and $V_{\text{sph}}^{\max} = 4\pi R^3/3$. With this constraint the bubble is forced to touch the walls regardless of its position. According to Eqs. (11.39) and (11.44b) the internal pressure of the bubble is

$$P_{i,1} = P_R + 2\gamma_{\text{lg}}\frac{\cos\theta}{R}. \tag{11.47}$$

The volume of the bubble is the sum of two spherical cap volumes and the volume of a cylinder of initial length L. Once the length L is known, the relevant interfacial areas A_{lg} and A_{sg} may be found.

The gas bubble is now moved to the cylindrical channel of radius r, and according to Eqs. (YoungLaplace), (11.40), and (11.44b) the pressure $P_{i,2}$ volume V_2 are,

$$P_{i,2} = P_R + 2\gamma_{\text{lg}}\frac{\cos\theta}{r}, \tag{11.48}$$

$$V_2 = \frac{P_{i,1}}{P_{i,2}}V_1. \tag{11.49}$$

By solving Eq. (11.49) it is straightforward to find the change in total free surface energy,

$$\Delta E_{\text{tot}} = E_{\text{tot},2} - E_{\text{tot},1} =$$
$$\gamma_{\text{lg}}(A_{lg,2} - A_{lg,1}) + \gamma_{\text{lg}}2\pi\cos\theta(rl - RL), \tag{11.50}$$

where l is the length of the bubble in the channel of radius $r < R$ (situation 2). In Eq. (11.50) the Young relation Eq. (11.38) has been used to eliminate the solid-liquid and solid-gas interfacial energies.
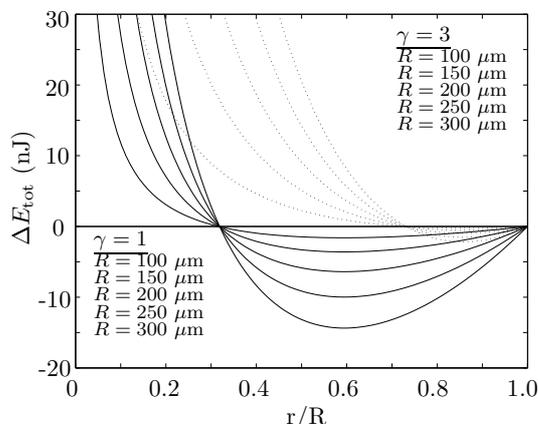
Figure 11.5: The energy ΔE_{tot} as a function of the ratio r/R for different values of the wide channel radius, $R = 100, 150, 200, 250$, and 300 μm. The plain curve corresponds to the smallest bubble for $\gamma = 1$ and the dotted to a larger bubble with $\gamma = 3$.

Based on Eq. (11.50) we can analyze the energy change when moving the bubble from the wide channel of radius R to the narrow channel of radius r. First we give the limiting values of ΔE_{tot}. In the limit $r/R \to 1$ we obviously get $\Delta E_{\text{tot}} \to 0$. In the opposite limit, $r/R \to 0$, the compressibility of the bubble results in convergence of ΔE_{tot},

$$\lim_{\frac{r}{R} \to 0} \Delta E_{\text{tot}} = \frac{\pi R^3}{3}\left(4\gamma R P_R - \gamma_{\text{lg}} \frac{4 + \sin(3\theta) - 3\tan\theta}{\cos^2\theta}\right). \tag{11.51}$$

To discuss ΔE_{tot} for general values of r/R we use a numerical example: an air bubble in a water filled PMMA channel for which we have the parameter values $P_R = 10^5$ Pa, $\gamma_{\text{lg}} = 72.5$ mJ, and $\theta = 72°$. The radius ratio r/R and the volume parameter γ are then varied.

In Fig. 11.4 the energy ΔE_{tot} (Eq. (11.50)) is plotted as a function of the ratio r/R for given values of γ. The figure shows that for large values of γ, i.e., large bubbles, it costs energy ($\Delta E_{\text{tot}} > 0$) to move the bubble from the wide to the narrow channel. However, there exists a critical value $\gamma_c \approx 4.75$ below which the system can gain energy by moving the bubble, if the radius ratio r/R is not too small. This behavior is generic for a bubble in a contracting channel, but the specific shape of the curve and the optimal minimum depend on the material parameters and the external pressure P_R.

The critical value γ_c, above which energy gain is impossible, is given by $\partial \Delta E_{\text{tot}}/\partial (r/R) = 0$ at $r/R = 1$,

$$\gamma_c = \frac{(3 - \cos(3\theta) + 2\sin\theta)(2\gamma_{\text{lg}}\cos\theta + RP_0)}{2RP_R\cos\theta(1 + \sin\theta)}. \tag{11.52}$$

Fig. 11.5 depicts the energy ΔE_{tot} as a function of the ratio r/R for $\gamma = 1$ and $\gamma = 3$, and for five values of the wide channel radius, $R = 100, 150, 200, 250$, and 300 μm. From Eq. (11.50) it may be seen that $\min\{\Delta E_{\text{tot}}\} \propto R^2$ as the area is proportional to R^2 and L is proportional to R. Deviations from this proportionality arise for small values of R

because of compressibility. For $\gamma = 1$ in Fig. 11.5 we find $\max\{-\Delta E_{\text{tot}}\} = kR^2$ with $k = 0.159$ J/m^2. This proportionality is illustrated as the energy at a given r/R point is increased by a factor 4 when R is doubled, e.g., from $R = 150$ μm to $R = 300$ μm.

The previous calculations clearly show that for some geometries it is favorable to place the bubble in the narrow rather than in the wide part of the channel. In the following we shall address the question whether for such geometries the bubble will move spontaneously or it must cross an energy barrier to arrive at the low-energy state in the narrow channel.

11.3.3   Analytical results for contractions with energy gain

Combining the geometry defined in Fig. 11.3 with Eqs. (11.39) and (11.45) the central expression of our analysis is easily derived,

$$\Delta P_b = 2\gamma_{\text{lg}} \left(\frac{\cos[\theta - \theta_t(x_L)]}{r(x_L)} - \frac{\cos[\theta + \theta_t(x_R)]}{r(x_R)} \right). \tag{11.53}$$

From the discussion in Section 11.3.1 it follows that if $\Delta P_b < 0$ then the contraction causes bubble clogging, whereas for $\Delta P_b > 0$ the bubble tends to move spontaneously through the contraction towards the narrow part.

Based on Eq. (11.53) a number of design rules may be established specifying the geometric features that may prevent or decrease clogging. Consider a bubble that starts out in the wide straight section left of the contraction, where it has the length $L_0 = x_R - x_L$. The pressure drop ΔP_b is zero to begin with, but depending on the shape of the contraction, such as the two examples shown in Fig. 11.6, ΔP_b changes as the bubble advance quasi-statically through the contraction.

The first part of any contraction can always be approximated by a circle with an arc angle which is the local tapering angle θ_t. As the right contact line x_R just enters the contraction, Eq. (11.53) can be expanded to first order in θ_t yielding

$$\Delta P_b \approx \frac{2\gamma_{\text{lg}} \sin\theta}{R} \, \theta_t > 0. \tag{11.54}$$

Thus initially the bubble tends to move spontaneously into the contraction. The physical reason for this is that the local tapering angle allows the meniscus to flatten a little, which reduces the costly gas-liquid interface energy.

Once the bubble moves inside the contraction defined in Fig. 11.3, a complicated interplay between the initial bubble length L_0, the contact angle θ, the channel radii $r(x_L)$ and $r(x_R)$ at the contact lines, as well as the local tapering angle $\theta_t(x)$ decides whether bubble clogging occurs or not. We classify our systems in two main classes:

Class α comprises all cases where no clogging occurs, i.e., where the bubble can move spontaneously through the contraction without applying an external pressure.

Class β contains all cases with clogging, i.e., where $\Delta P_b < 0$ at some point or, equivalently, where $P_{\text{clog}} > 0$.

For class β four sub-classes can be identified according to where the bubble is when ΔP_b becomes negative and clogging occurs. This bubble position is classified by the position of
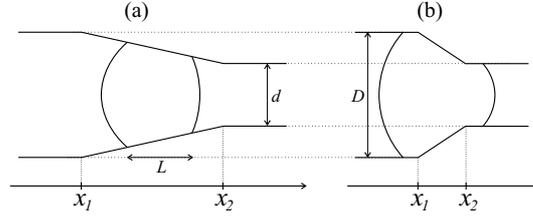
Figure 11.6: Two generic situations for a bubble of length $L = x_R - x_L$ near a microchannel contraction of length $x_2 - x_1$. (a) The contraction is long enough to contain the entire bubble, i.e., $x_R - x_L < x_2 - x_1$. (b) The contraction is so short that the bubble can span it completely, i.e., $x_R - x_L > x_2 - x_1$, which is a class β_4 bubble.

the contact lines x_L and x_R relative to the beginning x_1 and the end x_2 of the contraction region (see Figs. 11.3 and 11.6):

$$\begin{aligned}
\text{Class } \beta_1 : & & x_L < x_1 & & \text{and} & & x_1 < x_R < x_2, \\
\text{Class } \beta_2 : & & x_1 < x_L < x_2 & & \text{and} & & x_1 < x_R < x_2, \\
\text{Class } \beta_3 : & & x_1 < x_L < x_2 & & \text{and} & & x_2 < x_R, \\
\text{Class } \beta_4 : & & x_L < x_1 & & \text{and} & & x_2 < x_R.
\end{aligned} \tag{11.55}$$

A detailed analysis of Eq. (11.53) yields important relations for some of the clogging classes.

A β_2 clogging only occurs if the bubble can move entirely within the tapered region as shown in Fig. 11.6(a), and if at some point it has a length $L = x_L - x_R$ such that

$$L > \frac{r(x_L)}{\tan\theta_t} \left[1 - \frac{\cos(\theta - \theta_t)}{\cos(\theta + \theta_t)} \right]. \tag{11.56}$$

In β_4 where the bubble in fact spans the entire contraction as sketched in Fig. 11.6(b), there is always clogging and the clogging pressure is maximal. The value for ΔP_b is negative and independent of the shape of the contraction. From Eq. (11.53) we get

$$\Delta P_b = 2\gamma_{\text{lg}} \cos\theta \left(\frac{1}{R} - \frac{1}{r} \right) < 0. \tag{11.57}$$

The non clogging class α will in general happen if the bubble is short enough. According to the class β_4 analysis a necessary (but not sufficient) condition for avoiding clogging is that the bubble is short enough to be completely contained in the contraction region. An analysis of the β_2 and β_3 classes show that it should also be short enough to avoid clogging while the left meniscus is still in the tapered region. The β_1 class furthermore puts upper limits on tapering angles that allow for clog-free flow.
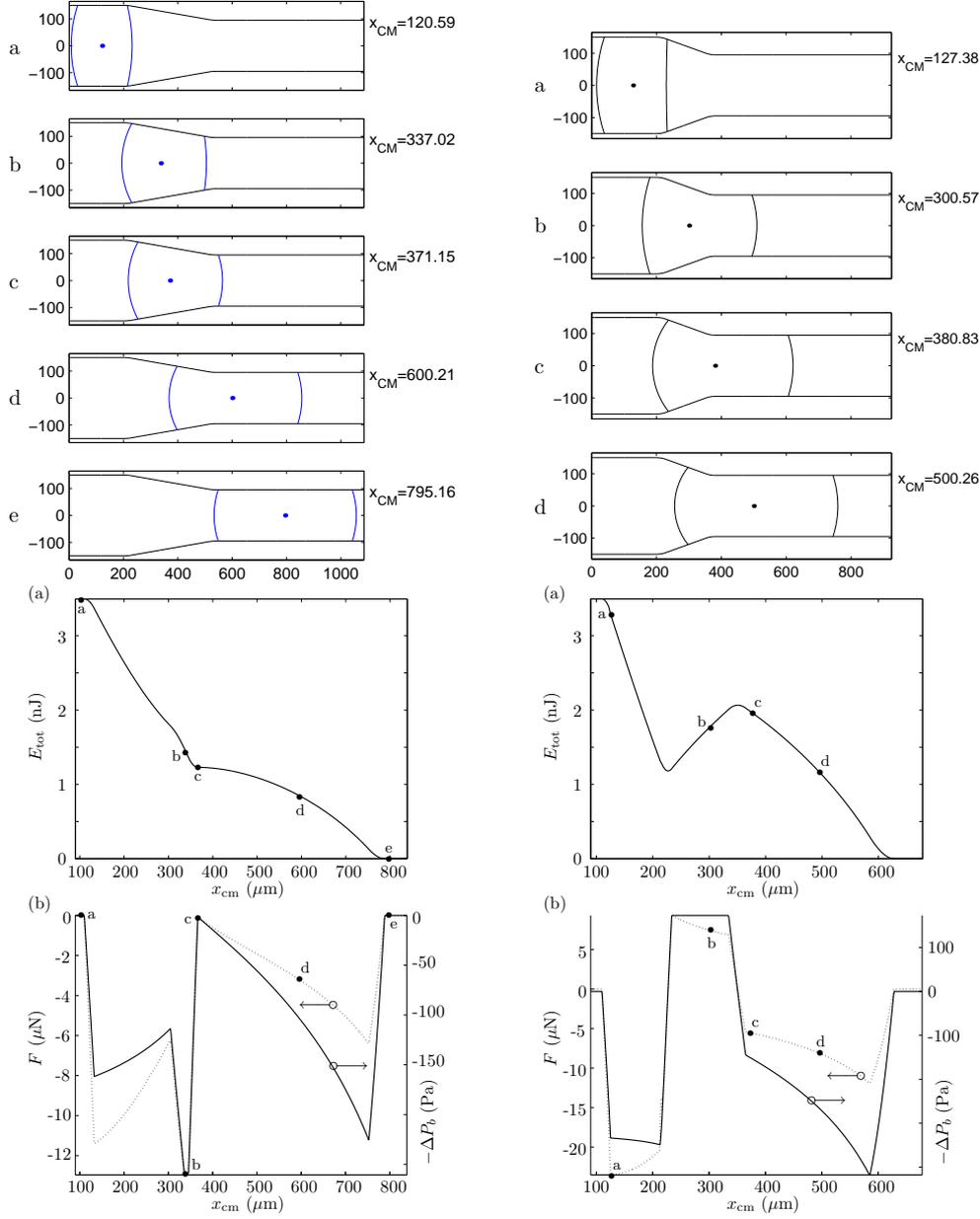
Figure 11.7: Numerical analysis of quasi-static bubble motion in a microchannel contraction. **(Top)** Different positions of a large bubble with $\gamma = 1.02$ inside a 1000 μm long hydrophilic channel with contact angle $\theta = 72°$. The tapering angle is $\theta_t = 10°$ and $20°$ in the left and right column, respectively. **(Bottom)** (a) For the same bubble positions as above (marked by dots), plots are shown of the total internal energy E_{tot} versus the center of mass coordinate x_{cm}, the balancing external force F, and the pressure drop across the bubble ΔP_b versus x_{cm}. Note that for the system to the right, $-\Delta P_b < 0$ for all positions, i.e., no clogging occurs (a class α system), while for the system to the left, $-\Delta P_b > 0$ for x_{cm} around 300 μm, i.e., clogging occurs (a class β system).

11.4 Exercises

Exercise 11.1
Two-phase Poiseuille flow
We study some aspect of the difference in hydrostatic pressure between points at different depths in some incompressible liquid.

(a) Give a qualitative argument based on basic physical considerations that the velocity profile shown in Fig. 11.1 is correct.

(b) Prove the correctness of Eq. (11.5) for the two constants h_1 and h_2 that determines the explicit expression for the velocity field in the two-phase Poiseuille flow.

Exercise 11.2
Kelvin's circulation theorem and potential flow
The integral $\Gamma = \oint_{\mathcal{C}} \mathbf{v} \cdot \delta\mathbf{r}$ taken along some closed contour $\mathcal{C}$ defined by certain fluid particles is called the velocity circulation. The infinitesimal curve length $\delta\mathbf{r}$ is defined as the difference of the position vectors $\mathbf{r}$ of neighboring fluid elements defining the contour $\mathcal{C}$.

(a) Argue why the time derivative of the circulation is given by

$$\frac{\mathrm{d}\Gamma}{\mathrm{d}t} = \frac{\mathrm{d}}{\mathrm{d}t} \oint_{\mathcal{C}} \mathbf{v} \cdot \delta\mathbf{r} = \oint_{\mathcal{C}} \frac{\mathrm{d}\mathbf{v}}{\mathrm{d}t} \cdot \delta\mathbf{r} + \oint_{\mathcal{C}} \mathbf{v} \cdot \frac{\mathrm{d}\delta\mathbf{r}}{\mathrm{d}t}. \tag{11.58}$$

(b) Since the time derivative of a fluid element position $\mathbf{r}$ is just the fluid element velocity $\mathbf{v}$, i.e., $\mathrm{d}\mathbf{r}/\mathrm{d}t = \mathbf{v}$, show that

$$\mathbf{v} \cdot \frac{\mathrm{d}\delta\mathbf{r}}{\mathrm{d}t} = \mathbf{v} \cdot \delta\mathbf{v} = \delta\left(\tfrac{1}{2}v^2\right). \tag{11.59}$$

(c) If the viscosity term can be neglected in the Navier–Stokes equation $\mathrm{d}\mathbf{v}/\mathrm{d}t = \boldsymbol{\nabla}(-p/\rho - gz) + \eta\nabla^2\mathbf{v}$, then show that the circulation Γ becomes

$$\frac{\mathrm{d}\Gamma}{\mathrm{d}t} = \oint_{\mathcal{C}} \boldsymbol{\nabla}(-p/\rho - gz) \cdot \delta\mathbf{r} + \oint_{\mathcal{C}} \delta\left(\tfrac{1}{2}v^2\right) = 0 \quad \Rightarrow \quad \Gamma = \text{const}. \tag{11.60}$$

(d) Consider a situation where the resulting velocity field $\mathbf{v}(t)$ is built up from rest $\mathbf{v}(t = 0) \equiv \mathbf{0}$. Argue that in this case $\Gamma(t) \equiv 0$, from which it follows that $\boldsymbol{\nabla} \times \mathbf{v} = 0$ and thus a scalar potential function ϕ exists such that

$$\mathbf{v} = \boldsymbol{\nabla}\phi. \tag{11.61}$$

When this equation is fulfilled the flow is for obvious reasons denoted a potential flow.

Exercise 11.3
Stability of gravity waves
The dispersion relation $\omega(k)$ for gravity waves is given by Eq. (11.28). Discuss the physical interpretation of this expression for $\rho_1 > \rho_2$ and for $\rho_1 < \rho_2$. Hints: note when the heaviest liquid is on top, and use that the time evolution is given by $e^{i\omega t}$ also when ω is a complex number.

Exercise 11.4
Capillary waves
The basic theory for capillary waves was given in Section 11.2.2.
    (a) Verify that the wave equation Eq. (11.34) is correct.
    (b) Verify and discuss the dispersion relation Eq. (11.36).

Exercise 11.5
The pressure drop across a gas bubble in a microchannel
Prove that the pressure drop across a bubble in a microfluidic channel indeed is given by
Eq. (11.53)

11.5 Solutions

Solution 11.1
To be added
In the next edition solutions to the exercises will be added.

Chapter 12

Complex flow patterns

Viscous forces dominate in microfluidics and tend to favor laminar flow at the expense of turbulence. Most laminar flow patterns are simple, and in the case of creeping flow they even closely follow the geometry of the enclosing channel. Nevertheless, it is possible by careful design to create complex flow patterns in microfluidic lab-on-a-chip systems. In this chapter we will study of two examples of such an increasing level of complexity in microflows.

12.1   Pressure-driven flow in patterned microchannels

The first example will just be mentioned briefly. Normally, the pressure gradient applied in microfluidics is axial thus leading to a forward running flow. However, if a row of parallel ridges are placed at the bottom of the channel at an oblique angle the result is an anisotropic hydraulic resistance. The strong dependence of the resistance on height in flat channels, $R_{\mathrm{hyd}} \propto h^{-3}$ according to Eq. (2.53), means that the flow direction will be turned away from the straight forward direction towards a direction more parallel to the ridges, as there is less resistance to a flow along the ridges than in the perpendicular direction. The effect is similar to rifling in a gun barrel. The viscous liquid begins to move in a helical pattern along the channel axis; the liquid circulates back at the top of the channel.

A more complicated flow pattern arises if one places groups of ridges with different tilt angles. One famous example is the so-called staggered herringbone mixer, where two set of ridges oriented in two different directions meet in a cusp somewhere inside the microfluidic channel. Instead of just one helical motion inside the channel, the herringbone mixer generates several counter-rotating helical flows. The resulting flow has proven to be very efficient for mixing, moreover, the design is very robust as it does not contain any moving mechanical parts.

Since the presentation of the design method in three papers from 2002 by Ajdari [Phys. Rev. E **65**, 016301, (2002)], Stroock *et al.* [Science **295**, 647, (2002)], and Stroock *et al.* [Anal. Chem. **74**, 5306 (2002)], several research groups have taken up this design idea. In Fig. 12.1 is shown a staggered herringbone device fabricated at MIC. The flow is visualized using fluorescein, a molecule that can be made fluorescent and hence visible.
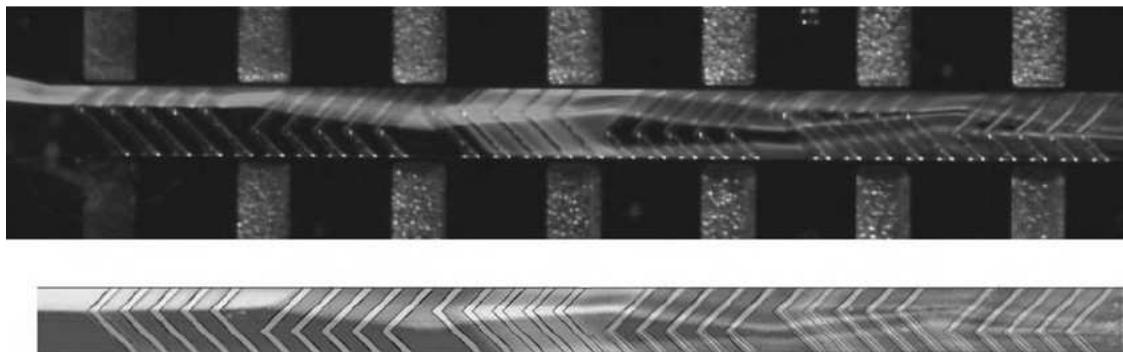
Figure 12.1: The top panel is a micrograph of a staggered herring mixer fabricated at MIC. Water is entering from the left containing fluorescein in the top quarter of the stream. Bottom panel is the result of a FemLab simulation. A good agreement is observed between experiment and simulation. Courtesy the groups of Fougt Hansen and Bruus at MIC.

The top panel is a micrograph of a 200 μm with a set of staggered herringbone ridges at the bottom of the channel. Water is injected from the left with fluorescein in the top quarter of the stream. The ridges are grouped in sets of five, and it is seen that already after passing two of these groups the fluorescein is spreading widely in the channel. The bottom panel in Fig. 12.1 is a FemLab simulation of the staggered herringbone mixer flow. A good agreement is shown between experiment and simulation.

A more theoretical treatment of the complex flow can be done by making a perturbation expansion in powers of the amplitude of the ridges relative to the total channel height. This perturbation calculation is more complicated than the one presented in Section 2.5, because in the latter the pressure gradient remained parallel to the flow direction.

With this remark we end this short presentation of the pressure-driven flow in patterned microchannels and move on to discuss flow-patterns generated by the induced-charge method.

12.2   Induced-charge electrolytic flow

The charged Debye layer in electrolytes provides a handle to manipulate with electrolytes by externally applied potentials. The basic physics of the Debye layer was treated in Section 7.3, and in Chapter 8 we studied electroosmosis, where an electrolyte is brought in motion by sending an electrical current through it. In the following we will study an example of the so-called induced-charge electrolytic flow. In contrast to electroosmosis, where charge is exchanged between the electrolyte and the electrodes providing the external potential, no such charge transfer takes place in an induced-charge flow. Instead, the electric coupling is purely capacitive and motion is brought about by applying AC potentials on electrodes situated at the wall of the microchannels but electrically insulated from the electrolyte. An example of an actual induced-charge flow device is shown in Fig. 12.2

In the following we study a simple example of an induced-charge system with spatially
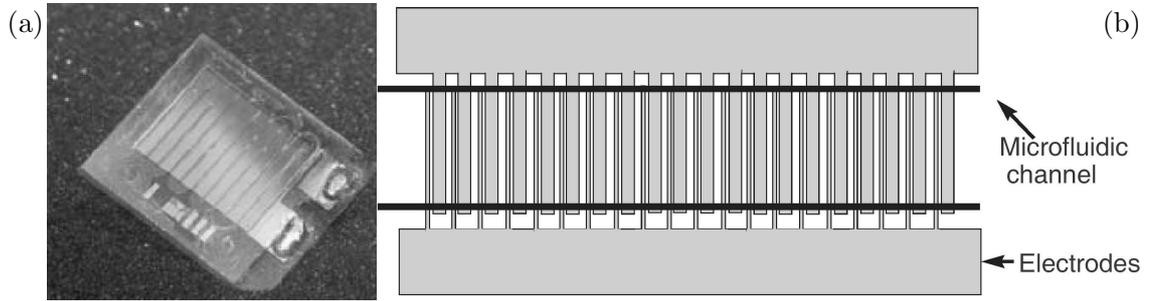
Figure 12.2: (a) A picture of a polymer-based microfluidic channel with surface electrode for controlling induced-charge flows. The channel forms a meander with ten turns. A pair of intercalating gold electrodes are placed at the bottom of the channel. The two contact pads are seen on the right-hand edge of the chip. (b) The design of the electrode pair. One set of the electrodes are wide and the other narrow. This spatially asymmetric design leads to a non-zero time-average of the induced-charge flow initiated when an AC voltage bias is applied to the electrode pair. Courtesy the group of Bruus at MIC (2004).

symmetric electrodes. Although the problem involves the coupling between the velocity field $\mathbf{v}$, the pressure field $\mathbf{p}$, the ionic density fields $c_\pm$, and the electrical potential ϕ, the relative simplicity does allow us to find an analytical solution. In such spatial symmetric systems the time-average of the AC motion is zero, but if the spatial symmetry is broken it is possible to generate a non-zero average motion. For systems with a zero average flow, the AC induced-charge method can be used to create mixers of electrolytes, while a non-zero average can by exploited to design micropumps, admittedly with a low capacity and efficiency. The following example is a simplified version of a more complete treatment by Mortensen, Olesen, Belmon and Bruus, Phys. Rev. E **71**, 056306 (2005).

12.2.1 The microchannel with surface electrodes

We reconsider the binary electrolyte of Section 7.3 containing ions with charges $+Ze$ and $-Ze$, respectively. Like in Fig. 7.3 the electrolyte is confined to the semi-infinite space $x > 0$ by an impenetrable, homogeneous and planar wall. However, now the wall is an insulating layer with dielectric constant ϵ_s placed at $-d < x < 0$, see Fig. 12.3. The metallic electrode is attached at the back-side of the insulator at $x < -d$, and it is biased at the surface $x = -d$ by a spatially modulated, external AC potential $V_{\text{ext}}(y, t)$ given by

$$V_{\text{ext}}(y, t) = V_0 \cos(qy)e^{i\omega t}, \tag{12.1}$$

where V_0 is the amplitude, q the wavenumber of the spatial modulation, and ω the driving angular frequency using complex notation as in Section 9.6.

There is complete translation invariance along the z axis, so the z coordinate drops out of our analysis, and all positions $\mathbf{r} = x\mathbf{e}_x + y\mathbf{e}_y$ in the following are therefore just referring to the xy plane.
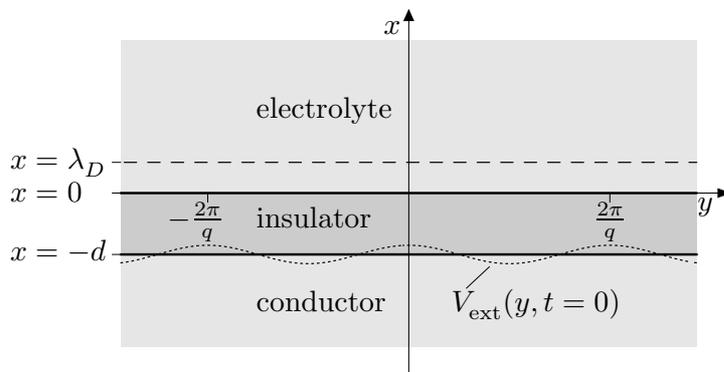
Figure 12.3: A sketch of the induced-charge system under study. The binary electrolyte is situated in the half space $x > 0$. Below it, for $-d < x < 0$, is a planar wall consisting of an insulating dielectric slab of thickness d and below that, for $x < -d$, is a semi-infinite conductor. The top surface, $x = -d$, of the conductor is biased by a periodically modulated potential $V_{\text{ext}}(y, t)$ of period $2\pi/q$ (dotted line), which gives rise to the formation of a Debye screening layer of thickness λ_D in the electrolyte (dashed line).

12.2.2 Non-equilibrium description

The following analysis combines the methods from Section 7.3 on the electrostatic De-bye layer and Section 8.1 on the electrohydrodynamic Nernst–Planck transport equation. We imagine that the intrinsic zeta-potential due to un-passivated surface charges on the insulator-electrolyte interface has been compensated by a corresponding DC shift, so that any non-zero potential at the $x = 0$ wall is entirely due to the applied AC potential. To simplify further, we treat the insulating layer as a simple capacitor with the surface capacitance $C_s = \epsilon_s/d$ per area assumed to be much larger that the Debye capacitance $C_D = \epsilon/\lambda_D$ of Eq. (7.39),

$$\frac{C_D}{C_s} = \frac{\epsilon}{\epsilon_s}\,\frac{d}{\lambda_D} \ll 1. \tag{12.2}$$

In the liquid electrolyte we consider the ionic densities $c_\pm(\mathbf{r}, t)$, the potential $\phi(\mathbf{r}, t)$, the ionic current densities (the ionic flux densities) $\mathbf{J}_\pm(\mathbf{r}, t)$, the velocity field $\mathbf{v}(\mathbf{r}, t)$ of the electrolyte, and the pressure $p(\mathbf{r}, t)$. In the following we suppress $(\mathbf{r}, t)$ unless needed for clarity.

The number densities of the ions couple to the potential via Poisson's equation,

$$\nabla^2\phi = -\frac{Ze}{\epsilon}\big(c_+ - c_-\big). \tag{12.3a}$$

The ionic current densities are coupled to the ionic densities by a continuity equation, which in the absence of any chemical reactions in the system is

$$\partial_t c_\pm = -\boldsymbol{\nabla} \cdot \mathbf{J}_\pm. \tag{12.3b}$$

Spatial modulation	q^{-1}	10^{-5} m
Insulator thickness	d	10^{-8} m
Debye length	λ_D	10^{-8} m
Resonance frequency	ω^*	10^5 rad/s
Debye frequency	$\omega_{\mathrm{D}} = \sigma_\infty/\epsilon$	10^7 rad/s
Critical frequency	$\omega_{\mathrm{c}} = (\eta/\rho)\,q^2$	10^4 rad/s
Thermal voltage	$V_T = (1+\delta)k_{\mathrm{B}}T/Ze$	250 mV
Convective voltage	$V_c = \sqrt{(1+\delta)\eta D/\epsilon}$	100 mV
Ionic density	c_0	10^{-3} mol m^{-3}
Viscosity	η	10^{-3} Pa s
Mass density	ρ	10^3 kg m^{-3}
Ionic diffusivity	D	10^{-9} m^2 s^{-1}
Capacitance ratio	$\delta = C_D/C_s$	10

Table 12.1: Typical values of central parameters in the induced-charge problem.

The presence of convection or of gradients in the densities $c_\pm$ and the electric potential ϕ will generate ionic current densities $\mathbf{J}_\pm$. The Nernst–Planck equation gives these currents

$$\mathbf{J}_\pm = -D\boldsymbol{\nabla} c_\pm + c_\pm \mathbf{v} \mp \mu c_\pm \boldsymbol{\nabla}\phi, \tag{12.3c}$$

where, for simplicity, we have assumed that the two types of ions have the same diffusivity D and the same mobility μ. Note that both the diffusivity D and the electric conductivity σ are linked to the mobility μ via the Einstein relation $D = (k_{\mathrm{B}}T/Ze)\mu$ and $\sigma^\pm = Zec_\pm\mu$, see Exercise 4.5 and Section 7.2.2.

Finally, the velocity field and pressure of the liquid are coupled to the potential and ionic densities by the Navier–Stokes equation

$$\rho\big[\partial_t \mathbf{v} + (\mathbf{v}\cdot\boldsymbol{\nabla})\mathbf{v}\big] = -\boldsymbol{\nabla}p + \eta\nabla^2\mathbf{v} - Ze\big[c_+ - c_-\big]\boldsymbol{\nabla}\phi, \tag{12.3d}$$

where ρ is the mass density, η is the viscosity of the liquid, and p is the pressure. Furthermore, treating the electrolyte as an incompressible fluid we have

$$\boldsymbol{\nabla}\cdot\mathbf{v} = 0. \tag{12.3e}$$

The coupled field-equations, Eqs. (12.3a) to (12.3e), fully govern the physical fields ϕ, $c_\pm$, $\mathbf{J}_\pm$, $\mathbf{v}$, and p.

We now turn to the boundary conditions of the fields, beginning with the potential. Assuming a vanishing intrinsic zeta-potential and noting that in the extreme limit $C_D/C_s \to 0$ the entire potential drop happens across the Debye layer, the potential $\phi(\mathbf{r})$ of the electrolyte must satisfy the boundary conditions

$$\phi(\mathbf{r},t)\big|_{x=0} = V_{\mathrm{ext}}(y,t) = V_0\,\cos(qy)\,e^{i\omega t}, \tag{12.4a}$$

$$\phi(\mathbf{r},t)\big|_{x=\infty} = 0. \tag{12.4b}$$

At the interface between the electrolyte and the insulating region the normal component of the ionic current density vanishes,

$$0 = \partial_x c_\pm(\mathbf{r}, t)\big|_{x=0} \pm \frac{Ze}{k_\mathrm{B}T} c_\pm(\mathbf{r}, t) \partial_x \phi(\mathbf{r}, t)\big|_{x=0}. \tag{12.5}$$

Here, we have utilized Eq. (12.3c) and the absence of convection at the interface due to the no-slip boundary condition,

$$\mathbf{v}(\mathbf{r}, t)\big|_{x=0} = \mathbf{0}. \tag{12.6}$$

For the ionic densities we have charge neutrality in the bulk,

$$c_\pm(\mathbf{r}, t)\big|_{x=\infty} = c_0, \tag{12.7}$$

where c_0 is the homogeneous density of either of the two types of ions in the absence of an external perturbation, i.e., when $V_0 = 0$. For the pressure, we assume that we have no externally applied pressure gradients so that p is the internal pressure caused by fluid flow and the electrical forces on the ions.

12.2.3   Linearized dynamic regime, $\omega > 0$

We now solve Eq. (12.3) in the dynamic regime, $\omega > 0$. First the ionic current densities are eliminated by inserting Eq. (12.3c) into Eq. (12.3b). Using the incompressibility of the fluid, Eq. (12.3e), we get the continuity equation

$$\partial_t c_\pm = D\, \nabla^2 c_\pm - \left(\boldsymbol{\nabla} c_\pm\right)\cdot\mathbf{v} \,\pm\, \mu \boldsymbol{\nabla}\cdot\left(c_\pm\, \boldsymbol{\nabla}\phi\right). \tag{12.8}$$

To advance further by analytical methods, we linearize this continuity equation in the density as follows. Using Eq. (12.7) we write

$$c_\pm(\mathbf{r}, t) = c_0 + \delta c_\pm(\mathbf{r}, t), \qquad \lim_{x\to\infty} \delta c_\pm(\mathbf{r}, t) = 0. \tag{12.9}$$

Since we assume a zero intrinsic zeta-potential it is a non-zero V_0 that spawns $\delta c_\pm \neq 0$, and when the applied voltage V_0 is much smaller than the thermal voltage V_T, defined by $V_T \equiv k_\mathrm{B}T/Ze \approx 25\,\mathrm{mV}$, we have $|\delta c_\pm| \ll c_0$. In this limit the Debye–Hückel approximation is valid, and $c_\pm \boldsymbol{\nabla}\phi$ is substituted by $c_0 \boldsymbol{\nabla}\phi$ in Eq. (12.8). We subsequently use Eq. (12.3a) to replace $\nabla^2\phi$ with $-Ze\nu/\epsilon$ where

$$\nu \equiv c_+ - c_- = \delta c_+ - \delta c_-. \tag{12.10}$$

Finally, we form the difference of the "$\pm$"-versions of Eq. (12.8) and obtain the diffusion equation for the density difference ν,

$$\partial_t \nu = \left[D\nabla^2 - D\frac{1}{\lambda_D^2} - \mathbf{v}\cdot\boldsymbol{\nabla}\right]\nu \approx \left[D\nabla^2 - D\frac{1}{\lambda_D^2}\right]\nu, \tag{12.11}$$

where we have neglected the convection term. This approximation is valid as the net charge density is non-zero only in the Debye layer, $x \lesssim 3\lambda_D$, and in this region convection will be suppressed due to the no-slip boundary condition. Thus, convection can be

neglected, diffusion will dominate (corresponding to a low Péclet number), and the electrodynamics can be solved independently of the hydrodynamics. On the other hand, the hydrodynamics of course still depends on the electrodynamics via the body force. Since the density difference ν changes over the length scales λ_D and q^{-1} for the x and y directions, respectively, the condition for the decoupling is $|v_x|/\lambda_D + |v_y|q \ll Dq^2$ for $0 < x \lesssim 3\lambda_D$. In this limit Eq. (12.11) has a general $\cos(qy)e^{i\omega t}$ modulated decaying solution of the form

$$\nu = \mathcal{C}_1 e^{-\kappa x} \cos(qy)e^{i\omega t}, \quad x > 0, \tag{12.12a}$$

where the decay parameter κ via Eq. (12.11) is seen to depend on the ratio between the frequency ω and the Debye frequency ω_D,

$$\kappa \equiv \frac{1}{\lambda_D} \sqrt{1 + (q\lambda_D)^2 + i\,\frac{\omega}{\omega_\mathrm{D}}}, \tag{12.12b}$$

$$\omega_\mathrm{D} \equiv \frac{D}{\lambda_D^2}. \tag{12.12c}$$

For the potential we seek a solution to the Poisson equation Eq. (12.3a) of a form similar to Eq. (12.12a), $\phi \propto \cos(qy)e^{i\omega t}$,

$$\nabla^2\phi = (\partial_x^2 + q^2)\phi = -\frac{Ze}{\epsilon}\,\nu = -\frac{Ze}{\epsilon}\,\mathcal{C}_1 e^{-\kappa x}\cos(qy)e^{i\omega t}. \tag{12.13}$$

The full solution to this inhomogeneous differential equation is the sum of a particular solution $\phi_1 \propto \mathcal{C}_1 e^{-\kappa x}\cos(qy)e^{i\omega t}$ and the full solution ϕ_2 to the homogeneous equation $\nabla^2\phi = 0$, i.e., $\phi_2 \propto \mathcal{C}_1 e^{-qx}\cos(qy)e^{i\omega t}$. Demanding $\phi(\mathbf{r},t)\big|_{x=\infty} = 0$ the solution becomes

$$\phi = \frac{Ze/\epsilon}{q^2 - \kappa^2}\left[\mathcal{C}_1 e^{-\kappa x} + \mathcal{C}_2 e^{-qx}\right]\cos(qy)e^{i\omega t}, \quad x > 0. \tag{12.14}$$

In order to determine $\mathcal{C}_1$ and $\mathcal{C}_2$ we first consider the boundary condition for the current. Applying the Debye–Hückel approximation to the second term in Eq. (12.5) and forming the difference of the "$\pm$" solutions we arrive at

$$0 = \partial_x\left[\nu(\mathbf{r},t) + \frac{\epsilon}{Ze\lambda_D^2}\phi(\mathbf{r},t)\right]\bigg|_{x=0}. \tag{12.15}$$

Inserting Eqs. (12.12a) and (12.14) into Eq. (12.15) we find

$$\mathcal{C}_2 = i\frac{\kappa}{q}\frac{\omega}{\omega_\mathrm{c}}\mathcal{C}_1. \tag{12.16}$$

Combining Eqs. (12.4a), (12.14), and (12.16) leads to

$$\mathcal{C}_1 = \frac{Ze/\epsilon}{\lambda_D^2}\frac{\omega_\mathrm{D} + i\omega}{\omega_\mathrm{D} + i\frac{\kappa}{q}\omega}. \tag{12.17}$$

From the expressions for the coefficients $\mathcal{C}_1$ and $\mathcal{C}_2$ we get the final results for the potential,

$$\phi(x,y,t) = \frac{V_0}{\omega_\mathrm{D} + i\frac{\kappa}{q}\omega}\left(\omega_\mathrm{D}e^{-\kappa x} + i\,\frac{\kappa}{q}\,\omega e^{-qx}\right)\cos(qy)\,e^{i\omega t}, \quad x > 0. \tag{12.18}$$

Next, we consider the regime where the spatial period of the modulation is much longer than all other length scales, i.e., $q\lambda_D \ll 1$ and $qd \ll 1$. We also assume that $\omega \ll \omega_{\mathrm{D}}$ so that in the following

$$\kappa \simeq \frac{1}{\lambda_D}. \tag{12.19}$$

In this limit we get a simple expression for the potential in the bulk beyond the Debye layer, $x \gtrsim 3\lambda_D$, see Fig. 12.4(a) where the fast decaying term $e^{-\kappa x} \approx e^{-x/\lambda_D}$ has vanished,

$$\phi(x, y, t) = V_0 \frac{i\omega}{\omega^* + i\omega} \, e^{-qx} \cos(qy) \, e^{i\omega t}, \quad x \gtrsim 3\lambda_D, \tag{12.20}$$

where we have introduced the characteristic resonance frequency ω^* given by

$$\omega^* \equiv q\lambda_D \, \omega_{\mathrm{D}}. \tag{12.21}$$

Until this point we have used the exponential notation for the temporal dependence. However, since the electrical body force in the Navier–Stokes equation Eq. (12.3d) is non-linear due to the product of the potential and the ionic density difference we have to take the real part to get the body force, i.e., $\mathbf{f} = -Ze\nu\boldsymbol{\nabla}\phi = -Ze\mathrm{Re}\{\nu\}\mathrm{Re}\{\boldsymbol{\nabla}\phi\}$. Utilizing that

$$\mathrm{Re}\left\{\frac{e^{i\omega t}}{i\omega + \omega^*}\right\}\mathrm{Re}\left\{\frac{i\omega e^{i\omega t}}{i\omega + \omega^*}\right\} = \frac{-\cos(2\omega t + \varphi)}{2\omega^*\left(\frac{\omega}{\omega^*} + \frac{\omega^*}{\omega}\right)}, \tag{12.22}$$

we get the following expression for the body force $\mathbf{f}$,

$$\mathbf{f} = F_0 \, e^{-x/\lambda_D} \left[2\cos^2(qy)\mathbf{e}_x + \sin(2qy)\mathbf{e}_y\right], \tag{12.23a}$$

where we have introduced the force amplitude F_0, the velocity v_1, and the frequency dependent phase shift φ,

$$F_0 \equiv \frac{\eta v_1}{\lambda_D^2} \frac{\cos(2\omega t + \varphi)}{\frac{\omega}{\omega^*} + \frac{\omega^*}{\omega}}, \tag{12.23b}$$

$$v_1 \equiv \frac{q\epsilon V_0^2}{4\eta}, \tag{12.23c}$$

$$\varphi \equiv -\arctan\left(\frac{\omega}{2\omega^*} - \frac{\omega^*}{2\omega}\right). \tag{12.23d}$$

At low frequencies, $\mathbf{f} \propto \omega$, it becomes maximal at the resonance frequency ω^*, and then it falls off again at higher frequencies. We note that $\lim_{\omega\to 0} \mathbf{f} = \mathcal{O}\big([q\lambda_D]^2\big)$, but this small force will just be balanced by a pressure gradient so that $\lim_{\omega\to 0} \mathbf{v} = \mathbf{0}$ and $\lim_{\omega\to 0} \mathbf{J}_\pm = \mathbf{0}$.
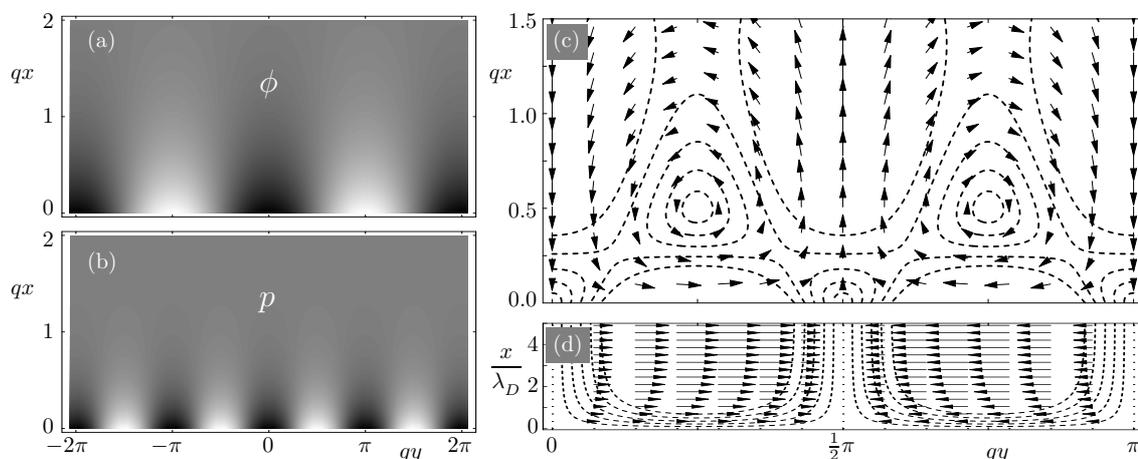
Figure 12.4: The potential ϕ, pressure p, and velocity field $\mathbf{v}$. (a) A gray scale plot of the amplitude of the potential ϕ as a function of qx and qy, Eq. (12.20). (b) A gray scale plot of the pressure p, Eq. (12.34c). Notice the period doubling in the pressure compared to the electric potential. (c) A snapshot of the harmonically oscillating velocity field $\mathbf{v}$ in the bulk, Eq. (12.34), and (d) likewise in the Debye layer, Eq. (12.29). The flow pattern contains rolls, which are indicated by contours of constant velocity (dashed lines).

12.2.4 Linearized flow and separation of length scales

In order to solve the Navier–Stokes equation, Eq. (12.3d), we note that for a body force of small magnitude and with slow temporal variation the fluid response is linear and the flow will approximately be at steady state at each moment in time. We begin by comparing the inertial terms on the left-hand side (LHS) with the viscous term (second term) on the right-hand side (RHS). The body force has a characteristic frequency ω and two characteristic length scales λ_D and q^{-1} for the x and y-directions, respectively. Since ∂_t essentially gives a factor of ω, and $\boldsymbol{\nabla}$ essentially gives $\lambda_D^{-1}\mathbf{e}_x + q\mathbf{e}_y$, we can show that the viscous term dominates over the LHS when $\omega \ll \omega_c$ where

$$\omega_c \equiv \frac{\eta}{\rho}\,\min\{q^2, \lambda_D^{-2}\}. \tag{12.24}$$

For $q\lambda_D \ll 1$ this means that $\omega_c = \frac{\eta}{\rho}\,q^2$. In this way, for small Reynolds numbers, we get the linearized Navier–Stokes equation

$$\mathbf{0} = -\boldsymbol{\nabla}p + \eta\nabla^2\mathbf{v} + \mathbf{f}, \quad \omega \ll \omega_c \tag{12.25}$$

which is the resulting quasi-steady flow problem, linear in the velocity field. Eq. (12.25) with Eq. (12.23a) can be solved exactly, but in the follwing we restrict ourselves to an approximate solution based on the separation of length scales, $\lambda_D \ll q^{-1}$.

From Eq. (12.23a) we note that the electrical body force $\mathbf{f}$ Eq. (12.23a) decays in the x-direction over the short length scale λ_D, while along the y-direction it varies on the much longer length scale q^{-1}. Moreover, the no-slip condition forces the velocity $\mathbf{v}$ to be

zero at the wall, but due to shear flow it is much easier for the parallel component v_y to acquire a significant value within the Debye layer than for the perpendicular component v_x. Thus $v_x \approx 0$ for $0 < x < 3\lambda_D$, and the x component of the Navier–Stokes equation becomes

$$-\partial_x p + f_x = 0 \qquad \Rightarrow \qquad p(x,y) = \lambda_D F_0 \, 2\cos^2(qy) e^{-x/\lambda_D}. \tag{12.26}$$

From this we easily find the y component of $\boldsymbol{\nabla} p$,

$$\partial_y p = q\lambda_D F_0 \, 4\cos(qy)\sin(qy) e^{-x/\lambda_D} = 2\lambda_D q \, f_y \ll f_y. \tag{12.27}$$

So the y component of the Navier–Stokes equation can be approximated by

$$\eta(\partial_x^2 + \partial_y^2) v_y = -f_x = -F_0 \, \sin(2qy) \, e^{-x/\lambda_D}. \tag{12.28}$$

From the functional dependencies we see that $|\partial_x^2 v_y| \approx |v_y|/\lambda_D^2$ and $|\partial_x^2 v_y| \approx |v_y| \, q^2$, and since $q\lambda_D \ll 1$ the $\partial_y^2 v_y$-term can be neglected. So by straightforward integration twice after x and taking the boundary condition $v_y(0,y,t) = 0$ into account we arrive at

$$v_y(x,y) = \frac{\lambda_D^2}{\eta} \, F_0 \, \sin(2qy) \left(1 - e^{-x/\lambda_D} \right), \quad \text{for } 0 < x \lesssim 3\lambda_D. \tag{12.29}$$

In analogy with the EO slip velocity introduced in Eqs. (8.10) and (8.11), we now define the slip velocity $v_s(y,t)$ for the induced-charge flow as the limit at infinity of $v_y(\infty,y,t)$,

$$v_s(y,t) \equiv v_1 \, \frac{\cos(2\omega t + \varphi)}{\frac{\omega}{\omega^*} + \frac{\omega^*}{\omega}} \, \sin(2q y). \tag{12.30}$$

We now leave the narrow Debye layer and study the flow in the bulk beyond the $3\lambda_D$-limit. Here, according to Eq. (12.23a) the body force vanishes, and the Navier–Stokes equation Eq. (12.25) contains only the pressure and viscosity term. The system of equations to be solved can be summarized as

$$\left(\partial_x^2 + \partial_y^2 \right) \mathbf{v} = \frac{1}{\eta} \, \boldsymbol{\nabla} p, \tag{12.31a}$$

$$v_y(0,y,t) = v_1 \, \frac{\cos(2\omega t + \varphi)}{\frac{\omega}{\omega^*} + \frac{\omega^*}{\omega}} \, \sin(2q y), \tag{12.31b}$$

$$\boldsymbol{\nabla} \cdot \mathbf{v} = 0. \tag{12.31c}$$

Taking the divergence of Eq. (12.31a) and using the incompressibility condition $\boldsymbol{\nabla} \cdot \mathbf{v} = 0$ we arrive at a Laplace equation for the pressure,

$$\nabla^2 p = 0. \tag{12.32}$$

The boundary condition Eq. (12.31b) for v_y contains a $\sin(2qy)$-factor, so it is natural to seek a solution for p proportional to $\cos(2qy)$, which has the right y-derivative. The Laplace equation Eq. (12.32) then forces the x dependence e^{-2qx},

$$p(x,y) = P_0 \, e^{-2qx} \cos(2qy) \quad \Rightarrow \quad \left(\partial_x^2 + \partial_y^2 \right) \mathbf{v} = \frac{-2qP_0}{\eta} \, e^{-2qx} \Big(\cos(2qy)\mathbf{e}_x + \sin(2qy)\mathbf{e}_y \Big).$$

$$\tag{12.33}$$

Finally, using the trial solutions $v_x = G(x)e^{-2qx}\cos(2qy)$ and $v_y = H(x)e^{-2qx}\sin(2qy)$ we find the solutions for v_x, v_y, and p,

$$v_x(x, y, t) = -v_1 \frac{\cos(2\,\omega\,t + \varphi)}{\frac{\omega}{\omega^*} + \frac{\omega^*}{\omega}}\, e^{-2qx}\, 2qx \cos(2qy), \tag{12.34a}$$

$$v_y(x, y, t) = +v_1 \frac{\cos(2\,\omega\,t + \varphi)}{\frac{\omega}{\omega^*} + \frac{\omega^*}{\omega}}\, e^{-2qx}\, (1 - 2qx)\sin(2qy), \tag{12.34b}$$

$$p(x, y, t) = -4q\eta v_1 \frac{\cos(2\omega t + \varphi)}{\frac{\omega}{\omega^*} + \frac{\omega^*}{\omega}}\, e^{-2qx}\cos(2qy). \tag{12.34c}$$

If we now substitute into Eq. (12.3d) we get RHS $-$ LHS $\propto e^{-x/\lambda_D} + \mathcal{O}(\omega/\omega_{\mathrm{D}}) + \mathcal{O}([q\lambda_D]^2)$ which shows that Eq. (12.34) is indeed an excellent approximation to the full solution of the non-linear time-dependent Navier–Stokes equation, Eq. (12.3d), for $x \gtrsim 3\lambda_D$. For the incompressibility constraint, Eq. (12.3e), our solution gives $\boldsymbol{\nabla} \cdot \mathbf{v} = \mathcal{O}([q\lambda_D]^2)$.

In Fig. 12.4(c) we show a plot of the velocity field, Eq. (12.34), along with the contours for constant velocity. It is seen how a complex flow pattern involving counter-rotating rolls appears.

12.3 Exercises

Exercise 12.1
The diffusion equation for the density difference
In Section 12.2.3 a diffusion equation is set up for the ionic density difference ν.

(a) Derive the continuity equation for the two densities c_+ and c_-, Eq. (12.8).

(b) Based on this and the Debye-Hückel approximation derive the diffusion equation for the density difference ν, Eq. (12.11).

(c) Insert the trial solution Eq. (12.12a) for ν into the diffusion equation Eq. (12.11) and show that the decay parameter κ is given by Eq. (12.12b).

Exercise 12.2
The solution for the electrical potential
In Section 12.2.3 the solution is presented for the electrical potential ϕ in the linearized regime.

(a) Why are there two decaying terms present in the solution Eq. (12.14)?

(b) Show, based on Eq. (12.13), that the solution for the potential ϕ is given by Eq. (12.14).

(c) Derive the expression Eq. (12.16) for the coefficient $\mathcal{C}_2$ by inserting Eqs. (12.12a) and (12.14) into Eq. (12.15).

(d) Derive the expression Eq. (12.17) for the coefficient $\mathcal{C}_1$ by combining Eqs. (12.4a), (12.14), and (12.16).

(e) Verify expression Eq. (12.20) for the potential ϕ in the bulk, and make some representative plots revealing the form of the potential.

Exercise 12.3
The solution for the flow and pressure fields
In Section 12.2.3 the solutions are presented for the flow field $\mathbf{v}$ and the pressure p in the linearized regime.

(a) Prove that the pressure p indeed must be a solution to the Laplace equation Eq. (12.32).

(b) Argue why solutions to the Laplace equation must have the form $p(x,y) = P_0\,e^{-2qx}\cos(2qy)$ as stated in Eq. (12.33).

(c) Show that it is possible to determine the functions $G(x)$ and $H(x)$ such that the trial solutions $v_x = G(x)e^{-2qx}\cos(2qy)$ and $v_y = H(x)e^{-2qx}\sin(2qy)$ indeed solves the Navier–Stokes equation given in Eq. (12.33). Hint: insert the trial solutions in each component of the Navier–Stokes equation and obtain simple ordinary differential equations for $G(x)$ and $H(x)$.

(d) Verify the final expressions Eq. (12.34) for the velocity field $\mathbf{v}$ and the pressure p.

Exercise 12.4
Physical interpretation of the flow rolls
Discuss the physical contents of the front page picture or Fig. 12.4. Write down the chain of physical mechanisms that lead from the applied external potential to the final induced-charge flow.

12.4 Solutions

Solution 12.1
To be added
In the next edition solutions to the exercises will be added.

Chapter 13

Acoustics in compressible liquids

When acoustic radiation, mainly in the form of ultrasound waves, are propagating in liquids, the associated fast moving and rapidly oscillating pressure and velocity fields can impart a slow velocity component to the liquid or to small particles suspended in the liquid. In microfluidic systems these normally quite minute effects can be of significance. Interestingly, the origin of these effects can be traced back to two hydrodynamic properties largely ignored in the preceding chapters, namely the non-linearity of the Navier–Stokes equation and the compressibility of ordinary liquids.

In this chapter, after establishing the basic equations of motion of the acoustic fields, we shall in particular study two examples of significant acoustic effects in microfluidic: acoustic streaming, where the velocity field of the entire liquid acquires an extra slowly varying component induced by the incoming acoustic waves, and acoustic radiation force, where small particles suspended in a liquid is moved by the momentum transfer from sound waves propagating in the liquid.

13.1   Linear equations of motion in acoustics

In contrast to electromagnetism, where the wave equation of the electromagnetic field follows directly from the basic Maxwell equations, the wave equation for acoustics is only an approximate equation derived by combining the thermodynamic equation of state, the kinematic continuity equation Eq. (1.30), and the dynamic Navier–Stokes equation Eq. (1.46). Discarding all external fields such as gravitation and electromagnetism, the three equations form the starting point for the theory of acoustics or sound,

$$p = p(\rho), \tag{13.1a}$$

$$\partial_t \rho = -\boldsymbol{\nabla}\cdot\big(\rho\mathbf{v}\big), \tag{13.1b}$$

$$\rho\partial_t\mathbf{v} = -\boldsymbol{\nabla}p - \rho(\mathbf{v}\cdot\boldsymbol{\nabla})\mathbf{v} + \eta\nabla^2\mathbf{v} + \left(\tfrac{1}{3}\,\eta + \zeta\right)\boldsymbol{\nabla}(\boldsymbol{\nabla}\cdot\mathbf{v}). \tag{13.1c}$$

These coupled non-linear, partial differential equations are notoriously difficult to solve numerically, not to mention analytically. Fortunately, in many important cases of physical

importance, it suffices to solve a linearized version of the equations. The acoustic contributions to the pressure, density, and velocity fields, are considered to be small perturbations, p_1, ρ_1, and $\mathbf{v}_1$, to the starting point, a state in thermal equilibrium given by p_0, ρ_0, and $\mathbf{v}_0$, respectively. For simplicity, we will assume the liquid to be at rest before applying the acoustic field, i.e., $\mathbf{v}_0 = \mathbf{0}$. Hence we are going to work with the expressions

$$p = p_0 + p_1 = p_0 + c_0^2 \rho_1, \tag{13.2a}$$

$$\rho = \rho_0 + \rho_1, \tag{13.2b}$$

$$\mathbf{v} = \mathbf{0} + \mathbf{v}_1. \tag{13.2c}$$

Note, that for the pressure we have performed a Taylor expansion around $p_0 = p(\rho_0)$. The first-order derivative $\partial_\rho p$ has the dimension of velocity c_0 squared,

$$c_0^2 \equiv \left(\frac{\partial p}{\partial \rho}\right)_s. \tag{13.3}$$

This velocity, which in a more thorough thermodynamic treatment turns out to be the isentropic derivative of the pressure, will shortly be shown to be the speed of sound in the liquid.

Let us first consider the zero-order equations that appear when all first-order terms in Eq. (13.2) are put to zero, and the resulting expressions are inserted intoacoustic Eq. (13.1),

$$p = p(\rho_0) = p_0, \tag{13.4a}$$

$$\partial_t \rho_0 = 0, \tag{13.4b}$$

$$0 = -\boldsymbol{\nabla} p_0. \tag{13.4c}$$

We find that a consistent solution is obtained by having all zero-order terms being constant.

Then we insert both zero and first-order terms from Eq. (13.2) into Eq. (13.1). Clearly, all terms containing only zero-order terms cancel, as they are solutions to Eq. (13.4). For the remaining terms we make two simplifications. Firstly, we linearize, i.e., we cancel all terms containing more than one factor of order 1. This is a good approximation if indeed the acoustic fields are small. Secondly, we neglect the viscosity of the liquid. Below in Eq. (13.27) we will show that the damping of the acoustic field induced by viscosity in fact is a minor effect. As a result we obtain the first-order equations of the acoustic field,

$$p_1 = c_0^2 \rho_1, \tag{13.5a}$$

$$\partial_t \rho_1 = -\rho_0 \boldsymbol{\nabla} \cdot \mathbf{v}_1, \tag{13.5b}$$

$$\rho_0 \partial_t \mathbf{v}_1 = -c_0^2 \boldsymbol{\nabla} \rho_1 \quad (\eta = \zeta = 0), \tag{13.5c}$$

where we in the Navier–Stokes equation have combined $\boldsymbol{\nabla} p = \boldsymbol{\nabla} p_1$ with Eq. (13.5a).

13.1.1   The linear acoustic wave equation

From Eq. (13.5) it is easy to obtain the acoustic wave equations by utilizing that the differential operators ∂_t and $\boldsymbol{\nabla}$ commute. The wave equation for ρ_1 is obtained by taking

the divergence of Eq. (13.5c) and inserting Eq. (13.5b) on the resulting left-hand side. Likewise, the wave equation for $\mathbf{v}_1$ is obtained by taking the gradient of Eq. (13.5b) and inserting Eq. (13.5c) on the resulting left-hand side. Finally, using Eq. (13.5a), the wave equation for p_1 is obtained by dividing the wave equation for ρ_1 by c_0^2. The three resulting wave equations read

$$\partial_t^2 p_1 = c_0^2 \nabla^2 p_1, \tag{13.6a}$$

$$\partial_t^2 \rho_1 = c_0^2 \nabla^2 \rho_1, \tag{13.6b}$$

$$\partial_t^2 \mathbf{v}_1 = c_0^2 \nabla^2 \mathbf{v}_1. \tag{13.6c}$$

From these equations follows the interpretation of c_0 as the speed of sound.

As the three acoustic fields obey the same wave equation, it is quite natural to seek a more economical formalism. This is provided by the velocity potential $\phi(\mathbf{r}, t)$ introduced in Eq. (11.6) as $\mathbf{v} = \boldsymbol{\nabla}\phi$. According to Kelvin's circulation theorem Exercise 11.2, the velocity potential can be introduced whenever viscosity is negligible, and this is indeed the case of acoustics. When inserting $\mathbf{v}_1 = \boldsymbol{\nabla}\phi$ into Eq. (13.5c) we get $\boldsymbol{\nabla}(\rho_0 \partial_t \phi) = \boldsymbol{\nabla}(-c_0^2 \rho_1)$ and thus both ρ_1 and $p_1 = c_0^2 \rho_1$ can also be expressed by ϕ,

$$p_1 = -\rho_0 \, \partial_t \phi, \tag{13.7a}$$

$$\rho_1 = -\frac{\rho_0}{c_0^2} \, \partial_t \phi, \tag{13.7b}$$

$$\mathbf{v}_1 = \boldsymbol{\nabla}\phi. \tag{13.7c}$$

All fields can thus be obtained from ϕ, and by inserting Eqs. (13.7b) and (13.7c) into Eq. (13.5b) we find, not surprisingly, the wave equation for ϕ to be

$$\partial_t^2 \phi = c_0^2 \nabla^2 \phi. \tag{13.8}$$

One simple solution to the wave equation is the plane wave propagating along the wave vector $\mathbf{k} = k \, \mathbf{e}_k$ with angular frequency ω,

$$\phi(\mathbf{r}, t) = \phi_0 \, e^{i(\mathbf{k}\cdot\mathbf{r} - \omega t)}. \tag{13.9}$$

This is a solution to the wave equation, as seen by direct substitution into Eq. (13.8), for waves fulfilling the acoustic dispersion relation,

$$\omega^2 = c_0^2 k^2 \quad \text{or} \quad \omega = c_0 k. \tag{13.10}$$

Another class of simple solutions to the wave equation are the standing waves,

$$\phi(\mathbf{r}, t) = \phi_k(\mathbf{r}) \, e^{-i\omega t}. \tag{13.11}$$

Inserting this in the wave equation (13.8) leads to Helmholtz equation,

$$\nabla^2 \phi_k(\mathbf{r}) = -\frac{\omega^2}{c_0^2} \phi_k(\mathbf{r}) = -k^2 \phi_k(\mathbf{r}), \tag{13.12}$$

which is an eigenvalue problem that for given boundary conditions allows only certain values of the wavevector k or frequency ω, and which results in the so-called eigenmodes or resonance modes $\phi_k(\mathbf{r})$.

13.1.2   Energy, intensity and momentum of acoustic waves

The acoustic waves carry energy, intensity and momentum. The total energy density E_{ac} associated with the sound wave can be divided into a kinetic and a potential energy density, E_{kin} and E_{pot}, respectively. To lowest order, which in fact is second order, of the acoustic fields, we have

$$E_{\text{kin}} = \tfrac{1}{2}\rho_0 u_1^2 = \tfrac{1}{2}\rho_0 (\boldsymbol{\nabla}\phi)^2. \tag{13.13}$$

To calculate the potential energy we note that when changing the volume by $\mathrm{d}V$ the acoustic pressure work $p_1 \mathrm{d}V$ is stored as the potential energy density $\mathrm{d}E_{\text{pot}} = -(p_1 \mathrm{d}V)/V$. By integration of these contributions we therefore get to lowest (second) order,

$$E_{\text{pot}} = -\int_{V_0}^{V} \mathrm{d}V \, \frac{p_1}{V} = -\int_{\rho_0}^{\rho} \mathrm{d}(\rho^{-1}) \, \frac{c_0^2 \rho_1}{\rho^{-1}} = \int_{0}^{\rho_1} \mathrm{d}(\rho_1) \, \frac{c_0^2 \rho_1}{\rho} \approx \frac{1}{2} \frac{c_0^2}{\rho_0} \rho_1^2 = \frac{1}{2}\rho_0 \left(\frac{1}{c_0^2} \partial_t \phi \right)^2. \tag{13.14}$$

The total energy density in the acoustic field is therefore

$$E_{\text{ac}} = \tfrac{1}{2}\rho_0 \left[u_1^2 + c_0^2 \frac{\rho_1^2}{\rho_0^2} \right] = \tfrac{1}{2}\rho_0 \left[\left(\boldsymbol{\nabla}\phi \right)^2 + \left(\frac{1}{c_0^2} \partial_t \phi \right)^2 \right]. \tag{13.15}$$

Still neglecting damping of the acoustic waves due to viscosity, the energy density must fulfill a continuity equation,

$$\partial_t E_{\text{ac}} = -\boldsymbol{\nabla} \cdot \mathbf{J}_E, \tag{13.16}$$

which can then be used to determine the acoustic energy current density $\mathbf{J}_E$, also known as the acoustic intensity I_{ac}. Taking the time-derivative of E_{ac} and using the wave equation for ϕ along the way, leads to

$$-\boldsymbol{\nabla}\cdot\mathbf{J}_E = \rho_0 \left[\boldsymbol{\nabla}\phi\cdot\boldsymbol{\nabla}(\partial_t\phi) + \frac{1}{c_0^2}\partial_t\phi\partial_t^2\phi \right] = \rho_0 \left[\boldsymbol{\nabla}\phi\cdot\boldsymbol{\nabla}(\partial_t\phi) + \partial_t\phi(\nabla^2\phi) \right] = \rho_0 \boldsymbol{\nabla}\cdot\left[(\boldsymbol{\nabla}\phi)(\partial_t\phi) \right], \tag{13.17}$$

so the acoustic energy current density $\mathbf{J}_E$ becomes

$$\mathbf{J}_E = -\rho_0 \, (\boldsymbol{\nabla}\phi)(\partial_t\phi). \tag{13.18}$$

Likewise, we can determine the acoustic momentum current density tensor $\mathbb{J}_m$ from the acoustic momentum density $\mathbf{m}$, which to lowest (first order) is given by

$$\mathbf{m} = \rho_0 \mathbf{v}_1. \tag{13.19}$$

The continuity equation for momentum density tensor becomes

$$\boldsymbol{\nabla} \cdot \mathbb{J}_m = -\rho_0 \partial_t \mathbf{v}_1 = -c_0^2 \boldsymbol{\nabla}\rho_1 - \boldsymbol{\nabla} \cdot \left(c_0^2 \rho_1 \mathbb{I} \right), \tag{13.20}$$

and thus

$$\left(\mathbb{J}_m \right)_{ij} = c_0^2 \rho_1 \delta_{ij} = p_1 \delta_{ij}. \tag{13.21}$$

13.1.3 Viscous damping of acoustic waves

Hitherto, we have neglected viscous damping. By maintaining non-zero viscosities in Eq. (13.1c), the first-order part of the Navier–Stokes equation (13.5c) becomes

$$\rho_0 \partial_t \mathbf{v}_1 = -c_0^2 \boldsymbol{\nabla} \rho_1 + \eta \nabla^2 \mathbf{v}_1 + \left(\frac{1}{3}\eta + \zeta\right) \boldsymbol{\nabla}(\boldsymbol{\nabla}\cdot\mathbf{v}_1). \tag{13.22}$$

The modified wave for ρ_1 is obtained by taking the divergence of Eq. (13.22) and substituting $\boldsymbol{\nabla} \cdot \mathbf{v}_1$ using Eq. (13.5b) in the resulting equation. For the viscous terms we get

$$\boldsymbol{\nabla}\cdot\left[\eta\nabla^2\mathbf{v}_1 + \left(\frac{1}{3}\eta + \zeta\right)\boldsymbol{\nabla}(\boldsymbol{\nabla}\cdot\mathbf{v}_1)\right] = \left(\frac{4}{3}\eta + \zeta\right)\nabla^2(\boldsymbol{\nabla}\cdot\mathbf{v}_1) = -\frac{\tilde{\eta}}{\rho_0}\nabla^2(\partial_t\rho_1), \tag{13.23}$$

where we for brevity have introduced the constant

$$\tilde{\eta} \equiv \frac{4}{3}\eta + \zeta. \tag{13.24}$$

The wave equation for ρ_1 with viscous damping thus becomes,

$$\partial_t^2 \rho_1 = c_0^2 \nabla^2 \rho_1 + \frac{\tilde{\eta}}{\rho_0}\nabla^2(\partial_t\rho_1). \tag{13.25}$$

Assuming harmonically varying time-dependencies as in Eqs. (13.9) and (13.11), we get $\partial_t\rho_1 = -i\omega\rho_1$ and obtain a Helmholtz equation with a complex prefactor,

$$-\omega^2 \rho_1 = c_0^2 \left[1 - i\frac{\tilde{\eta}\omega}{c_0^2\rho_0}\right]\nabla^2\rho_1. \tag{13.26}$$

we note that for ultrasound waves with $\omega = 10^6$ s^{-1} in water, the complex correction α is quite small,

$$\alpha \equiv \frac{\tilde{\eta}\omega}{c_0^2\rho_0} \approx \frac{10^{-3}\ \mathrm{Pa\,s} \times 10^6\ \mathrm{s}^{-1}}{\left(10^3\ \mathrm{m\,s}^{-1}\right)^2 \times 10^3\ \mathrm{kg\,m}^{-3}} = 10^{-6} \ll 1, \tag{13.27}$$

So by a first-order Taylor expansion we arrive at the modified Helmholtz equation

$$\nabla^2\rho_1 = -\frac{\omega^2}{c_0^2}\left[1 + i\frac{\tilde{\eta}\omega}{2c_0^2\rho_0}\right]^2\rho_1 = -(k_0 + i\kappa)^2\,\rho_1, \tag{13.28}$$

where

$$k_0 = \frac{\omega}{c_0} \approx 10^3\ \mathrm{m}^{-1}, \qquad \kappa = \frac{\tilde{\eta}\omega^2}{2c_0^3\rho_0} \approx 10^{-3}\ \mathrm{m}^{-1}. \tag{13.29}$$

The tiny positive imaginary part implies damping. This attenuation of the acoustic wave is most clearly seen by studying a plan wave of the form $\rho_1 \propto \exp[i(\tilde{k}x - \omega t)] = \exp[i(k + i\kappa x - \omega t)] = \exp[i(kx - \omega t)]\exp[-\kappa x]$.

13.2   Second order equation of motion in acoustics

The linear theory of acoustics just presented offers no possibilities of achieving a DC drift velocity due to the presence of acoustic waves. The reason is that in a linear theory the harmonic drive $\exp(-i\omega t)$ enters all terms, which consequently have a zero time-average over a full period. However, the Navier–Stokes equations are non-linear, and expanding it to second order will introduce products of two factors $\exp(-i\omega t)$, products that have the time-average $\frac{1}{2}$ over a full period. Including the second-order terms in Eq. (13.2) leads to

$$p = p_0 + p_1 + p_2, \tag{13.30a}$$
$$\rho = \rho_0 + \rho_1 + \rho_2, \tag{13.30b}$$
$$\mathbf{v} = \mathbf{0} + \mathbf{v}_1 + \mathbf{v}_2. \tag{13.30c}$$

Combining Eqs. (13.1) and (13.30) we obtain the second-order equation of motion for the acoustic field,

$$p_2 = c_0^2 \rho_2 + \frac{1}{2}\left(\partial_\rho c^2\right)_0 \rho_1^2, \tag{13.31a}$$

$$\partial_t \rho_2 = -\rho_0 \boldsymbol{\nabla}\cdot\mathbf{v}_2 - \boldsymbol{\nabla}\cdot(\rho_1 \mathbf{v}_1), \tag{13.31b}$$

$$\rho_0 \partial_t \mathbf{v}_2 = -c_0^2 \boldsymbol{\nabla}\rho_2 - \rho_1 \partial_t \mathbf{v}_1 - \rho_0(\mathbf{v}_1\cdot\boldsymbol{\nabla})\mathbf{v}_1 - \frac{1}{2}\left(\partial_\rho c^2\right)_0 \boldsymbol{\nabla}\rho_1^2 + \eta\nabla^2\mathbf{v}_2 + \left(\frac{\eta}{3}+\zeta\right)\boldsymbol{\nabla}(\boldsymbol{\nabla}\cdot\mathbf{v}_2). \tag{13.31c}$$

13.2.1   Acoustic streaming

If we assume that the time-dependence of all first-order fields is harmonic, $e^{-i\omega t}$, then Eq. (13.31) has solutions for ρ_2 and $\mathbf{v}_2$ with a non-zero time-averages for $\langle\rho_2\rangle \neq 0$ and $\langle\mathbf{v}_2\rangle \neq 0$. In other words, the oscillating acoustic field imparts a time-independent component to the density and velocity field of the liquid. This phenomena is known as acoustic streaming, and an experimental example of this is shown in Fig. 13.1.

According to Exercise 9.7 the time-average of a product is given by $\langle A(t)B(t)\rangle = \frac{1}{2}\,\mathrm{Re}\left[A_0 B_0^*\right]$, we find the time-average of Eq. (13.31b) to be

$$\boldsymbol{\nabla}\cdot\langle\mathbf{v}_2\rangle = -\frac{1}{\rho_0}\boldsymbol{\nabla}\cdot\langle\rho_1\mathbf{v}_1\rangle, \tag{13.32}$$

while that of Eq. (13.31c), after taking the divergence and inserting Eq. (13.32), becomes

$$\nabla^2\langle\rho_2\rangle = -\frac{1}{2c_0^2}\left(\partial_\rho c^2\right)_0 \nabla^2\langle\rho_1^2\rangle - \frac{\rho_0}{c_0^2}\boldsymbol{\nabla}\cdot\langle(\mathbf{v}_1\cdot\boldsymbol{\nabla})\mathbf{v}_1\rangle + i\frac{\omega}{c_0^2}\langle\rho_1\boldsymbol{\nabla}\cdot\mathbf{v}_1\rangle - \frac{\tilde{\eta}}{\rho_0 c_0^2}\nabla^2\left(\boldsymbol{\nabla}\cdot\langle\rho_1\mathbf{v}_1\rangle\right). \tag{13.33}$$

To estimate the time-averaged speeds $\langle\mathbf{v}_2\rangle$ one can hope to obtain using acoustic streaming, one can assume plane wave solutions for the first-order fields. The calculations are straight forward, and using the usual parameters for water and an ultrasound frequency of the order 1 MHz, one finds $|\langle\mathbf{v}_2\rangle| \approx 10\ \mu\text{m/s}$ in agreement with the measurements presented in Fig. 13.1(a).
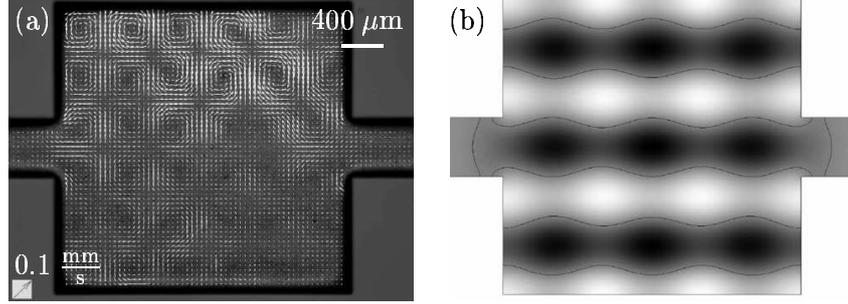
Figure 13.1: (a) Top view of the steady-state acoustic streaming velocities (white arrows) of water inside a 200 μm deep, glass-lid covered, square silicon microchamber after turning on a $f = 2.17$ MHz piezo-actuator emitting ultrasound through the chamber from below. The liquid motion is detected by particle-image velocimetry on $a = 500$ nm beads suspended in the liquid. (b) Gray-scale plot of the numerical solution to the Helmholtz equation (13.12) with $\omega/(2\pi) = 2.417$ MHz and Neumann boundary conditions. The pressure nodes are marked by thin black lines. Note how the streaming vortices in the experiment is period-doubled compared to the pressure field. Courtesy Sundin, Jensen, Bruus and Kutter, MIC 2006.

13.2.2 Acoustic radiation force

The second effect concerns the motion of suspended particles due to the radiation force from the acoustic fields. The radiation force stems from the momentum transferred from the incoming ultrasound wave to the particle. In the following we will not go through a complete calculation of the radiation pressure on a bead suspended in a liquid. Instead, we will restrict our analysis to the simple case of the partial transmission and reflection of a plane wave moving along the x-axis hitting an interface at $x = 0$ between two semi-inifinite media, medium a for $x < 0$ and medium b for $x > 0$.

Let the wave be described by the normalized velocity potential $\phi(x,t)$ given by

$$\phi(x,t) = \begin{cases} \phi_a(x,t) & = e^{i(k_a x - \omega t)} + A e^{i(-k_a x - \omega t)}, & \text{for } x < 0, \\ \phi_b(x,t) & = B e^{i(k_b x - \omega t)}, & \text{for } x > 0. \end{cases} \tag{13.34}$$

The incoming wave has unity amplitude, the reflected and transmitted waves have amplitudes A and B, respectively. To find A and B we employ the boundary conditions corresponding to continuous pressure and continuous velocity at the interface. By use of Eqs. (13.7a) and (13.7c) these boundary conditions can be formulated in terms of the velocity potential as

$$\rho_a \partial_t \phi_a(0,t) = \rho_b \partial_t \phi_b(0,t), \tag{13.35a}$$

$$\partial_x \phi_a(0,t) = \partial_x \phi_b(0,t). \tag{13.35b}$$
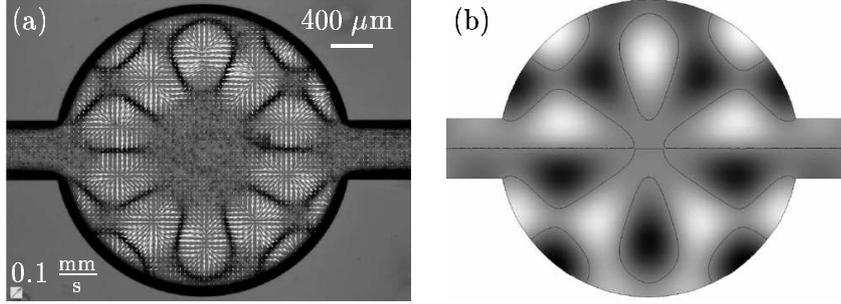
Figure 13.2: (a) Top view of the acoustic radiation-force induced, initial velocities (white arrows) of $a = 5$ μm beads inside a 200 μm deep, glass-lid covered, water-filled, circular silicon microchamber just after turning on a $f = 2.417$ MHz piezo-actuator emitting ultrasound through the chamber from below. Also shown are the steady-state positions of the beads (bands of black spots) at the pressure nodes of the acoustic field. (b) Gray-scale plot of the numerical solution to the Helmholtz equation (13.12) with $\omega/(2\pi) = 2.417$ MHz and Neumann boundary conditions. The pressure nodes are marked by thin black lines. Courtesy Sundin, Jensen, Bruus and Kutter, MIC 2006.

With the plane wave Eq. (13.34) the derivatives are simple, and we get

$$1 + A = \frac{\rho_b}{\rho_a}\, B, \tag{13.36a}$$

$$1 - A = \frac{k_b}{k_a}\, B. \tag{13.36b}$$

Solving for A and B we get

$$A = \frac{\frac{\rho_b}{\rho_a} - \frac{k_b}{k_a}}{\frac{\rho_b}{\rho_a} + \frac{k_b}{k_a}}, \tag{13.37a}$$

$$B = \frac{2}{\frac{\rho_b}{\rho_a} + \frac{k_b}{k_a}}. \tag{13.37b}$$

Already this little calculations demonstrate the central role played by the density ratio, ρ_b/ρ_a, and the wavenumber or inverse speed of sound ratio, $k_b/k_a = c_a/c_b$.

For the more complicated case of a spherical particle of radius a in a standing acoustic pressure field $p(x,t) = p_0\,\sin(kx)e^{i\omega t}$, like the experimental result shown in Fig. 13.2, similar principles are used in the calculation. However, as with the case of acoustic streaming, it is necessary to use the second-order acoustic field to obtain the end-result, the average radiation pressure $\langle p_{\text{sph}} \rangle$ acting on the particle. The result is

$$p_{\text{sph}}(x) = \left[\frac{\frac{5}{3}\frac{\rho^*}{\rho} - \frac{2}{3}}{1 + 2\frac{\rho^*}{\rho}} - \frac{\left(\frac{k^*}{k}\right)^2}{3\frac{\rho^*}{\rho}} \right] \pi a^2 (4ka)\langle E_{\text{ac}} \rangle\, \sin\left(2kx\right), \tag{13.38}$$

where unmarked and star-marked quantities refer to the liquid and the particle, respectively, and $\langle E_{\text{ac}} \rangle$ is the average energy density of the incoming acoustic wave. It should be

noted that the sign of prefactor determines whether a particle is moved towards pressure nodes or pressure anti-nodes.

13.3 Exercises

Exercise 13.1
To be added
In the next edition exercises in acoustics will be added.

13.4 Solutions

Solution 13.1
To be added
In the next edition solutions to the exercises will be added.

Appendix A

Curvilinear coordinates

In this appendix we present the explicit coordinate representations of the equation of motion in Cartesian, cylindrical polar, and spherical polar coordinates. The choice of coordinates for solving a given problem is often dictated by the symmetry of the boundary conditions.

A.1   Cartesian coordinates

In Cartesian coordinates x, y, and z the position vector $\mathbf{r}$ of a point is given by

$$\mathbf{r} = x\mathbf{e}_x + y\mathbf{e}_y + z\mathbf{e}_z, \tag{A.1}$$

where the vectors $\mathbf{e}_x$, $\mathbf{e}_y$, and $\mathbf{e}_z$ are independent of the coordinates (x, y, z) and form an orthonormal basis, i.e., $\mathbf{e}_i \cdot \mathbf{e}_j = \delta_{ij}$ for $i, j = x, y, z$.

Any scalar function S depends on the three coordinates as

$$S = S(\mathbf{r}) = S(x, y, z), \tag{A.2}$$

while any vector function $\mathbf{V}(\mathbf{r})$ takes the form

$$\mathbf{V} = \mathbf{V}(\mathbf{r}) = \mathbf{e}_x V_x(x, y, z) + \mathbf{e}_y V_y(x, y, z) + \mathbf{e}_z V_z(x, y, z). \tag{A.3}$$

The differential operator $\boldsymbol{\nabla}$, denoted nabla, is defined as

$$\boldsymbol{\nabla} \equiv \mathbf{e}_x \partial_x + \mathbf{e}_y \partial_y + \mathbf{e}_z \partial_z, \tag{A.4}$$

Note that the differential operators ∂_i are written to the right of the basis vectors. While not important in Cartesian coordinates it is crucial when working with curvilinear coordinates. Once nabla has been introduced we can proceed and write down a number of important derivatives of scalar and vector functions.

A.1.1   Single derivatives

For a scalar function S only one quantity can be formed using the nabla operator, namely the gradient $\boldsymbol{\nabla} S$, which is a vector,

$$\boldsymbol{\nabla} S = \mathbf{e}_x(\partial_x S) + \mathbf{e}_y(\partial_y S) + \mathbf{e}_z(\partial_z S). \tag{A.5}$$

For a vector function $\mathbf{V}$ three quantities can be formed using the nabla operator. They are relatively simple to derive as the three basis vectors are independent of the coordinates. First, the divergence $\boldsymbol{\nabla}\cdot\mathbf{V}$ of a vector is a scalar,

$$\boldsymbol{\nabla}\cdot\mathbf{V} = \partial_x V_x + \partial_y V_y + \partial_z V_z, \tag{A.6}$$

second, the rotation $\boldsymbol{\nabla} \times \mathbf{V}$ of a vector is a vector,

$$\boldsymbol{\nabla} \times \mathbf{V} = \mathbf{e}_x(\partial_y V_z - \partial_z V_y) + \mathbf{e}_y(\partial_z V_x - \partial_x V_z) + \mathbf{e}_z(\partial_x V_y - \partial_y V_x), \tag{A.7}$$

and third, the gradient $\boldsymbol{\nabla}\mathbf{V}$ of a vector is a tensor

$$\begin{aligned} \boldsymbol{\nabla}\mathbf{V} = {}& + (\partial_x V_x)\mathbf{e}_x\mathbf{e}_x + (\partial_x V_y)\mathbf{e}_x\mathbf{e}_y + (\partial_x V_z)\mathbf{e}_x\mathbf{e}_z \\ & + (\partial_y V_x)\mathbf{e}_y\mathbf{e}_x + (\partial_y V_y)\mathbf{e}_y\mathbf{e}_y + (\partial_y V_z)\mathbf{e}_y\mathbf{e}_z \\ & + (\partial_z V_x)\mathbf{e}_z\mathbf{e}_x + (\partial_z V_y)\mathbf{e}_z\mathbf{e}_y + (\partial_z V_z)\mathbf{e}_z\mathbf{e}_z. \end{aligned} \tag{A.8}$$

A.1.2   Double derivatives

The well-known Laplacian operator ∇^2 acting on a scalar function S is a scalar,

$$\nabla^2 S = \partial_x^2 S + \partial_y^2 S + \partial_z^2 S, \tag{A.9}$$

and the Laplacian acting on a vector function $\mathbf{V}$ is likewise a vector,

$$\nabla^2\mathbf{V} = \mathbf{e}_x\nabla^2 V_x + \mathbf{e}_y\nabla^2 V_y + \mathbf{e}_z\nabla^2 V_z. \tag{A.10}$$

A.1.3   Integrals

When integrating over the entire 3D space the integral takes the following form in Cartesian coordinates

$$\int_{\text{all}} \mathrm{d}\mathbf{r}\, f(\mathbf{r}) = \int_{-\infty}^{\infty} \mathrm{d}x \int_{-\infty}^{\infty} \mathrm{d}y \int_{-\infty}^{\infty} \mathrm{d}z\, f(x,y,z). \tag{A.11}$$

A.2   Cylindrical polar coordinates

As sketched in Fig. A.1, choosing the z-axis as the cylinder axis, the cylindrical polar coordinates r, ϕ, and z are related to the Cartesian coordinates x, y, and z by

$$x = r\,\cos\phi, \tag{A.12a}$$

$$y = r\,\sin\phi, \tag{A.12b}$$

$$z = z, \tag{A.12c}$$

$$x = r \cos \phi \qquad \mathbf{e}_r = + \cos \phi \, \mathbf{e}_x + \sin \phi \, \mathbf{e}_y$$
$$y = r \sin \phi \qquad \mathbf{e}_\phi = - \sin \phi \, \mathbf{e}_x + \cos \phi \, \mathbf{e}_y$$
$$z = z \qquad \mathbf{e}_z = \mathbf{e}_z$$
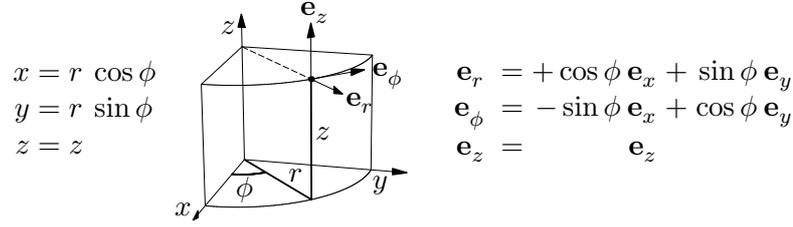
Figure A.1: The cylindrical polar coordinates (r, ϕ, z) and the associated orthonormal basis vectors $\mathbf{e}_r$, $\mathbf{e}_\phi$, and $\mathbf{e}_z$.

defined in the intervals $0 \leq r < \infty$, $0 \leq \phi \leq 2\pi$, and $0 \leq z < \infty$. The associated basis vectors $\mathbf{e}_r$, $\mathbf{e}_\theta$, and $\mathbf{e}_\phi$ are given by the derivatives of the Cartesian position vector $\mathbf{r}$ of Eq. (A.1) with respect to the cylindrical polar coordinates as

$$\mathbf{e}_r \equiv \partial_r \mathbf{r} = + \cos \phi \, \mathbf{e}_x + \sin \phi \, \mathbf{e}_y, \tag{A.13a}$$

$$\mathbf{e}_\phi \equiv \frac{1}{r} \partial_\phi \mathbf{r} = - \sin \phi \, \mathbf{e}_x + \cos \phi \, \mathbf{e}_y, \tag{A.13b}$$

$$\mathbf{e}_z \equiv \partial_z \mathbf{r} = \mathbf{e}_z. \tag{A.13c}$$

Note that the two basis vectors $\mathbf{e}_r$ and $\mathbf{e}_\phi$ depend on the coordinate ϕ, but all three vectors nevertheless form an orthonormal basis, i.e., $\mathbf{e}_i \cdot \mathbf{e}_j = \delta_{ij}$ for $i, j = r, \phi, z$.

Any scalar function S depends on the three coordinates as

$$S = S(\mathbf{r}) = S(r, \phi, z), \tag{A.14}$$

while any vector function $\mathbf{V}(\mathbf{r})$ takes the form

$$\mathbf{V} = \mathbf{V}(\mathbf{r}) = \mathbf{e}_r V_r(r, \phi, z) + \mathbf{e}_\phi V_\phi(r, \phi, z) + \mathbf{e}_z V_z(r, \phi, z). \tag{A.15}$$

Using the chain rule of differentiation and Eq. (A.13) the nabla operator of Eq. (A.4) can be transformed to cylindrical polar coordinates,

$$\boldsymbol{\nabla} \equiv \mathbf{e}_r \partial_r + \mathbf{e}_\phi \frac{1}{r} \partial_\phi + \mathbf{e}_z \partial_z. \tag{A.16}$$

In contrast to Cartesian coordinates, as noted above, the basis vectors of the cylindrical polar coordinates depend on the coordinates; in fact $\mathbf{e}_r$ and $\mathbf{e}_\phi$ both depend on ϕ leaving us with two non-vanishing derivatives of the basis vectors,

$$\partial_\phi \mathbf{e}_r = \mathbf{e}_\phi, \quad \text{and} \quad \partial_\phi \mathbf{e}_\phi = -\mathbf{e}_r. \tag{A.17}$$

Based on Eqs. (A.16) and (A.17) we can calculate the various derivatives in cylindrical polar coordinates.

A.2.1   Single derivatives

For a scalar function S only one quantity can be formed using the nabla operator, namely the gradient $\boldsymbol{\nabla} S$, which is a vector,

$$\boldsymbol{\nabla} S = \mathbf{e}_r(\partial_r S) + \mathbf{e}_\phi \frac{1}{r}(\partial_\phi S) + \mathbf{e}_z(\partial_z S). \tag{A.18}$$

For a vector function $\mathbf{V}$ three quantities can be formed using the nabla operator. Due to the dependence of the basis vectors on the coordinate ϕ, the expressions in cylindrical polar coordinates for these three quantities are slightly more complicated than those of the Cartesian coordinates. First, the divergence $\boldsymbol{\nabla} \cdot \mathbf{V}$ of a vector yielding a scalar,

$$\boldsymbol{\nabla} \cdot \mathbf{V} = \frac{1}{r}\, \partial_r(rV_r) + \frac{1}{r}\, \partial_\phi V_\phi + \partial_z V_z, \tag{A.19}$$

second, the rotation $\boldsymbol{\nabla} \times \mathbf{V}$ of a vector yielding a vector,

$$\boldsymbol{\nabla} \times \mathbf{V} = \mathbf{e}_r\left(\frac{1}{r}\, \partial_\phi V_z - \partial_z V_\phi\right) + \mathbf{e}_\phi \frac{1}{r}\left(\partial_z V_r - \partial_r V_z\right) + \mathbf{e}_z \frac{1}{r}\left(\partial_r[rV_\phi] - \partial_\phi V_r\right), \tag{A.20}$$

and third, the gradient $\boldsymbol{\nabla} \mathbf{V}$ of a vector is a tensor, which, however, we will not present here.

A.2.2   Double derivatives

In cylindrical polar coordinates the Laplacian operator ∇^2 acting on a scalar function S is the following scalar,

$$\nabla^2 S = \frac{1}{r}\, \partial_r\left(r\partial_r S\right) + \frac{1}{r^2}\partial_\phi^2 S + \partial_z^2 S. \tag{A.21}$$

Taking the ϕ-dependence of the basis vectors into account, we obtain the vector resulting from applying the Laplacian on a vector function $\mathbf{V}$,

$$\nabla^2\mathbf{V} = \mathbf{e}_r\left(\nabla^2 V_r - \frac{2}{r^2}\, \partial_\phi V_\phi - \frac{1}{r^2}V_r\right) + \mathbf{e}_\phi\left(\nabla^2 V_\phi + \frac{2}{r^2}\, \partial_\phi V_r - \frac{1}{r^2}V_\phi\right) + \mathbf{e}_z\left(\nabla^2 V_z\right), \tag{A.22}$$

where the Laplacian acting on the scalar components V_i, $i = r, \phi, z$ is calculated from Eq. (A.21).

A.2.3   Integrals

When integrating over the entire 3D space the integral takes the following form in cylindrical polar coordinates

$$\int_{\text{all}} d\mathbf{r}\, f(\mathbf{r}) = \int_0^\infty dr \int_0^{2\pi} d\phi \int_{-\infty}^\infty dz\, r\, f(r, \phi, z). \tag{A.23}$$

$$x = r \, \sin\theta \, \cos\phi$$
$$y = r \, \sin\theta \, \sin\phi$$
$$z = r \, \cos\theta$$

$$\mathbf{e}_r = \sin\theta \, \cos\phi \, \mathbf{e}_x + \sin\theta \, \sin\phi \, \mathbf{e}_y + \cos\theta \, \mathbf{e}_z$$
$$\mathbf{e}_\theta = \cos\theta \, \cos\phi \, \mathbf{e}_x + \cos\theta \, \sin\phi \, \mathbf{e}_y - \sin\theta \, \mathbf{e}_z$$
$$\mathbf{e}_\phi = -\sin\phi \, \mathbf{e}_x + \cos\phi \, \mathbf{e}_y$$
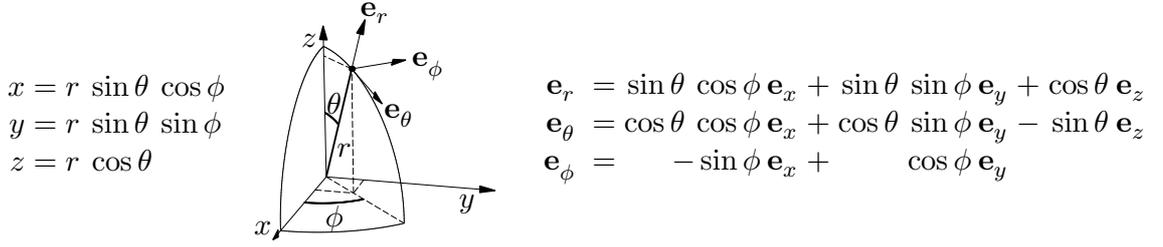
Figure A.2: The spherical polar coordinates (r, θ, ϕ) and the associated orthonormal basis vectors $\mathbf{e}_r$, $\mathbf{e}_\theta$, and $\mathbf{e}_\phi$.

A.3 Spherical polar coordinates

The spherical polar coordinates r, θ, and ϕ are related to the Cartesian coordinates x, y, and z by

$$x = r \, \sin\theta \, \cos\phi, \tag{A.24a}$$
$$y = r \, \sin\theta \, \sin\phi, \tag{A.24b}$$
$$z = r \, \cos\theta, \tag{A.24c}$$

as sketched in Fig. A.2. They are defined in the intervals $0 \le r < \infty$, $0 \le \theta \le \pi$, and $0 \le \phi \le 2\pi$. The associated basis vectors $\mathbf{e}_r$, $\mathbf{e}_\phi$, and $\mathbf{e}_z$ are given by the derivatives of the Cartesian position vector $\mathbf{r}$ of Eq. (A.1) with respect to the spherical polar coordinates as

$$\mathbf{e}_r \equiv \partial_r \mathbf{r} = +\sin\theta \, \cos\phi \, \mathbf{e}_x + \sin\theta \, \sin\phi \, \mathbf{e}_y + \cos\theta \, \mathbf{e}_z, \tag{A.25a}$$

$$\mathbf{e}_\phi \equiv \frac{1}{r} \, \partial_\theta \mathbf{r} = +\cos\theta \, \cos\phi \, \mathbf{e}_x + \cos\theta \, \cos\phi \, \mathbf{e}_y - \sin\theta \, \mathbf{e}_z, \tag{A.25b}$$

$$\mathbf{e}_z \equiv \frac{1}{r \sin\theta} \, \partial_\phi \mathbf{r} = -\sin\phi \, \mathbf{e}_x + \cos\phi \, \mathbf{e}_y. \tag{A.25c}$$

Note that all three basis vectors depend on the coordinates θ and ϕ, but that they nevertheless form an orthonormal basis, i.e., $\mathbf{e}_i \cdot \mathbf{e}_j = \delta_{ij}$ for $i, j = r, \theta, \phi$.

Any scalar function S depends on the three coordinates as

$$S = S(\mathbf{r}) = S(r, \theta, \phi), \tag{A.26}$$

while any vector function $\mathbf{V}(\mathbf{r})$ takes the form

$$\mathbf{V} = \mathbf{V}(\mathbf{r}) = \mathbf{e}_r V_r(r, \theta, \phi) + \mathbf{e}_\theta V_\theta(r, \theta, \phi) + \mathbf{e}_\phi V_\phi(r, \theta, \phi). \tag{A.27}$$

Using the chain rule of differentiation and Eq. (A.25) the nabla operator of Eq. (A.4) can be transformed to spherical polar coordinates,

$$\boldsymbol{\nabla} \equiv \mathbf{e}_r \partial_r + \mathbf{e}_\theta \frac{1}{r} \, \partial_\theta + \mathbf{e}_\phi \frac{1}{r \sin\theta} \, \partial_\phi. \tag{A.28}$$

In the case of spherical polar coordinates the dependence of the basis vectors on the coordinates θ and ϕ leads to five non-vanishing derivatives of the basis vectors,

$$\partial_\theta \mathbf{e}_r = +\mathbf{e}_\theta, \qquad\qquad \partial_\phi \mathbf{e}_r = +\sin\theta\,\mathbf{e}_\phi, \qquad\qquad (A.29a)$$

$$\partial_\theta \mathbf{e}_\theta = -\mathbf{e}_r, \qquad\qquad \partial_\phi \mathbf{e}_\theta = +\cos\theta\,\mathbf{e}_\phi, \qquad\qquad (A.29b)$$

$$\partial_\phi \mathbf{e}_\phi = -\sin\theta\,\mathbf{e}_r - \cos\theta\,\mathbf{e}_\theta. \qquad\qquad (A.29c)$$

Based on Eqs. (A.28) and (A.29) we can calculate the various derivatives in spherical polar coordinates.

A.3.1 Single derivatives

For a scalar function S only one quantity can be formed using the nabla operator, namely the gradient $\boldsymbol{\nabla}S$, which is a vector,

$$\boldsymbol{\nabla}S = \mathbf{e}_r \partial_r S + \mathbf{e}_\theta \frac{1}{r}\,\partial_\theta S + \mathbf{e}_\phi \frac{1}{r\sin\theta}\,\partial_\phi S. \qquad\qquad (A.30)$$

For a vector function $\mathbf{V}$ three quantities can be formed using the nabla operator. Due to the dependence of the basis vectors on the coordinate ϕ, the expressions in spherical polar coordinates for these three quantities are slightly more complicated than those of the Cartesian coordinates. First, the divergence $\boldsymbol{\nabla}\cdot\mathbf{V}$ of a vector yielding a scalar,

$$\boldsymbol{\nabla}\cdot\mathbf{V} = \frac{1}{r^2}\,\partial_r\left(r^2 V_r\right) + \frac{1}{r\sin\theta}\,\partial_\theta\left(\sin\theta\,V_\theta\right) + \frac{1}{r\sin\theta}\,\partial_\phi V_\phi, \qquad\qquad (A.31)$$

second, the rotation $\boldsymbol{\nabla}\times\mathbf{V}$ of a vector yielding a vector,

$$\boldsymbol{\nabla}\times\mathbf{V} = \mathbf{e}_r \frac{1}{r\sin\theta}\left(\partial_\theta\left[\sin\theta V_\phi\right] - \partial_\phi V_\theta\right) + \mathbf{e}_\theta \frac{1}{r}\left(\frac{1}{\sin\theta}\partial_\phi V_r - \partial_r\left[r V_\phi\right]\right) + \mathbf{e}_\phi \frac{1}{r}\left(\partial_r\left[r V_\theta\right] - \partial_\theta V_r\right), \qquad (A.32)$$

and third, the gradient $\boldsymbol{\nabla}\mathbf{V}$ of a vector is a tensor, which, however, we will not present here.

A.3.2 Double derivatives

In spherical polar coordinates the Laplacian operator ∇^2 acting on a scalar function S is the following scalar,

$$\nabla^2 S = \frac{1}{r^2}\,\partial_r\left(r^2 \partial_r S\right) + \frac{1}{r^2\sin\theta}\,\partial_\theta\left(\sin\theta\,\partial_\theta S\right) + \frac{1}{r^2\sin^2\theta}\,\partial_\phi^2 S. \qquad\qquad (A.33)$$

Taking the angular dependence of the basis vectors into account, we obtain the vector resulting from applying the Laplacian on a vector function $\mathbf{V}$,

$$\nabla^2\mathbf{V} = \mathbf{e}_r\left(\nabla^2 V_r - \frac{2}{r^2\sin^2\theta}\partial_\theta\left[\sin\theta\,V_\theta\right] - \frac{2}{r^2\sin\theta}\,\partial_\phi V_\phi - \frac{2}{r^2}\,V_r\right)$$

$$+ \mathbf{e}_\theta\left(\nabla^2 V_\theta - \frac{2\cos\theta}{r^2\sin^2\theta}\,\partial_\phi V_\phi + \frac{2}{r^2}\,\partial_\theta V_r - \frac{1}{r^2\sin^2\theta}\,V_\theta\right)$$

$$+ \mathbf{e}_\phi\left(\nabla^2 V_\phi + \frac{2}{r^2\sin\theta}\,\partial_\phi V_r + \frac{2\cos\theta}{r^2\sin^2\theta}\,\partial_\phi V_\theta - \frac{1}{r^2\sin^2\theta}\,V_\phi\right), \qquad\qquad (A.34)$$

where the Laplacian acting on the scalar components V_r, V_θ, and V_ϕ is calculated from Eq. (A.33).

A.3.3 Integrals

When integrating over the entire 3D space the integral takes the following form in spherical polar coordinates

$$\int_{\text{all}} d\mathbf{r}\, f(\mathbf{r}) = \int_0^\infty dr \int_{-\frac{\pi}{2}}^{\frac{\pi}{2}} d\theta \int_0^\infty dz\, r^2 \sin\theta\, f(r, \theta, \phi) = \int_0^\infty dr \int_{-1}^1 d(\cos\theta) \int_0^\infty dz\, r^2\, f(r, \cos\theta, \phi).$$

$$(A.35)$$

Appendix B

Physical constants

In this appendix we a few tables containing the values of physical constants of interest to microfluidics.

B.1 Water

density	1.0×10^3	$\mathrm{kg\,m^{-3}}$
viscosity	1.0×10^{-3}	$\mathrm{Pa\,s}$
surface tension	72.9×10^{-3}	$\mathrm{J\,m^{-2}}$

Table B.1: Table of various physical constants relating to water at 20°C.

t [°C]	0	5	10	15	20	25	30	35	40	45	
η [mPa s]	1.787	1.519	1.307	1.139	1.002	0.8904	0.7975	0.7194	0.6529	0.5960	
t [°C]	50	55	60	65	70	75	80	85	90	95	100
η [mPa s]	0.5468	0.5040	0.4665	0.4335	0.4042	0.3781	0.3547	0.3337	0.3147	0.2975	0.2818

Table B.2: Table of the viscosity η of water as a function of the temperature t in centigrades [CRC Handbook p. F-51]

B.2 Diffusivity

$$D \approx 2 \times 10^{-9} \;\; \mathrm{m^2/s}, \quad \text{small ions in water}, \tag{B.1a}$$

$$D \approx 4 \times 10^{-11} \;\mathrm{m^2/s}, \quad \text{30-mer DNA molecules in water}, \tag{B.1b}$$

$$D \approx 1 \times 10^{-12} \;\mathrm{m^2/s}, \quad \text{5000-mer DNA molecules in water}, \tag{B.1c}$$

229

ions at $T = 25°C$	H$^+$	Ag$^+$	K$^+$	Li$^+$	Na$^+$	Br$^-$	Cl$^-$	F$^-$	I$^-$	OH$^-$
mobility μ_{ion} $\left[10^{-8} \text{ m}^2 \text{ (V s)}^{-1}\right]$	36.2	6.42	7.62	4.01	5.19	8.09	7.91	5.70	7.96	20.6
diffusivity D_{ion} $\left[10^{-9} \text{ m}^2 \text{ s}^{-1}\right]$	9.31	-	1.96	1.03	1.33	2.08	2.03	1.46	2.05	5.30

Table B.3: Experimental values for ionic mobility and diffusivity for small ions in aqueous solutions at small concentrations. Note how H$^+$ and OH$^-$ have significantly different values due to their special modes of propagation by exchange of electron orbitals with the neutral water molecules.

B.3   Contact angle

liquid	γ [mJ/m^2]		liquid	solid	θ
water	72.9		water	SiO$_2$	52.3°
mercury	486.5		water	glass	25.0°
benzene	28.9		water	Au	0.0°
methanol	22.5		water	Pt	40.0°
blood	~60.0		water	PMMA	73.7°
			mercury	glass	140.0°

Table B.4: Measured values of the surface tension γ at liquid-vapor interfaces and of the contact angle θ at liquid-solid-air contact lines. All values are at 20 °C.

B.4   Add your own constants here

Index